Orbit simulations and optical phase locking techniques for an atom interferometric test of the universality of free fall

Von der QUEST-Leibniz-Forschungsschule
der Gottfried Wilhelm Leibniz Universität Hannover
zur Erlangung des akademischen Grades

Doktor der Naturwissenschaften
Dr. rer. nat.

genehmigte Dissertation

von
Dipl.-Phys. Ulrich Velte

2018

This work is licensed under the Creative Commons Attribution-NonCommercial-ShareAlike 3.0 Unported (CC BY-NC-SA 3.0) license.

You are free to:

Share – copy and redistribute the material in any medium or format

Adapt – remix, transform, and build upon the material

for any purpose under the following terms:

Attribution – You must give appropriate credit, provide a link to the license, and indicate if changes were made. You may do so in any reasonable manner, but not in any way that suggests the licensor endorses you or your use.

NonCommercial – You may not use the material for commercial purposes.

ShareAlike – If you remix, transform, or build upon the material, you must distribute your contributions under the same license as the original.

No additional restrictions – You may not apply legal terms or technological measures that legally restrict others from doing anything the license permits.

The licensor cannot revoke these freedoms as long as you follow the license terms.

You do not have to comply with the license for elements of the material in the public domain or where your use is permitted by an applicable exception or limitation.

The license does not extend to any material that is identified as being protected by copyright owned by a third party.

Referent: Apl. Prof. Gerhard Heinzel
Korreferent: Prof. Dr. Kai Bongs, University of Birmingham
Tag der Promotion: 29. Juni 2018

Speech has allowed the communication of ideas
Enabling human beings to work together to build the impossible
Mankind's greatest achievements have come about by talking
Our greatest hopes could become reality in the future
With the technology at our disposal, the possibilities are unbounded

All we need to do is make sure we keep talking

– Pink Floyd — Talkin' Hawkin'

Abstract

The Einstein equivalence principle is the foundation of the theory of general relativity. It postulates — besides the validity of special relativity and local position invariance — the equivalence of gravitational and inertial mass, also known as the universality of free fall (UFF). Since it is a postulate, it cannot be derived from any theory we know today. The only way for its validation is the development of experiments and the continued improvement of experimental methods. The most precise results have been achieved using torsion pendulums and lunar laser ranging (LLR) so far.

Experiments involving ultra-cold atoms provide a new approach. They allow test mass materials that are not accessible by the classical tests. Considering various theories that predict a violation of the universality of free fall, I analyzed different combination of isotopes for their applicability in a cold atom test of the universality of free fall. It should be mentioned that many of the theories including a violation of the universality of free fall conflict neither with the general theory of relativity nor with the Einstein Equivalence principle. Many beyond Standard Model theories lead to an apparent violation of the equivalence principle by introducing new interaction, often referred to as *fifth force*. Hence, the search for a violation of the equivalence principle is an important topic in modern cosmology.

Meanwhile atom interferometers have evolved into highly sensitive intertial sensors. As part of the CAPRICE experiment (Cold Atom PRInCiple of Equivalence test) we have realized an atom interferometer based on Rubidium measuring the local gravitational acceleration g. Frequency stabilized laser systems are utilized for trapping and cooling the atoms in a magneto-optical trap. For the coherent manipulation of the atoms during the inteferometer sequence those laser have to be phase stabilized. I developed an optical phase-locked loop (OPLL), set up a low phase noise reference oscillator and performed measurements for the determination of the OPLL's phase noise.

The atom interferometer's intrinsic sensitivity (fundamentally limited by shot noise) is the higher, the longer the free fall period of the atomic ensemble. In ground based experiments one second free fall requires a drop distance of 10 m. As a possible answer to the limitation of drop time, we have developed the spaceborne experiment QUEST (QUantum Equivalence principle Space Test). On an orbit around Earth a violation of the equivalence of gravitational and inertial mass would lead to a difference in gravitational and centrifugal force. Together with the STE experiment (Space-Time Explorer) yielding for a test of gravitational redshift, QUEST was proposed to ESA within the scope of the Cosmic Vision program. While we envisaged a sun-syncronous orbit for maximising the sensitivity of the QUEST experiments, a highly elliptical orbit is mandatory for STE. For the joint mission STE-QUEST an orbit design incorporating the requirements of both experiments had to be found. To quantify the reduction of sensitivity caused by the orbit's ellipticity, I developed a numerical orbit simulation. During ESA's assessment period I calculated the developement of QUEST's sensitivity over a five year mission, including different orbit geometries and other effects like the impact of gravitational gradients on the atom interferometer's sensitivity. Concerning orbit geometry I could show that the target sensitivity of 10^{-15} is still feasible on the STE-QUEST joint mission.

Zusammenfassung

Das Einstein-Äquivalenzprinzip ist die grundlegende Annahme, auf Basis derer die Allgemeine Relativitätstheorie entwickelt wurde. Es postuliert neben der Gültigkeit der Speziellen Relativitätstheorie und der lokalen Positionsinvarianz insbesondere die Äquivalenz zwischen schwerer und träger Masse, bekannt auch als Universalität des freien Falls (UFF). Da es sich, wie erwähnt, um ein Postulat handelt, das sich aus keiner bisher bekannten Theorie ableiten ließe, besteht der einzig gangbare Weg zu seiner Überprüfung in der Entwicklung immer genauerer Messmethoden. Die bisher genauesten Ergebnisse konnten mit Hilfe von Torsionspendeln und *Lunar Laser Ranging* (LLR) erzielt werden.

Experimente mit ultrakalten Atomen bieten gegenüber diesen klassischen Tests einen neuen Ansatz und erlauben beispielsweise die Verwendung bisher nicht zugänglicher Testmassenmaterialien. Unter Berücksichtigung verschiedener Theorien, die eine Verletzung der Universalität des freien Falls vorhersagen, habe ich daher untersucht, welche Kombinationen von Isotopen sich besonders für den Nachweis einer solchen Verletzung eignen. Bemerkenswert ist dabei, dass ein Großteil dieser Effekte nicht im Widerspruch zur Allgemeinen Relativitätstheorie und dem Einstein-Äquivalenzprinzip steht. Viele über das Standardmodell der Teilchenphysik hinausgehende Theorien können durch Einführung einer in diesem Zusammenhang oft als *fifth force* bezeichneten neuen Wechselwirkung zu einer Abweichung von der Universalität des freien Falls und damit zu einer scheinbaren Verletzung des Äquivalenzprinzips führen. Daher ist das Thema über den Bereich der Gravitationsphysik hinaus auch innerhalb der Kosmologie von Bedeutung.

Atominterferometern lassen sich insbesondere als Intertialsensoren zur Messung von Rotationen und Beschleunigungen einsetzen. Im Rahmen des CAPRICE-Experiments (Cold Atom PRInCiple of Equivalence test) haben wir zunächst ein auf Rubidium basierendes Atominterferometer zur Messung der lokalen Erdbeschleunigung g aufgebaut. Zum Fangen und Kühlen von Rubidiumatomen werden frequenzstabilisierte Diodenlasersysteme verwendet. Für die kohärente Manipulation der Atome während der Interferometriesequenz müssen die verwendeten Laser zusätzlich eine feste Phasenbeziehung untereinander aufweisen. Neben dem Bau der Laser habe ich daher die Elektronik zur Implementierung einer optischen Phasenregelschleife entwickelt, einen phasenrauscharmen Referenzoszillator aufgebaut und verschiedene Messungen zur Bestimmung des Phasenrauschens im Gesamtsystem durchgeführt.

Die mit Atominterferometern erzielbare intrinsische Sensitivität (fundamental begrenzt durch-Schrotrauschen) ist umso höher, je länger die Atome sich im freien Fall befinden. Da für eine Fallzeit von einer Sekunde auf der Erde bereits eine Fallstrecke von 10 m benötigt wird, haben wir das Design des weltraumbasierten Experiments QUEST (QUantum Equivalence principle Space Test) vorangetrieben. Ein Unterschied zwischen schwerer und träger Masse würde in der Erdumlaufbahn als Ungleichgewicht zwischen Erdanziehung und Fliehkraft sichtbar werden. Da QUEST im Rahmen des Cosmic Vision-Programms der ESA gemeinsam mit dem STE-Experiment (SpaceTime Explorer) zum Test der gravitativen Rotverschiebung als kombinierte Mission beantragt wurde, musste ein geeigneter Orbit gefunden werden, der den Anforderungen beider Experimente gerecht wird. Während für QUEST zur Maximierung des Signals zuvor ein erdnaher, zirkularer Orbit geplant war, benötigt STE zwingend ein hochelliptisches

Orbit. Im Rahmen des Evaluierungsprozesses habe ich daher eine numerische Orbitsimulation entwickelt, mit der die zwangsläufig mit der Elliptizität verschiedener Orbitgeometrien einhergehende Reduzierung der Sensitivität quantitativ über einen Missionszeitraum von 5 Jahren untersucht wurde und weitere Effekte wie z.B. der Einfluss von Gravitationsgradienten berücksichtigt wurden. Dadurch konnten ich zeigen, dass der für die kombinierten Mission STE-QUEST vorgeschlagene hochelliptische Orbit in Bezug auf die angestrebte Sensitivität von 10^{-15} kein grundsätzliches Hindernis darstellt.

Contents

1. Introduction

> *There is a Chinese curse which says, “May he live in interesting times.” Like it or not, we live in interesting times…*
>
> — John F. Kennedy, 6 June 1966

What is said to be a curse sounds more like a blessing to scientists' ears. And as a matter of fact, we do live in interesting times. Nowadays, this is especially true for physicists working in cosmology, the field of fundamental physics that explores the origin, the evolution and the structure of the universe.

The term **cosmology** originates from Greek Κοσμολογία, “the science of the world”.

And here is why: When we try to explain the processes in the universe or even the universe as a whole, we produce maps of reality [2]. These maps are always incomplete. They may contain holes, white spaces or parts that do not fit in. On the other hand, some of these maps may be beautiful and give an intriguingly perfect image of reality. The map produced by cosmology is called the ΛCDM model. It is based on the idea that the universe evolved from a nearly pointlike initial state (the Big Bang) to the universe we observe now. Technically it is a Friedman-Lemaître universe with a non-zero cosmological constant Λ — identified with what we call *dark energy* — and Cold Dark Matter (CDM). Although containing the hypothetical dark energy, the ΛCDM model is the simplest model in agreement with observations. In the view of physicists, it is a beautiful map.

Based on the **ΛCDM model**, the results of the WMAP satellite mission (Wilkinson Microwave Anisotropy Probe) yield that the universe is 13.75 billion years old, contains 4.6% ordinary (visible) matter, 23.6% dark matter and 71.8% dark energy [63].

However, it, too, has its insufficiencies: The two main constituents of the ΛCDM model are the standard model of particle physics and Einstein's general theory of relativity. Both these individual parts are undeniably beautiful. The standard model describes the constitution of matter and the interaction within matter with an amazing accuracy. General relativity is one of the most precisely tested theories in the history of modern physics. And yet, they could not be more different: The standard model is a set of quantum field theories, based on quantum mechanics. In contrast, general relativity is a geometry of space. These two are seen as complementary, yet, since their mathematical structures are entirely different, there

In the picture of general relativity gravity is not even considered a force. Massive particles exposed to a gravitational field are supposed to be moving on straight lines — the so-called geodetics — of the curved **geometry of** Riemannian **space**.

has not been a single successful attempt to describe quantum field theories and general relativity in one unified and mathematically consistent theory of quantum gravity. Thus, the link between the standard model and general relativity is one of the white spaces in our map.

Although gravity is by far weaker than for example the electro-magnetic interaction, it is the dominating interaction on cosmological **length scales**. Positive and negative electro-magnetic charges neutralise each other and the universe is electrically neutral. But there is no corresponding anti-charge within the gravitational interaction. Thus, gravity is the only remaining long-range interaction acting on cosmological length scales that we currently know.

One might argue, if there is no obvious way to melt the two theories together, why do so in the first place? After all, they are working perfectly well in their domains, and — due to the different length scales — are complementary. So, is it mandatory to have a unified theory of everything? Some say, the strive for a theory of everything is merely for elegance's sake, but elegance alone is not enough to prove a theory to be mandatory.

However, apart from the "missing link" between quantum field theories and the general theory of relativity, there are other white spots on our ΛCDM map, that the standard model of particle physics and general relativity are not able to fill. Lee Smolin once said about the standard model of particle physics [154]:

> *The fact that there are that many freely specifiable constants in what is supposed to be a fundamental theory is a tremendous embarrassment.*

Lee Smolin (* 1955 in New York City) is an American theoretical physicists. He mainly works on quantum gravity — particularly loop quantum gravity — and also contributed to cosmology [107].

Furthermore, neither the standard model of particle physics nor general relativity imply an explicit physical theory for the origin and the physical nature of dark matter and dark energy. For dark matter, there is at least indirect evidence. In fact, most of the candidates for dark matter originate from theories beyond standard model, the most common being supersymmetry. Unfortunately, there is no experimental evidence for any of these candidates. The situation is even worse for dark energy. There are merely some ideas, like for example quintessence [175, 167], but neither is there experimental evidence, nor are any of these ideas backed by observations. The most severe problem of those ideas might be that they hardly make any predictions that could be tested with our current repertoire of experimental methods.

It is these holes in our map that make science and the times we live in particularly interesting.

The Theory of Everything and the Universality of Free Fall

Quantising gravity has not helped to unify general relativity and quantum field theory. An entirely different approach towards a theory of everything is string theory. Opposed to the standard

String theory is not a sole theory, but a theoretical framework for theories with similar characteristics. The basic idea is to represent the pointlike elementary particles of the standard model by one-dimensional objects called strings, usually living in more than 4 dimensions. Initially sneered at, string theory has arrived in the mainstream physics community during the 1980s. The hope of theoretical physicists is that dumping many of the characteristics of the established theories might be the loophole to overcome the problems of modern cosmology. Promising candidates are super string theories, a group of string theories including the ideas of supersymmetry. Related to string theory is supergravity (SUGRA), a field theory combining the principles of supersymmetry and general relativity. The different kinds of superstring theories and supergravity are believed to be special cases of an even more fundamental 11-dimensional theory called M-theory.

model of particle physics, string theory naturally includes gravity; and there are actually string theories that contain consistent explanations for the occurrence of dark energy [178]. String theory is not the only option to go beyond the standard model, but many beyond-standard-model theories have one thing in common: They include a violation of the equivalence principle [1, 11, 21, 22, 34, 33, 73, 88, 102, 120, 177]. Especially in string theory the existence of UFF violating fields is assured [178]. This is why testing the equivalence principle is so important to fundamental physics.

But what do we actually mean when we talk of "testing the equivalence principle"? Due to the fact that different equivalence principles have been formulated, this is ambiguous. The term *equivalence principle* goes down to Albert Einstein. In his *Essays in Science* he refers to [44]:

> *...the old experimental fact that all bodies have the same acceleration in a gravitational field.*

We might regard this finding as our first formulation of what is called the Universality of Free Fall (UFF). Based on the UFF, Einstein introduced the hypothesis of the complete equivalence of gravitational fields and accelerated systems, which he called "the principle of equivalence" [44]:

> *In a homogeneous gravitational field all motions take place in the same way as in the absence of a gravitational field in relation to a uniformly accelerated co-ordinate system.*

This — the equivalence of inertial and gravitational mass — is the only equivalence principle formulated by Einstein himself. For Einstein it *"was an indication that the principle of relativity needed to be extended"*, in order to reach a theory of the gravitational field [44]. Hence, the UFF is one of the most basic assumptions the general theory of relativity relies on.

The UFF is sometimes called the Weak Equivalence Principle (WEP). However, to avoid confusion with other *equivalence principles* — the strong equivalence principle and the Einstein equivalence principle — we will use the term *universality of free fall* throughout this thesis.

Albert Einstein (* 1879 in Ulm, † 1955 in Princeton, New Jersey) probably was the most famous physicists of all times. The impact of his work is not restricted to the theory of relativity. The award ceremony speech of the Nobel prize Einstein received *for his services to Theoretical Physics, and especially for his discovery of the law of the photoelectric effect* in 1922, dignifies the theory of relativity, his explanation of the Brownian motion and his contribution to quantum theory. His career progression, however, was far from being straightforward. As pupil he was reckoned rather strange than talented. He completed his degree as teacher for mathematics and physics in 1900, but took up a job at Swiss patent office, where he was isolated from the scientific community. In 1909 word of his revolutionary theories got around in the physics community. Not till then he took up his academic career in Zürich, Prague and Berlin. However, his scientific reputation did not guard him from the Nazis. His books were burned in Berlin in 1933 and Einstein left for the USA, never to return to Germany. [151, 150, 76]

Don't confuse **Einstein's equivalence principle** (the one he formulated himself) with the **Einstein equivalence principle** (named after Einstein, but formulated by others) [93]. See chapter 2 for a detailed discussion.

Violations of the UFF

As we already mentioned, the general theory of relativity does not imply the UFF, but vice versa: The UFF itself is the most basic assumption the theory relies on.

So why question the UFF? From Newton's point of view, the UFF appears to be quite a natural thing. In fact, this can already be found in Newton's equation of motion for a massive body in an external gravitational field:

$$m \cdot \vec{a} = m \cdot \vec{g} \tag{1.1}$$

Attributing an gravitational field as **external** gravitational field basically refers to the case that the gravitational field is not influenced by the body itself. See the remarks on test masses on page 13.

Since we can cancel m on both sides of (1.1), yielding $\vec{a} = \vec{g}$, the motion of a massive body in a given gravitational field is independent from the body's mass. However, it is not at all that straight forward. When we canceled the mass m in equation (1.1) we assumed that the left-hand side m is actually the same as the right-hand side m. On the left-hand side we have the inertial mass, determining the body's inertia. On the right-hand side we have the gravitational mass, which determines how the body is attracted by the gravitational field. Both, the body's inertia and the body being influenced by gravity, are completely different concepts, whose only connection is equation (1.1). This was already noticed by Heinrich Hertz in *Die Constitution der Materie*, published in 1884 (translation taken from [93]):

> *Even in textbooks it is usually presented as something obvious and hardly worth mentioning that the gravity of a body, its weight, is proportional to its* [inertial] *mass, independent of the substance it is made of. And yet, in reality, we are dealing with two properties, two essential properties, of matter which may be contemplated quite independent of one another and which prove by experience, and only by it, to be completely equivalent. This coincidence is rather to be considered a most wonderful mystery which requires an explanation.*

Only the mass of free elementary particles — for instance the proton is composed of quarks and thus not elementary — is generated by the Higgs mechanism. This mass is called the rest mass. Only 6 % of a proton's mass is actually due to the rest mass of the contained quarks. The missing 94% are caused by **binding energy** constituted of the strong interaction between the quarks.

Although this thought is more than 100 years old, the mystery remains. If a particle's mass is mostly governed by its binding energy content via $E = mc^2$ (Einstein), but the rest mass of its elementary constituents is determined by the Higgs mechanism (QFT): Might there be a difference of those contributions to inertial mass on the one hand and gravitational mass on the other hand? There is no *higher* theory or concept that would imply inertial and gravitational mass being the same.

The quantum field theories of the 1960s had one weakness: They did only work with massless elementary particles. The **Higgs mechanism** — developed independent from one another by the British physicist Peter Higgs (*1929 in Newcastle upon Tyne) and the Belgian physicist François Englert (*1932 in Etterbeek) — is a mathematical trick to fix the shortcomings of these early quantum field theories. The Higgs mechanism was confirmed, when experimental evidence for the existence of the Higgs boson was found at the Large Hadron Collider (LHC) in 2013 [9]. In 2013 Higgs and Englert were awarded the Nobel prize *"for the theoretical discovery of a mechanism that contributes to our understanding of the origin of mass of subatomic particles [...]".* [76]

Why do we search for violations of the UFF? In the first place, the answer might seem quite obvious: After all the equivalence principle is still a postulate. For physicists that is an inadmissible condition, for they always seek for the most basic mechanisms underlying experimental observations.

But there is more to it. As mentioned above, some beyond-standard-model theories provide good reasons to actually believe that the

UFF is violated at some point. This could, but does not necessarily mean that Einstein's theory is wrong. An alternative explanation would be the existence of an additional macroscopic force, coupling to other properties of matter than its mass. If this *fifth force* was composition dependent and if it would act on length scales comparable with gravity, then it makes test masses fall differently in a given gravitational field. This would lead to an apparent violation of the UFF, but leaves gravity untouched. Although in most cases string theory is not yet capable of calculating their strength, the existence of UFF violating fields is assured in string theory [178]. Even though there is no experimental evidence for string theory yet, our technical possibilities slowly approach the accuracy neccessary to experimentally check the predictions of beyond-standard-model theories. Thus, observing a violation of the equivalence principle might be the first experimental hint towards string theory.

In a nutshell: Since a violation of the UFF is not possible within the range of general relativity it would either imply that general relativity is wrong or it would be a hint to hitherto unknown physics.

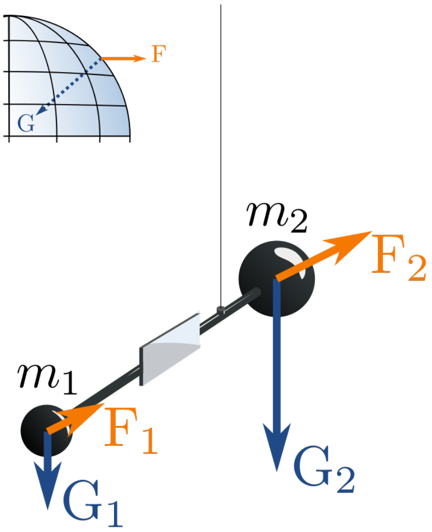

Figure 1.1.: The Eötvös experiment basically consists of two test masses, m_1 and m_2, attached to opposite ends of a bar. The bar is suspended from a thin fiber, which acts as very weak torsion spring. The test masses experience two forces (small picture): the gravitational force directed towards the centre of the Earth and, due to the rotation of the Earth, the (inertial) centrifugal force. If the equivalence between gravitational and inertial mass holds the forces cancel out exactly, independent the test masses' constitution and mass. Since the forces are in equilibrium, the bar rotates with the Earth rotation, which corresponds to a zero rotation seen from the lab system. A violation of the equivalence principle would unbalance the forces resulting in a net torque. In the lab frame of reference this would be seen as a spontaneous rotation. [151]

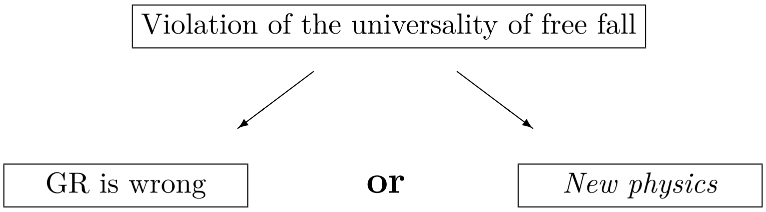

The search for a violation of the UFF plays an important role of understanding the universe and completing our current map of fundamental physics. Since in natural sciences pure logic often comes to its limitations, it is experiments leading the way into exploring the white spots of our map.

A short history of UFF tests

The universality of free fall is under investigation since ancient times. In the strict hierarchy of the Aristotelian system the case is clear: Heavy bodies strive downwards, light ones upwards. This is equivalent to the statement that heavier bodies fall faster than lighter ones. In the 6th century John Philoponus held a completely different view. In his comments on Aristotle — *Aristoteles physicorum libri* — he writes that the peripatetic dynamics of the Aris-

John Philoponus (* around 490 in Alexandria, † around 570) was a Byzantine theologian and physicist. Among others he wrote several works in which he analyses Aristotle's works. [151]

totelian system with respect to the free fall of massive bodies can be refuted by actual observations:

> *If we drop two weights from equal height, while one shall be much heavier than the other, we notice that the ratio of the times needed for the motion is independent from the ratio of the masses: The difference between the drop times is very small.*

This is not yet the universality of free fall, since it only states a *very small* difference. One of the first resources for a null result — backed by experiments — comes from Simon Stevin. In his book *De Beghinselen der Weeghconst*, published in 1586, he describes the following experiment:

> *We take two lead balls, where one is ten times in size and weight as the other, and simultaneously drop them from a height of 30 feet* [...]. *We will notice* [...], *that the balls hit the [ground] that simultaneously, that the two sounds appear to be one and the same.*

Simon Stevin (* 1548 in Bruges, † 1620) was a Flemish mathematician. After working as book-keeper and tax collector he started his academic studies at University of Leyden at the age of 35. Besides his works on free fall he introduced the parallelogram of forces and dealt with decimal fractions, hydrostatics and magnetism. [151]

A modern version of this kind of free fall experiments using macroscopic test masses (copper and depleted uranium) was performed by Niebauer et al. in 1987 yielding $\eta \leq 5 \cdot 10^{-10}$ [161].

However, modern precision experiments using macroscopic test masses are based on torsion balances as first performed by Lorand Eötvös. (see figure 1.1). His original experiment yielded $5 \cdot 10^{-8}$ for certain test mass materials already in 1890 [45]. In a later version the sensitivity was increased to $1 \cdot 10^{-8}$ [168]. The experiment was afterwards repeated many times by various scientists, e.g [137]. A modern version is the experiment of the Eöt-Wash group, which is performed since 1987. In 2008 they yielded and Eötvös ratio of $(0.3 \pm 1.8) \cdot 10^{-13}$ for titanium and beryllium [141].

Baron Loránd Eötvös de Vásárosnamény (* 1848 in Buda, † 1919 in Budapest) was a Hungarian physicist. He is renowned for his work on surface tension and above all for his research in the Earth's gravity field. The University of Budapest, where he researched from 1886 until his death, was renamed *Eötvös Loránd University* in 1950. Finally, since the spelling of his name is a constant source of confusion: ['lora:nd 'øtvø∫]. [151, 166]

Lunar Laser Ranging (LLR) — which is the only experimental test sensitive to the Nordtvedt effect (see section 2.2.2) — achieved $\eta = (1.0 \pm 1.4) \cdot 10^{-13}$ [180].

Tests using quantum objects have not yet reached the preceding level of precision. Basically there are two types of tests involving quantum objects: those comparing the acceleration of matter waves to classical objects [61, 118] and those comparing the acceleration of two matter waves composed from different atomic species [78, 18, 142, 162, 187]. An overview including the achieved Eötvös ratio η is given in table 1.1.

The earliest demonstration of an UFF test including quantum objects was performed in 1975 using neutrons [28]. The first experiment involving an atom interferometer compared the fall of ^{133}Cs

Experiment	Test masses (A,B)	$\eta_{\mathrm{A,B}}$	Ref.
Palo Alto	(^{133}Cs, SiO$_2$)	$(7.0 \pm 7.0) \cdot 10^{-9}$	[61]
Paris	(^{87}Rb, SiO$_2$)	$(4.4 \pm 6.5) \cdot 10^{-9}$	[118]
München	(^{85}Rb, ^{87}Rb)	$(1.2 \pm 1.7) \cdot 10^{-7}$	[78]
Palaiseau	(^{85}Rb, ^{87}Rb)	$(1.3 \pm 3.2) \cdot 10^{-7}$	[18]
Wuhan	(^{85}Rb, ^{87}Rb)	$(2.8 \pm 3.0) \cdot 10^{-8}$	[187]
Hannover	(^{87}Rb, ^{39}K)	$(0.3 \pm 5.4) \cdot 10^{-7}$	[142]
Firence	(^{87}Sr, ^{88}Sr)	$(0.2 \pm 1.6) \cdot 10^{-7}$	[162]
Wuhan[1]	(^{87}Rb, ^{87}Rb)	$(0.2 \pm 1.2) \cdot 10^{-7}$	[41]

Table 1.1.: Performed UFF tests involving quantum objects. SiO$_2$ refers to the (macroscopic) corner cube included in the FG5 gravimeter.
— [1] Compares atoms with opposite spin orientation (m_F=-1 vs. m_F=+1).

with that of a corner cube (FG5) and achieved $\eta \approx 10^{-8}$ in 1999 [61]. A comparison of ^{85}Rb and ^{87}Rb using an atom interferometer has been performed in 2007 [78]. However, since the measurements were performed sequentially, the experiment could not benefit from common noise suppression. Thus, the sensitivity of $\eta \approx 10^{-7}$ is low compared to the classical tests. The first simultaneous measurement in a Raman-type dual atom interferometer operated with ^{87}Rb and ^{39}K has been performed in 2013 at the CAPRICE experiment. Since at that time it was in the state of a proof-of-principle measurement it yielded an Eötvös ratio of only $\eta_{(\mathrm{Rb,K})} = (0.3 \pm 5.4) \cdot 10^{-7}$ [142], however, with the clear perspective to achieve an improvement by technical optimisation of the apparatus.

As the classical techniques are essentially exhausted major achievements in sensitivity can only be achieved with new concepts, basically meaning space-borne experiments. There are several projects curently being discussed and aiming for $\eta < 10^{-15}$. Please see section 5.1 for further details on planned space-borne missions.We will present QUEST (QUantum Equivalence principle Space Test) as part of the joint STE-QUEST mission in chapter 5 and discuss its sensitivity in chapter 6.

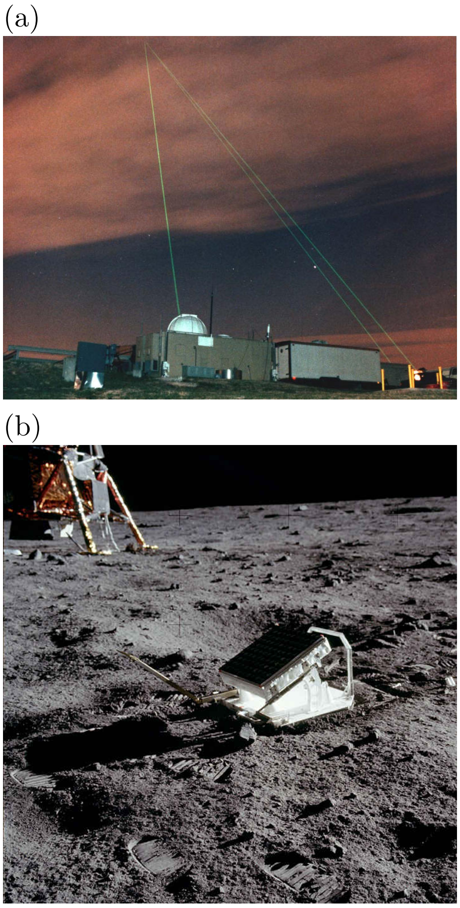

Figure 1.2.: (a) Lunar laser ranging is routinely performed at the Goddard Geophysical and Astronomical Observatory [123]. (b) Retroreflector left on the moon on the Apollo 11 mission [124].

The Scope of this Thesis

This thesis covers three different aspects related to spaceborne tests of the UFF using atom interferometers. Each of the three aspects is covered in one separate part.

Part I covers the theoretical background of the UFF. **Chapter 2**

introduces the mathematical formulation of the UFF within Newtonian mechanics, discusses the enhanced scheme of the Einstein Equivalence Principle (EEP) and gives a survey on theories that are a potential origin of UFF violations. With this theoretical basis, **chapter 3** specifically focuses on the issue of cold atoms as test masses in UFF testing. The question is, whether they provide any advantage compared to macroscopic test masses or provide insight into effects that cannot be accessed with macroscopic test masses. If so, how must tests using cold atoms be designed in terms of test mass configuration to not only show a UFF violation, but also allow for insights into its origin? The results of part I are summarised and discussed in **section 3.6**.

QUEST is a mission concept for a spaceborne test of UFF using an atom interferometer. It is a technical successor of the earlier mission proposals HYPER [47] and MWXG [46]. It was proposed in 2012 as part of the joint mission **STE-QUEST** (Space Time Explorer and Quantum Equivalence Principle Space Test) within ESA's Cosmic Vision program [52].

Part II looks into the aspect of spaceborne UFF testing using the example of Quantum Equivalence Principle Space Test (QUEST). This mission is a spaceborne dual atom interferometer using the test mass pair ^{85}Rb/^{87}Rb. In **chapter 4**, we start with a general technical description of atom interferometers used as accelerometers for UFF testing. **Chapter 5** describes and summarises the design of the STE-QUEST mission and discusses the scope of spaceborne UFF tests in general. One of the challenges in spaceborne testing is the calculation of the instrument's integrated sensitivity. The contribution of this thesis is the development of a numeric simulation of sensitivity, subject to orbit design. **Chapter 6** describes the design and functionality of this simulation and can also be used as a tutorial to use this numeric simulation. The C++ source code can be found in appendix B. Here, the simulation is applied to the sensitivity of the STE-QUEST mission in the *baseline orbit*, resulting in recommendations for orbit optimisation (section 6.3). The general summary of part II can be found in **section 6.4**.

The **Cold Atom test of the PRInCiple of Equivalence (CAPRICE)** is a lab-based test of the UFF, based on a dual atom interferometer using ^{85}Rb and ^{39}K. Besides demonstrating the first test of the UFF using a dual atom interferometer [142], it also served as a test bed for techniques that were later implemented within the QUANTUS project and thus contributed to the technical advancement towards spaceborne atom interferometers.

Part III looks into a far more technical aspect of atomic accelerometers: Optical phase locking of lasers. **Chapter 7** provides the theoretical background of phase-locked loops (PLL), in particular their mathematical description using Laplace transforms. **Chapter 8** describes the “OPLL reference setup”, which was implemented at the CAPRICE atom interferometer. We used the Laplace transforms described in chapter 7 to model the transfer function of the OPLL reference setup. The model was confirmed and calibrated with experimental measurement of the loop's actual transfer function. The final model can be found in section 8.5; the corresponding `Mathematica` source code is in appendix D. In **chapter 9**, we assess the phase noise in the OPLL reference setup. The crucial question is: Can the transfer function model developed in chapter 8 be used to understand the loop's behaviour and determine the individual components' impact on loop performance? This would allow for a prediction of the behaviour of any OPLL of this type and systematically optimise its performance. Based on this, we developed recommendations for optimisation of the OPLL reference setup as implemented at CAPRICE in section 9.4. The results of part III are summarised and discussed in **section 9.5**.

In **chapter 10**, the essential results of the three parts as presented in sections 3.6, 6.4 and 9.5 are discussed in the wider context of spaceborne atom interferometer missions. We draw conclusions on feasibility, specific challenges of spaceborne missions as opposed to lab-based experiments, the technical progress in building more compact and reliable atom interferometers achieved in the QUANTUS project and we also make crucial recommendations, in particular related to phase-noise.

Part I.

The Universality of Free Fall

The equivalence principle (EP) is a mystery that has been puzzling physicists for decades. Being the foundation of Einstein's theory of general relativity, it is a postulate backed by observation only. It cannot be explained by any theory we know. One of the core implications of the EP as was formulated by Einstein himself is the universality of free fall (UFF). Being a postulate it is challenged by continuous efforts to find a violation. Atom interferometers provide exciting new possibilities within this search. We will start with a review of the mathematical nature of the UFF, discuss possible mechanisms for its violation and finally analyse the potential of atom interferometers within the scope of possible UFF violations.

2. Theory of the Equivalence Principle

In this chapter we will shed light on the mathematical details of the equivalence principle. We start with expressing the Universality of Free Fall (UFF) within the framework of Newtonian mechanics in section 2.1. This will enable us to define a measure for deviations from the equivalence of inertial and gravitational mass, the Eötvös ratio. In section 2.2 we look at the Einstein Equivalence Principle (EEP), which nowadays is the common canonical formulation of the equivalence principle being the basis of the General Theory of Relativity (GTR). Afterwards we ask the question what might lead to a violation of the UFF. There are various mechanisms, that propose a violation of the UFF, but none of them has been observed yet. We will finally discuss in chapter 3 if there are combinations of test mass materials that are preferable over others, to maximise the chance of seeing the predicted violation.

2.1. The Universality of Free Fall within Newtonian Mechanics

To understand the UFF within Newtons framework, we will start with Newton's equation of motion for a test mass m in an external gravitational field g:

$$\mathrm{m} \cdot \ddot{\vec{x}} = \mathrm{m} \cdot \vec{g} \quad . \tag{1.1}$$

We derived the UFF from the assumption, that the inertial mass on the left-hand side of (1.1) cancels the gravitational mass on the right-hand side. As a start, we want to discuss the different mass terms. Within Newtonian mechanics we can even distinguish three terms of mass [93]: The inertial mass, the active gravitational mass and the passive gravitational mass. We assume a pointlike test mass at point $\vec{x}$. The **inertial mass** determines a response force $\vec{F}_\mathrm{i}$ to an imposed acceleration, relative to an inertial frame of reference:

$$\vec{F}_\mathrm{i} = m_\mathrm{i} \cdot \ddot{\vec{x}} \quad . \tag{2.1}$$

What is a **test mass**? No higher multipoles in mass distribution, no charge, no spin, no significant gravitational self-energy! The latter requirement does imply, that the test mass must not be too small, because the concentration of its mass to a very small volume would result in a significant gravitational self-energy. So, how small is pointlike? Much smaller than typical length over which g varies appreciably. Obviously, there are no ideal test masses. But especially with respect to atom interferometry we can claim, that neutral atoms are at least a good approximation of a test mass, since they provide some properties (small, no higher multipoles in mass distribution), which are very difficult to achieve with macroscopic test masses. However, irrespective of wether using atoms or macroscopic masses, there are no ideal test masses, which do only couple to gravity. Therefore it is impossible to make a gravity-only test of the equivalence principle! [93]

The force on a massive body in a given gravitational field $\vec{g}(t,\vec{x})$ is governed by the **passive gravitational mass**:

$$\vec{F}_{\mathrm{g}} \;=\; m_{\mathrm{g,p}} \cdot \vec{g} \quad . \tag{2.2}$$

Vice versa the mass determining the gravitational field created by a massive body is called **active gravitational mass**. For a pointlike massive body sitting at $\vec{y}$ we get

$$\vec{g}(\vec{x}) \;=\; \mathrm{G} \cdot m_{\mathrm{g,a}} \cdot \frac{\vec{y}-\vec{x}}{\|\vec{y}-\vec{x}\|^3} \quad , \tag{2.3}$$

with the gravitational constant G. However, it can be easily shown, that the ratio $m_{\mathrm{g,p}}/m_{\mathrm{a,p}}$ between active and passive gravitational mass must be a universal constant. Assume two pointlike particles A and B at $\vec{x}_A$ and $\vec{x}_B$ respectively. The force on particle A arising from B's gravitational field $\vec{g}_B(\vec{x})$ is

$$\vec{F}_{AB} \;=\; m_{\mathrm{g,p}}^{(A)} \cdot \vec{g}_B(\vec{x}_A) \;=\; \mathrm{G} \cdot m_{\mathrm{g,p}}^{(A)} \cdot m_{\mathrm{g,a}}^{(B)} \cdot \frac{\vec{x}_B-\vec{x}_A}{\|\vec{x}_B-\vec{x}_A\|^3} \quad . \tag{2.4}$$

We get the analog expression for the force on particle B in particle A's gravitational field $\vec{g}_A(\vec{x})$:

$$\vec{F}_{BA} \;=\; m_{\mathrm{g,p}}^{(B)} \cdot \vec{g}_A(\vec{x}_B) \;=\; \mathrm{G} \cdot m_{\mathrm{g,p}}^{(B)} \cdot m_{\mathrm{g,a}}^{(A)} \cdot \frac{\vec{x}_A-\vec{x}_B}{\|\vec{x}_A-\vec{x}_B\|^3} \quad . \tag{2.5}$$

From Newton's *actio* $=$ *reactio* follows

$$\vec{F}_{AB} \;=\; -\vec{F}_{BA} \quad \Leftrightarrow \quad \frac{m_{\mathrm{g,p}}^{(A)}}{m_{\mathrm{g,a}}^{(A)}} \;=\; \frac{m_{\mathrm{g,p}}^{(B)}}{m_{\mathrm{g,a}}^{(B)}} \quad . \tag{2.6}$$

Since this only fixes the ratio $m_{\mathrm{g,p}}/m_{\mathrm{g,a}}$ but not the absolute values of $m_{\mathrm{g,p}}$ and $m_{\mathrm{g,a}}$ we are free to choose

Note that by choosing $m_{\mathrm{g,p}}/m_{\mathrm{g,a}} = C$ we only scale the gravitational constant G with the factor C. By setting $C=1$ we adjust the gravitational constant to the common value $\mathrm{G} = 6.67 \cdot 10^{-11}\,\mathrm{m}^2/\mathrm{kgs}^2$.

$$\frac{m_{\mathrm{g,p}}}{m_{\mathrm{g,a}}} \;\equiv\; 1 \quad . \tag{2.7}$$

We will not distinguishing active and passive gravitational mass anymore, but only talking of **the** gravitational mass m_{g} from now on.

How about gravitational mass m_{g} and inertial mass m_{i}? Equalising (2.2) and (2.1) yields

$$m_{\mathrm{g}}\vec{g} \;=\; m_{\mathrm{i}}\ddot{\vec{x}} \quad . \tag{2.8}$$

For two test masses, A and B, sitting in an external gravitational field $\vec{g}$ at the exact same place $\vec{x}$ we get

$$\ddot{\vec{x}}_A(t) = \left(\frac{m_\mathrm{g}^{(A)}}{m_\mathrm{i}^{(A)}}\right)\vec{g}(t,\vec{x}(t)) \qquad \ddot{\vec{x}}_B(t) = \left(\frac{m_\mathrm{g}^{(B)}}{m_\mathrm{i}^{(B)}}\right)\vec{g}(t,\vec{x}(t)) \quad . \tag{2.9}$$

What remains unexplained is the nature of the ratio $m_\mathrm{g}/m_\mathrm{i}$. Let's assume for a while, that the UFF holds, that is the test masses A and B experience the same accelerate, $\ddot{\vec{x}}_A(t) = \ddot{\vec{x}}_B(t)$. Then (and only then) equating the left side of (2.9) with the right side of (2.9) leads to

$$\frac{m_\mathrm{g}^{(A)}}{m_\mathrm{i}^{(A)}} = \frac{m_\mathrm{g}^{(B)}}{m_\mathrm{i}^{(B)}} \quad . \tag{2.10}$$

This means $m_\mathrm{g}/m_\mathrm{i}$ is a universal constant and the motion of a pointlike test mass in an external gravitational field depends only on its initital position and velocity. By appropriate choice of units we even yield $m_\mathrm{g}/m_\mathrm{i}$ to be unity. However, this assumption is arbitrary, a postulate so to say. There is no fundamental physics-determining $m_\mathrm{g}/m_\mathrm{i} \equiv 1$!

This statement is only valid for *test masses* as defined on page 13. Higher multipoles in the mass distribution can change the drop rate of A and B even if $m_\mathrm{g}/m_\mathrm{i} \equiv 1$ is true.

The Eötvös Ratio

When comparing different tests of UFF this is often done by comparing the relative difference in acceleration of two test masses towards a third massive body. The natural choice for a composition-dependent parameter would be $m_\mathrm{g}/m_\mathrm{i}$. For the comparison of two test masses A and B we hence use the difference

$$\eta(A,B) = \left|\frac{m_\mathrm{g}^{(A)}}{m_\mathrm{i}^{(A)}} - \frac{m_\mathrm{g}^{(B)}}{m_\mathrm{i}^{(B)}}\right| \quad , \tag{2.11}$$

the so-called Eötvös ratio. We have to admit that in the form of (2.11) η is of no practical use, since the only gaugeable parameter accessible in free fall experiments is acceleration. We can again make use of (2.8) to express $m_\mathrm{g}/m_\mathrm{i}$ in terms of accelerations,

$$\frac{m_\mathrm{g}}{m_\mathrm{i}} = \frac{a}{g} \quad , \tag{2.12}$$

where a is the acceleration of the test mass in the gravitational field g. Put into (2.11) this yields

$$\eta(A,B) = \frac{|a_A - a_B|}{g(r)} \quad , \tag{2.13}$$

The Eötvös ratio η is neither to be mistaken for the Nordtvedt parameter η (violation of $\mathrm{m}_i = \mathrm{m}_g$ due to gravitational self-energy contribution, see section 2.2.2), nor for the post-newtonian parameter η (difference between radial and transverse stress on gravity in beta-delta noation). Furthermore, it is neither identical with the eotvos, a unit used for the gravitational field gradient, nor with the Eötvös number, a concept in fluid dynamics.

with a_A and a_B being the measured accelerations of two test masses. This is used for space-borne test of the UFF. On ground based experiments we make use of the fact that the violation — if it even exists — is very small and thus

$$g \approx \frac{1}{2}(a_A + a_B) \quad . \tag{2.14}$$

Hence we get

$$\eta(A,B) = 2 \cdot \frac{|a_A - a_B|}{(a_A + a_B)} \quad , \tag{2.15}$$

which is the most prevalent form of the Eötvös ratio.

2.2. The Einstein Equivalence Principle (EEP)

In the previous chapter we learned that on Einstein's way to the general theory of relativity the equivalence principle was of central importance. We also learned it implies the UFF. Furthermore Einstein assumed that the laws of special relativity are still valid in a more general theory of gravity. Finally, the cosmological principle states that the universe is homogenous and isotropic. In other words:

1. All bodies in a given gravitational field fall in the same way.
2. The outcome of any local non-gravitational test experiment is independent of the velocity of the (freely falling) apparatus.
3. The outcome of any local non-gravitational test experiment is independent of where and when in the universe it is performed.

Although the terms **Einstein equivalence principle** and Einstein's equivalence principle are often misleadingly used synonymously, we should note that they strictly speaking denominate two different things [93]. Einstein himself never formulated the Einstein equivalence principle in the canonic form as presented here, but named the equivalence of accelerated systems and gravitational fields as *equivalence principle* [44]. Literally speaking, Einstein's equivalence principle thus denotes the equivalence principle as formulated by Einstein himself, which is different from the Einstein equivalence principle, that we are about to introduce here.

This is what we call the **Einstein Equivalence Principle (EEP)**. It is usually canonised in the form depicted in figure 2.1. According to Clifford Will [178] the canonical form goes back to Robert Dickes *"influential Les Houches lectures of 1964"*, where he summarised the ideas about the foundations of gravity he developed in the preceding years.

The EEP is the foundation of the general theory of relativity. To stress it once more: It cannot be derived from GTR. It was put into the theory as a basic assumption!

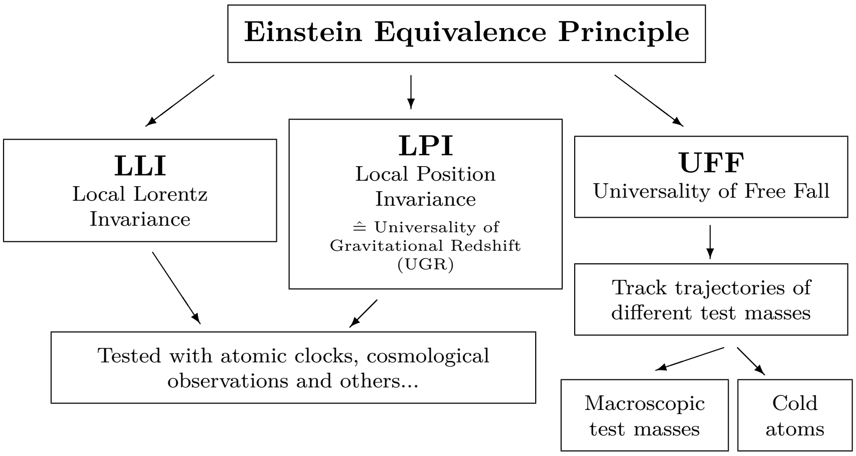

Figure 2.1.: The Einstein equivalence principle: Here Local Lorentz Invariance (LLI) represents the laws of special relativity while Local Position Invariance (LPI) assures the validity of the cosmological principle. Local position invariance can be tested by measurements of the gravitational redshift (Not to be mistaken for the cosmological redshift!) [178]. Therefore the EEP is often described to comprise, besides UFF and local Lorentz invariance, the Universality of the Gravitational Redshift (UGR) instead of local position invariance.

2.2.1. The Equivalence Principle within Metric Theories

When we push forward into the jungle of GTR, we will soon realise, that the EEP does not necessarily imply Einstein's general theory of relativity. In fact it is rather the more general class of metric theories, that already complies with the postulates of the EEP. Therefore usually only metric theories or theories that are metric apart from short-range or weak non-metric couplings (e.g. string theory) are considered applicable as theories of gravity. Metric theories fulfill the following conditions [178]:

1. there exists a symmetric metric
2. test masses follow geodesics of the metric
3. in local Lorentz frames, the non-gravitational laws of physics are those of the Special Theory of Relativity (STR)

This is also a canonisation of the EEP [87]. All metric theories state, that — besides matter — also all non-gravitational fields respond only and in the same manner to the spacetime metric g. This assumption is sometimes called *universal coupling*. Its implication however is that the metric must be a property of spacetime itself rather than a field over spacetime [178]. This sustains the notion of gravity being a geometry of spacetime itself as opposed to the quantum field theories, that constitute the standard model.

With equations (2.11) and (2.15) we introduced the Eötvös ratio as a measure for possible violations of the UFF. However, even if finding a non-zero value, the Eötvös ratio does not give us any insight into the underlying mechanism. To reveal the origin of the violation, we have to introduce model-specific assumptions into our considerations. Within the scope of metric theories the idea behind violations of the UFF is the following: Various forms of energy contribute to the mass of a body. For instance, the rest mass of the three quarks constituting the proton — *uud* — is only ∼6% of the protons rest mass. The remaining amount is binding energy, primarily caused by the strong interaction keeping the quarks together with minor contributions from other forces. If the relative contribution to inertial mass m_i and gravitational mass m_g differed among the fundamental interactions, this can be expressed as

$$m_{\mathrm{g}} = m_{\mathrm{i}} + \sum_\alpha \eta^\alpha \frac{E_\alpha}{m_{\mathrm{i}} c^2} \quad , \tag{2.16}$$

with α labeling the fundamental interactions. E_α is the energy contribution of interaction α to the particle's rest mass. The η^α are universal constants, which do not depend on the test mass' composition, but only on the interaction α. Putting (2.16) into (2.11), the Eötvös ratio for test masses A and B becomes [87]:

It is worth mentioning, that (2.17) features four variables. It cannot be solved with only one single experiment! Finding values for all η_α using free fall experiments requires at least four independent pairings of test mass materials A and B.

$$\eta(A,B) \approx \sum_\alpha \eta^\alpha \left(\frac{E_\alpha^{(A)}}{m_{\mathrm{i}}^{(A)} c^2} - \frac{E_\alpha^{(B)}}{m_{\mathrm{i}}^{(B)} c^2} \right) \quad . \tag{2.17}$$

If the EEP is valid, the η^α for strong, electromagnetic and weak interaction have to be zero. This is compatible with observations so far, as the experimental bounds are [178]:

$$|\eta^{\mathrm{S}}| < 5 \cdot 10^{-10}, \quad |\eta^{\mathrm{EM}}| < 4 \cdot 10^{-10}, \quad |\eta^{\mathrm{W}}| < 2 \cdot 10^{-2} \quad .$$

2.2.2. The Nordtvedt Effect

A special case is gravitational self-interaction. The parameter η^{N}, which is experimentally bound to $|\eta^{\mathrm{N}}| < 4.4 \cdot 10^{-4}$ [178], is known as the Nordtvedt parameter. It refers to the Nordtvedt effect, which states that the gravitational self-energy of a body contributes to its gravitational mass only, but not to its inertial mass. This implies a violation of the UFF, according to (2.17). However, the EEP is restricted explicitly to experiments, where the self-gravitation of the test mass can be neglected. Hence, the observation of the Nordtvedt effect would not violate the EEP. Thus — although not present in GTR — it is fully compatible with metric theories in general.

A more restrictive formulation, which also forbids the Nordtvedt effect, is called the **Strong Equivalence Principle (SEP)**. If it holds, the postulates of the EEP are valid not only for test masses, but also for self-gravitating bodies and experiments involving gravitational forces [178]. Most tests of the UFF are designed with respect to the EEP. That is, the test masses are intentionally designed such, that their gravitational self-interaction can be neglected. Hence, they are not sensitive to effects that violate the SEP, while leaving the EEP untouched. The only exception is Lunar Laser Ranging (LLR), which uses Earth and Moon — obviously having significant gravitational self-interaction — as test masses, while they fall around the Sun. Among the range of experiments probing the UFF, lunar laser ranging its the only one that could possibly make a point between GTR and other metric theory, which do not obey the SEP. The current experimental bound for violations of the SEP is [180]

$$\eta\,(\mathrm{Earth}, \mathrm{Moon}) \;\leq\; (2.0 \pm 2.0) \cdot 10^{-13} \quad .$$

2.2.3. Schiff's Conjecture

When people speak of testing the equivalence principle they usually mean testing the EEP. At first glance, this seems to imply also a test of GTR. However, this does not necessarily need to be the case. In 1960 L.I. Schiff wrote *On Experimental Tests of the General Theory of Relativity* [140]. He investigated if the three crucial tests of GTR (gravitational redshift, deflection of light and perihelion precession of Mercury)

> *support the full structure of the general theory of relativity, and do not merely verify the equivalence principle* [meaning UFF] *and the special theory of relativity [...].*

He concludes that the gravitational redshift and the deflection of light can be deduced from UFF and STR alone and that only the planetary orbit precession provided a real test of GTR. With respect to experimental tests of GTR he concluded that it would be *extremely difficult* — meaning impossible with the then-available techniques — to design an experiment that really tests GTR, and not only UFF and STR. As a response Dicke wrote [36], where he judged Schiff's statement as

> *serious indictment of a very expensive government-sponsored program to put an atomic clock into an artificial satellite.*

Schiff on his part responded with a *note added in proof* to his original paper:

Leonard Isaac Schiff (* 1915 Fall River, Massachusetts, † 1971) was a US-American theoretical physicist. He entered Ohio State University at the age of 14 and achieved his doctorate Massachusetts Institute of Technology in 1937. In the 1960s he wrote papers about space-borne gyroscopes to test GTR, which later left its mark on Gravity Probe B satellite mission. Bloch actually didn't hold any interest in *his* conjecture. When he came back to the topic 10 years later, he died before having published anything. [17]

Robert Henry Dicke (* 1916, † 1997) was an US-American physicist. After having worked on microwave technology for many years he turned to gravitational physics in 1956 and became a central figure in modern cosmology of that time. He contributed in an Eötvös-type experiment on the equivalence principle yielding 1 part in 10^{11} and later on lunar laser ranging. Both, Schiff and Dicke, had great impetus in coining precision tests of general relativity using the framework of the equivalence principle. [95]

> *The Eötvös experiments show with considerable accuracy that the gravitational and inertial masses of normal matter are equal. This means that the ground state eigenvalue of the Hamiltonian for this matter appears equally in the inertial mass and in the interaction of this mass with a gravitational field. It would be quite remarkable if this could occur without the entire Hamiltonian being involved in the same way, in which case a clock composed of atoms whose motions are determined by this Hamiltonian would have its rate affected in the expected manner by a gravitational field.*

Although it is not obvious at first sight, this is the origin of what we now call *Schiff's conjecture* [87]. Todays interpretation is that any complete, self-consistent theory of gravity containing the UFF necessarily comprises EEP [178]. If we put it the other way round this means that validating the UFF alone guarantees the validity of local Lorentz invariance, local position invarance and thereby of the EEP. There have been quite some attempts to prove Schiff's conjecture, see e.g. [178] for a survey, but none of them holds mathematically [87].

2.3. Violations of the UFF beyond Metric Theories

As we already stated in the introduction, a violation of the UFF is not possible within the range of GTR. Hence, finding such a violation would either imply that GTR is wrong or it would be a hint to hitherto unknown physics. The theoretical concepts introducing new macroscopic interactions can be categorised into three groups [1]:

1. phenomenological attempts to account for discrepancies in experimental results
2. demonstrations that a macroscopic interaction is compatible with certain extensions of the Standard Model
3. examination of astrophysical or cosmological consequences of such an interaction

The classical example for the first category is the *fifth force* suggested by Fischbach et al. in 1986, after they made a re-analysis of Eötvös' original data [75]. Their analysis gave rise to the idea of a deviation from the inverse-square law of Newton's gravitation, as measurements of gravity gradients and some ideas from particle physics did before. As a result they suggested a new macroscopic force with a Yukawa potential, a range of a few hundred meters and a strength of about one percent of gravity [178]. Up to now there is no experimental evidence for Fischbach's proposal. Nevertheless, the term *fifth force* survived the idea and is still found as a literary paraphrase for a hitherto unknown fundamental interaction.

Most approaches towards a new interaction fall into the second and the third category [1]. These are actually strongly correlated to each other: It is consensus that the Standard Model can barely be complete, which inevitably leads to the postulation of new fields and their mediating particles. But while the search for a theory of everything is one motivation, this is often triggered by cosmological observations, that cannot be explained with our current knowledge. However, the main difficulty is that we have no clue — not even a vague experimental hint — what the properties of such a new interaction should be. One reason for it to not have been discovered yet could be that the mediating bosons are too massive. The consequence is that we strive to the highest energies in particle accelerators. The other possibility lies on the opposite end of the energy spectrum: particles so light that they could generate a new long range interaction.

In general we can assert that most theories predicting a violation of the EEP are dealing with a new coupling and most theories dealing with a new coupling also predict an (apparent) violation of the EEP [35]. So, when searching for a violation of the UFF this is in fact a hunt for new physics.

2.3.1. Mocking a Violation of the EEP

To give a concrete example, we imagine a violation of the UFF that is due to the modification of the gravitational law by a new composition dependent inverse square law. In the simplest case ($1/r$) the violation would just be proportional to the strength of gravity. Transferring this to the picture, where we leave gravity untouched and add a fifth force (e.g. by a new scalar interaction), we could assume there is a new massless long-range interaction with coupling constant H, generic charges Q_A,Q_E and $1/r$ behaviour [16]:

$$F_{AE} = \overset{\text{Earth's mass/charge}}{\underbrace{-\frac{G m_A m_E}{r}}_{\text{Gravitational potential}} - \underbrace{\frac{H Q_A Q_E}{r}}_{\text{New interaction}}} \tag{2.18}$$

The **Yukawa potential** can be interpreted as screened Coulomb potential. Due to the factor $\mathrm{e}^{r/\lambda}$ it approaches zero while r increases. In the 1930s the Japanese physicist **Hideki Yukawa** (* 1907 in Tokio, † 1981 in Kyōto) introduced the Yukawa potential to describe the nuclear forces, belting the atomic nucleus against the Coulomb repulsion. He showed that such a potential arises from a massive scalar field, i.e. the exchange of pions between protons and neutrons. Due to the non-zero mass m of the pion the field has a limited range, inversely proportional to m. Today we regard the pion interaction as the residual interaction of the strong interaction between the quarks, that outreaches the borders of the nucleons. [76]

There are more general expressions for possible modifications of the gravitational interaction, for example a power law different from 1/r or — in case of a gauge boson of finite mass — a Yukawa potential [75, 179],

$$V_{\mathrm{NF}} = \pm \frac{H}{4\pi} Q \frac{\mathrm{e}^{-r/r_0}}{r} \quad , \tag{2.19}$$

with $r_0 = \hbar / m_b c$ being the Compton wavelength of the virtual exchange boson. The minus and plus signs refer to interactions mediated by scalar and vector bosons, respectively.

Just to depict the idea of a fifth force, we assume our *unknown* new interaction was the Coulomb interaction. With (2.15) we would get:

$$\eta(A,B) = \frac{\alpha}{G} \frac{Q_E}{m_E} \left(\frac{Q_A}{m_A} - \frac{Q_B}{m_B} \right)$$

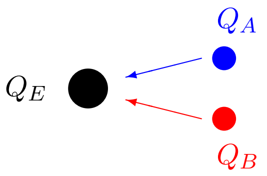

It is obvious that this violates the UFF, but that nevertheless GTR remains untouched! Clifford Will condenses the possibilities arising from this fact into the statement [178]:

> *Thus, the Einstein Equivalence Principle and related tests are now viewed as ways to discover or place constraints on new physical interactions, or as a branch of "non-accelerator particle physics", searching for the possible imprints of high-energy particle effects in the low-energy realm of gravity.*

2.3.2. New Scalar Fields, String Theory and the Dilaton

Attempts to go beyond the Standard Model of particle physics often introduce scalar or pseudo-scalar fields, e.g. in supersymmetry the scalar superpartners of the Standard Model fields [22]. In cosmology it's in particular the gravitational sector that we're interested in. When trying to quantise gravity, it is usually mediated by a hypothetical spin-2 boson, the graviton. In search for an explanation of the early (inflationary) or recent (quintessential) accelerated expansion of the universe we can introduce scalar partners of the graviton. In scalar-tensor theories of gravity additional scalar fields lead to a modification of Newton's law, where especially ultra-light scalar fields are a potential source of new long range interactions [22, 34].

When it comes to unify gravity with quantum field theories, all superstring theories contain a complex scalar field, comprising a pseudo-scalar named axion and a scalar: the dilaton. The dilaton first appeared in Kaluza-Klein theory and also in all non-supersymmetric string theories [33], where it directly couples to matter [163]. Hence, the experimental discovery of the dilaton would provide strong evidence for string theory [110]. At tree level, the dilaton is massless and has gravitational-strength couplings to matter which violates the UFF [33]. This is clearly in conflict with observations. However, there are several models aiming to reach consistency with experimental bounds, but even they comprise residual violations of the EEP.

Axions — which are actually named after a laundry detergent — are possible candidates for dark matter. They are searched with e.g. light-shines-through-a-wall experiments like ALPS at DESY or CAST looking for solar axions at CERN. These are based on the Primakoff effect, causing conversions of photons to axions in strong magnetic fields and vice versa. [92]

Including one space-like extra dimension **Kaluza-Klein theory** was the first theory with more than 4 dimensions. It was developed in the 1920s by the German physicist Theodor Kaluza (* 1885 in Wilhelmsthal, † 1954 in Göttingen), attempting to unify two fundamental interactions, being gravity and electromagnetism. The Swedish physicist Oskar Klein (* 1894 in Mörby, † 1977 in Stockholm) later explained the fact that the additional dimension was not observable by it being compactified. Hence, the compactification of extra dimensions in string theory is sometimes called Klein-Kaluza compactification. [127, 183]

Due to the complex structure of atoms it is difficult to specify their coupling to a new scalar field, even if the scalar coupling is simple in terms of the fundamental field. Thus, it is not an easy task to construct a new scalar interaction that does not have a composition dependence [1]. With respect to UFF tests Blaser and Damour have created a framework, deriving possible charges the dilaton field might couple to [31]. It is assumed, that the strength of the new coupling is in some way related to baryon number, lepton number and nuclear binding energy, which allows to infer combinations of test mass materials so as to maximise the hypothetical UFF violating signal. In section 3 we will deploy this formalism on elements used in cold atom experiments and assess the potential of atom interferometers compared with macroscopic test masses.

An intermediate-range interaction has been proposed by Fayet [73]. Within supersymmetry he introduced an additional U(1) group. Its spontaneous breaking entails the existence of a new boson, the U-boson, that could interact by vector and axial couplings. The charge is again a linear combination of baryon number and lepton number with the weak hypercharge. Another possibility is the cosmon field (see below) that could also manifest in a intermediate-range interaction. After all, the variety of models containing new interactions seems as wide as the number of free parameters in string theory. Improving the sensitivity of UFF tests can help to improve the bounds on several of those models as well as distinguishing between them.

2.3.3. Varying Fundamental Constants

A characteristic of theories featuring extra-dimensions, such as Kaluza-Klein theory and string theory, is that the universal constants are defined in the full set of dimensions. Thus, the effective value of the constants in 4 dimensions might depend on the structure and the size of the extra-dimensions [167], suspected of changing over time. Variation of fundamental constants is frequently considered as approach to hitherto unexplained cosmological observations, e.g. the cosmic expansion. However, the variation of fundamental constants contradicts EPP, because it violates the local position invariance. Dicke pointed out, that confirmations of the UFF give strong constraints on the variability of the fine structure constant α [37]. This was picked up by Beckenstein, who formulated a general, largely model independent framework for variations of α, first published in 1982 [11], including a mechanism leading to the violation of the UFF. Bekenstein himself later retracted this conclusion, arguing that a more detailed calculation revealed a complete cancellation of the effect [12]. He concludes that temporal and spatial variations of α are completely ruled out by current tests of the UFF within his framework. Nevertheless based on the original 1982 publication other authors later still assumed that a variation of α automatically leads to a violation of the UFF within this framework.

A special case of varying fundamental constants is the variation of the cosmological constant. While there is no observational evidence yet, the most promising candidate for varying the cosmological constant are quintessence scenarios [167], where the cosmological constant would be replaced by — again — a scalar field. In most scenarios dealing with quintessence it has a cosmological expectation value varying over the history of the universe [177, 176]. In fact quintessence was introduced as an explanation for the accelerated expansion of the universe and becomes manifest in what we call *dark energy*. It was also proposed that the quintessence field is identical to the dilaton. If the dilaton fulfils certain conditions necessary for realistic cosmological consequences, then it is called cosmon [175].

The term **quintessence** originates from the classical elements of ancient Greece, where the aether filling the Universe beyond Earth was thought to be the fifth element — Latin: *quinta essentia* — in addition to air, earth, fire and water.

2.3.4. Others

Standard Model Extension

Standard Model Extension (SME) is a phenomenological framework inspired by a symmetry breaking scenario within string theory. It allows to parametrise all possible modifications of Lagrangians including gravity. These modifications can picture violations of all aspects of the EEP. Since this is not a physical model rather than a parametrisation framework no definite predictions can be made. An examination with respect to atomic clocks and atom interferometers within the SME framework has been done by Hohensee et al. [102, 103]. The conclusions concerning the sensitivity of atom interferometers to violations of the UFF lead into the same direction as the ones we will draw from [31] in section 3.

Coupling of Spin to curved Spacetime

Within the formalism of GTR spinning test masses no longer move on geodesics. According to the Mathisson-Papapetrou-Dixon formalism they experience a force caused by a spin-curvature coupling, see e.g. [39]. We can think of this analogous to the coupling of the magnetic moment to the gradient of a magnetic field, which yields a force on moving particles with non-zero magnetic moment. There are, however, approaches that assume additional spin-spin, spin-mass and mass-mass interactions, e.g. the Moody-Wilczek approach [120], introducing axion mediated interactions. As this would violate the universal coupling of gravity to matter (minimal coupling) it implies a violation of the EEP. While this deals with macroscopically spinning test masses, another question is whether microscopic spin, e.g. nuclear spin, could also couple to new interactions. The applicability of macroscopic test masses in this respect is rather limited. First of all it requires some effort to produce mono isotopic test masses and even then only a small fraction of the atoms would have their spins aligned [1]. This is different in atom interferometers since they are inherently mono isotopic and in principle allow the production of spin polarised atomic samples.

Space-time Fluctuations

A general feature of quantum gravity are random fluctuations in the geometry of spacetime. Already the heuristic implementation of stochastic fluctuations in the spacetime metric lead to an apparent violation of the UFF for quantum systems [88]. Some scenarios are already ruled out by experimental bounds, but the holographic noise scenario predicts a violation at the 10^{-15} level. This is within the reach of the next generation UFF experiments. With regard to atom interferometry it should be mentioned, that the violation is stronger the smaller the systems. This is a strong argument for quantum level tests of the UFF, since they might be different from tests with macroscopic test masses.

Dark Matter

Astronomic observations have given convincing evidence that the majority of the galactic mass is constituted by dark matter. Based on the known four fundamental interactions we have to assume that gravity is the only interaction between dark matter and ordinary matter. However, if there was an additional scalar long range interaction this would manifest in an anomalous acceleration towards the galactic centre. It could even appear if the long range interaction only couples to dark matter by coupling to virtual pairs of dark matter in ordinary atomic nuclei [21]. In a rotating ground-based or an orbiting spaceborne UFF test, whose sensitive axis sweeps out the galactic centre, this should be visible as a sinusoidal signal [153].

3. Test Mass Material Choice

The outcome of tests of the UFF is often reduced to the Eötvös ratio. What's usually forgotten is the fact, that a simple one-dimensional number can only be half the answer. If we want to make a serious comparison of different possibilities to test the Equivalence Principle we first have to answer the question:

What do we want to measure at all?

As we have seen in the previous chapter, there are theories predicting violations of the UFF. This implies a lot of additional questions to be answered: How exactly does the violation manifest in an experiment? Does it depend on the composition of the test masses? If so, to which property of the test masses does it couple? Can we find any quantum number it couples to? Does it act rather on long or short length scales? Does it depend on the size of the test masses? Does it depend on gravitational self interaction of the test masses? And finally: Where does this violation come from?

There are a lot of theories and we have absolutely now clue, how a complete theory of gravity will look like in the end. If one wants to cover all these eventualities with only one experiment, it would become arbitrarily complicated. The search for violations of the UFF should thus be divided into two steps:

1. Finding a violation of the UFF at all with a first generation discovery experiment.
2. If later technology has advanced and ideally there is already evidence from the discovery experiment, one or more second generation experiments can be designed for distinguishing between theoretical models, i.e. getting information about the underlying charge(s) and coupling constant.

In both steps it is possible to optimise the choice of test mass materials. In a first generation discovery experiment we only envisage one or two pairs of test masses. The expected signal can be maximised for as many models as possible by choosing the test mass materials as *different* as possible with respect to as many theories as possible. This is the applicable scenario for the QUEST satellite mission introduced in chapter 5 and also for the STEP mission (see section 5.1).

3.1. The theoretical Framework

As we realised in section 2.3.1 an apparent modification of the gravitational law by a new composition dependent inverse square law may lead to a violation of the UFF. We modelled the case of a new massless long-range interaction with coupling constant H as

$$F_{AE} \;=\; -G \cdot \frac{m_A m_E}{r} - H \cdot \frac{Q_A Q_E}{r} \quad , \tag{2.18}$$

where Q_E and Q_A are the generic charges of the Earth and the test mass moving in the Earth's gravitational field respectively. The $1/r$ behaviour leads to a violation of the UFF proportional to the strength of gravity. However, free fall experiments measure the overall acceleration of the test masses, independent of it's actual origin. Hence, it is reasonable to combine gravity with the new interaction by defining an *effective gravitational constant* [31]:

$$G_{AE} \;=\; G + H \frac{Q_A}{m_A} \frac{Q_E}{m_E} \quad . \tag{3.1}$$

This is the combined coupling due to gravitation and the hypothetical new interaction. It is specific for the combination of test mass A with Earth E, or in the more general case with any external massive, charged body. Using G_{AE}, (2.18) turns into

$$F_{AE} \;=\; -G_{AE} \cdot \frac{m_A m_E}{r} \quad , \tag{3.2}$$

which is of the same form as the *normal* gravitational force. Inserting this into (2.15) yields

$$\eta(AB) \;=\; 2 \cdot \frac{a_A - a_B}{a_A + a_B} = 2 \cdot \frac{G_{AE} - G_{BE}}{G_{AE} + G_{BE}} \quad . \tag{3.3}$$

We will now write G_{AE} in a slightly different form [31]:

$$G_{AE} \;=\; G \left(1 + \frac{H}{Gu^2} \frac{Q_A}{\mu_A} \frac{Q_E}{\mu_E} \right) \;=:\; G\,(1 + q_A) \quad , \tag{3.4}$$

with $\mu_A = m_A/u$ and u being the atomic mass unit. The right hand side of equation (3.4) defines the *effective charge* [31]

$$q_A \;=\; \frac{H}{Gu^2} \cdot \frac{Q_A}{\mu_A} \frac{Q_E}{\mu_E} \quad , \tag{3.5}$$

which quanitfies the deviation of G_{AE} from the pure gravitational coupling G. It is thus a measure for the composition dependence of the effective coupling G_{AE}. Since we expect the composition-dependent contribution to be very small ($< 10^{-12}$) and hence G/G_{AE} be of the order of unity, we can write (3.3) as [31]

$$\eta(AB) \approx \frac{G_{AE} - G_{BE}}{G} = q_A - q_B \quad . \tag{3.6}$$

Now lets step back and think about the physical meaning of (3.6). Its implication is crucial for understanding the outcome of free fall experiments: The only quantity accessible by free fall experiments is the effective charge q_A. We have no direct access to the charge Q_A leave alone the coupling constant H. It is not possible to infer quantitative values for Q_A and H without making further assumptions about the underlying physical mechanism, i.e. the composition dependence of q_A [31].

3.2. Topology of Test Mass Material Configurations

The sensitivity of the experiment will not only depend on the chosen test mass materials and the number of measurements, but also on the topology of the combinations of test mass materials. When designing the experiment we will have to choose a specific configuration $\mathcal{C}$ of n test mass material pairings (AB). We will then perform n differential acceleration measurements $\eta(AB)$ and finally end up with a data set [31]

$$\mathcal{D}_{\mathcal{C}} = \{\eta(AB)|(AB)\,\epsilon\,\mathcal{C}\} \quad . \tag{3.7}$$

So far, this is completely model-independent. Since introducing a specific model bears the risk of misinterpreting the experimental data, we might want to ask: What is the ideal configuration $\mathcal{C}$, such as to maximise the information that can be extracted from the data set $\mathcal{D}_{\mathcal{C}}$, *without* making any assumptions about the composition dependence of the effective charges q_X? The first thing we want to derive from the data is the effective charges q_X themselves. Measurements of the type (3.6) give a set of linear equations for the q_X, where the number of unknown variables depends on the configuration $\mathcal{C}$: An open disconnected configuration

$$\mathcal{C} \;=\; \{(AB)(BC)(DE)\} \quad ,$$

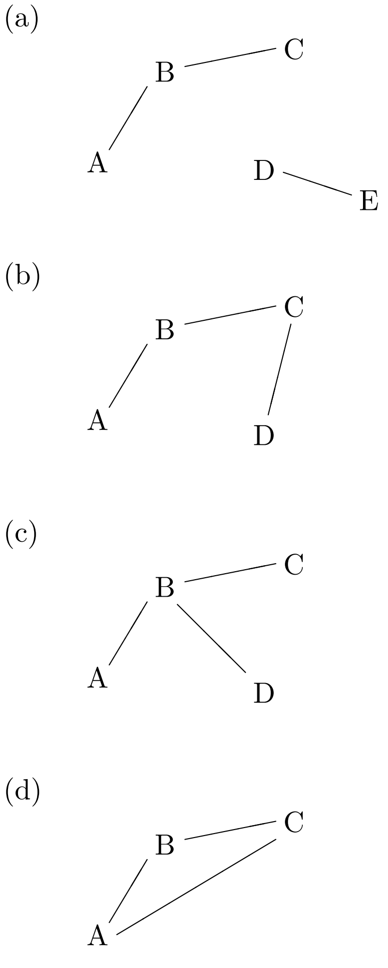

Figure 3.1.: Different pairings of test mass materials: (a) open disconnected configuration, (b) open connected configuration, (c) starlike configuration, (d) closed configuration. [31]

like depicted in figure 3.1 (a), has five unknown variables q_X, but only three measurements $\eta(XY)$. This is not enough to determine the q_X. Going to a connected configuration, e.g. (b) linear,

$$\mathcal{C} \ = \ \{(AB)(BC)(CD)\} \quad ,$$

or (c) starlike,

$$\mathcal{C} = \{(AB)(AC)(AD)\} \quad ,$$

reduces the number of variables to four, which is still not enough to determine the q_X. With a closed configuration (d),

$$\mathcal{C} = \{(AB)(BC)(CA)\} \quad ,$$

we finally have three variables and three measurements. Unfortunately, the set of three linear equations of the form (3.6) is not linearly independent. Thus, it only allows the determination of the q_X modulo an unknown additional constant. The Q_X and the coupling constant H cannot be separated at all.

However, the use of topological loops yet has another advantage: It provides a kind of consistency check, in case of a non-zero result in one or more measurements. When using macroscopic test masses, which in general consist of an inner and an outer test mass, such checks can also be performed by using double configurations like $\{(AB)(BA)\}$ [31]. Dual atom interferometers do not have an analogue to inner and outer test mass, but only a single atomic cloud containing both isotopes. Topological loops are thence the only way to introduce consistency checks in an atom interferometric test of the UFF.

3.3. Model-dependent Approach

The model-independent approach serves us well, when aiming for the discovery of a violation of the UFF. However, it only provides the effective charges q_X with the bare charges Q_X and the coupling constant H hidden insight. For revealing the new interaction, we need direct access to Q_X and H. Using (3.5) introduces two additional variables, H itself and Q_E. Our set of linear equations — being already under-determined — becomes even more under-determined. In fact, the only way to insert additional information into our calculation is to assume, we already knew the violation-causing mechanism. When introducing a specific model with a finite number of well-known charges, the experiment could be used to determine the coupling coefficients related to these charges for all of the theoretical models in question. Those charges would obviously be a function of some properties of the atoms, as there are (without making a claim to be complete):

- atomic mass (light vs. heavy elements),
- spin (either atomic or nuclear),
- isospin (proton/neutron ratio),
- nuclear binding energy
- the size of the test masses (or rather its wave function) or
- any other quantum number.

Although the variety of theoretical ideas is at least as wide as the number of possible charges, the number of baryons B and the number of leptons L can be found in many of them [73]. An example for a model-dependent approach based on this finding was suggested in [31], where three elementary charges have been established: The number of protons $Z = L$, the number of neutrons $N = B - Z$ and a contribution proportional to the Coulomb interaction energy E of the nucleus. The functions with the best sensitivity and smallest correlations were found to be:

What's called the **Coulomb interaction energy** in [31] is simply the Coulomb part of the Bethe-Weizsäcker formula, also known as the semi-empirical mass formula (SEMF) based on the liquid drop model of nuclear physics. It is used to approximate the mass and various other properties of atomic nuclei. It was first established in 1935 by the German physicist Carl Friedrich von Weizsäcker (* 1912 in Kiel, † 2007 in Söcking, Bavaria). [115, 151]

$$\begin{aligned} \xi^1 &= (N+Z)/\mu & (3.8) \\ \xi^2 &= (N-Z)/\mu & (3.9) \\ \xi^3 &= E/\mu \approx Z(Z-1)/((N+Z)^{1/3}\mu) & (3.10) \end{aligned}$$

Having specified those functions, we can write the composition dependence of the scalar charge as a linear combination of the (known) *elementary charges* ξ^i_A,

$$\frac{Q_A}{\mu_A} = \beta_0 + \sum_{i=1}^{m} \beta_i \xi^i_A \quad , \tag{3.11}$$

with unknown coupling parameters β_0 (composition-independent) and β_i (composition-dependent). The effective charges (3.5) become

$$q_A = \alpha_0 + \Sigma_{i=1}^{n} \alpha_i \xi^i_A \quad , \tag{3.12}$$

with linear combinations $\alpha_0 = \frac{H}{Gu^2}(\beta_0 + \Sigma_{j=1}^{n} \beta_j \xi^j_E)$ (A-independent) and $\alpha_i = \frac{H}{Gu^2}(\beta_0 + \Sigma_{j=1}^{n} \beta_j \xi^j_E)\beta_i$ (A-dependent). Even if fixing the elementary charges ξ^i, this is still under-determined and will not yield quantitative results without making further assumptions. However, it allows us to take a deeper insight into the structure of the observed UFF violation and to determine exclusion bounds for certain models.

3.4. Cold Atoms vs. Macroscopic Test Masses

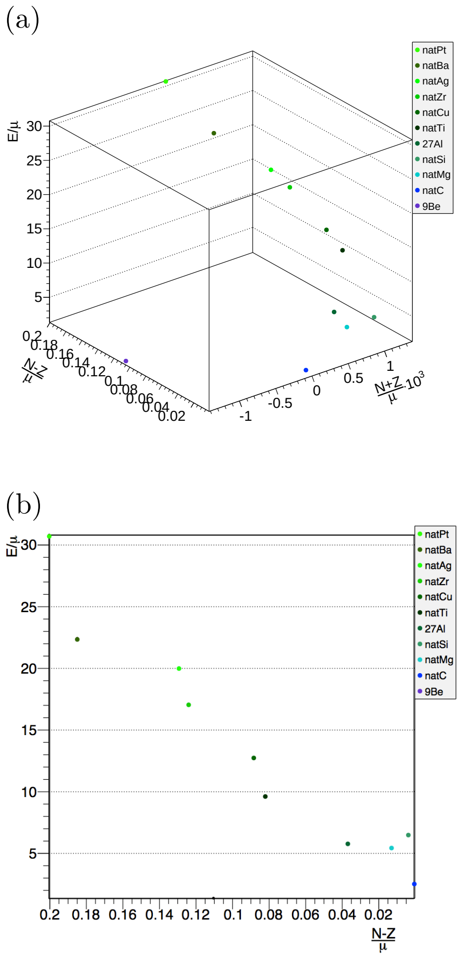

Figure 3.2.: (a) Distribution of various test mass materials eligible for the STEP mission in the phase space of the effective charges (3.8) to (3.10); “natX” denotes natural abundance of the element X. (b) 2D plot of the E/μ over $(N-Z)/\mu$ plane: Except for the isotope ^{9}Be the test mass materials lie more or less in one plane, only covering a small volume of the three-dimensional phase space.

Bigger versions of the plots are given in figure 3.5. See also figure 3.7 for a stereoscopic plot.

The choice of test mass materials within the framework of the effective charges (3.8) to (3.10) was first formulated in 1994 by Blaser and Damour [31] and was further developed in succeeding publications [35, 16, 32]. At this point it should be stressed, that those calculations have been done with respect to the STEP mission: a satellite missions based on macroscopic test masses. Within the scope of STEP the most severe limitations actually resulted from the necessity of being able to process the test mass materials into sufficiently stable test mass objects. Only few elements comply with these requirements. The *macroscopic* test mass materials considered for the STEP mission [32] are displayed in figure 3.2 (a), where natural isotopic composition has been assumed. Unfortunately, all of these elements except $^{9}_{4}\mathrm{Be}$ lie closely spaced on a hyperplane of the three-dimensional phase space, as can be seen in figure 3.2 (b). Thus, it is difficult to cover a considerably large volume of the three-dimensional phase space. At the latest for a second generation experiment, the isotope $^{9}_{4}\mathrm{Be}$ gains in importance, since it is the only metallic candidate sticking out of the plain.

All these elements are rather heavy and thus provide a large neutron excess ($N-Z>0$). To get a proton excess ($N-Z<0$) or at least equal number of protons and neutrons ($N-Z=0$), only $^{2}_{1}\mathrm{H}$, $^{3}_{2}\mathrm{He}$ and $^{6}_{3}\mathrm{Li}$ come into consideration. None of them can be shaped into a stable macroscopic test mass. The picture changes if we look at alkaline and alkaline earth metals: materials which neither can be shaped into stable macroscopic test masses, but which on the other hand are tools of the trade for the cold atom physicist. A selection of elements, that can be trapped in cold atom experiments, is marked with solid dots in figure 3.3 (a). (The *macroscopic* test mass materials are included with hollow dots for comparison.) Clouds of cold atoms trapped in a magneto-optical trap are intrinsically mono-isotopic. Even if only considering the stable isotopes of the regarded materials, this significantly blows up the covered phase space volume. Beyond that and similar to $^{9}_{4}\mathrm{Be}$, the two light isotopes $^{6}_{3}\mathrm{Li}$ and $^{7}_{3}\mathrm{Li}$ assume an important role, due to their exposed position in the phase space. In this context it lends itself to quote Blaser and Damour [32]:

> *It is interesting to note that light elements provide a much wider range of differences than the other elements. This is firstly, because the binding energies vary much more and influence the isotopic mass and, secondly because one nucleon more or less makes a larger fractional change.*

Thus, the covered phase space volume could be increased even more if considering the hypothetical possibility of building an atom interferometer based on Helium or Hydrogen, as can be seen from figure 3.3 (b).

However, let's first look at the combinations from table 1.1 that have already been used in dual isotopic atom interferometers. Their differential values for the charges (3.8) to (3.10) are listed in table 3.1. The combinations (^{85}Rb, ^{87}Rb) and (^{87}Rb, ^{39}K) are also marked with solid black lines in figure 3.3 (a). With these combinations we are still stuck to the hyperplane discussed above, that also challenges the use of macroscopic test masses. It is not until we include (^{6}Li, ^{7}Li), as discussed above, that we are expanding our configuration to the $(N+Z)/\mu$ axis and are stacking out the edges of a quite reasonable phase space volume. Beyond these isotopes also Yb, Cs and Mg would be of some interest, since they would further expand the covered volume.

Of course, we are still dealing with a disconnected configuration, that does not allow for a systematic analysis of an tentative UFF violation. Thus, it is advisable to cover the missing cross-element combinations to achieve a closed-loop configuration, as was discussed above. (See the references in table 3.1 for cross-element combinations that are under development or have already been proposed.)

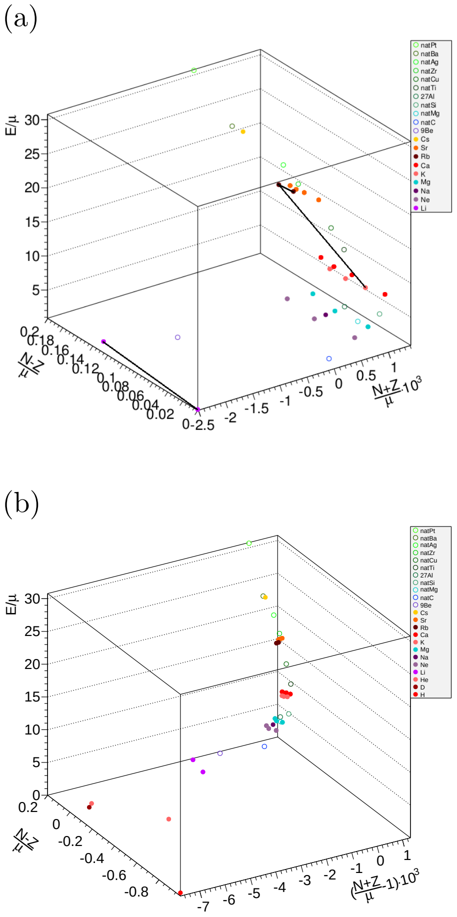

Figure 3.3.: (a) Distribution of cold atom test mass materials in the phase space of the effective charges (3.8) to (3.10) The STEP materials are included for comparison. The pairs (^{87}Rb,^{85}Rb), (^{87}Rb,^{39}K) and (^{6}Li,^{7}Li) are connected by solid black lines respectively; "natX" denotes natural abundance of the element X. (b) Same viewing angle as before, but with the $(N+Z)/\mu$ and the $(N-Z)/\mu$ axis zoomed out as to include also Hydrogen and Helium.

Bigger versions of the plots are given in figure 3.6. See also figure 3.8 for a stereoscopic plot.

Test masses (A,B)	Ref.	$\Delta\frac{N-Z}{\mu}$	$\Delta\frac{N+Z}{\mu}$	$\Delta\frac{E}{\mu}$
(^{85}Rb, ^{87}Rb)	[18]	0.020035	0.006108	0.108915
(^{87}Rb, ^{39}K)	[142]	0.123917	0.113499	0.870575
(^{87}Sr, ^{88}Sr)	[162]	0.009941	0.025254	0.055123
(^{6}Li, ^{7}Li)	[94]	0.142531	0.232976	0.101882
(^{87}Rb, ^{168}Yb)	[96]	0.017151	0.651289	1.753562
(^{87}Rb, ^{170}Yb)	[96]	0.026957	0.661084	1.671909
(^{6}Li, ^{85}Rb)	[186]	0.149581	3.559006	2.909916
(Pt, Ti)		0.118405	1.153140	2.650952
(Pt, Nb)		0.082109	0.844750	1.411859
(Nb, Be)		0.007438	2.359493	3.256032
(Be, Pt)		0.089547	1.514744	4.667890

Table 3.1.: Realised cold atom UFF tests from table 1.1 (top). Proposed test mass materials for cold atom experiments (middle). Possible combinations for macroscopic test masses are added for comparison (bottom). Nuclear data taken from [106].

3.5. Assessment of Noise

Beyond those highly theoretical considerations on how to maximise phase space volume we haven't mentioned another, technical issue yet: Every measurement will contain a *fifth force* contribution $q_A - q_B$, but also a noise contribution n_{AB} [35]:

$$m_{AB} = q_A - q_B + n_{AB} \tag{3.13}$$

For the "noise" contributions n_{AB} [35] assumes that it contains statistical as well as systematic errors. Statistical errors mainly come from shot noise, laser phase noise and vibrations. Systematic errors may arouse from electric and magnetic stray fields, wave front errors or misalignement of the Raman lasers and others.

So for the optimisation of test mass material choice the contribution of different noise sources should be assessed. This, however, can only be done based on a specific experimental design. Based on the assessment of noise it has for instance been decided, to stick to (^{87}Rb,^{85}Rb) in favour of (^{87}Rb,^{39}K) within the STE-QUEST mission. Although (^{87}Rb,^{39}K) theoretically has a significantly bigger sensitivity on the $(N - Z)/\mu$ and although (^{87}Rb,^{85}Rb) is practically blind for the E/μ and the $(N + Z)/\mu$ axis, it could not outweigh the better suppression of common-mode noise, when using two isotopes of a single element [146]. For a detailed discussion of a mathematical model aiming on optimisation of test mass material choice including noise see again [35].

3.6. Summary & Discussion

It is widely accepted consensus that the standard model is incomplete. Many theories developed to fill this gap predict an (apparent) violation of the universality of free fall (UFF). Chapter 2 provides a general overview about the mathematical nature of the equivalence principle and the prevalent theories of what could cause a violation of the UFF — other than the possibility that the Einstein equivalence principle is simply wrong. However, all of these possibilities are hypothetical with no direct experimental and observational evidence.

Despite their theoretical nature, many of the beyond-standard-model theories predict a violation of the universality of free fall caused by a new long-range interaction. As we have seen many of the theories agree that the new interaction might couple to baryon and lepton number in some way.

In chapter 3 we saw Blaser and Damour's framework, which is motivated by this findings. Their framework is based on the dilatonic scenario and allows a systematic assessment of atomic properties. It is clear that a systematic search for an UFF violation requires not just one, but several pairs of test masses being "*as different as possible*". The framework approaches the question what "*as different as possible*" means. Blaser and Damour were able to compare the sensitivity of different pairs of test mass materials with respect to the charge of the hypothetical fifth force. In any case, at least some model dependent assumptions concerning the underlying charges have to be made. In the framework presented here these are lepton number, baryon number and the electrostatic part of the Bethe-Weizsäcker formula.

While the assessment of Blaser and Damour was restricted to macroscopic test masses, we applied their scheme to isotopes that are used in cold atom experiments. We showed that alkaline and alkaline earth metals offer a comparable potential in maximising the covered volume in the phase space of possible charges, as materials that can be formed into macroscopic test masses.

But also beyond the framework of Blaser and Damour, the use of atomic test masses might provide access to effects that are not accessible with macroscopic test masses at all, e.g. spin-dependence or space-time fluctuations. Hence, the presented results should be handled with great caution. The fact that many theories come down to lepton number and baryon number is remarkable on first sight only, since the number of Lorentz invariant parameters is quite limited. Some of them do not even show up in baryonic matter; e.g. all atomic nuclei feature the same colour charge. It is not surprising that the work of Hohensee et al. [102], though using a completely different approach, suggests very similar implications. Even so, experimental bounds do not exclude any approach featuring spin dependence or space-time fluctuations just as they do not exclude theories related to lepton number and baryon number. Especially when dealing with atom interferometers, where the test masses are quantum objects, we should always keep these possibilities in mind.

Resuming the assumptions made in the Blaser-Damour framework in chapter 3, we approached the question: What is the best combination to use in a cold atom test of the universality of free fall? Equations (3.12) and (3.6) show, that the strength of an UFF violation depends linearly on the charges (3.8) to (3.10). A big difference in those charges implies a higher probability of unveiling a violation. But it neither makes sense nor is it even possible to choose one pair of test mass materials as superior over all other possible combinations. First of all, in a three-dimensional phase space it is reasonable to cover all three dimensions with several combinations. Second — and this is the more substantial argument in the long-term perspective — a systematic study of the mechanism underlying the UFF violation is only possible if using a linearly independent combination of test mass materials; at least one per dimension.

Fortunately, we could also show that the combinations of test mass materials from table 1.1, which are already being used in dual isotopic atom interferometers, are a good starting point within the framework of Blaser and Damour. Adding lithium [94, 186] this offers a sufficient coverage of phase space, comparable to a configuration of macroscopic test masses including beryllium.

While these combinations as such are a good choice, they still form an open configuration. Considering the possible topologies of test mass material pairs, it is desired to find a connected and closed configuration, most of all to ensure redundancy. Thus, it is advisable to assess further possibilities of inter-species combinations, like ^{87}Rb vs. ^{39}K demonstrated at the CAPRICE experiment [142] or ^{87}Rb vs. ^{6}Li proposed for the 10 m-fountain in Wǔhàn [186]. Figure 3.4 shows the configuration of the demonstrated and proposed combinations and also reveals the missing links for a closed configuration.

One question remains: Which pair of test mass materials is best suited to close the missing link? From the theoretical frameworks point of view all possible combinations to close the missing link are conceivable. Thus, the choice should be made based on the technical performance of the possible combinations. This should in particular include a noise assessment, because some combinations with greater difference in the violating charges might be less suitable due to a much higher — technical — noise level.

As next step, we recommend a complete assessment of the configuration shown in figure 3.4, to identify the combinations best suited to close the missing link.

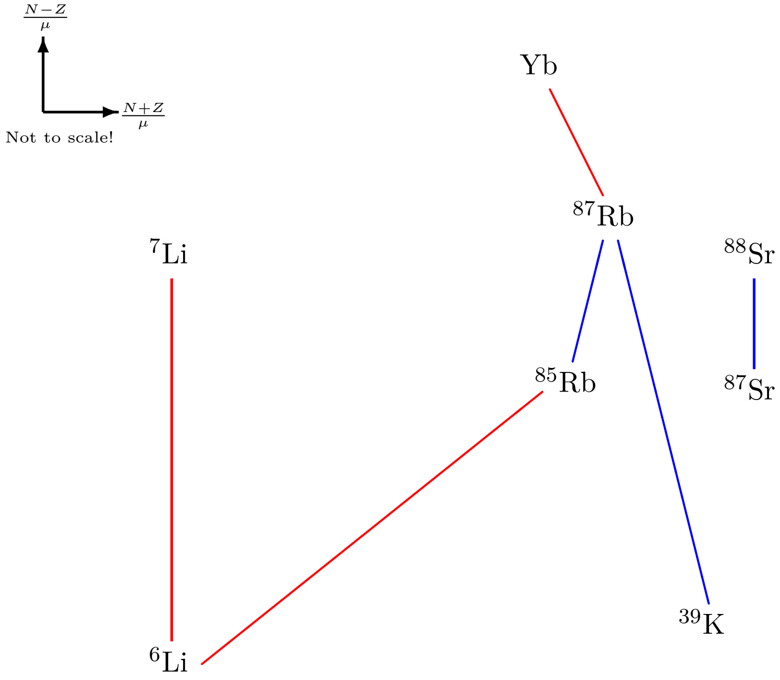

Figure 3.4.: Combinations of test mass materials that have been demonstrated (blue) in or proposed (red) for cold atom tests of the universality of free fall. There are several possibilities to enhance this set of test mass materials to a closed configuration.

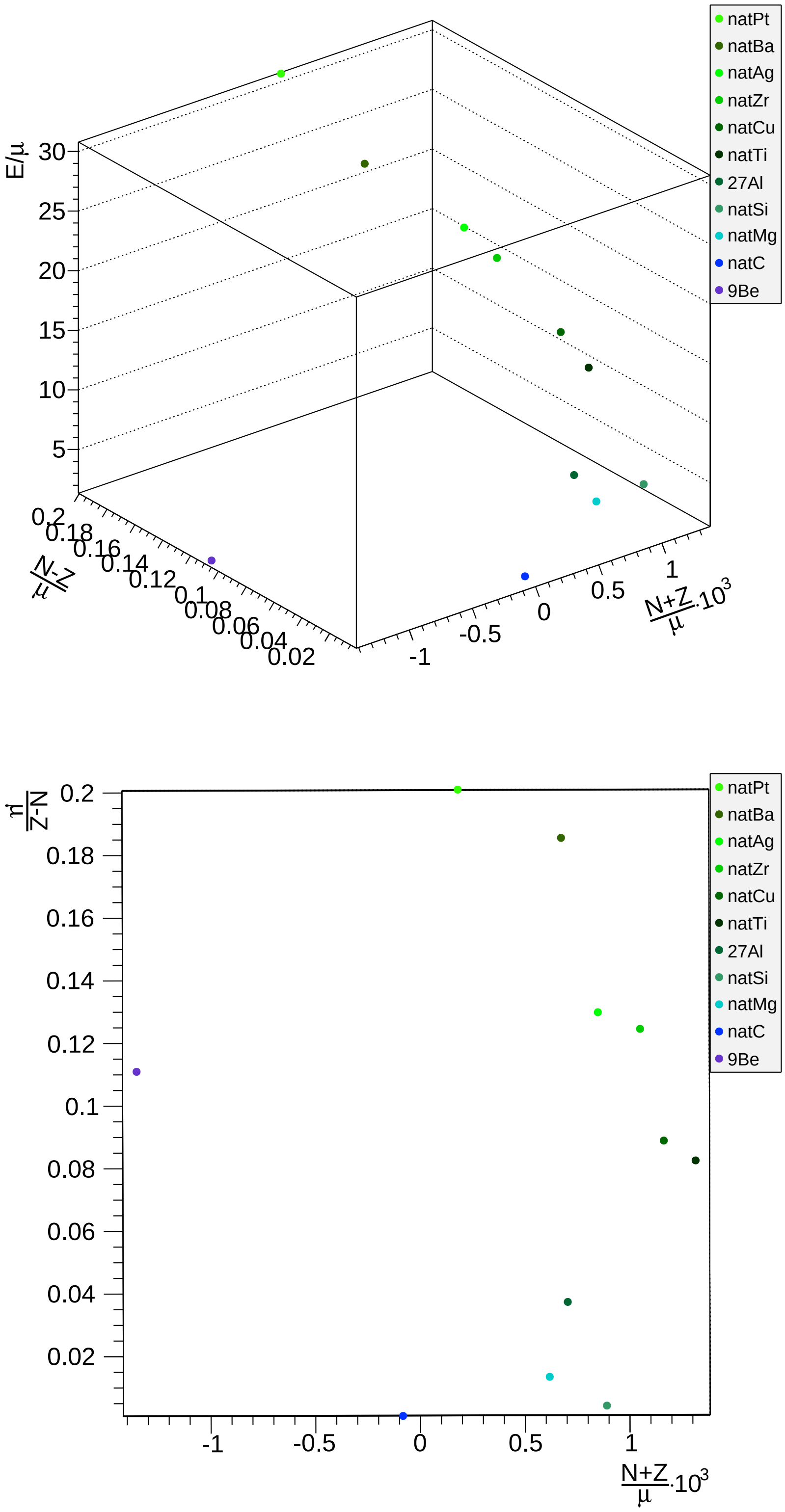

Figure 3.5.: Distribution of various test mass materials for macroscopic test masses as considered by [31] in the phase space of the effective charges (3.8) to (3.10); “natX” denotes natural abundance of the element X. Besides the 3D plot 2D projections onto the three hyperplanes are provided.

See figure 3.7 for a stereoscopic plot.

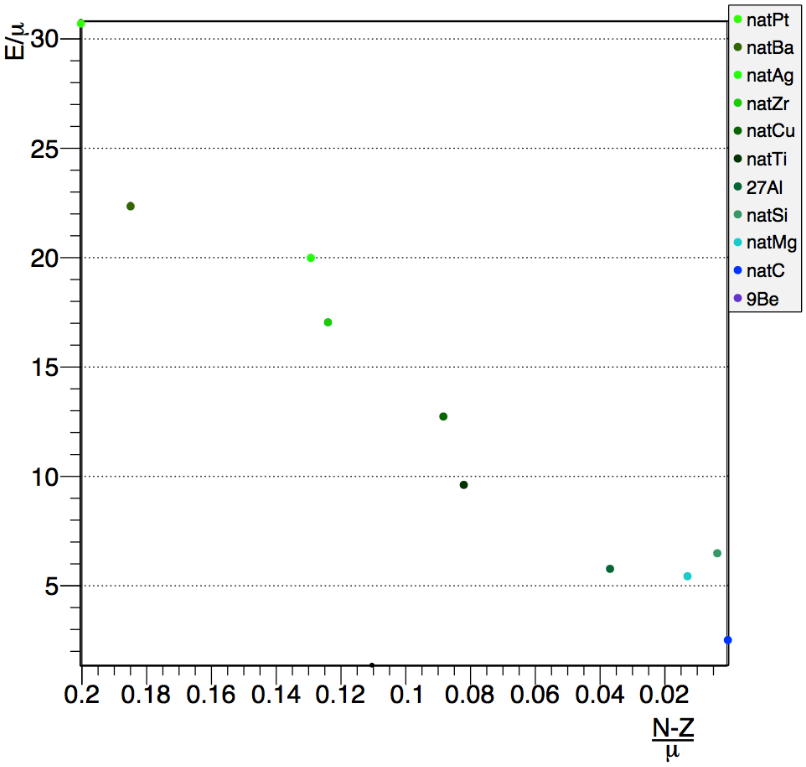
E/μ
30
25
20
15
10
5
0.2
0.18
0.16
0.14
0.12
0.1
0.08
0.06
0.04
0.02
N-Z
μ
natPt
natBa
natAg
natZr
natCu
natTi
27Al
natSi
natMg
natC
9Be

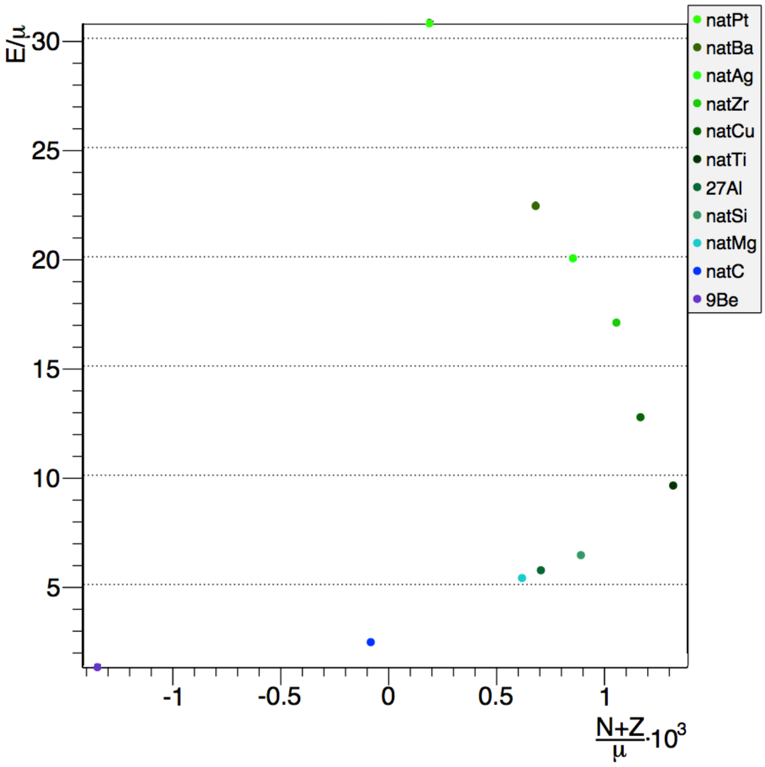
E/μ
30
25
20
15
10
5
-1
-0.5
0
0.5
1
N+Z
μ
$\cdot 10^3$
natPt
natBa
natAg
natZr
natCu
natTi
27Al
natSi
natMg
natC
9Be

Figure 3.6.: Distribution of various cold-atom type test mass materials (solid dots) in the phase space of the effective charges (3.8) to (3.10). Besides the 3D plot 2D projections onto the three hyperplanes are provided. The test mass materials considered for macroscopic test masses are included for comparison (hollow dots); "natX" denotes natural abundance of the element X.

See figure 3.8 for a stereoscopic plot.

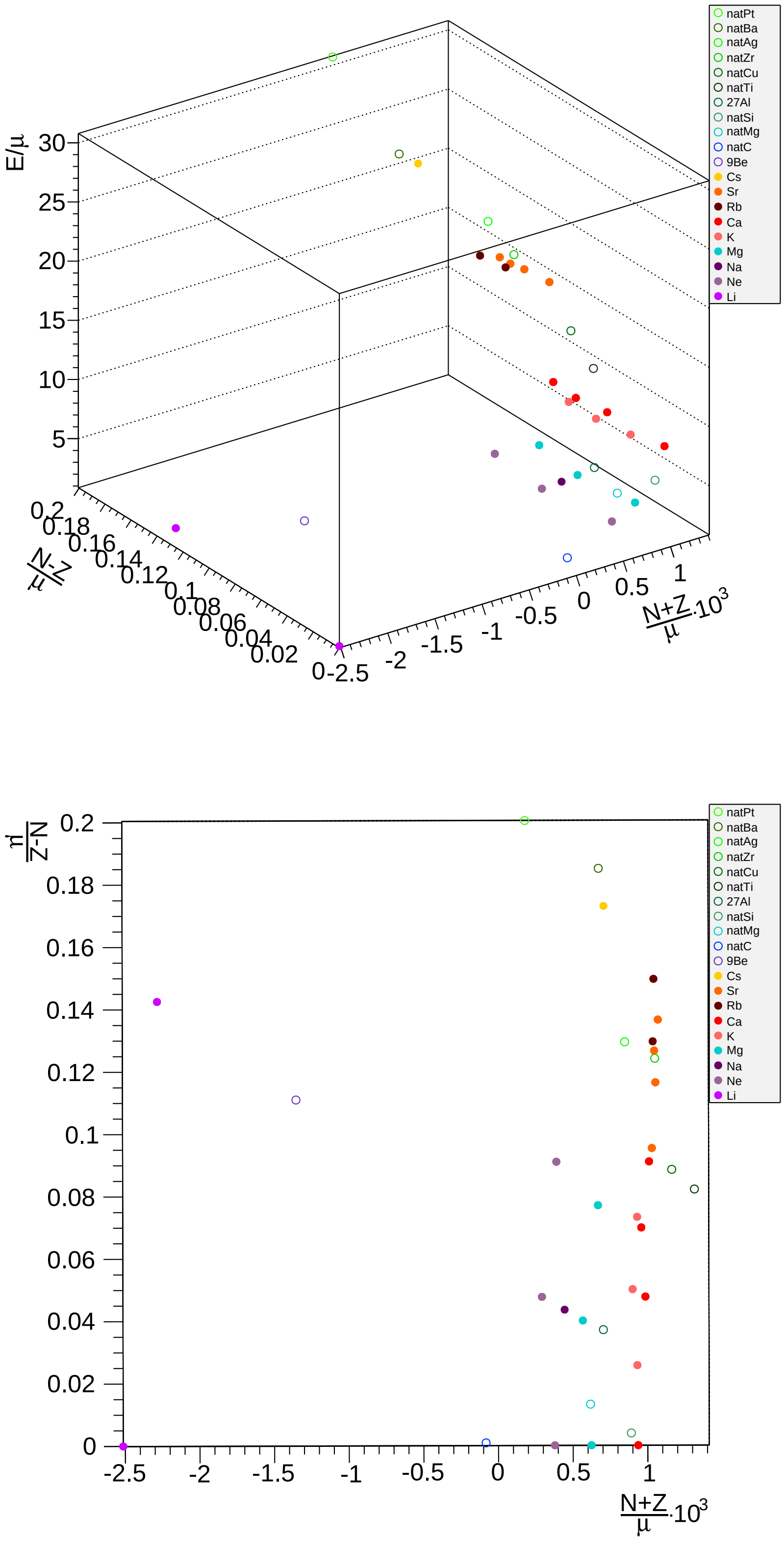

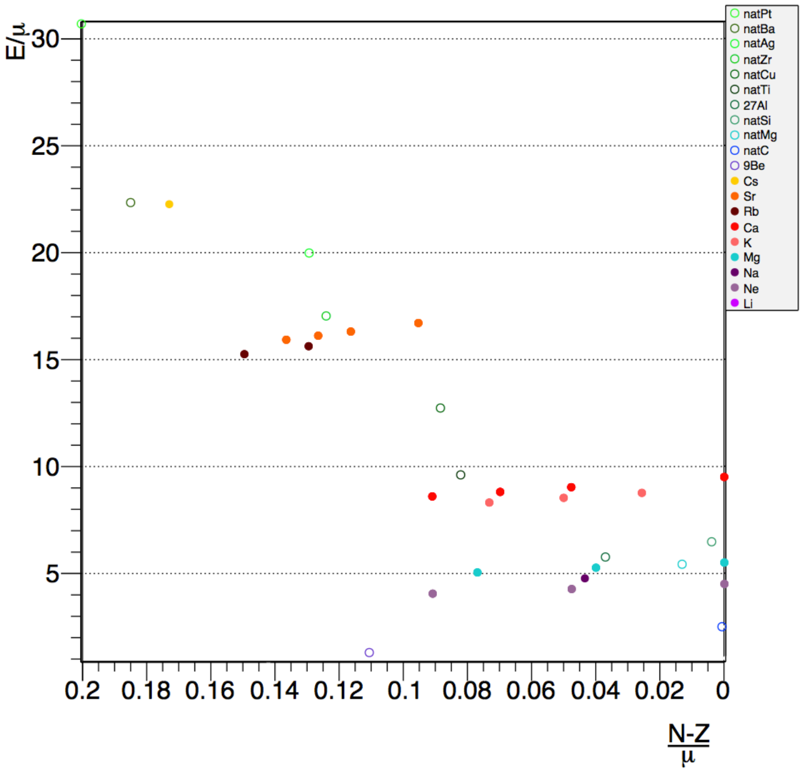
E/μ
30
25
20
15
10
5
0.2
0.18
0.16
0.14
0.12
0.1
0.08
0.06
0.04
0.02
0
N-Z/μ
natPt
natBa
natAg
natZr
natCu
natTi
27Al
natSi
natMg
natC
9Be
Cs
Sr
Rb
Ca
K
Mg
Na
Ne
Li

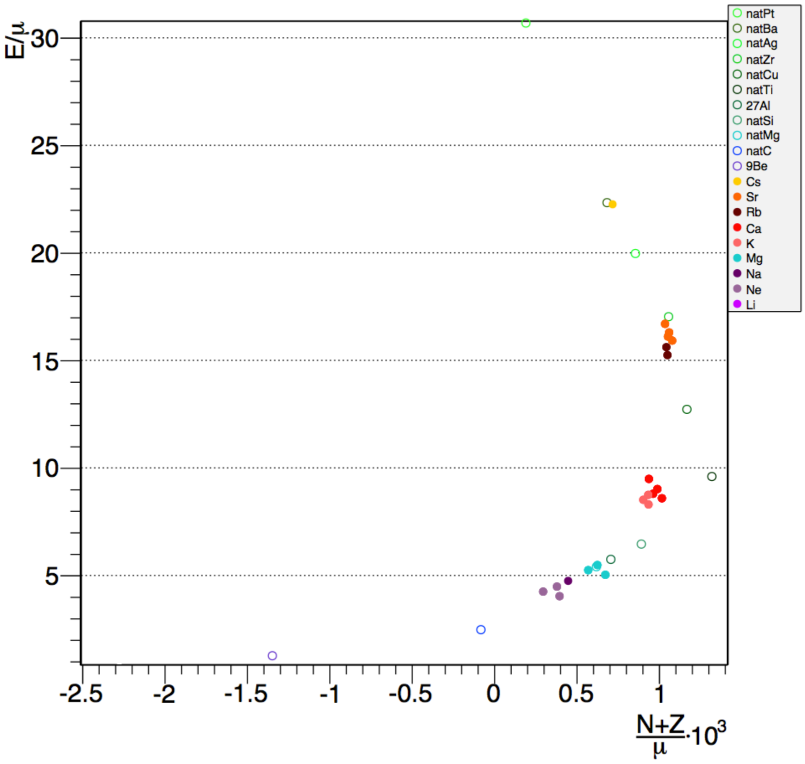
E/μ
30
25
20
15
10
5
-2.5
-2
-1.5
-1
-0.5
0
0.5
1
N+Z/μ·10³
natPt
natBa
natAg
natZr
natCu
natTi
27Al
natSi
natMg
natC
9Be
Cs
Sr
Rb
Ca
K
Mg
Na
Ne
Li

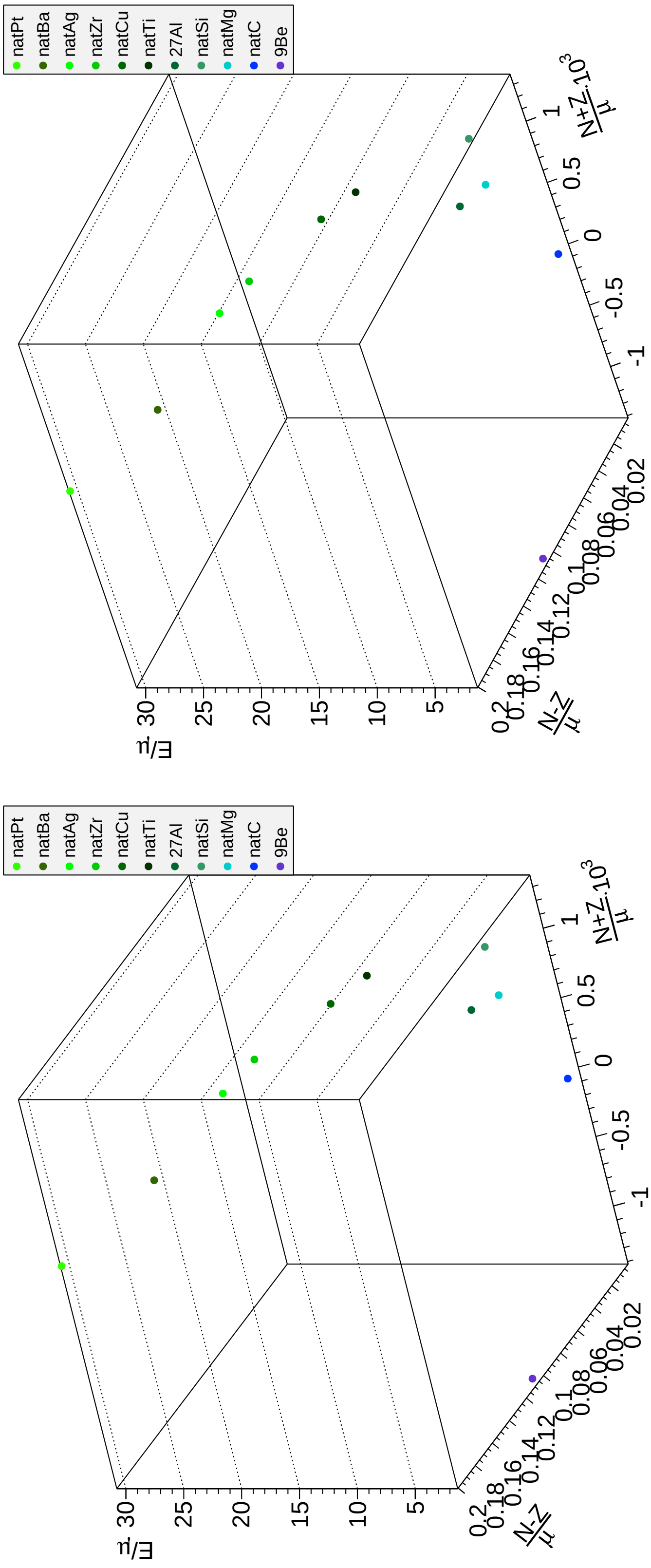

Figure 3.7.: Stereoscopic version of figure 3.5, showing the distribution of various test mass materials for macroscopic test masses as considered by [31] in the phase space of the effective charges (3.8) to (3.10).

This is a cross-view plot. To view the stereo pair, cross eyes slightly until a third plot appears between the two. The new centre plot is 3D.

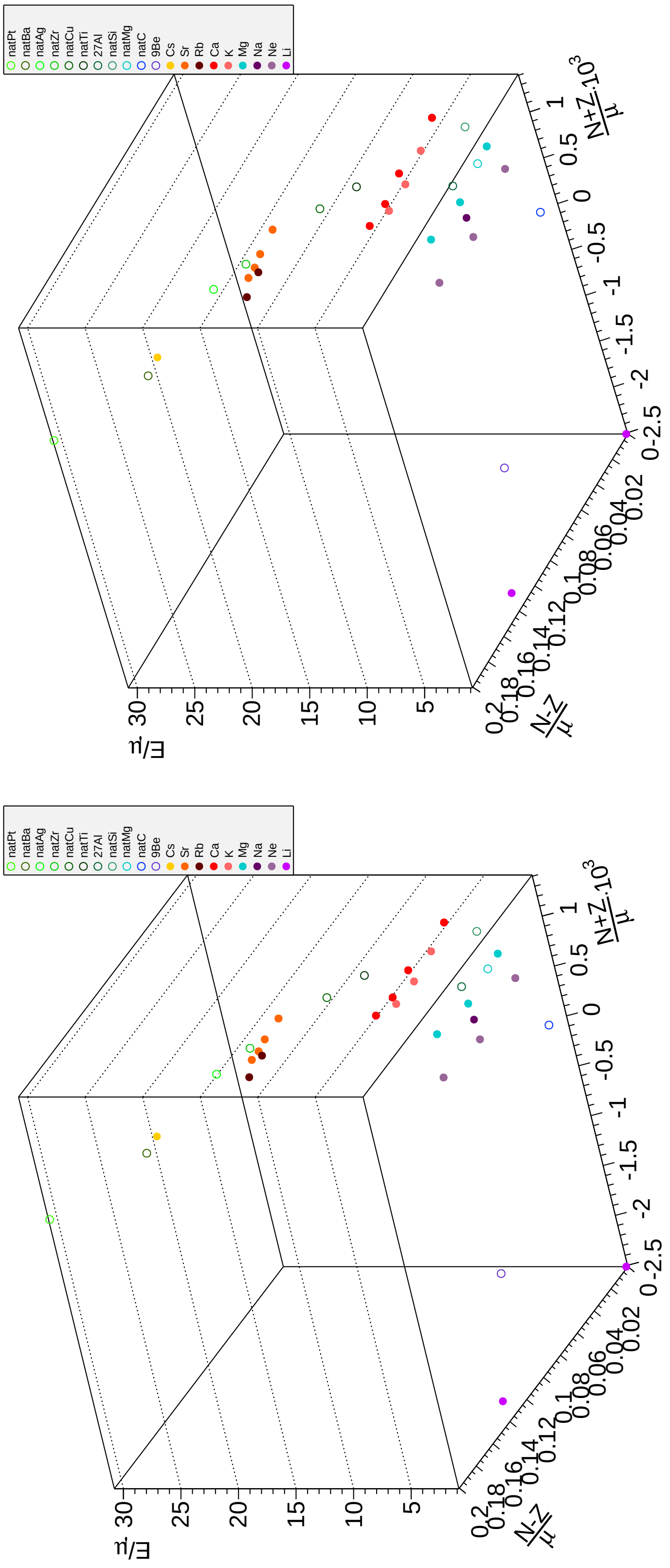

Figure 3.8.: Stereoscopic version of figure 3.6, showing the distribution of various cold-atom type test mass materials (solid dots) in the phase space of the effective charges (3.8) to (3.10). The test mass materials considered for macroscopic test masses are included for comparison (hollow dots).

This is a cross-view plot. To view the stereo pair, cross eyes slightly until a third plot appears between the two. The new centre plot is 3D.

Part II.

QUEST — The Quantum Equivalence Principle Space Test

Space-borne atom interferometers offer a promising approach to complement and overcome the limits of classical tests of the equivalence principle, that use macroscopic test masses. The STE-QUEST mission is a viable proposal for such a mission, assessed within the scope of ESA's Cosmic Vision program. Different from ground based experiments the sensitivity to violations of the UFF is not constant, but varies with the satellite's position on its orbit. Thus, the integrated sensitivity has to be calculated by means of a numerical simulation. In this part we will review the basic principle of atom interferometers, give an overview on the STE-QUEST mission and finally show that the mission is feasible despite perturbations due to gravity gradients and despite a challenging orbit design.

4. Atomic gravimeters

The observation of interference in matter is not a recent discovery. The probably most popular example of an atom interferometer are atomic clocks. However, applications are not at all limited to frequency standards. In the scope of inertial sensors the basic idea can be summarised as to reach a higher precision compared with laser based systems by using an ensemble of coherent atoms. In this context we often speak of using atoms as quantum sensors.

In general the ***quantum*** in **quantum sensor** means, that we exploit the quantum nature of the atoms to build a ultra precise sensor. Primarily, it does not mean, that we are using atoms to explore quantum effects, e.g. effects arising from quantum gravity.

4.1. Interferometers as inertial sensors

We have already mentioned the phenomenon of interference in the introduction. Thanks to quantum mechanics it is not limited to light, i.e. electromagnetic waves, but interference can also be observed in matter. We'll have a look at the Mach-Zehnder interferometer, since the Raman-based atomic accelerometer is based on that geometry.

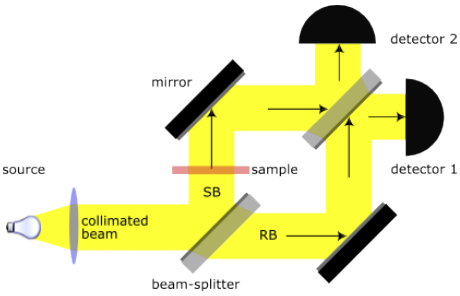

Figure 4.1.: Schematic view of a Mach-Zehnder interferometer. [4]

4.1.1. Light-based Mach-Zehnder interferometer

A schematic representation of a light-based Mach-Zehnder interferometer is depicted in figure 4.1. Light from an external source is distributed by a beam splitter into two paths SB and RB and redirected by two mirrors towards a second beam splitter. There, the two beams are superimposed and again distributed to two output ports 1 and 2. Assuming equal lengths of the paths SB and RB, all the light arrives in phase at port 1 yielding constructive interference. This can be explained by the phase inversion — corresponding to a phase shift of 180° — light encounters upon front face reflection at dielectric surfaces. According to the Fresnel equations there is a phase inversion if light is reflected off a dielectric surface with change from lower to higher refractive index. On the other hand, there is no phase inversion at change from higher to lower refractive index, i.e. back face reflection. Thus, on their way to port 1 both

The optical Mach-Zehnder interferometer was developed in 1891/1892 independently from each other by **Ludwig Mach** (* 1868, † 1951), son of Ernst Mach, and the Swiss physicist **Ludwig Louis Albert Zehnder** (* 1854, † 1949).

The Fresnel euqations were deduced by the French engineer and physicist **Augustin Jean Fresnel** (* 1788 in Broglie, † 1827 in Ville-d'Avray near Paris). They describe propagation of light between media with different refractive indices. [151]

beams SB and RB undergo two phase inversions, leading to constructive interference. This is different if heading towards port 2: Path SB undergoes two phase inversions, while path RB encounters only one, leading to destructive interference. However, if we insert a phase shifter into one of the paths, we can add an arbitrary phase shift and create inversely phased, sinusoidal signals on the output ports. Thus, the Mach-Zehnder interferometer is suited to detect differential phase shifts between the paths SB and RB. However, this phase needs not necessarily to originate from a phase shifter or other optical effects; e.g. the Mach-Zehnder interferometer inside the FG5 gravimeter is based on the change in length of one of the interferometer arms. A special case is the rotation of the whole setup around an axis perpendicular to the plane of the light beams. The Sagnac effect renders the Mach-Zehnder interferometer an inertial sensor, sensitive to rotations. In this respect it is also called *Sagnac interferometer*.

The **Sagnac effect** was discovered in 1913 by the french physicist **Georges Sagnac** (* in Périgueux, † 1928 in Meudon-Bellevue). Due to the finite speed of light, the beams in the two paths SB and RB traverse different path lengths. The beam traveling in direction of the rotation arrives later than the beam traveling contrary to the rotation. This leads to a phase shift that is directly proportional to the rotation rate. [138, 139]

4.1.2. Atomic Mach-Zehnder interferometer

In the light based interferometer (figure 4.1) it is light that interferes at the output ports. It is guided through the interferometer by mirrors and beam splitters made from matter. The purpose of matter and light is kind of reversed in an atom interferometer: Matter is being guided through the interferometer by mirrors and beam splitters made from light [61]. The interference, detected at the output ports is actually the interference between matter waves. Hence, atom interferometers are frequently called matter wave interferometers. While an optical Mach-Zehnder interferometer can already be realised with the cheapest laser pointer, the atoms forming the matter wave in the atomic Mach-Zehnder interferometer have to be provided and prepared in the appropriate atomic state by a source of ultra-cold atoms. Therefore, the atomic Mach-Zehnder interferometer is a comparatively complex apparatus.

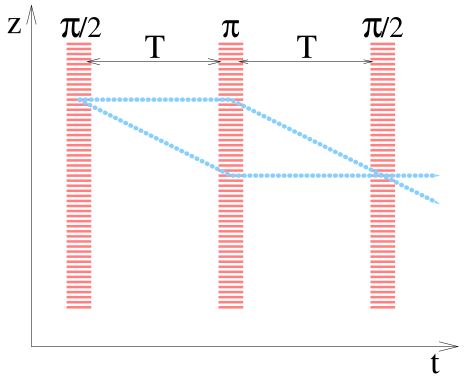

Figure 4.2.: Schematic view of an atomic Mach-Zehnder interferometer. The atomic cloud is splitted up by the first $\pi/2$ pulse, the partial clouds driving apart are reflected by a π pulse and finally recombined by another $\pi/2$ pulse.

Typical sequence of the atomic Mach-Zehnder interferometer

The geometry of the atomic Mach-Zehnder interferometer is best visualised with a time-space diagram like depicted in figure 4.2. We assume the atomic cloud initially being at rest with respect to the z axis. The cloud is then

The meaning of the terms **$\pi/2$-pulse** and **π-pulse** will be explained in the next section. For now it's sufficient to know, that the $\pi/2$-pulse and the π-pulse act like a 50%/50% beam splitter and a mirror respectively.

1. split by a $\pi/2$-pulse,
2. reflected by a π-pulse and

3. again recombined by a $\pi/2$-pulse.

The three light pulses are equally spaced in time by the free evolution time T. While the output ports of the atomic interferometer are represented by the output trajectories on the right-hand-side of figure 4.2, the number of atoms being in port 1 and port 2 respectively depends on the relative phase the atoms have collected on the two interferometer paths. The other way round we can infer from the number of atoms to the differential phase and a physical process contributing a phase shift — not different from the light-based interferometer.

At this point we should stress, that the sequential arrangement of splitting, reflecting and recombining the atoms is a temporally coherent process. Furthermore it is not only the entity of atoms that is equally distributed to the two interferometer paths, but each single atom has a probability of 50% for traveling the upper path and another 50% probability for traveling the lower path. So in principle, repeatedly performing 1000 measurements with a single-atom-interferometer yields the same result as one measurement with a cloud of 1000 atoms.

Beam splitters and mirrors using stimulated Raman transitions

Although there are also other methods to actually implement beam splitters and mirrors, we will focus on the technique of stimulated Raman transitions. Those are based on the Raman effect, which describes the inelastic scattering of photons at atoms and molecules. In elastic scattering processes — for instance Raleigh scattering — the incident photon has the same energy as the outgoing photon. Opposite to this, inelastic scattering processes comprise an energy difference between incident and outgoing photon. This effect is widely used in the technique of Raman spectroscopy, where it is usually applied to observe low-frequency — i.e. much lower, than the frequency of the individual photons — modes of molecular compounds. A special case is the *stimulated* Raman spectroscopy, which is also suited to observe atomic hyperfine levels. Those are low-frequency transitions in the previously mentioned sense. The probe is irradiated by a two colour pulse comprising photons of frequency k_1 and k_2. If the frequency difference Δk equals the frequency of the desired transition $\hbar\omega_{HF}$ and none of the two frequencies k_1 and k_2 corresponds to another transition itself, the hyperfine transition is excited by two coinciding photons. This is visualised in figure 4.3 where we have reduced the atom to a system of the

The Raman effect or Smekal-Raman effect was predicted [152] in 1923 by the Austrian physicist **Adolf Gustav Stephan Smekal** (* 1895 in Vienna; † 1959 in Graz) and experimentally discovered [134] in 1928 by the Indian physicist **Chandrasekhara Venkata Raman** (* 1888 in Tiruchirappalli; † 1970 in Bangalore). In 1930 Raman was awarded the Nobel prize *"for his work on the scattering of light and for the discovery of the effect named after him"* [76].

two hyperfine levels: the ground state $|g\rangle$ and the excited state $|e\rangle$. During the transition the atom is excited to a virtual energy level by a photon of frequency k_1, while the emission of the outgoing photon is stimulated by a photon of frequency k_2. The mentioned $\pi/2$- and π-pulses are simply light pulses driving a Raman transition between $|g\rangle$ and $|e\rangle$, where the transition probability can by adjusted by the pulse length. We'll resume the discussion on this aspect in section 4.2.

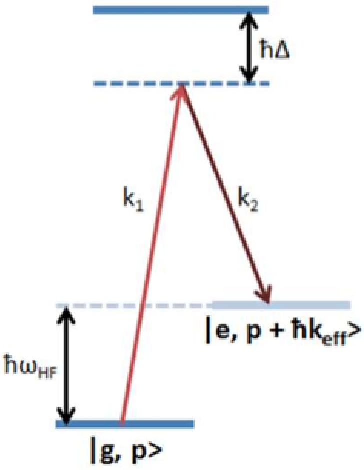

Figure 4.3.: Stimulated Raman transition between the two hyperfine levels labeled $|g\rangle$ and $|e\rangle$. During the transition a momentum of $\hbar k_{\text{eff}}$ is transfered to the atom.

Concerning the Mach-Zehnder atom interferometer there are three important issues:

- Both photons transfer momentum to the atom. This fact is used to implement the spatial splitting of the atoms during the interferometer sequence. Since the direction of the momentum transfer is determined by the direction of the light fields k_1 and k_2 the net momentum

  $$\vec{k}_{\text{eff}} = \vec{k}_1 - \vec{k}_2 \tag{4.1}$$

  can be externally controlled by the experimental setup. For co-propagating beams this is the difference of the momenta carried by the two Raman photons, $k_{\text{eff}} = k_1 - k_2$, corresponding to the momentum of the microwave transition between ground state $|g\rangle$ and excited state $|e\rangle$. On the other hand, if using counter-propagating waves the effective wave number is $k_{\text{eff}} = k_1 + k_2$, which is a multiple of the momentum in the co-propagating case.
- During the transition the relative phase of the two involved photons is imprinted onto the atom. Thus, by controlling the relative phase of the two Raman light fields ϕ, we have also control over the atomic phase Φ.
- The transfer of phase and momentum is coupled to a transfer between the two internal hyperfine levels $|g\rangle$ and $|e\rangle$. This issue, called *state labeling* can be used during the detection. Since the atoms in $|g\rangle$ and $|e\rangle$ can be addressed individually, it is possible to count the number of atoms in either states without spatial separation of the two interferometer output ports.

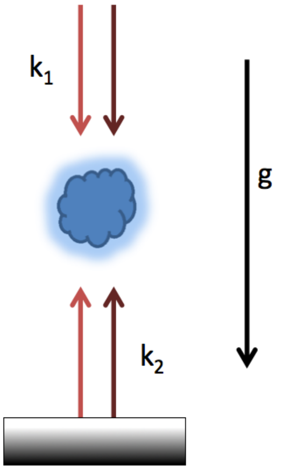

Figure 4.4.: The momentum transferred to the atoms depends on wether they interact with co-propagating beams or with counter-propagating waves. In the counter-propagating setup both beams are usually guided through the same optical fibre and retro-reflected by a mirror situated opposite to the fibre. Since the atoms move relative to the optics, the desired beams for the Raman transition can be selected by adding or subtracting the appropriate Doppler shift to the laser frequency.

4.1.3. Atomic inertial sensors

If aligning the atomic trajectories in the plane of rotation, the atomic Mach-Zehnder interferometer is sensitive to the Sagnac effect, just as in the light-based case. However, there's more to it than that! We can also adjust the Raman laser beams — that is the direction of momentum transfer — exactly vertical. The trajectory of the atoms is bend as depicted in figure 4.5, leading to an additional phase shift. Since this phase shift is proportional to the strength of the gravitational acceleration g, we can use the atomic Mach-Zehnder interferometer as a highly sensitive gravimeter.

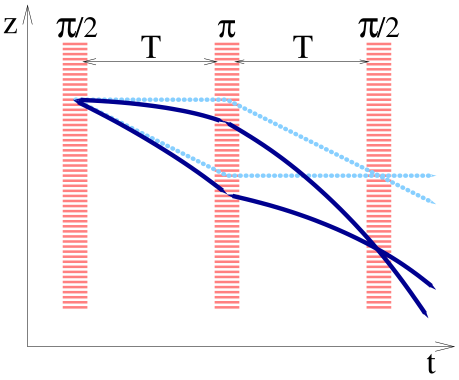

Figure 4.5.: Shape of the atomic Mach-Zehnder interferometer, when exposed to a linear gravitational field (blue). The bending of the trajectories causes an additional phase shift, which can be used to calculate the gravitational acceleration g. The trajectories of the undisturbed interferometer is included for comparison (light blue).

To get a basic understanding of the gravitational contribution to the atomic phase Φ, we think of the Raman laser field as a standing wave either fixed by the fiber (co-propagating beams) or the retro-reflection mirror (counter-propagating beams). Figuratively the laser field constitutes a fine ruler measuring relative displacement of mirror and atoms:

$$\Phi \; = \; k_{\text{eff}} \cdot z(t) \quad , \tag{4.2}$$

with $k_{\text{eff}} = k_1 + k_2 \approx 2 \cdot k$. The trajectory of the atomic cloud freely falling in a linear gravitational field is

$$z(t) \; = \; \frac{1}{2} \cdot g \cdot t^2 \quad . \tag{4.3}$$

With t being twice the free evolution time between the Raman light pulses T and summing up the phase contributions this yields

$$\Phi \; = \; k_{\text{eff}} \cdot g \cdot T^2 \quad . \tag{4.4}$$

Inserting the values for Rubidium and for Potassium,

$$k_{\text{eff}}^{\text{Rb}} \; = \; 2 \cdot \frac{2\pi}{780.2 \cdot 10^{-9}\,\text{m}} \; = \; 1.61 \cdot 10^{7}\,\text{m}^{-1}$$

$$k_{\text{eff}}^{\text{K}} \; = \; 2 \cdot \frac{2\pi}{767 \cdot 10^{-9}\,\text{m}} = 1.64 \cdot 10^{7}\,\text{m}^{-1} \quad ,$$

yields an atomic phase in the 10^6 range already for a free evolution time T of 100 ms. This emphasises the great potential lying in atomic gravimeters. However, to reach a sensitivity of $10^{-9}\,g$, we still have to resolve shifts of the atomic phase Φ in the mrad scale. This implies the essential requirements for the stability of the laser phase ϕ, which will be subject of chapters 7 through 9.

Since the two Raman lasers comprise a frequency difference, the combined electromagnetic field is actually not a **standing wave**. However, the the stimulated Raman transition is a two photon process; i.e. the atoms do not interact with the combined field, but (synchronously) with the two individual Raman laser fields. Since the relevant phase for this process is the differential laser phase ϕ, it works analogously to interaction with the phase of a standing wave.

4.2. From Raman transitions to Rabi oscillation

Before going to applications, we will treat some glimpses of theory of the atomic gravimeter. The basis for the atomic Mach-Zehnder interferometer is the observation of Rabi oscillations. In the case of the atom interferometer, they are the result of Raman transitions in an atomic two level systems. A lot of "*How does a Raman-based atom interferometer work?*" chapters have been written recently. Hence we will take an unorthodox approach to Rabi oscillations. For the usual derivation see for instance [121, 86, 24], to name only a few.

4.2.1. Rabi oscillation

Rabi oscillations can be found in various fields of physics. It occurs in systems with two states if the observable states – let's call them $|\Lambda\rangle$ – are not energy eigenstates (eigenstates of the Hamiltonian). As a first step we will solve the Schrödinger equation for the state $|\psi(t)\rangle$,

$$\mathrm{i}\hbar\partial_t|\psi(t)\rangle \;=\; \mathrm{H}|\psi(t)\rangle \quad , \tag{4.5}$$

in the Hamiltonian's eigenbasis:

$$\mathrm{i}\hbar\partial_t\begin{pmatrix}\psi_1(t)\\ \psi_2(t)\end{pmatrix} \;=\; \begin{pmatrix}E_1 & 0\\ 0 & E_2\end{pmatrix}\begin{pmatrix}\psi_1(t)\\ \psi_2(t)\end{pmatrix} \;=\; \begin{pmatrix}E_1\psi_1(t)\\ E_2\psi_2(t)\end{pmatrix} \quad . \tag{4.6}$$

This yields

$$\dot{\psi}_i(t) \;=\; -\frac{\mathrm{i}}{\hbar}E_i\psi_i(t) \quad\rightsquigarrow\quad \psi_i(t) \;=\; \mathrm{e}^{-\frac{\mathrm{i}}{\hbar}E_i}\psi_i(0) \quad . \tag{4.7}$$

What do we get now, if measuring the state $|\psi>$ after time t with an arbitrary operator A with eigenstates $|\Lambda\rangle \in \{|1\rangle, |2\rangle\}$? Introducing the abbreviations $\beta\mathrm{e}^{-\mathrm{i}\alpha} := \Lambda_1^*\psi_1(0)\Lambda_2\psi_2^*(0)$ and

Note that Λ_i is not the ith eigenstate of A, but the ith component of the eigenstate $|\Lambda>$ in the Hamiltonian's eigenbasis.

$$\Omega := \frac{E_1 - E_2}{\hbar}. \tag{4.8}$$

we get [40]

$$\begin{aligned} |\langle\Lambda|\psi\rangle|^2 \;&\doteq\; \left|(\Lambda_1^*, \Lambda_2^*)\begin{pmatrix}\psi_1(t)\\ \psi_2(t)\end{pmatrix}\right|^2 \;=\; |\Lambda_1^*\psi_1(t) + \Lambda_2^*\psi_2(t)|^2 \\ &\;| \\ &= \; |\Lambda_1^*\psi_1(0)|^2 + |\Lambda_2^*\psi_2(0)|^2 + \mathrm{e}^{-\mathrm{i}\Omega t}\beta\mathrm{e}^{-\mathrm{i}\alpha} + \mathrm{e}^{\mathrm{i}\Omega t}\beta\mathrm{e}^{\mathrm{i}\alpha} \\ &\;| \\ &= \; |\Lambda_1^*\psi_1(0)|^2 + |\Lambda_2^*\psi_2(0)|^2 + 2\beta\cos(\Omega t + \alpha) \end{aligned} \tag{4.9}$$

What does this mean? Obviously $|\langle\Lambda|\psi\rangle|^2$ oscillates with frequency Ω and amplitude β. One might already have guessed, that Ω is the famous *Rabi frequency*. It only depends on the difference of the Hamiltonian's eigenenergies $E_1 - E_2$. The oscillation vanishes if $|\psi(0)\rangle$ or $|\Lambda\rangle$ are energy eigenstates, because then the amplitude

$$\beta = |\Lambda_1^* \psi_1(0) \Lambda_2 \psi_2^*(0)| \tag{4.10}$$

vanishes. On the other extreme the oscillation gets maximal if Λ and $\psi(0)$ are superpositions of equal parts of $|1\rangle$ and $|2\rangle$, e.g. $\frac{1}{\sqrt{2}}(|1\rangle + |2\rangle)$.

4.2.2. Stimulated Raman transitions

Above, we mentioned that Rabi oscillations occur if the observable states are not energy eigenstates. So, where is the connection to our atom interferometer? The observable eigenstates $|\Lambda\rangle$ of our detection operator A are the two hyperfine states , $|g\rangle$ and $|e\rangle$, adressed by the Raman transition. Hence our detection operator, beeing sensitive to these two states, is

$$\mathrm{A} \;=\; A_1 |e\rangle\langle e| + A_2 |g\rangle\langle g| \tag{4.11}$$

In the experiment we usually tune $A_1 = 1$ and $A_2 = 0$ to get the number of atoms in the excited state $|e\rangle$.

On the other hand, the Hamiltonian is that of an atom in an external (electro-magnetic) laser field E,

$$\mathrm{H} \;=\; \frac{\mathrm{P}^2}{2m}\Big(\hbar\omega_e |e\rangle\langle e| + \hbar\omega_g |g\rangle\langle g|\Big) - \mathrm{D}E \quad . \tag{4.12}$$

The momentum operator P accounts for the momentum which is transferred during the stimulated Raman transition, while the projectors $|g\rangle\langle g|$ and $|e\rangle\langle e|$ address the atom's internal state. The crucial ingredient turning away the Hamiltonians eigenbasis from $\{|g\rangle, |e\rangle\}$ is the term $\mathrm{D}E$, where D is the dipol operator. It is obvious that the eigenstates of A, $|g\rangle$ and $|e\rangle$, are no eigenstates of the Hamiltonian H! Thus, since the atoms are prepared into either $|g\rangle$ or $|e\rangle$, there should be a Rabi oscillation. In fact, putting (4.12) into the Schrödinger equation yields a Rabi oscillation with effective Rabi frequency [86]

$$\Omega \;=\; \sqrt{\left|\frac{\langle e|\mathrm{D}E_0|g\rangle}{\hbar}\right|^2 + \delta^2} \quad . \tag{4.13}$$

It depends on the detuning δ of the Raman light and the amplitude of the external field E_0. The probability of finding an atom, initially prepared into the state $|\psi(0)\rangle = |g\rangle$, in the state $|e\rangle$ after interaction time τ is

$$|\langle e|\psi(\tau)\rangle|^2 = \frac{1}{2}(1 - \cos(\Omega\tau)) \quad . \tag{4.14}$$

As we can see, the transition probability depends only on the pulse length τ and the effecive Rabi frequency Ω. By adjusting these parameters one can realise an arbitrary superposition of the states $|e\rangle$ and $|g\rangle$. When choosing $\Omega\tau = \pi$ we transfer (in the ideal case) all the atoms into the excited state $|e\rangle$, while for $\Omega\tau = \pi/2$ we get a superposition $1/\sqrt{2}\,(|g\rangle + |e\rangle)$ with 50% excitation probability. These are the already mentioned π pulse and $\pi/2$ pulse, respectively. Typical values for Rubidium and Potassium are in the order of some tens of microseconds.

4.3. Evolution of the atomic phase

As a convention we denote the atomic phase with (uppercase) Φ, while we denote the differential phase of the two Raman laser fields with (lowercase) ϕ.

In the following we will describe the essential results of the derivation of the atomic phase given in [132]. What we call the atomic phase Φ is actually the difference of the phases, the atoms collect during their travel through the paths A and B. This difference can be divided into three contributions [132]:

$$\Phi = \Phi_{\text{propagation}} + \Phi_{\text{light}} + \Phi_{\text{separation}} \quad . \tag{4.15}$$

The propagation phase $\Phi_{\text{propagation}}$ describes the phase collected during free evolution of the atoms between the Raman laser pulses, whereas the light interaction phase Φ_{light} is caused by the interaction with the Raman pulses. The separation phase $\Phi_{\text{separation}}$ accounts for the final separation of the wave packets at the end of the interferometer sequence.

Using the path integral description of quantum mechanics, it can be shown, that the contribution $\Phi_{\text{propagation}}$ to the atomic phase vanishes [132]. Assuming an infinitesimal small atom cloud, the phase imprinted to the atoms during the Raman light pulse depends only on the local phase of the laser field,

$$\phi = k_{\text{eff}} z - \omega_{\text{eff}} t \quad , \tag{4.16}$$

where z is the atom's vertical position. If the atoms don't move with respect to the laser field — i.e. in a freely falling interferometer without any external fields — this in fact leads to a symmetric situation and $\Phi_{\text{light}} = 0$ [132]. However, introducing a gravitational field g acts as a symmetry breaking mechanism on the interferometer and reveals a phase shift related to g. A uniform gravitational field g (no gravity gradients) leads to [132]

$$z(t) \ = \ z(0) + v_0 t + \frac{1}{2} g t^2 \qquad (4.17)$$

for the atoms vertical position and an atomic phase of

$$\Phi \ = \ k_{\text{eff}} g T^2 \ = \ \frac{m v_{\text{rec}}}{\hbar} g T^2 \quad . \qquad (4.18)$$

For Rubidium, $g = 9.81\,\text{m/s}^2$ and $T = 80\,\text{ms}$ this leads to a atomic phase of $\Phi \approx 10^6\,\text{rad}$.

If aiming for sensitivities better than $10^{-5}\,g$, gravity gradients can no longer be neglected [38]. See equation (6.20) in section 6.3.1 for the contributions from first order gravity gradients. The second order gravity gradient term is more than one order of magnitude smaller, than effects arising from relativistic effects. Since beyond a sensitivity of $10^{-9} g$ relativistic effects give a significant contribution to the atomic phase [38], in the space borne mission QUEST (see chapter 5) higher order effects on the atomic phase would have to be calculated in a relativistic scheme.

4.4. Phase readout, noise and fundamental limitations

The complex phase of a quantum-mechanical wave function is a rather abstract quantity, which cannot be read out directly. We always have to find ways to encode the phase into some measurable quantity. In an light-based interferometer this is the intensity at the output ports whereas in an atom interferometer this is the transition probability of the atoms after the interferometer sequence. In an ideal Mach-Zehnder atom interferometer the transition probability at the end of the $\pi/2 - \pi - \pi/2$ sequence is

$$P \ = \ \frac{1}{2}\Big(1 - \cos(\Phi)\Big) \quad . \qquad (4.19)$$

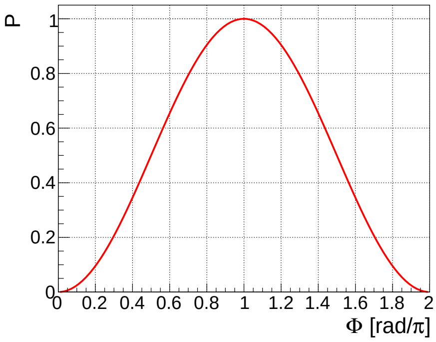

Figure 4.6.: Fringe pattern of the transition probability P over atomic phase Φ.

A plot of the transition probability P is depicted in figure 4.6.

In the atomic gravimeter using equation (4.19) in combination with equation (4.18) enables us to calculate local g from the excitation probability P. Both quantities are affected by noise. In state-of-the-art atom interferometers a fundamental limit is posed by quantum projection noise, also known as shot noise. Several atom interferometers measuring at or near the shot noise limit have been demonstrated [15, 158, 13, 83]. However, this requires substantial efforts to suppress noise since usually technical noise and systematic effects are much higher than shot noise. Also, the cited atom interferometers are gyroscopes. In contrast to those — due to the kind of measurement – the strongest source of noise in gravimeters typically is vibration noise [97], which makes it quite challenging to reach the shot noise limit with atomic gravimeters.

4.4.1. Quantum projection noise

As just mentioned P cannot be measured directly. For illustration we think of a single-atom interferometer: For all values of P with $0 < P < 1$, the result would be either 0 (atom in the ground state) or 1 (atom in the excited state). This corresponds to a statistical error of 100%. However, if we average over many atoms, we can extract P from the number of atoms that are in the excited state $|e\rangle$ and in the ground state $|g\rangle$, respectively:

$$P = \frac{N_{|e\rangle}}{N_{|e\rangle} + N_{|g\rangle}} \quad . \tag{4.20}$$

For a single measurement comprising N_{tot} atoms the statistical error is [24]:

$$\sigma_P = \sqrt{\frac{P(1-P)}{N_{\text{tot}}}} \quad . \tag{4.21}$$

Converting the error on the transition probability P to the error on the atomic phase Φ yields (100 % contrast assumed):

$$\sigma_\Phi = \sigma_P \cdot \left|\frac{d\Phi}{dP}\right| = \underbrace{\sqrt{\frac{P(1-P)}{N_{\text{tot}}}}}_{1.} \cdot \underbrace{\frac{2}{|\sin(\Phi)|}}_{2.} \quad . \tag{4.22}$$

From the two multiplicative terms in (4.22), we can directly identify the following two issues:

1. The achievable precision is limited by quantum projection noise, also referred to as shot noise. First of all, the extracted value is always quantised, as long as the number of atoms is finite. Secondly, the number of atoms, that is excited at the end of the interferometer sequence, fluctuates according to Poissonian statistics. In general we can state that the achievable precision increases with the square root of the number of atoms.

2. Due to the sinusoidal shape of P, the interferometer's sensitivity apparently depends on the operating point.

However, if we replace P in (4.22) by the expression from (4.19), we end up with

$$\sigma_\Phi = \frac{1}{2}\sqrt{\frac{1-\cos^2(\Phi)}{N_{\text{tot}}}} \cdot \frac{2}{|\sin(\Phi)|} = \frac{1}{\sqrt{N_{\text{tot}}}} \qquad (4.23)$$

for a single interferometer. The only thing remaining is the factor $1/\sqrt{N_{\text{tot}}}$ from Poissonian statistics. Thus, the error on the atomic phase does not depend on the operating point anymore, but only on the number of atoms. For 10^5 atoms (4.23) yields σ_Φ=3.2 mrad, while increasing the number of atoms to 10^6 reduces the phase error to σ_Φ=1.0 mrad. Opposed to technical noise, Poissonian statistics cannot be eliminated by improving the experimental setup, e.g. by changing to low noise components. This is a more fundamental limit called the standard quantum limit (SQL) or shot noise limit.

For a dual interferometer, as applied for a atom interferometric test of the UFF, the effect of quantum projection noise goes in twice. Assuming two identical atom interferometers, this yields an additional factor of $\sqrt{2}$:

$$\sigma_\Phi = \sqrt{\frac{2}{N_{\text{tot}}}} \quad .$$

State-of-the-art atom interferometers, like the CAPRICE apparatus presented in this chapter, utilise uncorrelated sources and cannot operate beyond the **standard quantum limit**. Using squeezed states and entangled probe particles, the resolution can be improved towards the more fundamental Heisenberg limit. Spin-squeezed atomic ensembles providing superior single shot sensitivity have been demonstrated, but as yet suffer from lower atom numbers than *conventional* atom interferometers. [105]

4.4.2. Contrast

Equation (4.19) is false. Or to be more precise it is only true for an ideal interferometer with a contrast of 100%. In a real interferometer we must take several effects into account, which lower the contrast. This leads us to the form

$$P(\Phi) = P_0 + A\cos(\Phi) \quad . \qquad (4.24)$$

In terms of the offset P_0 and the interference amplitude A the contrast is defined as

$$C = \frac{A}{P_0} \leq 1 \quad . \qquad (4.25)$$

If the sinusoidal shape of P is centred around $P_0 = \frac{1}{2}$, (4.24) becomes:

$$P(\Phi) = \frac{1}{2}\Big(1 + C\cos(\Phi)\Big) \quad . \qquad (4.26)$$

Although the reduction of contrast is not noise, it leads to an increase of the error on the atomic phase. Including contrast in equation (4.23) then yields:

$$\sigma_\Phi = \frac{1}{C\cdot\sqrt{N_{\text{tot}}}} \quad . \qquad (4.27)$$

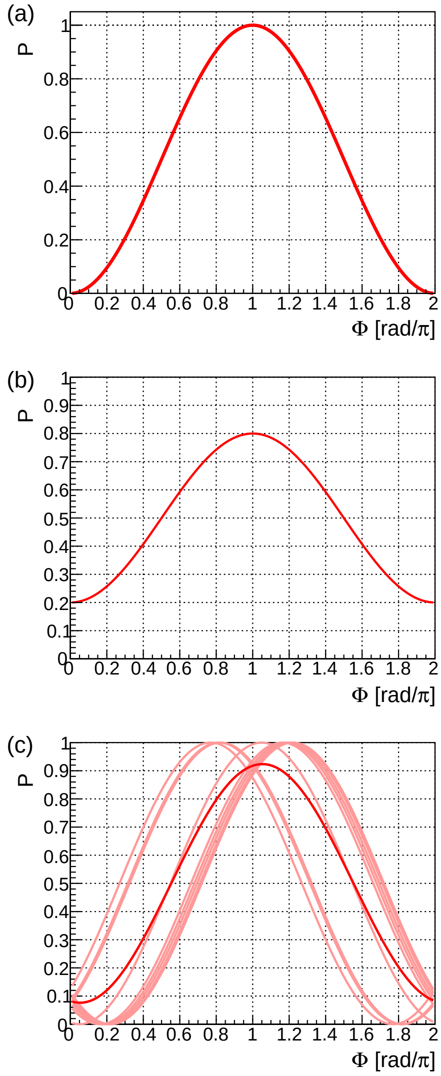

Figure 4.7.: Illustration of decoherence and dephasing effects. (a) Ideal fringe with 100% contrast. (b) The contrast is reduced due to decoherence. A portion of the atoms is kicked out of the coherent process and randomly populates the $|e>$ and the $|g>$ state. (c) The contrast is reduced by dephasing. The atom interferometer can be thought of as an ensemble of many small single-atom interferometers (light red). All of them yield 100% contrast, but the overall interferometer phase averaged over the small interferometers has a reduced contrast (dark red).

As can be seen from equation (4.27), the loss of contrast acts exactly like a reduction of the number of atoms. However, the loss of contrast itself is not fundamental in the true sense of the word. It is often caused by imperfections of the experimental setup. The reasons can basically be subdivided into mechanisms leading to either decoherence or dephasing.

Decoherence Decoherence is caused for example by spontaneous emission or by stimulated emission caused by stray light. During the interferometer sequence, the atom samples a phase imprinted to it by the Raman lasers. Since the Raman lasers are phase stabilised the interferometer sequence is coherent, as long as the atom interacts only with the Raman light field. But if an atom interacts with a non-Raman photon or emits a photon spontaneously, a random phase is added to the interferometric phase of this particular atom. It is no longer in a coherent state and practically drops out of the interferometer cycle. During the detection it will be seen as background, which is illustrated in figure 4.7 (b).

Dephasing In contrast to decoherence, dephasing is a multi-particle effect. It reduces contrast due to the fact, that the measured signal is always averaged over several thousands or even more atoms. The individual atoms – every one representing a small single-atom interferometer – are still coherent throughout the interferometer cycle. The central point is, that the atomic ensemble in the interferometer is not pointlike. Hence, an atom at the one side of the atomic cloud may sample a different phase than an atom on the other side or the centre of the cloud. To get the overall phase, we have to average over all these tiny single-atom interferometers, which are no longer perfectly in phase. If the dephasing of the individual atoms would be distributed perfectly uniform or symmetrical, the overall signal would still be a perfect cosine with 100% contrast. However, if not, the fringe washes out and the contrast is reduced as shown in figure 4.7 (c). In terms of formulas, this can be expressed by

$$P_{\text{total}} = \int d^3x\, d^3v \cdot f(\vec{x}) \cdot h(\vec{v}) \cdot P(\Phi(\textit{something})). \tag{4.28}$$

The spatial distribution $f(\vec{x})$ of the atomic cloud induces, that every atom might sense slightly different environmental conditions. Further more even a sample of ultra cold atoms has a non-zero temperature distribution $h(\vec{v})$. This means that during the interferometer sequence an atom might change its position within the

Raman light field, the gravitational field etc. Finally, the *something* in equation (4.28) might mean:

- In a Raman light beam with a gaussian profile: the atoms at the border of the beam will undergo a smaller Rabi frequency, than the atoms in the centre of the beam. [132, 61]
- Especially in an atomic gravimeter, due to spatial variations of the gravitational field — as the gravity gradient of the Earth gravitational field and even higher order effects of the surrounding lab building — every atom undergoes a different acceleration and hence samples a different phase. [101]
- Coriolis force due to Earth rotation. [113]
- Other environmental effects like magnetic fields or stray light might also have an influence on the excitation probability.

4.4.3. Technical noise and systematic effects

Equations (4.23) and (4.27) are valid if the interferometer is limited by quantum projection noise. However, quantum projection noise is often exceeded by other perturbing effects, like technical noise. In general we can distinguish two sorts of errors:

- **Statistical errors** contribute true random noise to the signal. Hence, they only reduce the precision, but not the accuracy. Beside quantum projection noise the main source of statistical errors is technical or electronic noise (see section 9.1.3). Technical noise can be reduced to some extent by improving the experimental setup, e.g. with low noise electronic components. As we saw in the previous subsection also quantum projection noise can be influenced within certain bounds by adjusting the experimental parameters. However, the residual statistical noise can only be compensated by integrating over multiple measurements.
- **Systematic errors** can contribute a constant offset or a fluctuation which may averages out over time. Examples are the AC Stark shift of the atomic levels in the electro-magnetic laser field, effects caused by electro-magnetic stray fields and mechanical drifts of the optical components due to temperature fluctuations. Although they sometimes are the objective of a gravimetry measurement, even tidal effects may constitute an undesired contribution to the measured signal. Some

of these effects can be compensated by neat choice of experimental parameters (AC Stark shift [112]), by improving the environmental conditions (temperature stabilisation) or by additional shielding (shielding against magnetic fields, thermal isolation). Others may also be measured or calculated and substracted during data post-processing (tidal effects, vibrations [97]).

As one of the main contribution to statistical noise we will treat phase noise of the Raman laser ruler in the next subsection and in chapters 7 through 9. Systematic errors will not be discussed further within this thesis (see [143] for an analysis of systematic effects within the CAPRICE experiment).

4.4.4. Laser phase noise

We will again focus on σ_Φ and ask the question: What, apart from quantum projection noise, causes fluctuations of the atomic phase? Usually, technical noise of the detection electronics can be neglected compared to quantum projection noise [24]. The biggest gateway for noise on the atomic phase Φ is the fluctuation of the laser ruler — or rather the laser phase ϕ — which on its part is mainly due to residual phase noise of the phase locked laser pair (see chapter 7 and 9) and vibrations (see e.g. [97]). During each Raman pulse the phase difference ϕ between the two lasers is imprinted on the atomic phase. Due to the setup with two counterpropagating lasers, ϕ depends on the position of the atoms relative to the wavefronts of the laser beam. Thus an atom interferometer based on the measurement of the atomic phase Φ is sensitive to phase noise on the laser phase ϕ. It can basically be summarised by [91]:

$$\sigma_\phi^2 = \sigma_{\text{optics}}^2 + \sigma_{\text{retro}}^2 + \sigma_{\text{laser}}^2 \quad . \tag{4.29}$$

The noise contribution due to intensity fluctuations of the Raman laser fields, $\sigma_{\text{intensity}}$, is sometimes mentioned in conjunction with laser phase noise. See for example [91], where it was found to be 0.5 mrad per measurement. However, we have not included it at this point, since the transfer mechanism to the atomic phase is not related to spatial fluctuation of the laser phase.

We identify three sources for fluctuation of the local laser phase ϕ:

1. The contribution σ_{optics} is caused by vibrations of the optics between laser source and laser ruler, which are transferred to the laser phase. Metaphorically speaking, the ticks of the laser ruler vibrate in exactly the same way as the laser phase. If using counter propagating beams and a retro-reflecting mirror, this effect is suppressed to some extent. The residual vibrations of fixed components (mirrors, beam splitters, lenses etc.) can usually be neglected [25], while the fluctuation of the atomic phase caused by vibrations of the optical fibre lies in the order of 1 mrad [24].

2. However, the use of an retro-reflecting mirror causes other effects, represented by σ_{retro} [117, 91]. Since the retro-reflecting mirror determines the spatial position of the standing laser wave, its vibrations are directly transferred to the phase of the Raman laser field and hence to the ticks of the laser ruler. In an average university building undamped vibrations of the retro-reflecting mirror can easily contribute several hundred mrad to the fluctuation of the atomic phase. See for example [97] for the treatment of vibration noise at the CAPRICE experiment. The second effect of the retro-reflection mirror is much smaller than the contribution from vibrations. Since the laser beam being reflected at the mirror travels a slightly longer way, it is delayed by 3 ns/m with respect to the unreflected beam. Thus, fluctuations of the laser phase at corresponding frequencies are not common mode any more. Since the lasers have finite line-width, this leads to an additional noise contribution [89]. For the ATLAS setup the upper bound of this noise contribution was calculated to be 0.4 mrad [97], assuming a constant distance of 80 cm between the atoms and the retro-reflecting mirror. However, during the acceleration measurement the atoms move towards the mirror and the effect will be reduced.

3. The last term, σ_{laser}, arises from the stability of the laser source itself, or rather the differential phase of the two diode lasers. To suppress their internal phase noise the laser phase ϕ is phase locked to a low-phase noise frequency reference. Thus, the residual laser phase noise depends primarily on the frequency reference and the gain of the optical phase-locked loop.

While we will not further discuss the first two items, the third is the subject of part III of this thesis: See chapter 7 and 8 for an introduction into optical phase locked loops. A detailed investigation of laser phase noise in an optical phase-locked loop will be made in chapter 9.

4.5. The sensitivity

Concerning gravimetry we are not primarily interested in the error of the atomic phase Φ, but in the error of the measurement of local Earth acceleration g. When calculating g from the atomic phase Φ

with equation (4.18),

$$\Phi \;=\; k_{\text{eff}} g T^2 \quad \Leftrightarrow \quad g \;=\; \frac{\Phi}{k_{\text{eff}} T^2} \quad ,$$

there are three possible sources of uncertainty — Φ, k_{eff} and T:

$$\sigma_g \;=\; \frac{1}{k_{\text{eff}} T^2} \cdot \sigma_\Phi \;+\; \frac{\Phi}{k_{\text{eff}}^2 T^2} \cdot \sigma_{k_{\text{eff}}} \;+\; \frac{2\Phi}{k_{\text{eff}} T^3} \cdot \sigma_T \tag{4.30}$$

Inserting for $\sigma_{k_{\text{eff}}}$ and σ_T shows that the contributions from k_{eff} and T can be neglected. This leaves only the atomic phase as relevant source of uncertainty. Hence, we can derive the *sensitivity* of the atomic accelerometer using equation (4.27):

$$\sigma_g \;=\; \sigma_\Phi \cdot \left| \frac{dg}{d\Phi} \right| \;=\; \frac{1}{C \cdot \sqrt{N_{\text{tot}}}} \cdot \frac{1}{k_{\text{eff}} T^2} \quad . \tag{4.31}$$

While σ_g is usually indicated in either m/s^2 or in units of g, we have to normalise the sensitivity to the strength of the gravitational field when calculating a sensitivity with respect to the Eötvös ratio. If we assume a violation of the UFF, that is proportional to the strength of the gravitational field g and in addition assume the use of two identical interferometers, the *Eötvös sensitivity* is:

$$\sigma_\eta \;=\; \sqrt{2} \cdot \frac{\sigma_g}{g} \;=\; \frac{\sqrt{2}}{C \cdot \sqrt{N_{\text{tot}}}} \cdot \frac{1}{k_{\text{eff}} T^2 \cdot g} \quad . \tag{4.32}$$

If averaging over $N \gg 1$ measurements, we come to the integrated sensitivity

$$\sigma_\eta^{(\text{N})} \;=\; \sqrt{\frac{1}{N(N-1)} \sum_{i=1}^{N} \left(\sigma_\eta^{(i)}\right)^2} \;\approx\; \frac{1}{N} \sqrt{\sum_{i=1}^{N} \left(\sigma_\eta^{(i)}\right)^2} \quad . \tag{4.33}$$

It can be simplified provided the experimental conditions do not change during the measurement campaign and all the $\sigma_\eta^{(i)}$ are identical:

$$\sigma_\eta^{(\text{N})} \;\approx\; \frac{1}{N} \sqrt{N \cdot \left(\sigma_\eta\right)^2} \;=\; \frac{\sigma_\eta}{\sqrt{N}} \quad . \tag{4.34}$$

We will make further remarks on this issue in section 6.2.

T [s]	σ_g [m/s^2]	
	$N_{\text{tot}} = 10^5$	$N_{\text{tot}} = 10^6$
0.1	$2.0 \cdot 10^{-8}$	$6.0 \cdot 10^{-9}$
1	$2.0 \cdot 10^{-10}$	$6.0 \cdot 10^{-11}$
5	$0.8 \cdot 10^{-11}$	$2.4 \cdot 10^{-12}$

Table 4.1.: The influence of atom number N_{tot} and free evolution time T on the shot noise limit: While increasing the number of atoms by one order of magnitude improvemes the sensitivity by a factor 3.25, increasing the free evolution time by one order of magnitude yields a factor 100. All values are calculated for 100% contrast.

4.5.1. Increasing T

Both, σ_g and σ_η, do not only depend on the square root of the atom number N_{tot}, but also on the free evolution time T squared.

Hence, doubling the free evolution time T leads to the same improvement of the sensitivity as increasing the atom number by a factor of eight! Some example values are given in table 4.1. In table-top experiments the free evolution time T is usually limited to a few milliseconds by the size of the vacuum chamber. Especially with respect to a test of the UFF, much effort is spent on different possibilities to increase T.

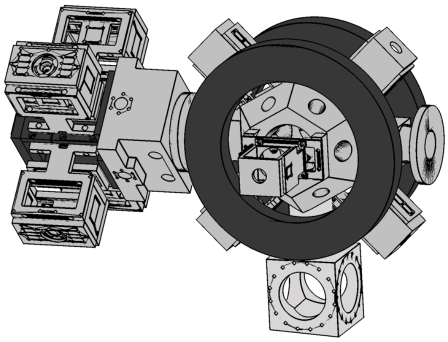

Figure 4.8.: Vacuum system of the ATLAS experiment, where CAPRICE is conducted.

The simplest solution is to enhance the vacuum chamber by attaching a tube, like it was implemented in the **CAPRICE** (Cold Atom test of the PRInCiple of Equivalence) experiment [97]. With a drop-distance of roughly 30 cm corresponding to a drop time of 210 ms this allows free evolution times of up to $T = 80$ ms. Enhancing the *drop tube* to 10 m would allow drop times of up to 1.4 s or even 2.8 s if operated with an atomic fountain. Suchlike projects are for instance planned at the HITech facility in Hannover and currently commissioned at Wuhan [186] and Stanford [64]. By comparing the acceleration of ^{85}Rb and ^{87}Rb atoms in the Earth's gravitational field, they allow for a test of the UFF.

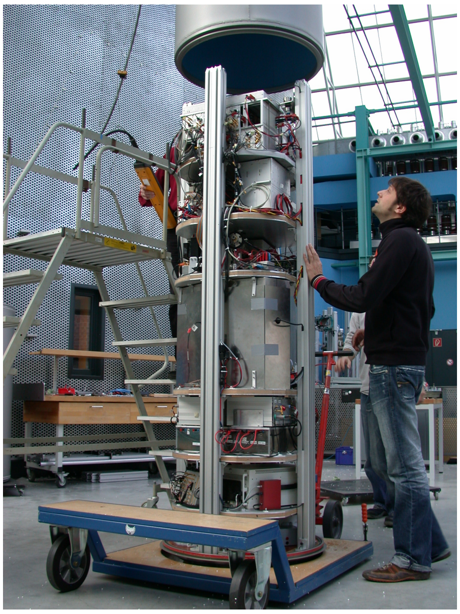

Figure 4.9.: Capsule of the QUANTUS I experiment.

The longer the drop tube, the more challenging are the technical constraints e.g. on convergence of the vertical laser beams. A completely different approach is pursued by drop tower experiments, where it is not the atoms but the whole experiment being dropped. The 110 m drop tower at **ZARM** (Zentrum für Angewandte Raumfahrttechnologie und Mikrogravitation) in Bremen allows drop times of 4 s (drop mode) or 9 s (catapult mode). The handicap of the drop tower experiments, like QUANTUS (QUANtengase Unter Schwerelosigkeit) is their limited repetition rate. For instance the operation of the drop tower at ZARM does only allow three measurements per day. Such a low repetition rate does not provide a sufficient amount of measurements to achieve an integrated sensitivity as required for an test of the universality of free fall.

Space-borne experiments pose an alternative to the proliferation of the physical dimensions of experimental setups. A satellite in orbit around Earth moves freely falling on a geodetic. Since the gravitational force is cancelled by centrifugal force, the atomic cloud essentially remains in the centre of the vacuum chamber. UFF violations would only become manifest in tiny differences in acceleration, corresponding to equation (2.13). Hence, a small and compact experimental setup is sufficient. The next chapters feature such a space-borne experiment: the QUEST (QUantum Equivalence principle Space Test) mission.

5. The STE-QUEST mission

STE-QUEST is a joint mission of the formerly independent projects *Space Time Explorer* (STE) and *QUantum Equivalence principle Space Test* (QUEST), aiming for different aspects of the Einstein Equivalence Principle. While STE aims for testing the UGR with an atomic clock, QUEST is dedicated to a test of the UFF using an atom interferometer. Due to the technical overlap of the two missions – e.g. both devices are now based on the atomic species of Rubidium – it was decided in 2010 to propose an M-class mission for the Cosmic Vision Program featuring both experiments. The original proposal was submitted to the European Space Agency (ESA) on December 3, 2010. In February 2011 it was recommended for further assessment by the ESA Space Science Advisory Committee as one of four mission out of 47 submitted proposals.

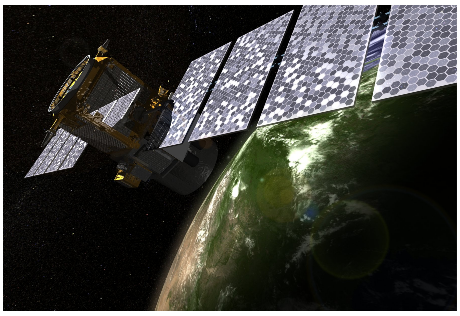

Figure 5.1.: Artist impression of a satellite based on the PROTEUS platform, which was originally considered for the STE-QUEST mission. [125]

In the following assessment process it became crucial to make a detailed analysis of the performance regarding effects inherent to atom interferometers, as well as effects originating from the environmental conditions in orbit around Earth. In this chapter, we will initially give a short summary of the STE-QUEST mission documents (see table 5.1). In chapter 6 we will constrain to the QUEST part of the mission and calculate the sensitivity of the atom interferometer to violations of UFF.

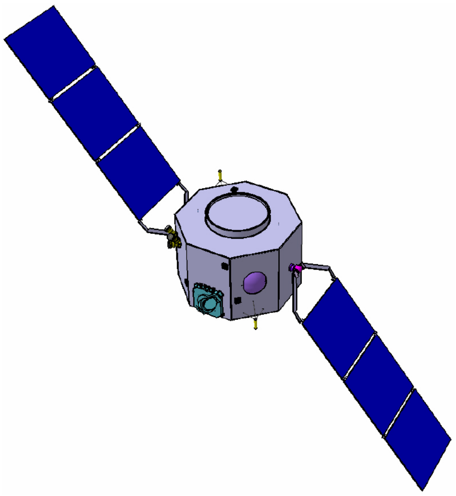

Figure 5.2.: CAD drawing of the STE-QUEST spacecraft. [52]

[46]	MWXG Proposal	29/06/2007
[52]	STE-QUEST Proposal	03/12/2010
[54]	Technology Readiness Review (TRR)	21/04/2011
[53]	Concurrent Design Facility (CDF)	30/06/2011
[57]	Payload Definition Document (PDD)	22/06/2012
[55]	Mission Analysis Guidelines (MAG)	20/06/2012
[56]	Mission Requirements Document (MRD)	18/09/2012
[58]	Science Requirements Document (SRD)	22/04/2013
[59]	Assessment Study Report (Yellow Book)	16/12/2013

Table 5.1.: STE-QUEST related documents.

5.1. Scope of space-borne UFF test

As discussed above the classical techniques for tests of the universality of free fall are essentially exhausted. Also atomic gravimeters suffer from limitations related to “being on the surface of the earth”, i.e. vibrations (see e.g. [97]) and limited drop time time (see section 4.5.1). This case pushes scientists on developing new concepts to overcome the limitations of current ground based tests, basically meaning space-borne experiments. There are currently several mission concepts worked on that are based on classical test masses.

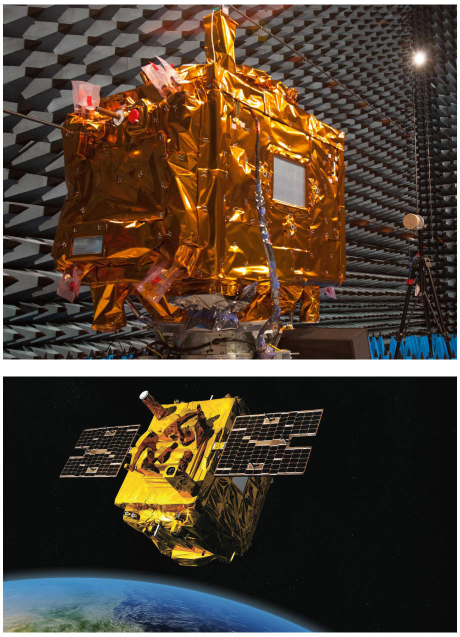

Figure 5.3.: The MICROSCPE satellite in an EMC chamber (top) and illustration of the spacecraft in orbit (bottom). [26]

5.1.1. Classical space-borne UFF tests

The **MICROSCOPE** mission (MICROSatellite pour l’Observation de Principe d’Equivalence) developed by the French space agency CNES and the French aerospace research agency ONERA aims for a sensitivity of $\eta < 10^{-15}$. The mission’s scientific instrument is called T-SAGE (Twin-Space Accelerometer for Gravity Experiment). It features two pairs of concentric cylindrical pairs of test masses: titanium and platinum-rhodium alloy for the science measurement and a test mass pair made from platinum as reference measurement. Also, the satellite comprises an Acceleration Attitude Control System (AACS) floating the satellite around the test masses [165]. MICROSCOPE was launched on 25 April 2016 from CSG (Centre Spatial Guyanais) near Kourou, French Guiana, on a Soyuz-2 carrier rocket and a Fregat upper stage into a sun-synchronous orbit. First high-precision measurements have already been performed during the in-orbit checkout phase, before the instrument will be switched into mission mode by end of 2016. The satellite is designed for a mission life time of two years. [27].

The choice of **test mass materials** (four pairs of Pt-Ir, Nb and Be test masses arranged in a cyclic configuration [130]) is based on the work of Blaser and Damour [31, 35, 16], which also was the basis of chapter 3 of this thesis.

Two other concepts for a space-borne UFF mission using macroscopic test masses are **STEP** (Satellite Test of the Equivalence Principle) [130] and GG (Galielo Galieli) [108, 60]. STEP is planed to include four pairs of concentric cylindrical test masses of different compositions in a drag-free satellite on a sun-synchronous orbit. By combining the data from the 4 differential accelerometers and due to the cyclical topography of test mass materials, STEP is expected to reach a sensitivity of up to 10^{-18} [130]. Although work on the STEP accelerometers dates back to 1972 and underwent Phase A studies at ESA (1989 - 1992) and NASA (1999 - 2002) as well as a NASA financed technology development phase (2004 - 2008), there is currently no ongoing work for the mission’s actual implementation.

A proposal for a mission with a sensitivity targeted in-between MICROSCOPE and STEP of 10^{-17} is **GG** (Galielo Galieli). The sensor is based on concentric cylindrical test masses, but different from the aforementioned missions those test masses will be rapidly rotating. The basic idea behind the rotation is to up-convert a low frequency modulation due to a violation of the equivalence principle to a higher frequency [70]. GG already underwent two phase A study phases in 2002 and 2009 [108]. A full scale sensor similar to the one to fly in GG has been setup on ground and a differential acceleration noise level of $7 \cdot 10^{-11}$ m/s^2 has been demonstrated [60]. It is planed to submit GG to the EXPLORER program of NASA.

5.1.2. Development of space-borne atom interferometers

One of the first efforts to bring an atomic inertial sensor into space was the **HYPER** mission proposal [47] developed in the late 1990's and submitted to ESA's *Horizons 2000* programme in January 2000 [46]. Although it was designed as a Sagnac interferometer for measuring the Lense-Thirring effect, HYPER can be seen as the earliest direct ancestor of QUEST. After being chosen for a study at assessment level, it was assessed by the Concurrent Design Facility (CDF) at ESTEC [47, 126, 50], followed by an industrial feasibility study [74]. The latter one concluded that *no show stoppers were identified*, but next activities should concentrate on improving the atom interferometer itself, including on-ground testing.


Figure 5.4.: Artist's impression of the HYPER spacecraft overall configuration. [47]

The original HYPER proposal already included a 700 km polar orbit. As part of the industrial feasibility study a 1000 km sun-synchronous orbit was evaluated favourably because it comprises a less perturbing environment, atmospheric drag reduced by one order of magnitude, a lower gravity gradient and more eclipse-free

Mission	Target sensitivity	Test mass	Type	Status	Latest resource
MICROSCOPE	10^{-15}	macroscopic	satellite	launched	[27]
STEP	10^{-17}	macroscopic	satellite	phase A study	[130]
GG	10^{-18}	macroscopic/rotating	satellite	phase A study	[60]
MWXG	10^{-16}	cold atoms	satellite	concept	[46]
STE-QUEST	10^{-15}	cold atoms	satellite	phase A study	[52]
QTEST	10^{-15}	cold atoms	ISS	proposed	[181]
Q-WEP	10^{-14}	cold atoms	ISS	proposed	[65]

Table 5.2.: Comparison of different concepts for space-borne missions testing the universality of free fall.

days [111]. A very similar orbit was later suggested for MWXG [46] and was also intended for QUEST (before it became part of the STE-QUEST joint mission with completely different orbit requirements). Also the secondary AOCS design (Attitude and Orbit Control System) assessed for HYPER [160] reappeared in the MWXG proposal. At the end of the day HYPER was not selected, because the technique of cold atoms was not considered mature enough for a space mission [46], i.e. the technology readiness level (TRL) was too low. And yet, although the idea of a space-borne gyroscope was not pursued any further, the parentage of HYPER spacecraft design to MXWG and QUEST is evident.

Figure 5.5.: CAD sketch of the MWXG instrument (top), MWXG logo (middle), and artist's impression of the MWXG spacecraft overall configuration (bottom). [46]

Part of the response to the critics on HYPER's insufficient TRL was the establishment of the **QUANTUS** [62, 72, 71, 69, 171, 67, 66] collaboration, being an impressive effort to improve the TRL of experiments involving ultra-cold atoms. Experiments filling medium sized lab rooms were supposed to be shrunk to fit volume and mass of the capsules used at the drop tower at ZARM, Bremen. After the successful demonstration of the first BEC created in a micro-g environment by QUANTUS I [171, 170], further projects had been initiated: QUANTUS II [100, 68] demonstrating an atom interferometer in the drop tower, LASUS promoting the miniaturisation of laser systems and MAIUS demonstrating the feasibility of atom-optical experiments on rocket missions. Key point of those projects is the development of new technologies for further miniaturisation of technical components, new ideas for the manipulation of cold atoms and a full automation of atomic inertial sensors as required for space-borne missions [128].

Eight years after the submission of the HYPER proposal another startup of an space-borne atom interferometer was made when the proposal for **MWXG** (Matter Wave eXplorer of Gravity) [46] was submitted to ESA in 2008. This was the first proposal for an space-borne quantum test of the UFF using atom interferometers. As aforementioned MWXG can be seen as a continuing revolution of the HYPER apparatus incorporating experiences gained with QUANTUS and also from the development of the ACES mission (including PHARAO) and LISA Pathfinder [46].

Several basic aspects – among orbit design, spacecraft, launcher, AOCS – were adopted from HYPER. For the atom interferometer the isotopes $^{85/87}$Rb and $^{40/41}$K were proposed as candidate test masses. The atoms should be trapped and cooled in a magneto-optical trap and an optical dipole trap; a combination also proposed for QUEST later on. Also, the proposal already included the possibility of using double diffraction. With the intended free evolution time of $T = 3\,\mathrm{s}$, this would have required to trap $2 \cdot 10^7$ atoms to achieve an integrated sensitivity of $5 \cdot 10^{-16}\,\mathrm{m/s^2}$ after an integration time of 3 months [46]. Thus, the baseline for the **QUEST** mission was largely primed by MWXG and HYPER. Improvements made in the iteration from MWXG to QUEST basically apply to the parameters of the atom interferometer ($T = 5\mathrm{s}$) and the atomic source (BEC), whereas particularly orbit requirements and space craft design were adopted [52].

5.2. Scientific objectives and requirements

The equivalence principle as formulated by Einstein — complete equivalence of gravitational fields and accelerated systems — is a generalisation of the UFF. Therefore a test of the UFF is a crucial contribution to the test of the equivalence principle. On the other hand, the gravitational redshift is usually depicted as an implication of GR. Strictly speaking, it is not. It can be derived alone from SR and the EP. Insofar the confirmation of the gravitational redshift effect does not confirm GR. Nevertheless it is, like the UFF, a test of the equivalence principle. However, as Einstein pointed out in [43]:

> *If the redshift* [...] *due to the gravitational potential existed not, the theory of general relativity would be untenable.*

Thus, we might consider both, the UFF and the UGR, as two sides of the equivalence principle. This is also mirrored by an alternative formulation of the Einstein equivalence principle (EEP), which also can be expressed to comprise local Lorentz invariance (LLI), UGR and UFF (see figure 2.1 for comparison). Besides the test of the equivalence principle in the narrower sense, both experiments might be sensitive to effects leading to an apparent violation of the equivalence principle. Those might be a hint for new physics, leaving the equivalence principle untouched, as was discussed in section 2.3.

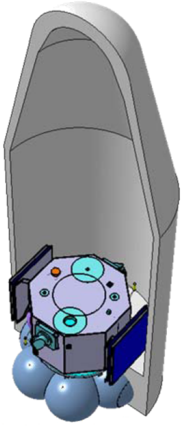

Figure 5.6.: The STE-QUEST spacecraft stowed in a Soyuz-Fairing. [52]

The current status of experiments testing the UFF were already discussed in chapter 1. Experimental evidence for the gravitational redshift was a long time coming. Although already predicted by Einstein in 1911 [42], it was not until 1960, when the Pound-Rebka experiment, base on the Mössbauer effect, verified the last of the classical tests of GR. It was performed over a vertical distance of 22.5 m at Harvard University's Jefferson tower. In 1964 it yielded an accuracy at the 1% level [133]. In 1980 another test was performed, when a hydrogen maser was lifted by a sounding rocket to an altitude of 10 000 km on a nearly vertical trajectory. By comparison with an identical clock on the ground, it confirms UGR with an accuracy of $7 \cdot 10^{-5}$ [173]. This is the best experimental result until today.

Primary scientific objectives

Summarised, the following primary scientific objectives have been formulated [58]:

#PSO-01: Measurement of the Earth gravitational red-shift effect to a fractional frequency unvertainty of $1 \cdot 10^{-7}$.

#PSO-02: Measuring of the Sun gravitational red-shift effect to a fractional frequency uncertainty of $2 \cdot 10^{-6}$, with an ultimate goal of $6 \cdot 10^{-7}$.

#PSO-03: Test the universality of the free propagation of matter waves to an unvertainty in the Eötvös parameter better than $2 \cdot 10^{-15}$.

Although the mission is in principle enabled to do LLI tests (thus enhancing the mission to all three pillars of the Einstein equivalence pricinple), they are currently not listed as primary mission objective. However, at a later stage when more detailed simulations are available a reassessement will be made [58].

Below we will concentrate on scientific objective #PSO-03, i.q. the QUEST part of the mission and will only review STE related instrumentation where it is relevant for the atom interferometer.

5.3. Spacecraft and payload

5.3.1. Spacecraft

Although it was originally proposed to build STE-QUEST upon the PROTEUS satellite bus, the study team of the Concurrent Design Facility (CDF) held in 2011 recommended to design a new spacecraft fitting to the mission's requirements [53].

Instead of having a modular design the satellite is now planned as an integral spacecraft, carrying the payload in a central cylinder. Using a custom design has the benefit of better adaptability to the missions need. Among others, it provides a better shielding against radiation and thermal fluctuations being inherent to the design.

5.3.2. Payload

Our main interest lies in the STE-QUEST payload, which yields the scientific instruments. It can be devided into three parts:

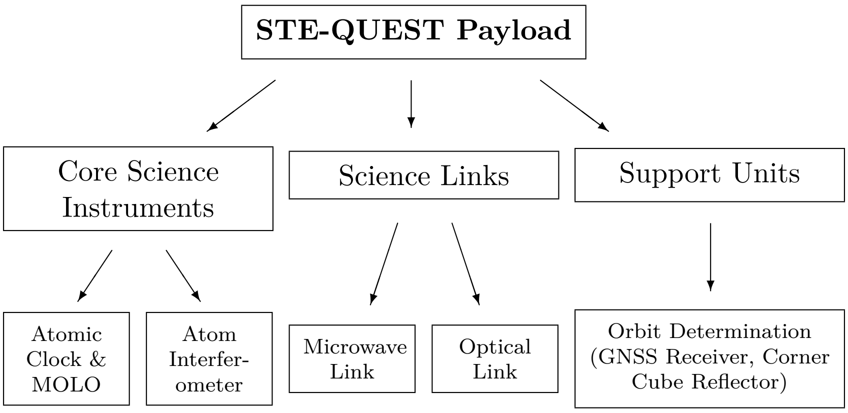

Figure 5.8.: Overview over the STE-QUEST payload. [57]

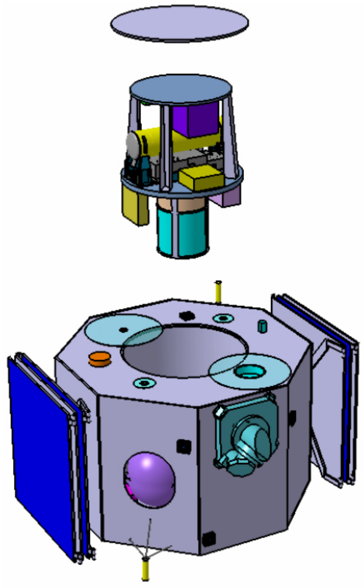

Figure 5.7.: The STE-QUEST spacecraft and payload. [53]

There are two *Core Science Instruments*, the atomic clock including a microwave-optical local oscillator (MOLO) and the atom interferometer. Although there is a lot of technological overlap among the two instruments, they will be designed such, that they can be run completely independent of each other. E.g. the atom interferometer will have its own reference oscillator (internal mode), but it *can* also be locked to the MOLO (external mode, see section 5.4). Each unit will have its own *Instrument Control Unit* (ICU), so that there is no onboard system required to handle both instruments. Thus a failure of one instrument will not prevent the other instrument of successfully accomplishing the mission. Knowledge about the actual orbit, needed for both experiments, is provided by the supporting units. A corner cube reflector allows for precise orbit determination by laser ranging from ground, while the GNSS receiver, besides position data, will also provide the time for time tagging of the on-board transmitter.

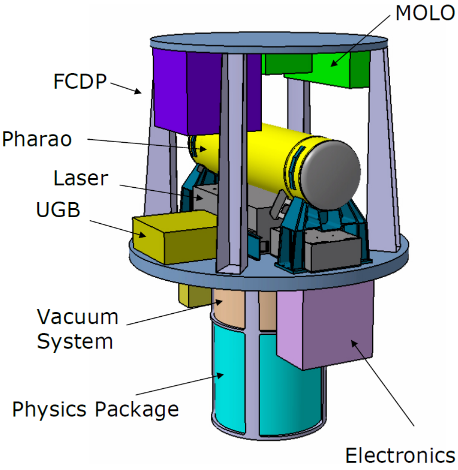

Figure 5.9.: The STE-QUEST payload. [53]

Figure 5.7 shows, how the payload module will be joined to the STE-QUEST spacecraft. This design will provide mechanical, thermal and electrical (power) contact to the STE-QUEST spacecraft, as well as a data interface between the ICUs and the satellite data bus. Further more there will be connections for the microwave and the optical ground link, since the link interfaces are attached to the outside of the spacecraft. A more detailed CAD sketch of the current payload layout is displayed in figure 5.9, with some of the subcomponents marked.

5.4. The STE atomic clock

Figure 5.10.: The PHARAO engineering model under test. The Pharao Cesium tube is approximately 1 m in length. [52]

The STE atomic clock is a combination of an microwave-optical reference oscillator (MOLO) and an atomic clock using ^{87}Rb. It is based on the cold Cs atoms clock PHARAO developed for the ACES mission, shown in figure 5.10. The microwave-optical local oscillator (MOLO) consists of a stabilised laser head at 1064 nm locked and an onto an ultra-low expansion (ULE) optical resonator and an optical frequency divider. The ground links, a microwave link and an optical link, are the second core component for the UGR test, since they enable the comparison with ground clocks.

The clock contains an additional unit for Microwave Synthesis and frequency Distribution (MSD), distributing the reference signal from MOLO to the laser links and the QUEST instrument. Quartz oscillators as designated for the QUEST frequency reference have increasing phase noise towards lower Fourier frequencies (see section 9). Therefore the quartz oscillator's phase noise at Fourier frequencies below 10 Hz generates the main part of technical phase noise of the QUEST frequency reference. Locking the QUEST frequency reference to the atomic clock can thus improve long term stability and reduce oscillator induced phase noise.

5.5. The QUEST atom interferometer

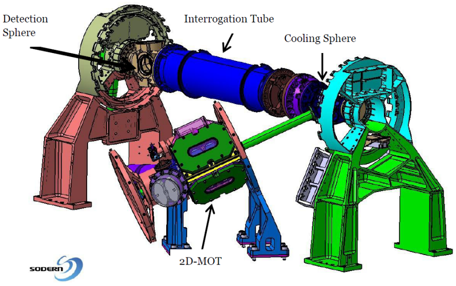

Figure 5.11.: Current baseline design of the Pharao clock, shown without μ-metal shields. [57]

The QUEST accelerometer is a dual atom interferometer, simultaneously measuring the acceleration of two atomic isotopes in the same place. In preparation of the proposal both options, K/Rb and ^{85}Rb/^{87}Rb, were discussed. The decision was for Rb/Rb, mainly due to consideration of the technology readiness level (TRL); see appendix A for further information. A substantial advantage is, that laser wavelength needed to handle the two isotopes are only separated by considerably less than 1 nm. Alongside this choice provides potential improvements in common-mode noise rejection and facilitates the superposition and distribution of the lasers. The instrument is subdivided into three parts:

- the physics package, containing the vacuum chamber, vacuum pumps and the atomic source,
- the laser system including the locking electronics, and
- the Instrument Control Unit.

The physics package contains the vacuum system, the atom source based on a combination of a two-dimensional and a three-dimensional magneto-optical trap (MOT), the laser optics for the atom chip and the optical dipole trap, as well as photodiodes and CCD sensors for detection. For the lasers system currently two possibilities are under investigation: a frequency doubled fibre laser [54] and the QUANTUS approach using diode lasers [100]. Intensive development for the space qualification of diode laser setups is currently performed within the LASUS (LASer Unter Schwerelosigkeit) collaboration with major contributions from Ferdinand-Braun-Institut (FBH), Berlin. The complete assembly will be an descendent of the MAIUS atom interferometer, currently being designed for sounding rocket experiments and presented in figure 5.12. The QUEST design will however need some modifications with the arrangements of the ports, since the sensitive axis has to be coaligned with the axis of the surrounding cylinder.

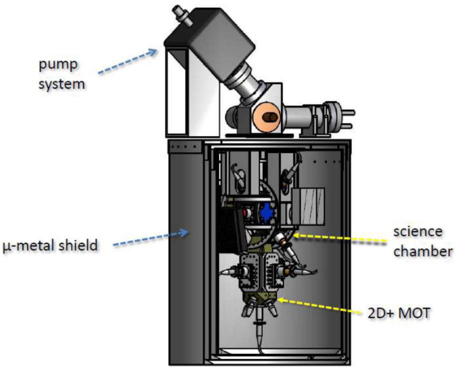

Figure 5.12.: CAD scetch of the MAIUS atom interferometer. [52]

5.5.1. The atomic source system

The heart of the QUEST atom interferometer is the vacuum system with integrated source for ultracold atoms. A 2D-MOT loaded by two ovens provides a mixed beam of cold ^{85}Rb and ^{87}Rb atoms. The beam passes a differential pumping stage to separate regions of high and low background pressure and will be collected in the science chamber by a 3D-MOT. The ovens will be adapted versions of the PHARAO ovens, while the 2D/3D-MOT will be a further development of the QUANTUS-II source system. All subsequent steps including interferometry will be conducted within the science chamber, which therefore has to maintain a pressure of 10^{-10} mbar. While the source system and the science chamber are surrounded by a multi-layer μ-metal shield, the vacuum pumps are kept outside the the μ-metal cylinder to keep the magnetic field generated by the pumps away from the science chamber. The plate separating vacuum pumps and science chamber will be dimensioned such, that it can provide the mechanical mounting interface to the spacecraft.

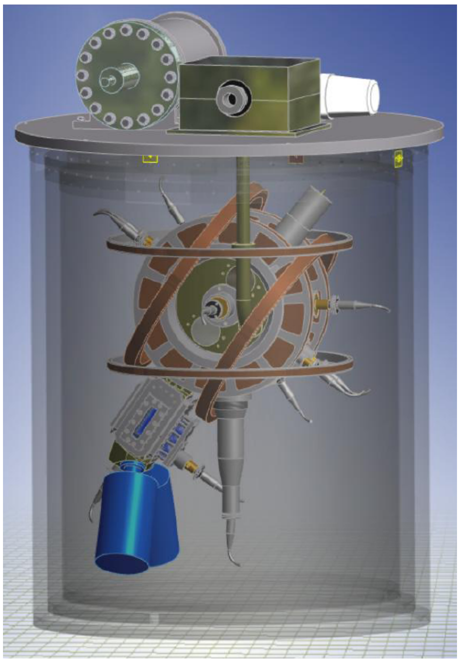

Figure 5.13.: CAD sketch of the STE-QUEST atom interferometer. [52]

The baseline is to collect a mixed cloud of ^{87}Rb and ^{85}Rb in the 3D-MOT. It will be generated on an atom chip within 2 seconds. As a first step the atoms will be cooled by optical molasses and subsequent evaporative cooling in the magnetic trap on the atom chip. This is achieved by dynamically reducing the strength of the magnetic trap potential. The process is a combination of evaporative cooling of ^{87}Rb and sympathetic cooling of ^{85}Rb. Thus it is accompanied by loss of ^{87}Rb atoms and a constant number of ^{85}Rb atoms, while lower temperatures for both isotopes are achieved due to rethermalisation.

The **scattering length** a results from the low-energy limit of the scattering cross-section σ:

$$4\pi a^2 = \lim_{E\to 0} \sigma$$

It can be interpreted as a measure for the interaction potential of the atoms within the ensemble. While a positive scattering length indicates a repelling potential, a negative scattering length represents an attractive potential. In a nutshell this attractive force between the atoms prevents the hottest atoms to be removed from the ensemble and hence precludes evaporative cooling.

The simultaneous production of BECs of both isotopes is hindered by the negative scattering length of ^{85}Rb. However, the scattering length can be tuned by applying an additional magnetic field. Since this is similar to the technique applied when generating feshbach resonances this has been referred to as *Feshbach field*. To tune the scattering length to positive values requires a Feshbach field of up to 168 G. This strong magnetic offset field on its part however prevents the further use of a magnetic trap. The backdoor out of this dodgy situation is an optical dipole trap (ODT).

The term **Feshbach resonance** is named after the US-american physicist **Herman Feshbach** (* 1917 in New York City, † 2000 in Cambridge). Within BECs it refers to a state, where the binding energy of a bound state between two atoms is equal to the kinetic energy of a colliding pair of atoms.

5.5.2. Interferometer sequence

The experimental cycle will have a total length of 20 s. This is distributed nearly equally to the preparation sequence and the interferometer sequence. During the preparation sequence a BEC with 10^6 atoms of ^{85}Rb and ^{87}Rb respectively is produced and prepared for the subsequent interferometer cycle. The complete preparation cycle is depicted in figure 5.14, while the baseline parameters of the atom source are summarised in table 5.3.

Parameter	Value
Number of Rb^{85} atoms	10^6
Number of Rb^{87} atoms	10^6
Initial BEC radius	300 μm
BEC expansion rates	82 μm/s

Table 5.3.: Baseline parameters for the QUEST atom source. The initial BEC radius refers to radius at the first beam splitter pulse. [59]

The interferometer sequence is a Mach-Zehnder type with two phases

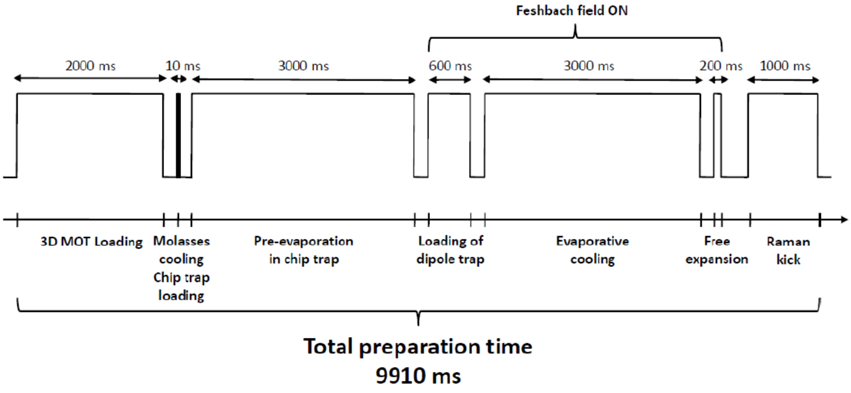

Figure 5.14.: The preparation sequence of the QUEST atom interferometer. [57]

of free evolution with a length of $T = 5\,\mathrm{s}$ each. Since the interferometer runs simultaneously for both isotopes, the corresponding Raman light beams are also irradiated simultaneously, using the same optical fibres and optics. Differing form the simple Mach-Zehnder interferometer sequence presented in figure 4.2, the QUEST atom interferometer will use the technique of double diffraction. This has the advantage that the interferometer arms are split symmetrically, thus suppressing certain noise and bias terms. The total amount of 10 s for the Mach-Zehnder sequence finally leaves 90 ms for detection. This is done by simultaneously reading out both ports of the interferometer, thus suppresssing normalization errors due to fluctuation of frequency and intensity of the detection light. The baseline parameters of the QUEST interferometer are summarised in table 5.4.

Parameter	Value
Single shot sensitivity	$1.75{\cdot}10^{-12}\,\mathrm{m/s^2}$
Release time t_0	1.4 s
Repetition rate	20 s
Free evolution time T	5 s

Table 5.4.: Baseline parameters for the STE-QUEST atom interferometer [59]. “Release time” refers to the time between the release of the atoms from the trap an the first Raman pulse.

Due to the long free evolution time of 10 s the impact of gravity gradients on the contrast can no longer be neglected. Depending on the actual position on the elliptical orbit, the contrast will vary between 0.62 and 0.92. The impact on the overall sensitivity will be assessed in detail in section 6.3.1.

5.6. Orbit design

The design of the STE-QUEST orbit needs a compromise between the requirements of the UFF test on the one hand and the requirements of the UGR test on the other hand. The most important parameter for the UFF test is a local value of the Earth’s acceleration g being as high as possible, which is best achieved with a low circular orbit. This conflicts with the UGR test aiming for a maximised amplitude in the modulation of g over time, which is achieved with a highly elliptical orbit.

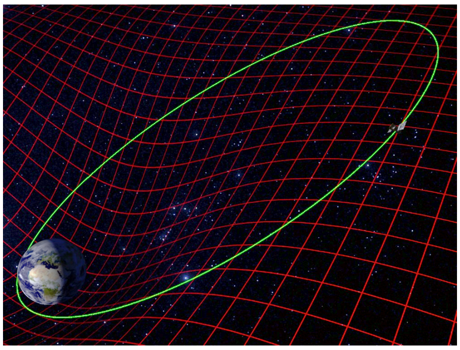

Figure 5.15.: Artist’s impression of the STE-QUEST orbit.

5.6.1. Launch

The launch will be from Kourou aboard a Soyuz rocket with a Fregat upper stage. The Soyuz carries the package containing the Fregat stage and the STE-QUEST spacecraft into a circular parking orbit. Conducting two Fregat burns the spacecraft will then be lifted to the desired apogee altitude of 50 600 km and inserted into the final high elliptical orbit. Afterwards the Fregat will be separated from STE-QUEST and ignited for de-orbiting. Within this scheme a maximum payload of 2 250 kg can be carried to the final orbit.

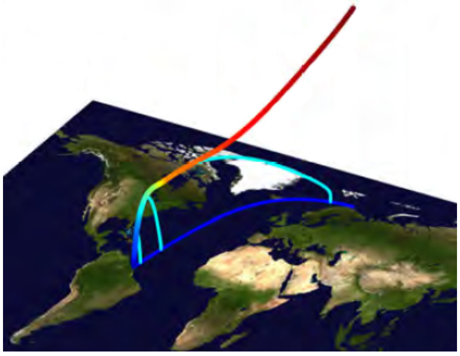

Figure 5.16.: Initial trajectory of the STE-QUEST launch on a Soyuz-Fregat system from Kourou. [55]

5.6.2. Reference orbit

First considerations concerning the orbit of a spaceborne UFF test have already been made in 2008 for the proposal of the *Matter Wave Explorer of Gravity* (MWXG) [46]. A tradeoff between scientific requirement of having a low orbit with large value of g on the one hand and technical considerations – such as the minimisation of radiation exposure and drag – on the other hand showed, that the satellite should preferably orbit at altitudes between 700 km and 1000 km. The proposed orbit was a circular, sun-synchronous orbit (SSO) at 1000 km altitude with a period of 105.12 min. With the parameters of the STE-QUEST atom interferometer, this would lead to a single shot sensitivity of $\sigma_\eta \approx 2.4 \cdot 10^{-13}$, reaching 10^{-15} after only 13 days and the low 10^{-16} regime after one year of integration.

A **sun-synchronous orbit** is a orbit whose orbital plane rotates at the same rate as the orbited planet itself orbits around the sun. A sun-synchronous satellite orbit carries out one complete revolution around the Earth within one year and thus has a fixed angle with respect to a line joining Earth and sun. For satellites moving along the dusk-dawn line the orbit can be design such, that there is (nearly) no eclipse time, which has great advantages for the satellite's power supply.

The orbit design for the UGR test has been pushed forward during the Concurrent Design Facility (CDF) for the STE mission. Key requirements were a large gravitational potential difference between apogee and perigee, a long contact time to at least one ground station at perigee and the simultaneous visibility of the satellite from distant continental observation stations for several hours to enable ground clock comparison. The proposed orbit was a highly elliptical orbit a perigee altitude of 700 km and a period time of 16 hours. The desired difference in the gravitational potential is then achieved with an apogee altitude of 51 000 km. [51]

Since having a highly elliptical orbit is a make-or-break criterion for the UGR test, it was a crucial question wether it is possible to achieve the final accuracy of the UFF test in a joint mission or not. It is in fact possible to achieve the final accuracy for the UFF test with the orbit developed for the STE mission, of course at the cost of a longer overall mission time [52]. Hence the STE orbit – with minor modifications – is still relevant as **reference orbit** for the STE-QUEST joint mission. The orbital key parameters are listed in table 5.5. It is important to note, that the reference orbit does not represent the actual orbit geometry, but is a starting point for basic considerations and especially orbit optimisation.

Parameter	Value
Semi-major axis (SMA)	32 028 km
Eccentricity	0.779
Period	16 hours
Apogee altitude	50 600 km
Perigee altitude	700 m

Table 5.5.: Reference orbit parameters for the STE-QUEST mission [55]. See section 6.1.2 for an explanation of the orbital elements.

Parameter	Value
Semi-major axis (SMA)	32 090 km
Eccentricity	0.779
Inclination	62.59°
RAAN	265.37°
Argument of Perigee	271.95°
True Anomaly	28.65°

Table 5.6.: Initial orbit elements of the STE-QUEST baseline orbit. Reference epoch is 1 June 2022, 20:11 [58]. See section 6.1.2 for an explanation of the orbital elements.

5.6.3. Baseline orbit

A cruicial point for the feasibility of the UGR test is the establishment of the microwave link at both, low and high altitudes. This requires a sufficient coverage of the orbit with ground stations. While there is a adequate number of ground stations on the nothern hemisphere, the fixed orbit geometry of the STE-QUEST reference orbit would require the installation of several new ground stations on the southern hemisphere. The Mission Analysis Guidelines [55], published in June 2012, present a new **baseline orbit** for the STE-QUEST mission. This orbit partially circumvents the problem of missing ground stations by slowly turning the orbit itself in such a way, that initially perigee, but later apogee lies over the northern hemisphere. Thus, a microwave link is possible over sufficient long periods of mission time at all parts of the ellipse.

In general changing orbital parameters requires steering units like additional thrusters. However, it is possible to design the orbit in a way, that it drifts passively over the entire mission time. Introducing e.g. an initial drift in the argument of periapsis causes the perigee to slowly turn from the northern to the southern hemisphere. Thus ground links at low altitudes will be established at the beginning and the end of the mission time, while ground links at higher altitudes can be realised in the middle of the mission time.

Please see section 6.1.2 for an explanation of the **argument of periapsis** and other orbital elements.

However, a secondary effect of the intended drift is, that also the eccentricity has to be adapted and hence the perigee altitude varies between 700 km and 2200 km over ground, as plotted in figure 5.17. Since the perigee altitude is of some importance for the EP test — in first approximation the sensitivity to EP violations decreases, when going to higher altitudes — we will in-depth discuss the impact of a drifting orbit geometry on the sensitivity in section 6.3.4.

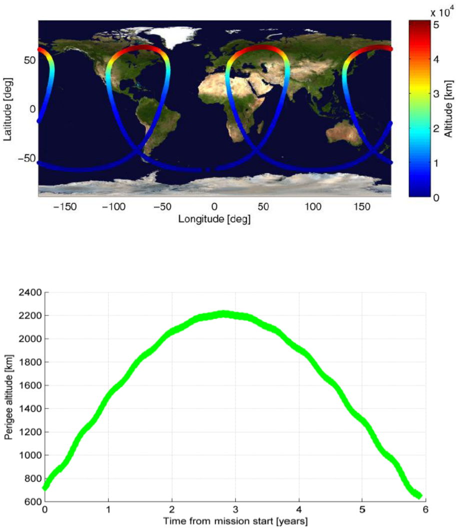

Figure 5.17.: Drift of the perigee altitude in the STE-QUEST baseline orbit. [55]

5.6.4. Lower perigee altitude with drag-free control

Having a perigee altitude below 600 km does apparently have advantages for both, the GGR measurement as well as the UFF measurement. However, descending below 600 km requires an active compensation of atmospheric drag [55]. Since this would of course raise the mission cost, this was for the time being not included in the STE-QUEST baseline orbit. In section 6.3.3 we will hence investigate if the scientific gain for the EP test would justify the significant expenses of an active drag free control.

Addendum

In February 2014, out of the four candidate missions PLATO was selected as M3, the third medium-class mission in ESA's Cosmic Vision Programme. [49]

The objective of the **PLAnetary Transits and Oscillations of stars (PLATO)** mission is the search for extrasolar planetary systems, with emphasis on Earth-like planets. [48]

6. Sensitivity of QUEST

In 4.27 we presented how the sensitivity of an atomic accelerometer depends on its internal properties. But the sensitivity depends also on environmental parameters. In case of an UFF test, this is first of all the local Earth acceleration g, which directly contributes to the Eötvös ratio

$$\eta(A, B) = \frac{|a_A - a_B|}{g(r)} \tag{2.13}$$

and hence determines the actual sensitivity for UFF violations. Secondly there is the gravity gradient, which has significant influence on the interferometers contrast. Since their magnitute depends on the shape of the orbit, we will start with the calculation of Kepler orbits in section 6.1 before we deal with the influence of g and the gravity gradient in sections 6.2 and 6.3.1 respectively. Finally we will spend some thoughts on orbit optimisation in section 6.3.

6.1. Calculating Kepler orbits

6.1.1. Kepler orbits

During the 17th-century scientific revolution, it was the accuracy of Tycho de Brahe's records of the planetary motions, combined with Johannes Kepler's persistence in trying to match them to the existing models, which lead to a turn in the understanding of the solar system [151]. Kepler realised, that neither the Ptolemaic geocentrism, nor the Copernican heliocentrism, nor the Tychonic compromise could match the observations exactly — and that all of them are in fact equivalent, barring the frame of reference.

Using the simplified Copernican system — sun in the centre with the planets orbiting around it on perfect circles — as a starting point, he constructed an oval orbit with the sun in one of its foci. Since the calculation of areas is more complicated in ovals than in ellipses, he introduced the latter one as approximation for the first one. But then — after a proof, that seems quite long-winded from today's point of view — he realised, that it was in fact the ellipse that could perfectly match the observations.

Kepler laws of planetary motion

The results of Kepler's research are condensed in the so-called **Kepler laws of planetary motion** or just Kepler's laws, as there are:

1. The planets move on elliptical orbits, with the sun in one of the two foci.
2. A line connecting a planet with the Sun sweeps out equal areas during equal intervals of time.
3. The square of a planet's orbital period is proportional to the cube of the semi-major axis of its orbit.

The first two were published in 1609 in Kepler's work *Astronomia nova*, while the third followed ten years later in his book *Harmonices mundi*. Orbits following these rules are called **Kepler orbits**.

While Kepler's attempt to explain the underlying physical reasons of the motion – he for example assumed that the motion was related to velocity and not acceleration – are obsolete by now, the laws themselves are still considered correct for any body orbiting around a second in a two-body system. Also in a many-body system like the solar system, it is applicable, since the orbits of the planets around the sun are ellipses to high accuracy. Even the trajectories of satellites orbiting around the Earth are approximately Kepler orbits with small perturbations by the sun, the moon, higher multipoles in the Earth gravitational field or atmospheric drag. That's why the Keplerian elements, being introduced in the next subsection are commonly used to define satellite orbits.

6.1.2. Orbit parametrisation

Ellipses

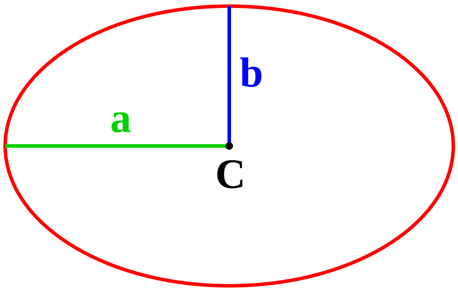

Figure 6.1.: Size and shape of an ellipse is defined by the semimajor axis a and the semiminor axis b, measured from the centre of the ellipse.

From the mathematical point of view an ellipse is a plane curve obtained by the intersection of a cone and a plane. Along with parabola and hyperbola it is a conic section. In its canonical form the ellipse can be described by the implicit equation

$$\frac{x^2}{a^2} + \frac{y^2}{b^2} = 1 \quad (a \geq b) \quad , \tag{6.1}$$

where **semimajor axis** a and **semiminor axis** b coincide with x and y axis, respectively. The distance between foci and centre of the ellipse $f = \sqrt{a^2 - b^2}$ is called linear eccentricity. Regarding satellite orbits it is favourable to switch to a polar view:

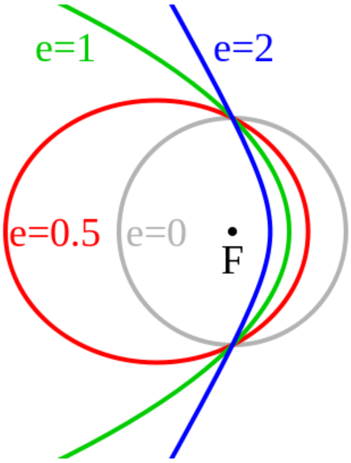

Figure 6.2.: Types of orbits. Blue: Hyperbolic orbit ($\varepsilon > 1$). Green: parabolic orbit ($\varepsilon = 1$). Red: elliptical orbit ($0 < \varepsilon < 1$). Gray: circular orbit ($\varepsilon = 0$). [7]

$$r(\varphi) = \frac{ab}{\sqrt{a^2 \sin^2 \varphi + b^2 \cos^2 \varphi}} \tag{6.2}$$

However, in Kepler orbits the central mass is always located in one of the foci. Hence we prefer a form with the point of origin ibidem:

$$r(\nu) = \frac{a(1 - \varepsilon^2)}{1 \pm \varepsilon \cos(\nu)} \tag{6.3}$$

The angle ν is called **true anomaly** in celestial mechanics. We have also introduced the **eccentricity**

$$\varepsilon = \frac{f}{a} = \frac{\sqrt{a^2 - b^2}}{a} = \sqrt{1 - \left(\frac{b}{a}\right)^2} \,, \tag{6.4}$$

which can be thought of as a measure for the ellipse's deviation from a circle. It is sometimes called *numerical* eccentricity to distinguish it from the *linear* eccentricity f. Depending on the value of ε we can construct all kinds of conic sections, displayed in figure 6.2:

$\varepsilon < 0$	circle
$0 < \varepsilon < 1$	ellipse
$\varepsilon = 1$	parabola
$\varepsilon > 1$	hyperbola

While all these trajectories appear in celestial mechanics, Kepler orbits have $0 \leq \varepsilon < 1$.

Apsides

When dealing with orbits, we will often find the terms of apsides, which refer to the points of greatest or least distance of the orbiting body from the central mass. **Periapsis** is the point of closest approach, while **apoapsis** is the point of greatest distance.

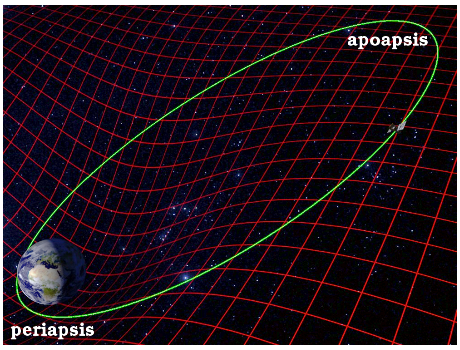

Figure 6.3.: Elliptical orbit with points of closest approach (periapsis) and greatest distance (apoapsis) to the central mass.

$$r_{\text{peri}} = a(1 - \varepsilon) \ , \qquad r_{\text{apo}} = a(1 + \varepsilon) \tag{6.5}$$

In solar orbits they are usually called perihelion and aphelion, while in Earth orbits we refer to **perigee** and **apogee**.

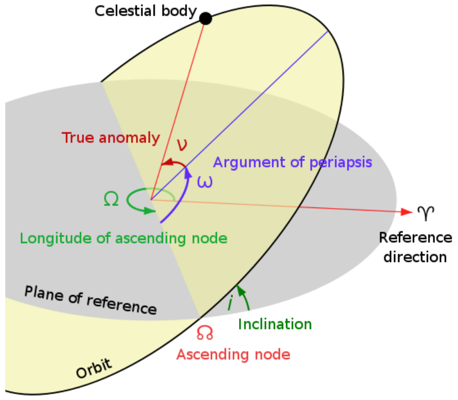

Figure 6.4.: A spacecrafts position on a Kepler orbit can be completely determined by the six Keplerian elements. [5]

There are several **reference systems** used in celestial mechanics: The *International Celestial Reference Frame* (ICRF) is the standard reference frame when defining the positions of astronomical objects (including planets). It is centred at the barycentre (centre of mass) of the Solar System and defined by the measured positions of 212 extragalactic sources (mainly quasars). The *Ecliptic coordinate system*, also centred in the barycentre of the Solar System, uses the Earth orbital plane (ecliptic) as its fundamental plane. While it was the coordinate system used by ancient astronomers, it can still be helpful when calculating the motions of planets around the sun. Finally, the *equatorial coordinate system* is widely used to specify artificial satellites' orbits around Earth. It is a geocentric one, using the Earth's equatorial plane as its fundamental plane and a reference direction ♈ towards vernal equinox – that means it does not rotate with the Earth. Vernal Equinox (also March Equinox, Vernal Point or First Point of Aries) is one of the two equinoctial points, where the equatorial plane intersects with the ecliptic. Due to the precession of the Earth's axis, the equatorial coordinate system changes over time. Hence one has to specify the time, called the equinox of date, when vernal point and equatorial plane are taken.

Keplerian elements

A Kepler orbit can be determined by five parameters. One additional parameter is needed, to parametrise the spacecrafts position on the orbit. Although there are other parametrizations, we often find the six Keplerian elements to be used.

The first two are the already mentioned **semimajor axis** a and the **numerical eccentricity** ε.

Three more parameters, illustrated in figure 6.4, are needed to define the orientation of the orbital plane with respect to a reference system:

- To measure the angle between the reference plane and the orbital plane we use the **inclination** i.
- The points where the orbit crosses the reference frame are called orbital nodes. The angle between a reference direction and the ascending node (upward crossing of the orbit in the reference plane) is defined by the **longitude of the ascending node** Ω. In the equatorial coordinate system Ω is also called right ascension of the ascending node (RAAN).
- Finally the **argument of periapsis** ω defines the angle between the ascending node and periapsis.

Since i, Ω and ω are angular measures, that only define the orbit's orientation with respect to an (arbitrary) reference frame, they are not necessary for calculations of a satellite's motion within the orbital plane. We will hence set $i = \Omega = \omega = 0$ in the simulation of the STE-QUEST orbit.

While we now have completely defined a (static) orbit we need one more element, when regarding the movement of a body along the trajectory. A geometric measure for the current position of a spacecraft is the **true anomaly** ν, which is the angle between the spacecrafts position and periapsis.

Another measure, important for us, is the **time since periapsis** t. It can be calculated from the true anomaly by

$$t = \frac{M}{\sqrt{\frac{G(m_1+m_2)}{a^3}}}, \tag{6.6}$$

using the mean anomaly

$$M = E - e\sin(E) \tag{6.7}$$

and the eccentric anomaly

$$E = \arccos\left(\frac{e + \cos(\nu)}{1 + e\cos(\nu)}\right). \tag{6.8}$$

Equation 6.7 is also known as Kepler equation. For our calculations of the atom interferometer's sensitivity we need to go the other way round, since we want to calculate the satellite's position for each measurement, which are equally separated in time with a constant repetition rate. Unfortunately there is no possibility to answer the question *"Where is the satellite after time T?"* Since (6.7) is a transcendental equation, there is no closed-form solution for E given M, but is has to be solved by numerical methods.

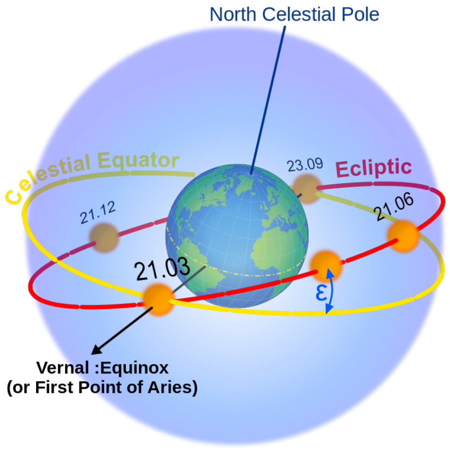

Figure 6.5.: The equatorial coordinate system. [8]

6.1.3. Numerical orbit propagators

There are different approaches of orbit propagators. In the most general case, we simply sum up all forces acting on the satellite (e.g. gravitation of Earth, Sun, Moon, atmospheric drag, etc.) and from the satellite's actual position and velocity calculate the movement of the satellite in finite timesteps. The accuracy of the simulated orbit apparently depends on the size of the timesteps.

However, we are not interested in the small deviations from a perfect Kepler orbit or the evolution of the orbit over multiple revolutions, but only in the global dependence of the achievable sensitivity from the satellite's altitude. Hence we will ignore perturbations and use a dedicated propagator for Kepler orbits, which iteratively solves the Kepler equation (6.7) by using Newton's method. This approach has two advantages: The accuracy of the simulated orbit is independent of the size of the timesteps, because the trajectory itself is determined by the Keplerian elements. Only the position on this trajectory after time since periapsis t is subject to the numerical algorithm. Consequently the satellite's position after a simulation step is not based on the previous steps and deviations in the individual steps do not sum up.

6.1.4. Implementation

The *Orbit Simulation Toolkit (OSTK)* written in C++ by Vitali Müller, Albert-Einstein-Institut Hannover [122] comes with a Kepler propagator implementing Newton's method, which is based on algorithms provided in [169]. It is adjusted to a precision of

$\Delta E \leq 10^{-9}$ in eccentric anomaly, which translates to $\Delta r \leq 16\,\mathrm{cm}$ for the STE-QUEST baseline orbit. This is quite sufficient for our calculations.

The orbit propagator from OSTK consists of only the two files `lutils.cpp` and `kepler.cpp` plus the corresponding header files `kepler.h` and `lutils.h`. To program a simple orbit propagator we basically need three things:

- A header file,
- a method to initialise the orbit and
- the orbit propagation loop.

Once the orbit propagator is working, the calculation of the sensitivity (or any other physical quantity depending on the satellite's position and motion) can be included in the orbit propagation loop.

Header file

In the header section of our simulation we include at least the following three header files and create an instance of the classes `tkepl` and `tkepl_elem` respectively.

```
#include "lutils.h"
#include "kepler.h"
#include <cmath>

tkepl kepl;
tkepl_elem elements;
```

Listing 6.1: Head of the orbit simulation

The class `tkepl` defined in `kepler.h` implements the actual orbit propagation and several methods for coordinate transformation. A complete set of Keplerian elements is implemented in the class `tkepl_elem` also defined in `kepler.h`. The instance `elements` holds the Keplerian elements, which store the actual position during the numerical simulation.

Orbit initialisation

Before running the actual propagator we need to set the Kepler parameters for our orbit and initialise the Kepler engine.

```
// Set Keplerian elements here
kepl.kepler_init(t, pos, vel, elements, GM);
kepl.coe2rv(elements, elements.GM, pos, vel);
kepl.rv2coe(pos,vel,GM,elements);
```

Listing 6.2: Initialisation of the orbit

Here `t` is a `double` holding the time variable, `pos` and `vel` are arrays of `double` holding kartesian position and velocity data of the spacecraft, `elements` is the already meantioned class holding the Kepler parameters and `GM` is the gravitational constant times the Earth's mass. Just to make sure that missing Keplerian elements not defined by us are not randomly initialised (what might mess up the simulation), it is advisable to initialise them by converting the Keplerian elements to kartesian coordinates and back by subsequently calling the methods `coe2rv` and `rv2coe`.

Orbit propagation loop

The orbit propagation loop basically calculates the radius (`r`) and true anomaly (`nu`) of an elliptical Kepler orbit. The coordinate system used for all simulations is the orbital plane with z-axis perpendicular to the orbital plane and perigee on the x-axis. This means Inclination, RAAN and argument of periapsis are set to zero without any loss of generality.

The core of the simulation is the propagation loop starting at perigee (`nu=0`) and ending at apogee (`nu=`π). The orbit is calculated numerically in steps of `timestep` seconds.

```
for (t=0; elements.nu<=M_PI; t+=timestep) {
  kepl.set_new_anomalies(t, elements);
  kepl.coe2rv(elements, elements.GM, pos, vel);
  // Put further simulation stuff here!
}
```

Listing 6.3: Orbit propagation loop

The method `set_net_anomalies` propagates the orbital elements to the new position at time `t`. Afterwards the Keplerian elements are converted to kartesian coordinates by calling `coe2rv`. Afterwards we can extract information about the spacecrafts position and movement from the Kepler parameters in `elements` as well as from the kartesian variables `pos` and `vel` to calculate the sensitivity of the STE-QUEST atom interferometer.

The complete source code of the STE-QUEST orbit simulation is organised in the C++ class `KeplerProgram` listed in appendix B.

6.2. Altitude dependence of the sensitivity

6.2.1. Statistical errors on non-circular orbits

One of the most crucial point for the design of the STE-QUEST atom interferometer is its sensitivity to differential accelerations. For the basic estimation we'll calculate the statistical error due to shot noise, which is a fundamental limit and cannot be underrun by technical improvements. The usual approach to deal with statistical errors is to repeat the measurement again and again. When averaging over the single measurements with uncertainty σ_{single} the overall error σ_{all} reduces with the number of measurements N according to

$$\sigma_{\text{all}} = \frac{1}{\sqrt{N}} \sigma_{\text{single}} \quad , \tag{6.9}$$

provided the experimental conditions do not change among the measurements.

Basically the STE-QUEST atom interferometer is an accelerometer, whose appropriate measure is the actual acceleration in $\mathrm{m/s^2}$. The standard deviation of the interferometer phase due to shot noise is

$$\sigma_{\Phi} = \frac{2}{C}\sqrt{\frac{P(1-P)}{N}} \quad , \tag{4.23}$$

with contrast C, number of atoms N and excitation probability P. If we assume running the interferometer mid-fringe ($P = 1/2$) (4.23) reduces to

$$\sigma_{\Phi} = \frac{1}{C} \cdot \frac{1}{\sqrt{N}} \quad , \tag{6.10}$$

This can easily be transferred to a standard deviation for acceleration using (4.4):

$$\sigma_a = \frac{\sigma_{\Phi}}{k_{\text{eff}} T^2} = \frac{1}{C} \cdot \frac{1}{\sqrt{N} k_{\text{eff}} T^2} \tag{6.11}$$

While this is true for a single interferometer, the UFF signal is the differential acceleration of two individual interferometers. The errors for the differential signal of two identical interferometers results according to propagation of uncertainty in a factor $\sqrt{2}$:

$$\sigma_a = \frac{1}{C} \cdot \frac{\sqrt{2}}{\sqrt{N} k_{\text{eff}} T^2} \tag{6.12}$$

For the STE-QUEST parameters (see table 5.3) this yields the already mentioned $1.75 \cdot 10^{-12}\,\mathrm{m/s^2}$. But that's not, what we're actually interested in! Since we aim for a test of the equivalence principle, we are interested in the Eötvös ratio

$$\eta(A,B) = \frac{|a_A - a_B|}{g(r)} \quad . \tag{2.13}$$

That's the point where it gets special with spaceborne atom interferometers. As long as we stay on a circular orbit and g can be assumed constant, we can still use (6.9). However, STE-QUEST travels on a highly elliptical orbit and $g(r)$ is not a constant anymore. While in terms of acceleration the desired signal is modulated with the satellite's position and σ_a is a constant, it is the other way round when dealing with Eötvös ratios. Assuming an UFF violation being proportional to g, the signal $\eta(A,B)$ shall stay constant while the error σ_η – now on its part scaled with g – varies over the orbit:

$$\sigma^{(a)}_{\eta,ss} = \frac{\sigma_{a,ss}}{g(r)} \quad , \tag{6.13}$$

When calculating the overall error, all measurements i will have to be weighted with the associated error σ_i. For one orbit with $N \gg 1$ measurements we get

$$\sigma_\eta^{(1\text{ orbit})} = \sqrt{\frac{1}{N(N-1)}\Sigma_{i=1}^N \sigma_i^2} \approx \frac{1}{N}\cdot\sqrt{\Sigma_{i=1}^N \sigma_i^2} \tag{6.14}$$

The uncertainty for M identical orbits is

$$\sigma_\eta^{(\text{M orbits})} = \frac{1}{MN}\sqrt{\Sigma_{i=1}^N M \cdot \sigma_i} = \frac{1}{\sqrt{M}}\sigma_\eta^{(1\text{ orbit})} \quad . \tag{6.15}$$

The number of orbits to reach the desired target sensitivity σ_{target} can then be calculated by

$$M = \left(\frac{\sigma_\eta^{(1\text{ orbit})}}{\sigma_{\text{target}}}\right)^2 \quad . \tag{6.16}$$

6.2.2. The optimal integration interval

To calculate the atom interferometers sensitivity for the UFF test, we translate (6.13) into C++ code:

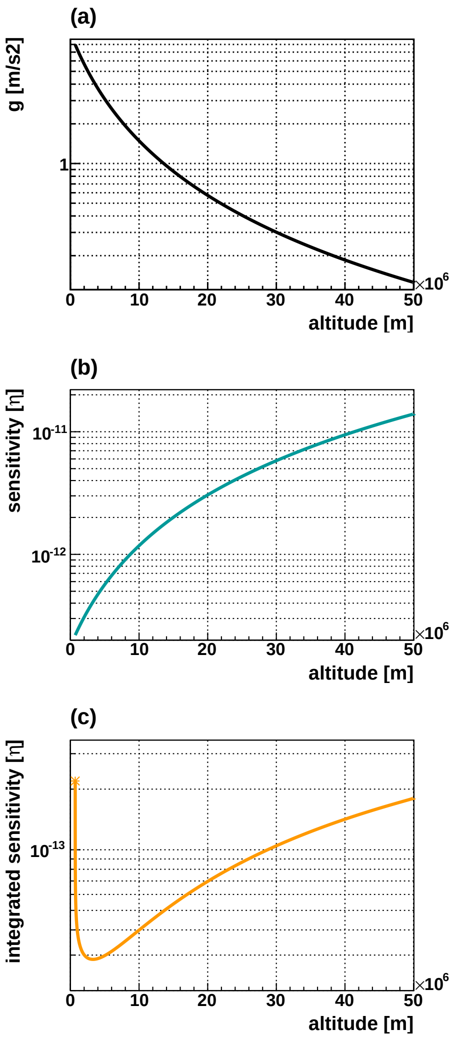

Figure 6.6.: Influence of the satellites altitude on the sensitivity. (a) Earth acceleration g (b) Single shot sensitivity (c) Integrated sensitivity, when starting at perigee. The single shot sensitivity is marked with $*$.

```
double D_eta = sshot/(GM/absvecl(pos)/absvecl(pos));
```

Listing 6.4: Calculation of the Eötvös sensitivity

While `sshot` is the sensitivity in $\mathrm{m/s^2}$, `D_eta` represents the single shot sensitivity in terms of Eötvös ratio. For summing up as in (6.14) we make use of the fact, that the orbit is symmetrical. We start the simulation at perigee and calculate only one half of the orbit. To obtain the result for a complete orbit all measurements are taken into account twice, except for the very first measurement at perigee (`t==0`). This will be realised with the following algorithm inside the orbit propagation loop (listing 6.3):

```
if (t==0) { // at perigee
  S_eta += D_eta*D_eta;
  step++;
  S_eta_orbit = sqrt(S_eta)/step;
}
else { // *2 since orbit is symmetric
  S_eta += 2*D_eta*D_eta;
  step += 2;
  S_eta_orbit = sqrt(S_eta)/step;
}
```

Listing 6.5: Integrated sensitivity

`S_eta` is the sum of the squared statistical errors since perigee, `S_eta_orbit` is the integrated sensitivity for the complete orbit. The integer `step` counts the number of measurements since perigee. All three have to be initialised to zero before starting the orbit propagation loop.

Results

The output of the simulation for the STE-QUEST reference orbit (see table 5.5) is plotted in figure 6.6 (c). It shows the evolution of the integrated sensitivity when starting integration at perigee. The upper integration bound expressed in terms of the spacecraft's altitude over ground is plotted against the x-axis. The integrated sensitivity starts at the single shot sensitivity and initially improves due to the cumulation of data points, as the satellite gains altitude on its way to apogee. However, the integrated sensitivity starts decreasing at some point, although taking more measurements. This contradicts the expectation only at first glance. On closer inspection this is not that astonishing any more, because the single shot sensitivity depends on the local gravitational field $g(r)$ and hence on altitude. Figure 6.6 (a) shows the Earth acceleration $g(r)$ decreasing while the satellite's altitude increases. Corresponding to 6.13 the single shot sensitivity $\sigma_\eta(r)$ behaves inversely proportional to g, as shown in figure 6.6 (b). While we have $\sigma_\eta \approx 2.2 \cdot 10^{-13}$ at perigee it degrades as far as $\sigma_\eta \approx 1.4 \cdot 10^{-11}$ at apogee, which are nearly two orders of magnitude. Consequently the integrated sensitivity initially improves to $\sigma_\eta^{(1\text{ orbit})} \approx 2.9 \cdot 10^{-14}$ at 3312 km altitude over ground. However, at higher altitudes the single shot sensitivity is so low, that the integrated sensitivity can not be improved further, but in contrary decreases if taking more measurements into account. If integrating over a complete orbit we would end up with $\sigma_\eta^{(1\text{ orbit})} \approx 1.8 \cdot 10^{-13}$, which is barely better than the single shot sensitivity at perigee of $\sigma_\eta \approx 2.2 \cdot 10^{-13}$.

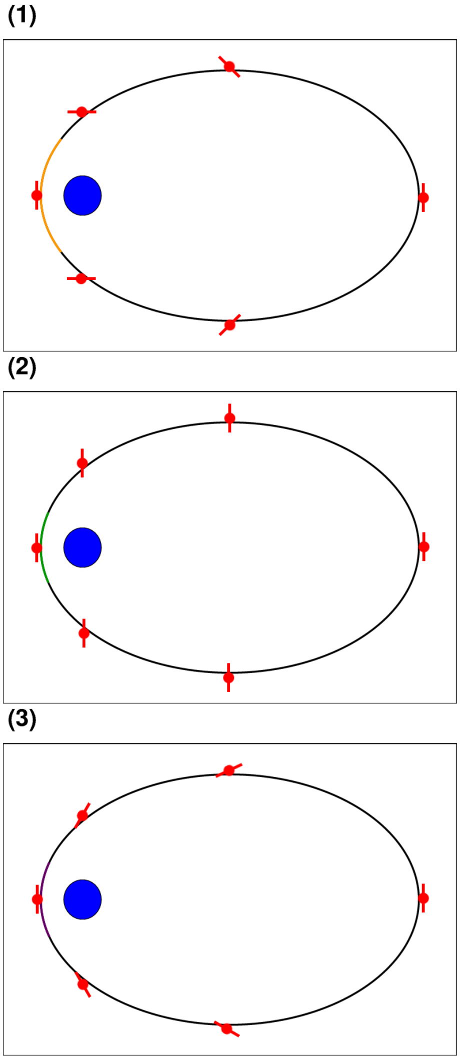

Figure 6.7.: Three possible rotation scenarios for the STE-QUEST mission: (1) The interferometer axis is pointing stabilised towards Earth, (2) the satellite does not rotate, (3) the satellite constantly rotates with the orbital period.

6.2.3. Rotation scenarios

QUEST was originally designed as an independent mission on a circular sun-synchronous orbit. As an heritage to that era we have up to now assumed, that the interferometer's sensitive axis points always towards earth. However, since on an elliptical orbit the true anomaly ν does not change at a constant rate, the rotation rate of the satellite would have to be actively controlled e.g. by pitch steering. This increases the complexity of the spacecraft and will at least raise the mission costs. It is a legitimate question to ask if the advantage of having the interferometer always pointing towards Earth can compensate for the subsequent effort.

In the following analysis we will consider three rotation scenarios:

(1) Stabilised pointing: The rotation of the satellite is synchronised with the orbit in a way, that the interferometer axis is always pointing towards Earth

(2) Non-rotating: The satellite does not rotate at all. The interferometer axis points towards Earth in perigee.

(3) Constant rotation: The satellite rotates at a constant rotation rate, synchronised with the orbital period. The interferometer axis points towards Earth in perigee.

In rotation scenarios (2) and (3) the interferometer axis is in general not pointing towards Earth, but the measured signal η is a projection of the real UFF signal on the interferometer axis. From the pointing-stabilised case (6.13) we deduce

$$\sigma^{(b)}_{\eta,ss} = \frac{\sigma_{a,ss}}{g(r) \cdot \cos(\nu)} \quad , \tag{6.17}$$

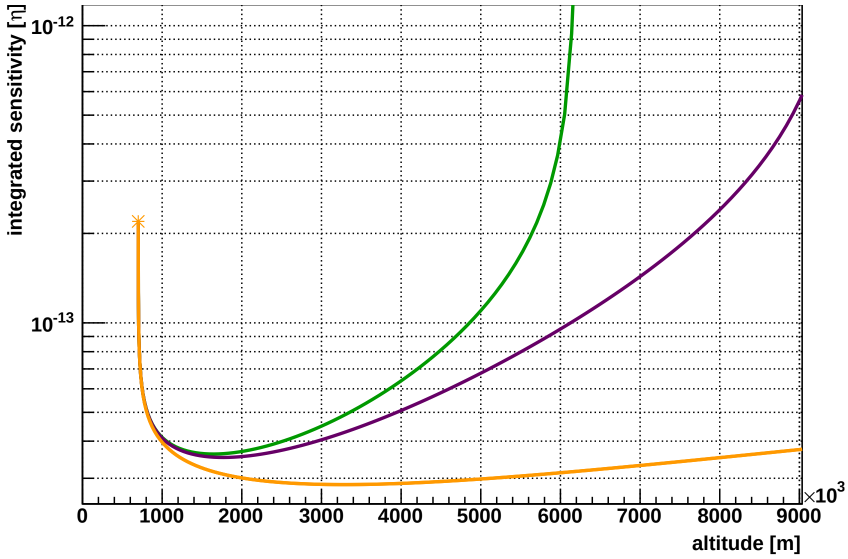

Figure 6.8.: Integrated sensitivity for the three considered rotation scenarios. While in the non-rotating (green) and the constant rotation case (violet) the loss of sensitivity at higher altitudes is much more severe than in the pointing-stabilised case (orange), the difference in the achievable sensitivity per orbit is rather small.

$$\sigma^{(c)}_{\eta,ss} = \frac{\sigma_{a,ss}}{g(r)\cdot\cos(\nu - 2\pi t/T_{\text{orbit}})} \quad , \tag{6.18}$$

for scenarios (2) and (3) respectively, with the true anomaly of the Kepler orbit ν, the orbital period time T_{orbit} and the time since periapsis t.

In terms of C++ code the three rotation scenarios look like this:

```
// pointing stabilised
double D_eta = sshot/(GM/absvecl(pos)/absvecl(pos));
// non-rotating
if (rotation_scenario == 2) {
  D_eta = D_eta/cos(elements.nu);
}
// constant rotation
else if (rotation_scenario == 3) {
  D_eta =
    D_eta/(cos(elements.nu-2*M_PI*t/elements.periodtime));
}
```

Listing 6.6: Implementation for the three rotation scenarios

Results

We again use the STE-QUEST reference orbit from table 5.5. The integrated sensitivities for the three rotation scenarios are plotted in figure 6.8. The key parameters are also summarised in table 6.1.

Apparently the scenarios (2) and (3) suffer from a degradation of sensitivity as the interferometer's sensitive axis turns away from the Earth and experience a complete loss of sensitivity when the sensitive axis is perpendicular to a line joining the satellite with the centre of the Earth. For the non-rotating case this is at $\nu = \pi/2$, which corresponds to an altitude of 6230 km over ground. It can be deferred by giving the satellite at least a constant rotation rate to approximately 9600 km over ground, but the gain in sensitivity by a factor of 1.03 compared to the non-rotating case is hardly worth mentioning.

However, the effect is less strong in the lower parts of the orbit and is insignificant around perigee, where the measurements with the highest sensitivity are taken. Although in the non-rotating and the constant rotation case the loss of single shot sensitivity at higher altitudes is tremendous compared to the pointing stabilised case, the loss in the achievable integrated sensitivity is much smaller as one might expect, since it is only a factor of 1.27.

Although the sensitivity loss in scenario (2) and (3) compared to scenario (1) is significant, the mission goals can still be reached. Furthermore scenario (1) would require a pointing stabilisation system, which would increase the overall mission costs. While scenario (3) provides only a marginal improvement over scenario (2), the non-rotating case has one big benefit over the other two: There will be no systematic effects or loss of sensitivity due to rotation, which has to be compensated by post-correction or even an active rotation compensation of the Raman lasers – both possible sources of errors and failures. From this point of view scenario (2) with a non-rotating satellite is the best choice for a UFF mission.

Scenario	(1) stabilised pointing	(2) non-rotating	(3) constant rotation
max-alt	3312 km	1650 km	1774 km
s	2100 s	1180 s	1260 s
shots	105	59	63
sens	$2.86{\cdot}10^{-14}$	$3.62{\cdot}10^{-14}$	$3.53{\cdot}10^{-14}$
N-orbits	816	1311	1243
mission time	544 d	874 d	829 d

Table 6.1.: Summary for the three rotation scenarios. “max-alt” refers to the altitude, where the AI measurement is stopped in order to achieve the best integrated sensitivity.

6.3. Orbit optimisation

At this point we should remember, that the STE-QUEST reference orbit as listed in table 5.5 does not represent the actual orbit on which the STE-QUEST spacecraft will fly. It should instead be seen as what it's called – a reference to ease basic calculations and the fundamental mission design.

The design of the actual orbit, however, will account for more detailed mission requirements and can of course be fine tuned for optimal performance. In the following we will discuss two orbit scenarios which were proposed for orbit optimisation in section 5.6: Low perigee orbits (section 6.3.3) and the drifting orbit scenario (section 6.3.4). As they significantly influence the sensitivity we will beforehand shed some light on gravity gradients and their impact on the free evolution time T.

6.3.1. Gravity gradient induced contrast reduction

When calculating the influence of gravity gradients, we will make use of the gravity gradient tensor

$$\Gamma = \begin{pmatrix} \Gamma_{xx} & \Gamma_{xy} & \Gamma_{xz} \\ \Gamma_{xy} & \Gamma_{yy} & \Gamma_{zz} \\ \Gamma_{xz} & \Gamma_{yz} & \Gamma_{zz} \end{pmatrix} \tag{6.19}$$

To put it simply, the main diagonal elements Γ_{xx}, Γ_{yy}, Γ_{zz} represent linear gravity gradients while the other elements are curvature components. For the assessment of gravity gradients in the QUEST interferometer we will only consider first order gravity gradients, that is the three main diagonal elements $\vec{\Gamma} = (\Gamma_{xx}, \Gamma_{yy}, \Gamma_{zz})$. The left elements of the gravity gradient tensor Γ can be neglected, since on the scale of the atomic cloud the equipotential spheres of the Earth's gravitational field can be approximated as a plane. This leads to [38]

$$\Phi(g(\vec{x}, \vec{v})) = k_{\text{eff}} T^2 \cdot g(\vec{x}) + k_{\text{eff}} T^3 \cdot \vec{\Gamma}\vec{v} \quad , \tag{6.20}$$

where $\vec{x}$ and $\vec{v}$ are position and velocity of the atom at the start of the interferometer sequence. When setting the coordinate origin to the centre of the atomic ensemble and assuming only linear gravity gradients, (6.20) becomes

$$\Phi(g(\vec{x}, \vec{v})) = k_{\text{eff}} T^2 \cdot (g(0) + \vec{\Gamma}\vec{x}) + k_{\text{eff}} T^3 \cdot \vec{\Gamma}\vec{v} \quad . \tag{6.21}$$

We assume, that the atom cloud is spherical symmetrically and switch to spherical coordinates,

$$\begin{aligned} \Phi(r,v) \;=\; & \frac{1}{2}k_{\mathrm{eff}}(r+\frac{1}{3}vt_0)\Gamma_{zz}t_0^2 \\ & -2\cdot 12k_{\mathrm{eff}}(1+\frac{1}{3}v(t_0+T))\Gamma_{zz}(t_0+T)^2 \\ & +\frac{1}{2}k_{\mathrm{eff}}(r+\frac{1}{3}v(t_0+2T))\Gamma_{zz}(t_0+2T)^2 \quad , \end{aligned} \tag{6.22}$$

where t_0 is the time between release of the atomic cloud and the first laser pulse. Putting this into (4.19) and (4.28) yields

$$P_{\mathrm{total}} = \int d^3x\, d^3v \cdot f(r)\cdot h(v)\cdot P(\Phi(r,v)) \quad , \tag{6.23}$$

with $f(r)$ being the spacial distribution and $h(v)$ the velocity distribution of the atom cloud. Integrating brings us back to the form

$$P_{\mathrm{total}} \;=\; \frac{1}{2}(1+C_0C_\Gamma\cos(\phi_{\mathrm{tot}}) \quad , \tag{6.24}$$

where

$$C_\Gamma \;=\; \mathrm{e}^{-\frac{1}{2}(k_{\mathrm{eff}}\sigma_r\Gamma T^2)^2}\cdot \mathrm{e}^{-\frac{1}{2}(k_{\mathrm{eff}}\sigma_v(t_0+T)\Gamma T^2)^2} \tag{6.25}$$

is the contrast reduction due to the gravity gradient and C_0 refers to effects caused by imperfect beam splitter efficiency [148]. The Γ in (6.25) refers to the satellite's z axis, which is the interferometer's sensitive axis. Provided the satellite does not rotate, the interferometer sees only the gravity gradient's projection onto its sensitive axis,

$$\Gamma \;=\; \cos(\nu)\Gamma_{rr}+\sin(\nu)\Gamma_\perp \quad , \tag{6.26}$$

where

$$\Gamma_{rr}(r) \;=\; -\frac{2GM}{r^3} \tag{6.27}$$

is the gravity gradient parallel to the gravitational field, while

$$\Gamma_\perp(r) \;=\; -\frac{GM}{r^3} \;=\; \frac{1}{2}\Gamma_{rr} \tag{6.28}$$

is the gravity gradient perpendicular to the position vector $\vec{r}$.

6.3.2. Optimal choice of T

The influence on the actual sensitivity depends highly on the shape and dynamic of the atomic cloud and the timing of the interferometer, especially the free evolution time T. Usually increasing T automatically leads to a higher sensitivity. However, if including gravity gradients this becomes different. Putting (6.25) into the single shot sensitivity for acceleration (6.12) we get

$$\sigma_a = \frac{e^{\frac{1}{2}(k_{\text{eff}}\sigma_r\Gamma_{zz}T^2)^2} \cdot e^{\frac{1}{2}(k_{\text{eff}}\sigma_v(t_0+T)\Gamma_{zz}T^2)^2}}{C_0} \cdot \frac{\sqrt{2}}{\sqrt{N}\,k_{\text{eff}}T^2} \,. \qquad (6.29)$$

As before we will treat C_0 as 1. Originally one aims for a free evolution time T as high as possible. Since the sensitivity scales with $1/T^2$, doubling T would have the same effect as e.g. increasing the atom number by a factor of 8. This is visualised in figure 6.9 (a). On the other hand, the degradation of contrast due to gravity gradients scales with at least e^{T^4}. Sooner or later it will subdue T^2, although the gravity gradient is very small. This raises the question of the optimal choice of T. Figure 6.9 (b) shows the gravity gradient induced contrast reduction C_Γ at different altitudes. Most noticeably the contrast is rather unaffected up to $T \approx 2\,s$, but completely breaks down above 5 s. Since the gravity gradient decreases with distance from the Earth, the effect is less severe at higher altitudes. However, within the range of relevant altitudes and possible values of T the effect of gravity gradients is still significant for the STE-QUEST mission.

To see its actual impact on the sensitivity, we combine figure 6.9 (a) and (b) and plot the results to figure 6.9 (c). It shows the single shot sensitivity σ_a as a function of T, using the colour code from figure 6.9 (b). As expected the loss in contrast exceeds the gain in sensitivity at a certain point, so that σ_a starts to degrade again at higher values of T. This means that there is in fact an optimal value for T, which is 4.8 s at 700 km altitude and rises up to 6.5 s at 3100 km. In the light of these results it seems reasonable to continuously adjust T while the altitude changes to achieve the best result in terms of sensitivity. However, when dynamically changing parameters of the atom interferometer during the mission we run the risk of additional — maybe untraceable — systematic errors. Therefore it is advisable to choose one fixed value for T, which offers the best overall sensitivity, when integrating over the orbit.

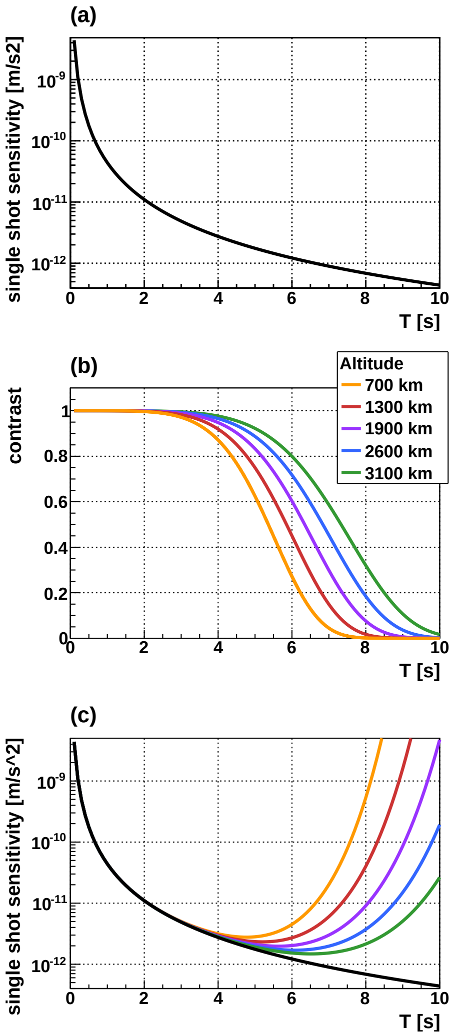

Figure 6.9.: (a) Single shot sensitivity in m/s^2 plotted against T. Disregarding gravity gradients it improves, when choosing higher values of T. (b) Contrast reduction due to gravity gradients as a function of T for the STE-QUEST parameters listed in table 5.5 at different altitudes over ground. (c) Single shot sensitivity in m/s^2 plotted against T with gravity gradients at different altitudes over ground (same colour code as in (b)). The single shot sensitivity without gravity gradient is added for comparison (black).

Since the satellite is in motion, all parameters have to be weighted accordingly and the optimal T for a complete orbit is not easily predictable, but can again only be calculated by simulation. To introduce the gravity gradient into our simulation, we alter the calculation of the sensitivity with the following snippet of C++ code:

```cpp
double G_rr, G_zz, C_grad;
G_rr = -2*GM/pow(absvecl(pos),3);
G_zz = cos(elements.nu)*G_rr + sin(elements.nu)*G_rr/2;
C_grad = exp(-0.5*pow(k_eff*sigma_r*G_zz*T*T,2))
  * exp(-0.5*pow(k_eff*sigma_v*(t0+T)*G_zz*T*T,2));
D_eta = D_eta/C_grad;
```

Listing 6.7: Contrast reduction due to gravity gradient

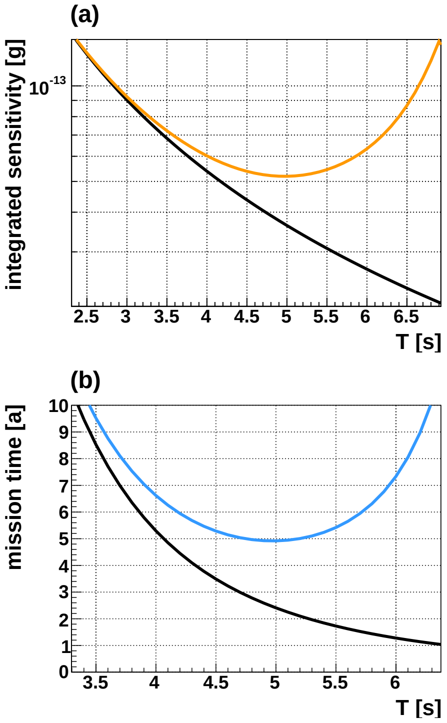

Figure 6.10.: (a) Integrated sensitivity for one orbit as a function of T. (b) Required mission time to achieve a overall sensitivity of $\sigma_\eta = 10^{-15}$. The black curves are in each case the corresponding curves without gravity gradient, added for comparison.

The result for the STE-QUEST reference orbit (table 5.5) is plotted in figure 6.10 (a), where we have the integrated sensitivity for one orbit as a function T. In addition we show the same result converted to the mission time required for an overall sensitivity of 10^{-15} in figure 6.10 (b). Interestingly there is only a small corridor for the choice of T that allows reaching 10^{-15} within reasonable mission time: It turns out that for the STE-QUEST reference orbit the optimal value for the free evolution time is in fact $T = 5.0\,s$. This is of course at the edge of what is technically possible today, but confirms less elaborate estimates for the best choice of T made before [52].

6.3.3. Low perigee orbits

One important consideration whilst the design of the final orbit is the perigee altitude. According to (2.13) the sensitivity is the better the higher g and thus the lower the perigee altitude. However, the reference orbit has been chosen with the lowest perigee possible without the need for an active compensation of atmospheric drag. Hence going to lower perigee altitudes entails substantial technical efforts to be made and should be justified by substantial scientific benefits.

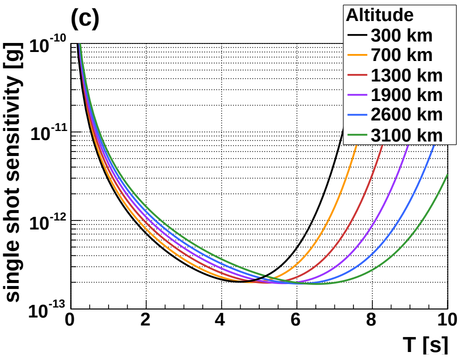

Figure 6.11.: The data from figure 6.9 (c), but normalised to g: Single shot sensitivity σ_η plotted against T with gravity gradients at different altitudes over ground. The single shot sensitivity without gravity gradient is added for comparison (black).

So, how big is the actual benefit of lower perigee altitudes for the atom interferometer? As a starting point we plot the data from figure 6.9 (c) again, but normalised to g this time, in figure 6.11. It shows — as we already observed with T — that the consideration of gravity gradients completely changes the basic assumption. The difference in the sensitivities that can be achieved at different altitudes is rather small, even if optimising T. This is stressed by the more detailed data in table 6.2: If staying with $T = 5\,s$, the achievable sensitivity differs by less than a factor of 1.3 within the interval of 300 km to 3000 km perigee altitude. If adjusting T the difference might be even smaller.

altitude	σ_η@T=5 s	T_{opt}	σ_η@T_{opt}
300 km	$2.197 \cdot 10^{-13}$	4.5 s	$2.024 \cdot 10^{-13}$
700 km	$2.029 \cdot 10^{-13}$	4.8 s	$2.003 \cdot 10^{-13}$
1300 km	$1.992 \cdot 10^{-13}$	5.2 s	$1.974 \cdot 10^{-13}$
1900 km	$2.086 \cdot 10^{-13}$	5.6 s	$1.951 \cdot 10^{-13}$
2500 km	$2.255 \cdot 10^{-13}$	6.1 s	$1.931 \cdot 10^{-13}$
3100 km	$2.472 \cdot 10^{-13}$	6.5 s	$1.913 \cdot 10^{-13}$

Table 6.2.: Achievable sensitivities at different altitudes.

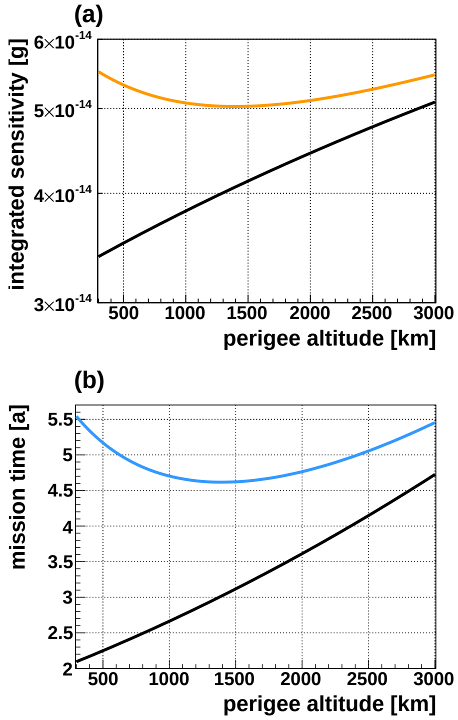

Figure 6.12.: (a) Integrated sensitivity for one orbit as a function of perigee altitude. (b) Required mission time to achieve a overall sensitivity of $\sigma_\eta = 10^{-15}$. T is kept constant at 5 s. The black curves are in each case the corresponding curves without gravity gradient, added for comparison.

To transfer this to a complete orbit, we'll now take the STE-QUEST reference orbit from table 5.5, but vary the perigee altitude. Figure 6.12 shows the integrated sensitivity achievable during one orbit. The black curve shows the expected behaviour when ignoring gravity gradients (lowering perigee improves sensitivity), while the orange curve is with gravity gradients taken into account. Lowering the perigee amplifies the effect of gravity gradients, so that the integrated sensitivity degrades. The optimal perigee altitude for T=5 s would be around 1400 km. According to that, there is no need for lower perigee altitudes, that would require active drag compensation. Altogether, we can say that the effect of the perigee altitude is quite small, when accounting for gravity gradients. An overall sensitivity of 10^{-15} can be reached at all perigee altitudes between 300 km and 3000 km within a mission time of 5.5 years, as shown in figure 6.12 (b).

6.3.4. Drifting orbit scenario

In section 5.6.3 we presented the STE-QUEST baseline orbit, that allows the establishment of microwave links at all altitudes, without the need of additional ground stations to be constructed. In passively varying the orbit over time, the intended alteration of the argument of perigee does also affect other orbital elements and thence leads to a variation of perigee altitude between 700 km and 2200 km.

Does this affect the mission's overall sensitivity to UFF violations? In the previous subsection we already saw, that the influence of perigee altitude is rather small in the respective altitude interval. However, to get a definite number of the overall outcome, we will simulate a complete mission of 6 years. The variation of perigee altitude displayed in figure 5.17 will be fitted by a cosine, plotted in figure 6.13 (a), while the semi-major axis is kept constant and the eccentricity is calculated according to (6.5). This does of course not represent the actual baseline orbit — which is incidentally not fixed yet, but is subject to recurring changes/optimisation. Nonetheless the simulation's statement about sensitivity is representative for the drifting orbit scenario.

The red curve in figure 6.13 (b) shows the integrated sensitivity per orbit modulated with the perigee altitude from 6.13 (a) plotted against mission time. The corresponding plot without the gravity gradient effect (black line) is plotted for comparison. However, if taking the gravity gradient into account, the integrated sensitivity per orbit does only vary between between $5.03{\cdot}10^{-14}$ and $5.26{\cdot}10^{-14}$ over the mission time. Finally, the red curve in 6.13 (c) shows the development of the overall sensitivity plotted against mission time. While after six years of mission time a overall sensitivity of $8.9{\cdot}10^{-16}$ is achieved, 10^{-15} is reached after 4.75 years or 1461 days. The difference to a fixed orbit geometry with a perigee altitude of 700 km is barely significant, as illustrated by the blue curve nearly vanishing behind the red one.

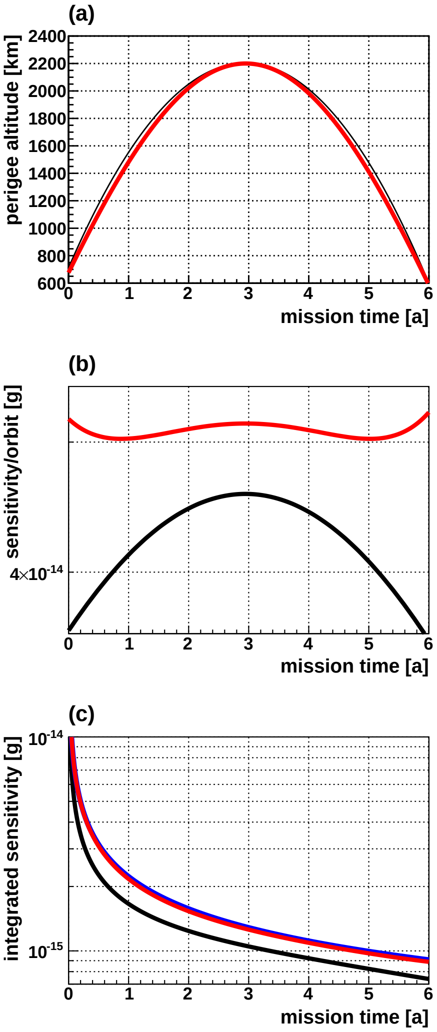

Figure 6.13.: (a) Variation of perigee altitude for the STE-QUEST baseline orbit over 6 years of mission time (red). (b) Integrated sensitivity for one orbit as a function of mission time. (c) Integrated sensitivity as a function of mission time (red). The integrated sensitivity for the (fixed) reference orbit is nearly identical (blue). The black curves are the corresponding results without gravity gradient, added for comparison.

6.4. Summary & discussion

STE-QUEST is a joint mission proposal of the formerly disjunct missions Space Time Explorer (STE) and QUantum Equivalence principle Space Test (QUEST). Its primary mission objectives are testing the universality of the gravitational redshift (UGR) and the universality of free fall (UFF). After STE-QUEST was chosen as one of four candidate missions for launch in 2022 within ESA's Cosmic Vision program, a detailed assessment process was started.

The crucial issue for the QUEST mission was if it is still feasible under the prevailing compromises of the joint mission. This essentially boils down to the question if the mission's key specification, the sensitivity for violations of the UFF, could still be reached. Before the merger of the two missions the sensitivity had only been calculated on basis of circular orbits, where altitude and thus the strength of the local Earth acceleration g is constant and therefore the methods for ground based atom interferometers were applied. However, for the STE mission a highly elliptical orbit is mandatory. Since the sensitivity depends on the value of g, it also depends on altitude. Hence, it needs to be calculated time-resolved throughout the orbit. Although Kepler trajectories can in principle be calculated analytically, the satellite's position as a function of time can only be obtained by means of numerical methods. Thus a numerical orbit propagator was applied to compute the satellite's altitude as a function of time. This enables us to calculate the single shot sensitivity for every single measurement with respect to the relevant environmental parameters.

The first vital result of the orbit assessment was that only measurements taken around perigee up to a critical altitude should contribute to the integrated signal. Since the amplitude of the desired signal is assumed to be proportional to g and the error in $\mathrm{m/s^2}$ remains constant, the relative error on the Eötvös ratio grows with altitude. In other words, the sensitivity declines with altitude. Performing measurements beyond the critical altitude would degrade the integrated sensitivity instead of improving it. Leading to a duty time of only 20 to 35 minutes on one 16 hour orbit, this creates some doubt about the capability of the UFF measurement within the joint mission. However, it turned out that a reasonable integrated sensitivity per orbit in the order of $\eta \sim 10^{-14}$ could still be reached.

Since a rotation of the atom interferometer would evoke a systematic error, it is favourable to have a non-rotating satellite. However this inevitably leads to divergence between sensitive axis and the nadir vector. By comparing three different rotation scenarios we showed that the choice of the rotation scenario has a rather minor influence on the sensitivity achievable during one orbit. Choosing a non-rotating satellite therefore does not corrupt the mission's target sensitivity.

In astrodynamics the **nadir vector** (from Arabic/ALA-LC: naẓīr, meaning *opposite*) refers to the direction of the gravitational force at that location.

For the final assessment it was needed to include gravity gradients in the simulation. Actually we are dealing with several counteracting effects: On the one hand the achievable single shot sensitivity depends on the strength of local g, which means the best single shot sensitivity is achieved with the lowest perigee altitude. On the other hand the satellite's perigee passage is the faster the lower the perigee. This means lowering perigee reduces the available integration time, which in turn reduces the sensitivity achievable during one orbit. These two effects are superimposed by the reduction of contrast due to gravity gradients. Since the complex interplay between these effects cannot be estimated, the numerical simulation was crucial for orbit optimisation. With respect to the atom interferometer this essentially means the choice of perigee altitude.

Introducing gravity gradients into the simulation revealed that the choice of the free evolution time as originally proposed (T=5.0 s) is in fact the optimal value. Furthermore it turned out that the QUEST part of the mission is much more robust concerning orbit design, than originally thought. The three counteracting effects — altitude, passage time and gravity gradients — nearly compensate each other. Thus, the integrated sensitivity per orbit is almost constant for perigee altitudes between 300 km and 3000 km. Scenarios with perigee altitudes down to 300 km, which would require expensive thruster systems to compensate atmospheric drag, are hence not required for QUEST. Moreover adjustments of the orbit favourable for STE could be made without worrying about the performance of the atom interferometer. This was especially beneficial when later on the drifting baseline orbit was introduced, which saves considerable expenses for steering equipment. Besides the drift of the desired orbital elements, it also leads to a parasitic drift in perigee altitude. The final simulation run was calculated time-resolved for the complete mission including 3285 orbits and some hundred thousands of data points. Considering gravity gradients as well as the drifting orbit it showed that the mission goal of reaching a sensitivity of 10^{-15} can be achieved within just under five years of mission time.

Thus, it could be shown that a spaceborne test of the UFF based on atom interferometers is definitely feasible. Due to the measurement's robustness against variation of the orbit parameters this applies even to the STE-QUEST orbit geometry being disadvantageous for the UFF measurement. However, we will not let go the eager reader without stressing the constraints emerging from the current TRL: The calculations in this chapter have been done with the implicit understanding that all sources of technical noise can be diminished below the shot noise limit (see section 9.5 for some remarks on clock noise). This is the challenge for the further development process.

The numerical model and the simulation results described in this chapter have been cross-checked and confirmed by an independent recalculation at ESA [20]. A summary of the simulation results has been included in the Science Requirements Document [58] published in 2013 and [146].

Addendum

The objective of the **PLAnetary Transits and Oscillations of stars (PLATO)** mission is the search for extrasolar planetary systems, with emphasis on Earth-like planets. [48]

In February 2014, out of the four candidate missions PLATO was selected as M3, the third medium-class mission in ESA's Cosmic Vision Programme [49]. Although this means that STE-QUEST will not be launched in 2022, the decision was to be expected. When the proposal was submitted in december 2010 it seemed unlikely that STE-QUEST will meet the required technology readiness level (TRL) within only 12 years. However, the actual primary goal of the past assessment process was to develop the idea that was proposed in 2010 into a more mature construction design. All the members of the STE-QUEST science team contributed in lifting the design of the QUEST apparatus to a higher level of detail. During this process many parts of the mission — where the relation between sensitivity and orbit design was only one among many others — were assessed to much higher extent than before.

Moreover, the fact that STE-QUEST was canceled is by no means the end of QUEST. In contrary it offers the chance of designing a distinct QUEST mission without the drawbacks of the joint mission. Especially an orbit design fitted to the needs of the UFF measurement allows a vast improvement in integration time and thus integrated sensitivity. With the STE-QUEST baseline orbit the atom interferometer is only operated between 20 and 35 minutes on one 16 hour orbit. This corresponds to a duty factor not exceeding 3.6 %. In contrast, a non-rotating satellite on a circular orbit at 1200 km altitude would run with a duty factor of 65 %. The instrument as designed for STE-QUEST would yield an integrated sensitivity of $\sigma_\eta = 3.07 \cdot 10^{-14}$ per orbit. The QUEST target sensitivity of 10^{-15} would be reached after only 72 days and after five years of mission time an integrated sensitivity of $2 \cdot 10^{-16}$ would be achieved. Thus, the final sensitivity could already be improved by nearly one order of magnitude, just by choosing an orbit geometry more attuned to the needs of the UFF test. It is worth studying if further optimisation of the orbit can help on improving the sensitivity, e.g. via variation of the measurement time at the apsides by choosing a slightly elliptical orbit or via choosing a rotating satellite always pointing nadir.

Part III.

Optical Phase-Locked Loops

Optical phase locked loops (OPLLs) are one of the core elements of Raman based atom interferometers. Moreover, phase noise of the Raman lasers is one of the strongest sources of technical noise. However, if done properly designing an OPLL is not rocket science. We will exemplarily demonstrate the design, commissioning, characterisation and optimisation of a simple OPLL and will discuss the impact of laser phase noise to the atom interferometer measurement, uncover the sources of noise within the phase locked loop's components and identify possibilities for improvements. The following three chapters are intended to serve as an introduction to the technique of OPLLs within the scheme of atom interferometers, and may also serve as a *how-to* for copycats.

7. Phase Locked Loops

The crucial point in understanding the phase-locking of lasers, is a basic understanding of phase-locked loops (PLL). In short a PLL is a special kind of control system, locking the phasing — and thus the frequency — of a variable oscillator to an external reference frequency. This leads directly to the next question: What is a control loop? Section 7.1 starts answering this question in giving a short introduction to control systems. We'll proceed with some glimpses of control theory needed for calculating PLLs in section 7.2 and close with a theoretical description of a PLL in section 7.3.

7.1. Control Loops

A control system is a device or a set of devices designed for the automated control of technical or physical systems. While the term *control system* covers a broad variety of machinery, we will stick with feedback or linear control systems. This is the domain of control loops. Basically we can distinguish open-loop from closed-loop configurations and feedback from feed-forward control. We'll explain these terms using the example of a voltage-controlled oscillator (VCO).

A **voltage-controlled oscillator** (VCO) is an electronic oscillator, whose frequency can be set by an external control voltage. High frequency VCOs are usually based on a oscillating circuit, whose frequency determining elements can be altered electrically. The broad majority of PLLs comprises a VCO.

Open-loop Configuration

The output frequency of a VCO depends on a control voltage. If the behaviour of the VCO at different reference voltages is known, e.g. in the form of a calibration curve, we can determine the VCO's output frequency by setting the appropriate reference voltage. This kind of control is called **feed-forward** control. However, disturbances like a frequency shift due to changes of the ambient temperature cannot be compensated with a feed-forward control. This shortcoming can be eliminated by using a closed control loop.

Closed-loop Configuration

In a closed-loop configuration the system output is used to generate the system's control signal. Thus a dynamic feedback to the actual state of the system is implemented. The basic principle of a **feedback control loop** is presented in figure 7.1. In general, a feedback control loop has four functions: Measure, Compare, Compute, and Correct.

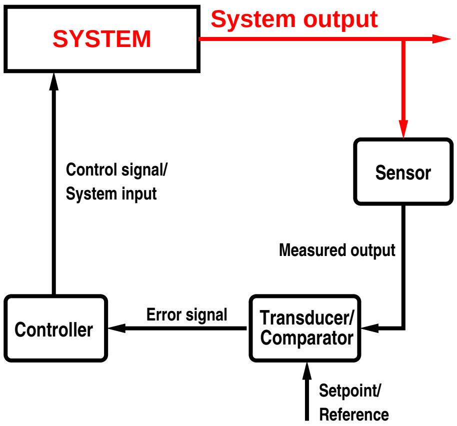

Figure 7.1.: Block diagram of a feedback control loop

In our example (figure 7.1) the *system* to be controlled is represented by a VCO. Its output frequency, the *system output*, is measured by a *sensor*. If necessary, the measured output can be transduced to another kind of signal. The VCO's output frequency is transduced to a voltage by a frequency-to-voltage converter. It can be compared to a reference voltage, which defines the system setpoint. *Transducer* and *comparator* are often combined into a single device. The difference between measured output and setpoint is the *error signal*. The error signal can be used by a *controller* to *compute* a *control signal*, which is suitable to correct the system output to the desired value — it is fed back to the VCO.

The advantage of feedback control over feed-forward control is obvious: The system output can be adjusted to the desired value independent and without precise knowledge of the perturbing mechanisms. However, combining both techniques might be useful to improve the control loop response during fast and large changes of the setpoint. Since a feedback control system does only react to the error signal, it cannot foresee the future. Hence it has always a finite response time. On the other hand, we as the users might know precisely when we are going to change the setpoint. Using feed-forward control, we can simply add an additional offset to the control signal simultaneously with the change of the setpoint. If the transfer function of the VCO is known precisely, we might be able to keep the error signal close to zero, without the feedback control even noticing the change of the setpoint. An example is the use of one pair of lasers for both, a MOT and Raman transitions, which requires the lasers being shifted by about 1 GHz in frequency within a few milliseconds. This has been demonstrated with the reference setup presented in section 8.4 and was described in [182].

7.1.1. PID Controllers

The controller is at the heart of every feedback control loop. Most commonly used to implement a feedback control loop are controllers with P, PI, PD or PID behaviour — generically condensed in the term proportional-integral-derivative controller. A block diagram of such a PID controller is depicted in figure 7.2. The control signal v_{pid} generated by a PID controller is the sum of a proportional, an integral and a derivative term:

$$v_{pid}(t) \quad = \quad P_{\text{out}} + I_{\text{out}} + D_{\text{out}} \tag{7.1}$$

The term

$$P_{\text{out}}(t) \quad = \quad K_p\, v_e(t) \tag{7.2}$$

is proportional to the instantaneous error signal $v_e(t)$. It reacts instantaneously, the response time is only limited by signal propagation time. However, as long as there is a non-zero control signal, there will always be a residual steady-state error, proportional to the control signal. This can be compensated by adding a bias-term to the set-point (feed-forward) or by adding an integral term. The integral term I_{out} sums up the instantaneous error signal over time:

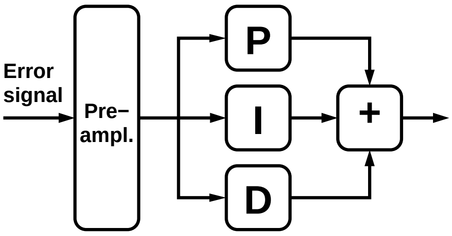

Figure 7.2.: Block diagram of a PID controller. The contributions from the proportional (P), integral (I) and derivative (D) term are summed up to form the control signal.

$$I_{\text{out}}(t) \quad = \quad K_i \int_0^t d\tau\, v_e(\tau) \tag{7.3}$$

I_{out} increases until the measured output has reached the setpoint (the error signal gets zero), but then keeps its value. Hence there is no residual steady-state error as with a P-only controller. The larger the integral gain K_i, the faster the integrator forces the system to reach the setpoint. However, a large value of K_i will lead to overshoot until oscillation, when reaching the setpoint. This can be damped with a derivative part:

$$D_{\text{out}}(t) \quad = \quad K_d\, \partial_t v_e(t) \tag{7.4}$$

It slows the rate of change of the control signal. However, since the D term slows down the transient response time of the controller and may also amplify noise, it must be used with caution. As we will see in section 7.2, the term $K_d \partial_t v_e(t)$ diverges for high frequencies, which might again lead to oscillations and poses a limit for the value of K_d. Thus the gain factors K_p, K_i and K_d have to be set individually to optimise the controllers response. A badly configured controller may lead to slow response and bad noise performance on the one hand or undamped oscillations on the other hand.

In order to understand performance and stability of control loops, we will introduce transfer functions, have a look at the characteristics of the proportional, integral and derivative term and introduce the Bode stability criterion in section 7.2.

7.2. Transfer Functions

The transfer function is one of the most significant parts of control theory. It describes the relation between input and output of a linear, time-invariant system (LTI). In the last section we already introduced gain factors. They are in fact the most simple example of a transfer function. In anticipation of phase-locked loops we will employ the example of a phase detector. It creates an electrical voltage linear to the phase difference of the oscillations at its two inputs,

Control theory is a mathematical theory describing the dynamic behaviour of linear, time-invariant systems. **Linear** means, that the system output depends linearly on one or more input variables. **Time-invariant** in this respect means, that the rules determining the systems behaviour are time-invariant, although the system's actual state does change over time. Like in our case, this is often about automatic control of the system output to an externally defined setpoint and the suppression of perturbing effects. The art of designing such control systems is called control engineering.

$$v_{pd} \quad = \quad K_{pd}\,(\phi_1 - \phi_2) \quad , \tag{7.5}$$

which is determined by the gain factor K_{pd}. Since the input signal is a phase and the output signal is a voltage, K_{pd} has units of

$$[K_{pd}] \quad = \quad \left[\frac{v_{pd}}{\phi_1 - \phi_2}\right] = \frac{\mathrm{V}}{\mathrm{rad}} \quad . \tag{7.6}$$

7.2.1. Fourier Transforms

Taking a constant factor as transfer function of course assumes, that the relation between input and output is actually constant, i.e. independent of frequency and other factors. In the more general case, especially when dealing with AC signals, a system's behaviour will depend on signal frequency. The spectral composition of a signal $v(t)$ can be specified by its Fourier transform:

The **Fourier transform** is named after the french mathematician and physicist Jean Baptiste Joseph Fourier (* 1768 near Auxerre, † 1830 in Paris). It is defined on real functions $v\colon]{-\infty}, \infty[\to \mathbb{R}$, it is real and continuous. The Fourier transform analyses signals in terms of sinusoids. Opposite to Fourier series, it is also applicable to aperiodic signals, provided $f(x) \to 0$ for $x \to \infty$. As a secondary effect of Fourier analysis we often speak of ω as the *Fourier frequency*, when dealing with power spectral densities, which we will introduce in chapter 9.

$$V(\omega) \quad = \quad \mathcal{F}\{v(t)\} = \int \mathrm{d}t\, \mathrm{e}^{-\mathrm{i}\omega t} v(t), \tag{7.7}$$

By convention, the Fourier transform of $v(t)$ is labeled with the corresponding upper case letter $V(\omega)$. Its parameter is the angular frequency. The other way round, we can obtain the signal $v(t)$ from a spectrum $V(\omega)$ by applying the reverse transform from frequency domain — or Fourier domain — to time domain:

$$v(t) \quad = \quad \mathcal{F}^{-1}\{V(\omega)\} = \frac{1}{2\pi} \int \mathrm{d}\omega\, \mathrm{e}^{\mathrm{i}\omega t} V(\omega). \tag{7.8}$$

Similar to a signal spectrum $V(\omega)$, we can also define a transformed transfer function $F(\omega)$ for linear electrical circuits, e.g. high or low pass filters. Describing frequency selective devices in time domain usually requires a convolution (see table 7.1). However, in Fourier domain the application of a filter on the signal reduces to a simple multiplication,

$$V_{out}(\omega) \quad = \quad F(\omega)V_{in}(\omega) \quad , \tag{7.9}$$

where the filter's transfer function $F(\omega)$ is can be interpreted as the filter's spectral response.

7.2.2. Laplace Transforms

Fourier transforms can be regarded as a special case of the more general Laplace transforms. The single-sided Laplace transform of a function $v\colon [0,\infty[\to \mathbb{C}$ is defined as

$$V(s) \quad = \quad \mathcal{L}\left\{v(t)\right\} = \int_0^\infty \mathrm{d}t \, \mathrm{e}^{-st} v(t), \tag{7.10}$$

where $s = \sigma + \mathrm{i}\omega$ and $\sigma, \omega \in \mathbb{R}$. As before we stay with the notation of using lower case letters in time domain and upper case letters for Laplace domain description. The Laplace transform can be thought of as an analytical extension of the Fourier transform. In particular setting $s = \mathrm{i}\omega$ yields the single-sided Fourier transform

$$\mathcal{L}\{v(t)\}(\mathrm{i}\omega) = \int_0^\infty \mathrm{d}t \, \mathrm{e}^{-\mathrm{i}\omega t} v(t) \quad = \quad \mathcal{F}_\infty\{v(t)\}(\omega) \quad . \tag{7.11}$$

While ω in Fourier transforms is a real number, s is complex. Besides frequency, we can thus also encode damping information into s. This is the reason, why in physics and engineering the Laplace transform is often used for input-output analysis of linear, time-invariant systems such as electrical circuits, harmonic oscillators, optical devices, and mechanical systems. Transfer functions for all kinds of linear electric devices can be defined similarly as above:

$$V_{out}(s) \quad = \quad F(s)V_{in}(s) \tag{7.12}$$

In Laplace domain $F(s)$ cannot directly be read as a spectrum like the Fourier transform. Nevertheless, Laplace transforms can still be interpreted as transformation from time domain to frequency domain. We obtain the spectral response of a device by setting $s = \mathrm{i}\omega$ and calculating the absolute value $|F(\mathrm{i}\omega)|$. In a similar manner the complex phase $\arg(F(\mathrm{i}\omega))$ yields the phase shift caused by the device.

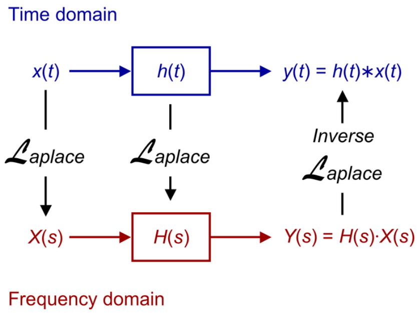

Figure 7.3.: Applying frequency selective devices to a signal requires integration in frequency domain, while it simplifies to a multiplication in Fourier/Laplace domain. The typical approach is to perform a transformation to Fourier/Laplace domain, apply the filter and transform back to frequency domain. [6]

The **Laplace transform** was introduced by the french mathematician and astronomer Pierre-Simon Laplace (* 1749 in Beaumont-en-Auge, Normandy, † 1827 in Paris) in his work on probability theory. As the Fourier transform it is linear and continuous. Although the parameter $s = \sigma + \mathrm{i}\omega$ is complex, there is still a physical interpretation: ω gives the angular frequency as in Fourier analysis, while σ represents the time constant of a damped sinusoid. Since the Laplace Transform analyses signals not only in terms of sinusoids, but also in terms of exponentials, it can handle dissipative and unstable systems. Hence Laplace transform do not need the constraint that the signals must disappear for $t \to \infty$; contrariwise it may even diverge.

7.2.3. Examples

PID controller

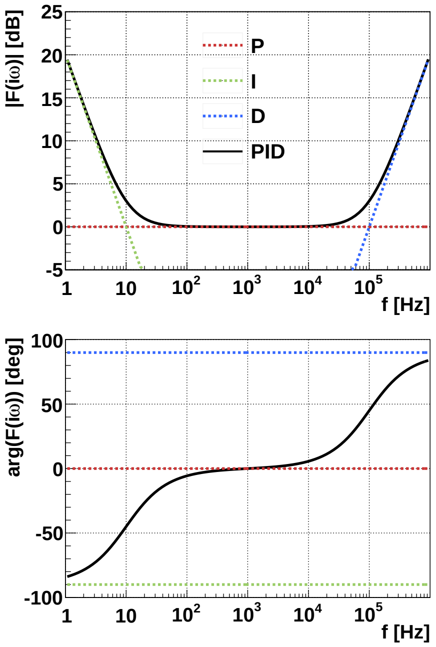

Figure 7.4.: Amplitude response (top) and phase resonse (bottom) of a PID controller.

A plot of frequency and phase response of a linear time-invariant system with a log-frequency axis like in figure 7.4 is often refered to as **Bode plot**.

To get a basic feeling for transfer functions of real devices, we will now have a look at some examples. Table 7.1 provides a set of Laplace transforms, which might be useful when calculating phase-locked loops. In setups featuring multiple devices those Laplace transforms can easily be combined: Parallel devices are represented as a sum of the corresponding transfer functions. A PID controller is hence written as

$$V_{out} = F_{pid}(s)V_{in} = \left(K_p + \frac{K_i}{s} + K_d \cdot s\right)V_{in}. \tag{7.13}$$

The upper plot in figure 7.4 shows the amplitude response $|F(\mathrm{i}\omega)|$ of our PID controller. While a proportional factor (red) has a flat amplitude response, the integrating circuit (green) with unity gain crossing at 10 Hz shows a -6 dB/octave slope, corresponding to the factor $1/s$ in Laplace domain. Analogous the derivative unit (blue) with unity gain crossing at 100 kHz has a +6 dB/octave rise, corresponding to the factor s. Combining those three, the black line represents the amplitude response of the transfer function $F_{pid}(s)$.

The phase response $\arg(F(\mathrm{i}\omega))$ is depicted in the lower plot in figure 7.4. Again the proportional factor (red) has a flat profile with zero phase shift. The integrating circuit on the other hand has a phase lag of 90°. This is easily explained by imagining a sine wave at the integrators input: During the positive half-wave the output signal rises, reaching its maximum slope at $\pi/2$ and its highest point at π, where the input signal has its zero crossing. Afterwards it starts decreasing, but doesn't reach its minimum until 2π, where the input signal has already completed its negative half-wave. Similar considerations yield, that the derivative unit has 90° phase lead. The combined transfer function $F_{pid}(s)$ (black) has zero phase shift at medium frequencies, but is dominated by the integrator at low frequencies and by the differentiator at high frequencies.

Filters

It is worth mentioning that for both, the integrator and the differentiator, the phase shift of the isolated device is constant over all frequencies! This is completely different to the phase characteristic of low-pass and high-pass filters, like depicted in figure 7.5. The low pass filter (green) shows no phase shift below its cut-off frequency at 100 Hz, but approaches a phase lag of 90° for frequencies $\gg$100 Hz. Correspondingly the high pass filter (blue) with cut-off frequency at 10 kHz approaches 90° phase gain for frequencies $\ll$10 kHz and has no phase shift within its pass-band. The first order high-pass and low-pass filters used in this example have a slope of ±6 dB/octave respectively in their frequency response.

As one might already have guessed, daisy-chained devices are represented by multiplying the corresponding transfer functions. Thus we can construct a primitive band-pass filter:

$$V_{out} \quad = \quad F_{bp}(s)V_{in} = F_{lp}(s)F_{hp}(s)V_{in} \tag{7.14}$$

The corresponding amplitude and phase response is depicted by the dashed black lines in figure 7.5. A completetly different phase response is generated when combining low-pass and high-pass to a primitive band-rejection filter. Summing up the individual transfer functions,

$$V_{out} \quad = \quad F_{bp}(s)V_{in} = \Big(F_{lp}(s) + F_{hp}(s)\Big)V_{in}, \tag{7.15}$$

results in the black line in figure 7.5. The shape of the phase response is characteristic for band-rejection and notch-filters, independent of order and technical implementation.

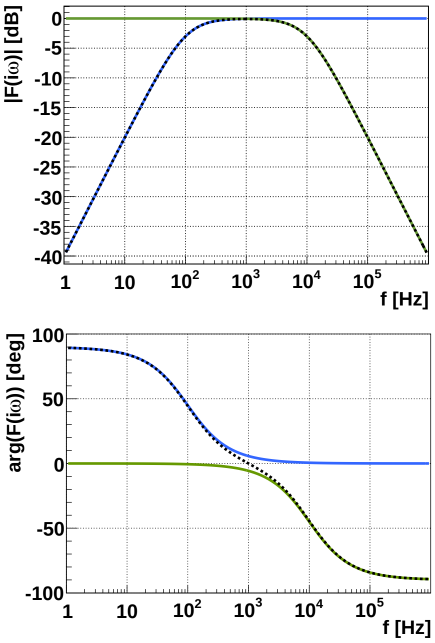

Figure 7.5.: Bode plots a high pass (blue), a low pass (green) and a band-pass filter (dashed, black).

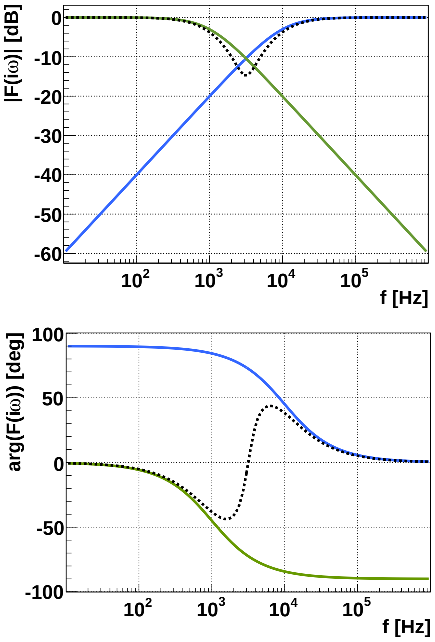

Figure 7.6.: Bode plot of a primitive band-rejection filter (dashed, black).

Time Delay

A time delay τ within the control loop has no effect on the amplitude, but leads to a phase lag

$$\phi_\tau \quad = \quad 2\pi\tau \cdot f = \omega\tau \tag{7.16}$$

proportional to signal frequency. A phase delay (7.16) corresponds to a rotation in the complex plane. It can hence be written as

$$\mathrm{e}^{-s\tau} \tag{7.17}$$

in the Laplace domain. While in a linear plot this corresponds to a straight line, a log-frequency axis results in figure 7.7. Assuming an inverse signal propagation speed of 5 ns/m, a time delay of 10 ns corresponds to only 2 m of coaxial cable — an amount easily reached when wiring diode laser setups. Thus, in an OPLL time delay might already get significant at Fourier frequencies in the single-digit MHz range.

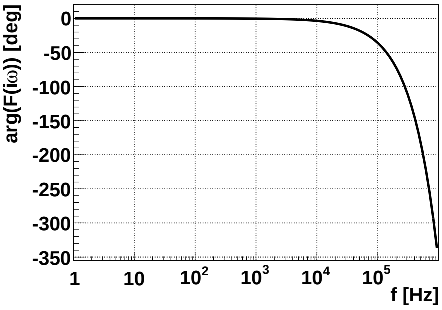

Figure 7.7.: Phase lag resulting from a time delay of τ=10 ns. A phase lag of 180° is already attained at a Fourier frequency of $1/2 \cdot \tau^{-1}$=5 MHz.

Device	Time domain	Laplace domain
notation	$v(t)$	$V(s)$
proportional factor	$K_p \cdot v(t)$	$K_p \cdot V(s)$
integration	$K_i \int dt\, v(t)$	$K_i/s \cdot V(s)$
differentiation	$K_d\, \partial_t v(t)$	$K_d \cdot s \cdot V(s)$
time delay	$v(t) \to v(t-\tau)$	$\mathrm{e}^{-s\tau} \cdot V(s)$
high pass filter	*convolution*	$\frac{s}{\omega_c+s} \cdot V(s)$
low pass filter	*convolution*	$\frac{\omega_c}{\omega_c+s} \cdot V(s)$
lead-lag network	*convolution*	$\frac{1+s/f_l}{1+s/f_h} \cdot V(s)$
notch filter	*convolution*	$\frac{s^2+{}^{d}\!/_{c}\,\omega_c s+\omega_c^2}{s^2+{}^{1}\!/_{c}\,\omega_c s+\omega_c^2} \cdot V(s)$

Table 7.1.: Some Laplace transforms helpful for analysing an OPLL.

7.3. PLL Basics

A phase-locked loop (PLL) is special kind of control loop. It locks the phase, and thus the frequency, of an oscillator to an external reference frequency. Locking the phase implies a frequency match of the oscillator with the reference frequency. This is equivalent to a frequency lock with infinitesimal linewidth (barring phase noise).

The most basic arrangement of a PLL is shown in figure 7.8. It contains three main components:

1. The **phase detector** compares the phase of the output signal to the phase of the reference signal. The error signal has to be linear to the phase difference of the two input frequencies. A zero error signal can correspond to a phase difference of either 0° or 90°, depending on the type of phase detector.

See section 7.4 for remarks on the non-**linearity** of real electronic devices.

2. The **loop filter** generates the control signal for the VCO. Thus it determines the PLL's reaction to phase errors and

hence its dynamics. Although *loop controller* would have been the better term, *loop filter* has become prevalent in PLL applications.

3. The variable **oscillator** is an VCO in most applications. As we will see in section 7.3.1, even a pair of lasers can be considered a VCO.

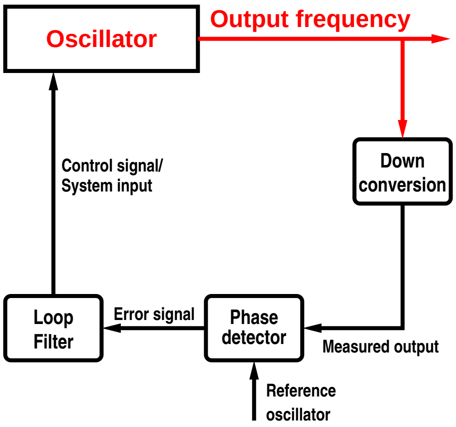

Figure 7.8.: The simplest form of an PLL consists of three components – phase detector, loop filter, oscillator – combined to a closed feedback loop. An optional frequency down conversion can be inserted between oscillator and phase detector.

The lower the output frequency, the easier signal processing. Optional down conversion of the output frequency using a frequency divider or a frequency mixer thus simplifies all subsequent electronics. This is especially useful when the output frequency is a multiple of the reference frequency. Hence, a PLL can be used for frequency multiplication. Since sufficiently stable reference oscillators are commonly available only at certain frequencies, like 5, 10 or 100 MHz, this might be the only way to produce ultra-stable signals at high frequencies.

If the PLL is in a stable condition, the output frequency is exactly equal — or if using a frequency divider for down conversion an exact multiple — of the reference frequency. We also say, that the PLL is locked. In this respect we can define the following operating ranges of a PLL:

- Lock-in range: The unlocked PLL can lock without leaving out a period.
- Pull-in range: The unlocked PLL can lock, but misses some periods.
- Hold-in range: The locked PLL can hold the lock.

7.3.1. Optical PLLs

To put it simple, an optical PLL is a PLL, where the VCO is a set of two lasers. But as the laser light operates in the THz regime, how is a *system output* frequency in the order of some hundreds of MHz generated? If the wavelengths of the lasers differ slightly — from some 10 MHz up to several GHz in our case — superimposing two laser fields

$$\begin{aligned} E_1(t) &= \hat{E}_1 \cdot \sin(\omega_1 t + \phi_1) \\ E_2(t) &= \hat{E}_2 \cdot \sin(\omega_2 t + \phi_2) \end{aligned} \tag{7.18}$$

generates an optical beat:

$$
\begin{aligned}
I_{\text{ges}} &= \Big(E_1(t) + E_2(t)\Big)^2 \qquad (7.19)\\
& \,| \\
&= E_1^2(t) + E_2^2(t)\\
&\quad + \hat{E}_1\hat{E}_2 cos\Big((\omega_1 + \omega_2)t + (\phi_1 + \phi_2)\Big)\\
&\quad + \hat{E}_1\hat{E}_2 cos\Big((\omega_1 - \omega_2)t + (\phi_1 - \phi_2)\Big)
\end{aligned}
$$

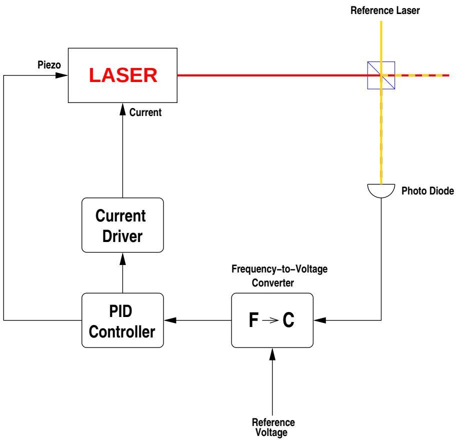

Figure 7.9.: Schematic of a servo loop for the stabilisation of a laser. A dual path PID controller creates control signals for the piezo and the laser diode current.

Since ω_1 and ω_2 are in the THz regime, only the term oscillating with $\omega_1 - \omega_2$ is detectable as intensity oscillation on a photo detector. That means the observable beat frequency ω_B is exactly the frequency difference of the two lasers:

$$\omega_B \quad = \quad \omega_1 - \omega_2 \qquad (7.20)$$

This relation is commonly used for frequency stabilisation of lasers: The laser controlled by the feedback loop — called the *slave* laser — is locked to a *master* laser. If the master laser is locked to an absolute reference, e.g. a spectroscopy, it is usually called a *reference* laser. Since this technique does only work if ω_B and thus the frequency offset between the two lasers is non-zero, it is called *offset locking*.

Figure 7.9 shows a block diagram of a feedback control loop using offset locking for the frequency stabilisation of an external cavity diode lasers (ECDL). The special thing about ECDLs as introduced in section 8.1 is, that they have two input paths for control signals: A piezo mounted to the outcoupling mirror changes the length of the external cavity. Also the current driving the laser diode can be used to vary the output wavelength. Slow components of the error, e.g. long-term drifts arising from temperature fluctuations in the lab, are compensated with the piezo. The control signal for faster fluctuations is modulated onto the laser current. The two control signals are usually created by PID controllers.

From the control loop's point of view the combination of two lasers and photo detector is just a voltage controlled oscillator running at ω_B. Remembering the scheme from 7.1 it is only a small step to the optical phase-locked loop in figure 7.10:

1. The system output is the optical beat measured by a photodiode.
2. The electric beat is transduced into an electrical voltage by a phase detector.

3. The phase detector generates an error signal by comparison with a frequency reference.
4. Two control signals with different control bandwidths, are generated from the error signal and fed back to the laser.

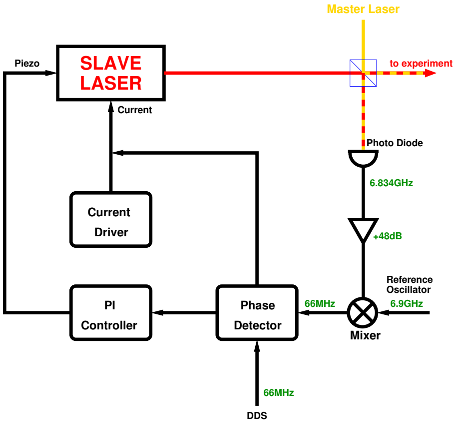

Figure 7.10.: Schematic of an optical phase lock loop. The laser is superimposed with a reference laser. The resulting beat is detected on a photo diode and then converted to an error signal by the phase detector. The laser frequency is controlled via piezo and laser diode current.

The modulation input of most current drivers is limited to some tens of kHz. Since an atomic gravimeter requires a bandwidth of at least 100 kHz, we skip the current driver and modulate the control signal directly onto the laser current. Following the convention of PLLs, we refer to the controller in the (fast) current control path as the loop filter.

In order to guard against misunderstandings, we should stress, that it is not the phase of the slave laser that is locked, but the relative phase between the master laser and the slave laser

$$\phi(t) \quad = \quad \int_{t_1}^{t} d\tau \omega_B(\tau) \quad . \tag{7.21}$$

Finally we have to consider, that an ECDL might have a more complicated transfer function than just a proportional gain factor like in (7.22). Thus, determining the transfer function of an OPLL setup will be the treated in chapter 8.

7.4. The OPLL Transfer Function

To mathematically describe the dynamics of a PLL, we have to quantify the behaviour of the involved components. The tool of choice for linear analysis are Laplace transforms and the concept of transfer functions as introduced in section 7.2. Transfer functions enable us to describe the relation between input and output of a PLL. It should be noticed, that in fact only linear circuits have transfer functions and non-linear circuits do not! Analog PLLs are highly nonlinear circuits. Nevertheless they can be well approximated by linear models if the error is small. Usually this is the case, when the PLL is operated in a locked condition. Therefore we keep in mind, that the following analysis is only applicable, when the PLL is in a state where the linear approximation is valid. Another thing to remark is, that transfer function usually relate voltages or currents of input and output signals. Here we are dealing with phases of the signal and hence the transfer functions in this section will relate phase modulations at the input with phase modulations at the output.

7.4.1. Transfer Function of Loop Components

Enough of introduction, let's start! We consider a simple PLL consisting of a VCO, a phase detector and a loop filter.

Transfer Function of the Voltage Controlled Oscillator

We start with the VCO, whose output frequency is determined by the control signal v_c. Assuming linear behaviour for the oscillator, the deviation of its output frequency from its center frequency (in units of radian per second) is

$$\Delta\omega_o = K_o \cdot v_c, \tag{7.22}$$

where K_o is the VCO's gain factor measured in units of rad·Hz/V. We express ω_o as the time derivative of the VCO phase ϕ_o,

$$\partial_t \phi_o(t) = K_o \cdot v_c \quad , \tag{7.23}$$

perform an integration,

$$\phi_o(t) = \int \mathrm{dt}\, K_o \cdot v_c \quad , \tag{7.24}$$

and go to the Laplace domain:

$$\begin{aligned} \mathcal{L}\{\phi_o(t)\} &= \mathcal{L}\Big\{\int \mathrm{dt}\, K_o \cdot v_c\Big\} \\ &\,| \\ \Phi_o(s) &= \frac{K_o}{s} \cdot V_c(s) \quad . \end{aligned} \tag{7.25}$$

Transfer Function of the Phase Detector

Assuming linear behaviour for the phase detector, the error signal is proportional to the phase error

$$\phi_e = \phi_r - \phi_o \quad , \tag{7.26}$$

which is the difference of the reference signal phase ϕ_r and the VCO phase ϕ_o. The output voltage of the phase detector is thus

$$v_{pd} \quad = \quad K_{pd} \cdot (\phi_r - \phi_o) \quad , \tag{7.27}$$

where K_{pd} is the *gain factor* of the phase detector, measured in units of volts per radian. This is what we earlier called *error signal.* In the Laplace domain (7.27) writes

$$V_{pd}(s) \quad = \quad K_{pd}(\Phi_r(s) - \Phi_o(s)) \quad . \tag{7.28}$$

Transfer Function of the Loop Filter

How do we close the gap that's still open in our control loop between phase detector and VCO? Or in other words: How do we describe the loop filter, which generates the control voltage v_c from the error signal v_{pd}? As long as the loop filter does only work as a proportional controller we can define a gain factor K_{lf} for the loop filter:

$$v_c \quad = \quad K_{lf} \cdot v_{pd} \tag{7.29}$$

In the more general case, however, K_{lf} will depend also on the frequency of v_{pd}. The behaviour of the loop filter is then characterised by a complex transfer function $F(s)$:

$$V_c(s) \quad = \quad F(s) V_{pd}(s) \tag{7.30}$$

For the general case we assume a PI controller with n integrators:

$$F_{pi}(s) \quad = \quad K_p + \sum_{i=1}^{n} \frac{K_i}{s^i} \tag{7.31}$$

Including an additional non-integrative filter with transfer function $F_{hf}(s)$ leads to:

$$F(s) \quad = \quad F_{pi}(s) \cdot F_{hf}(s) \tag{7.32}$$

The loop filter is the knob, which allows further adjustment of the loop's spectral behaviour. Figure 7.11 shows an example of a type 2 loop filter. It is composed of a proportional term with $K_p = 1$, one integral term with $K_i = 2\pi$ and a low pass filter with $f_c = 1\,\mathrm{kHz}$.

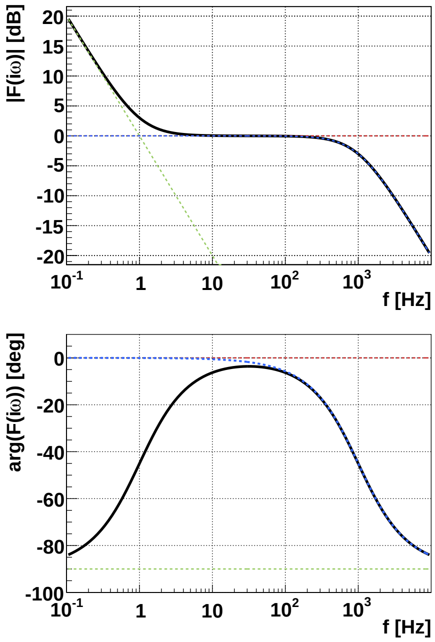

Figure 7.11.: Transfer function of a type 2 loop filter, composed of a PI controller and a low pass filter. The graphs for isolated proportional term (red), integral term (green) and low pass filter (blue) are added with dashed lines for comparison.

7.4.2. Type and Order

PLLs can basically be classified by type and order. The **type** of a PLL refers to the number of integrations. Since according to (7.24) we have already one integration in the VCO, every PLL is at least type 1. Having one or two integrators in the loop filter then results in a type 2 or type 3 PLL, while the most common PLL is a type 2. This is to be distinguished from the **order**, which refers to the number of poles of the transfer function. Every integrator within the loop contributes one pole to the transfer function. However, including an additional non-integrative filter can contribute additional poles to the transfer function, but leaves the type unchanged. Consequently the order can never be less than the type, but may be higher. According to this, the loop filter in figure 7.11 constitutes a PLL, which is type 2 but third order.

7.4.3. Open and closed Loop Transfer Function

Open loop Transfer Functions

The combined transfer function for VCO, phase detector and loop filter is called the *open loop transfer function*

$$G(s) \quad = \quad K_o \frac{K_{pd}}{s} F(s) \quad . \tag{7.33}$$

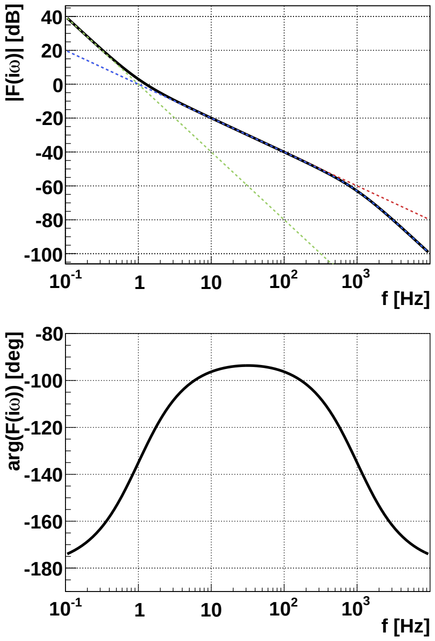

Figure 7.12.: Open loop transfer function for the loop filter from figure 7.11. Due to the factor $1/s$ from the VCO, the amplitude plot is tilted by -6 dB/octave, while the phase is shifted by -90°. The graphs for proportional term (red), integral term (green) and low pass filter (blue) are again added with dashed lines for comparison.

Figure 7.12 shows the Bode plot of $G(s)$ using the loop filter from figure 7.11. The gain factors K_o and K_{pd} only shift the amplitude plot vertically and don't affect the phase at all. For convenience we set $K_o = K_{pd} = 1$. However, the integration within the VCO contributes the additional factor of $1/s$ in the Laplace domain. This leads to a -6 dB/octave tilt in the amplitude plot and shifts the phase by -90°.

$G(s)$ relates the phase error $\Phi_e(s)$ and the output signal of the VCO $\Phi_o(s) = G(s)\Phi_e(s)$. Hence it can also be written as

$$G(s) \quad = \quad \frac{\Phi_o(s)}{\Phi_e(s)} \quad . \tag{7.34}$$

Closed loop Transfer Functions

Of course, a PLL cannot run in an open-loop condition. We can define two *closed loop transfer functions*. The **system transfer**

function relates the phase of the reference signal $\Phi_r(s)$ and the phase of the VCO:

$$\Phi_o(s) \quad = \quad H(s)\Phi_r(s) \quad . \tag{7.35}$$

It thus quantifies, how strong the phase of the reference signal is imprinted on the output signal. Therefore if $H(s)$ is high the phase of the reference frequency is transferred to the output with good efficiency and the inherent phase noise of the VCO is suppressed to a high degree. The other way round, the lower $H(s)$, the lower the transfer efficiency of the reference signal's phase to the output signal and thus the lower suppression of VCO phase noise. In this respect the **error transfer function**

$$E(s) \quad = \quad 1 - H(s) \tag{7.36}$$

suggests itself as a measure for the suppression of phase noise [30]. In terms of phases it describes the relation between $\Phi_r(s)$ and the phase error $\Phi_e(s) = E(s)\Phi_r(s)$. Making use of (7.33) $H(s)$ and $E(s)$ can be written as

$$H(s) = \frac{\Phi_o(s)}{\Phi_r(s)} = \frac{G(s)}{1+G(s)} = \frac{s}{s + K_o K_{pd} F(s)} \tag{7.37}$$

and

$$\begin{aligned} E(s) \quad &= \quad \frac{\Phi_e(s)}{\Phi_r(s)} = \frac{G(s)}{1+G(s)} = 1 - H(s) \\ &| \\ &= \quad \frac{K_o K_{pd} F(s)}{s + K_o K_{pd} F(s)} \quad . \end{aligned} \tag{7.38}$$

7.4.4. Stability Criterion

We already mentioned overcompensation and undamped oscillations, which might occur in badly configured control loops. In fact loop stability is a crucial feature of any PLL. In general, loop instabilities are a consequence of phase lag. To understand the phenomenon, we look at the phase plot of a generic PLL in figure 7.13. Naturally, the phase lag increases progressively with frequency, e.g. due to low pass filtering. Even a first order PLL sooner or later suffers from phase lag, by reason of the finite signal propagation speed within the loop (see section 7.2.3).

The crucial point is the *phase crossover frequency* ω_π (red vertical line in figure 7.13), where the phase lag exceeds 180°. This can be seen as the loop's resonance frequency, where control signals intended to compensate a phase error will go into reverse. Instead of being shifted in the opposite direction, the output phase is shifted in the same direction as the phase error. Thus, the phase error is not compensated, but on the contrary gets amplified!

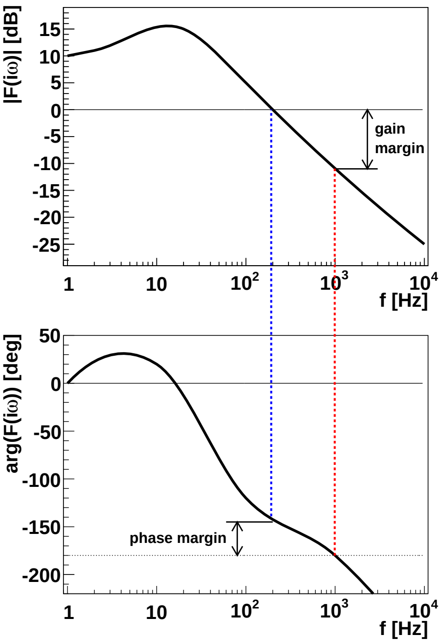

Figure 7.13.: Bode plot of a stable loop, with gain crossover frequency (blue) and phase crossover frequency (red). As long as gain crossover is left from the phase crossover in the Bode plot, the loop can be considered stable.

Every PLL would be doomed to instability if it wasn't for the gain crossover frequency ω_{gc} (blue vertical line in figure 7.13). The loop gain is greater than one for Fourier frequencies $f < \omega_{gc}$. For those frequencies the error signal is amplified within the loop. On the other hand, the error signal is not amplified for Fourier frequencies $f > \omega_{gc}$, since there the gain is smaller than one. As long as the gain crossover frequency is smaller than the phase crossover frequency, $\omega_{gc} < \omega_\pi$, no resonances within the loop will appear. Or to put it in the words of the **Bode stability criterion** [82]:

> A PLL will be stable if its phase lag at the gain crossover frequency ω_{gc} is less than 180°.

This is a very convenient criterion, since it can be evaluated just by looking at the Bode plot and has only the following restrictions:

1. The amplitude plot crosses 0 dB at only one frequency.
2. The open loop transfer function $G(s)$ is stable (no poles in the right half plane).

The damping within the closed loop is the better, the higher the phase margin

$$PM = \mathrm{Arg}(G(i\omega_{gc})) + 180^\circ \quad . \tag{7.39}$$

A PLL is stable if its phase margin is positive and unstable if its phase margin is negative. As a guide value, the phase margin should be at least +20° for stable loop operation [82].

8. The OPLL Reference Setup

The purpose of an optical phase-locked loop (OPLL) is the suppression of phase noise inherent to the lasers. Central components are a phase detector and a low phase noise frequency reference. Optical phase-locking of diode lasers has been demonstrated e.g. by Steele in 1983 [156] or Telle and Li in 1990 [164]. Meanwhile the use of OPLLs has become a state-of-the-art technique for atom interferometers [19] and has proved its worth in various experiments [23, 25, 89, 90, 14, 144].

We already gave a general description of the OPLL's mode of operation in section 7.3.1. Since the functionality of the used extended cavity diode lasers (ECDL) is important for the understanding of the OPLL, we proceed with an introduction to the laser setup in section 8.1. The phase detector and the frequency reference developed within the scope of this work are described in sections 8.2 and 8.3 respectively. First part of the characterisation of the OPLL, namely the measurement of the laser transfer function is done in section 8.4. The treatment of laser phase noise is the central point here and will be explained separatly in chapter 9.

8.1. The Laser Setup

It would be hard to imagine our modern world without diode lasers. They are one of the most uncomplicated and robust sources for coherent light, covering nearly the complete spectrum from blue to near infrared. With a ratio of output power to pumping power of in many cases above 0.5, they have a high efficiency compared to other laser types. Applications range from products of everyday life like CD players or laser pointers, over technical applications such as telecommunications, to employment at the forefront of physical research. Since they are mass-produced articles, there is a multitude of inexpensive products available. This especially applies to the manipulation of cold Rb atoms, since we benefit from CD and DVD drives being operated at 780 nm.

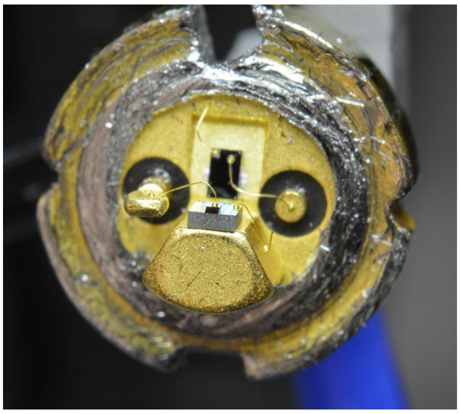

Figure 8.1.: The inner workings of a laser diode package. The actual laser diode chip is the small black box at the front. [116]

We assume an example laser diode with refractive index $n = 3.6$ (GAs) and length $l = 0.8$. The free spectral range is then given by

$$\Delta f \approx \frac{c}{2nl}.$$

Assuming furthermore a reflectivity of $R = 0.3$ for the end faces of the crystal,

$$\Delta f_{1/2} = \frac{\Delta f}{\mathcal{F}}$$

gives the mentioned linewidth, where

$$\mathcal{F} = \frac{\pi\sqrt{R}}{1-R}$$

the finesse of the optical cavity.

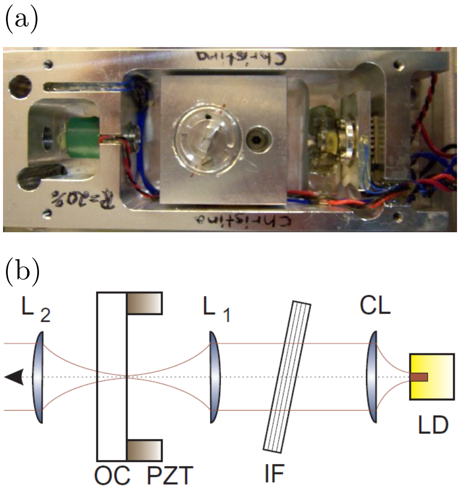

Figure 8.2.: (a) Photograph [136] and (b) schematic [84] of an extended cavity diode laser (ECDL).

An **interference filter** is formed of a series of dielectric coatings on an optical substrate with anti-reflection coating back face. The filters used at the ATLAS experiment transmit more than 90 % of the intensity at 780 nm. The fullwidth at half maximum (FWHM) of the transmission curve is chosen as 0.3 nm, which is about twice the mode spacing of our example laser diode. By varying the filter's angle of incidence between 0° and 30° relative to the optical axis, the wavelength can be coarsely adjusted from 766 nm to 785.5 nm, while the nominal wavelength of 780 nm is achieved at 6° incidence [99].

8.1.1. Laser Diodes

A laser diode is essentially just an optical cavity built around a light emitting diode. In most laser diodes — so-called *edge emitters* — the light is emitted perpendicular to the pump current from the edge of the crystal. In laser diodes emitting in the near infrared the crystal is typically made from gallium arsenide (GaAs). Due to its high refractive index the end faces of the active laser medium reflect enough light to serve as end mirrors of the optical cavity. The active volume is formed by a very thin layer on the surface of the crystal wafer, typically less than 1 μm thick. Using a defined layer structure leads to a particular linear polarisation. From the technical point of view this is advantageous, because it enables the use of polarised optics. This is of great importance for laser cooling in the magneto-optical trap and for driving Raman transitions.

Assuming typical values a laser diode has a free spectral range of about 50 GHz and a linewidth around 20 GHz. On the other hand, the band gap in GaAs allows a spectral amplification profile of several nanometers in width. Figure 8.3 shows a schematic view of the cavity modes (black) compared to the GaAs emission spectrum (yellow). If there was a substantial difference in net amplification of the cavity modes, only one mode with the highest amplification should get excited. However, since there are a lot of cavity modes fitting into the amplification profile, a free-running laser diode usually emits multi-mode. Furthermore we want the laser linewidth to be significantly smaller than the natural linewidth of the involved atomic transition — in this case ~6 MHz for the D_2 line of rubidium [155].

8.1.2. External Cavity Diode Laser

Both issues can be solved by an external cavity and an additional frequency selective element. We use external cavity diode lasers (ECDL) similar to those presented in [188, 10], but adjusted to 780 nm. A more detailed design guide can also be found in [157]. They typically provide a narrow linewidth around ~150 kHz with some 10 mW of output power [84].

The setup is displayed in figure 8.2. The laser diode LD is mounted on a Peltier element for active temperature control, since altering the temperature of the active medium changes its spectral emission profile as well as — due to change in refractive index and thermal expansion — the cavity length. The laser beam is collimated by the lense CL and passes through the interference filter IF. Compared to setups based on optical gratings, e.g. Littrow-type, the sensitivity of the laser frequency to angular alignment of the interference filter is reduced by a factor of 60 [10]. The optical cavity is completed by the outcoupling mirror OC. The outcoupling mirror is mounted on a piezo electrical element PZT to allow tuning of the laser frequency by changing the cavity length. It has a reflectivity between 0.2 and 0.4, depending on the type of laser diode. The use of common laser diodes without any anti-reflection (AR) coating, laser diodes with AR coated front facet and distributed feedback (DFB) laser diodes has been demonstrated and leads to comparable characteristics [84].

The special thing about this design is the so-called cat-eye configuration, constituted by the lenses L_1 and L_2. They have equal focal length and are mounted at a distance of twice the focal length with the outcoupling mirror being at the focus. This configuration can improve the angular alignment tolerance of the outcoupling mirror by more than two orders of magnitude, compared to the grating in Littrow-type setup [188]. An additional advantage of this design is the interference filter being separated from the outcoupling mirror, while in Littrow-type setups the grating serves as the frequency selective element and the outcoupling element at the same time. This allows independent optimisation of laser frequency and feedback.

In ray optics the **cat-eye configuration** makes the ray matrix independent of mirror tilt, which leads to the superior stability of this design. In addition the laser frequency can be adjusted by turning the interference filter without affecting the cavity alignment, since the cat eye greatly reduces the system's sensitivity to transverse displacements of the beam inside the cavity [188].

However, how does the interplay of the mentioned elements actually work? We start with the emission spectrum of the active laser medium, illustrated by the yellow line in figure 8.4. Having an external cavity of 70 mm length leads to a free spectral range of approx. 2.1 GHz. Again a lot of cavity modes (black) fit into the yellow emission spectrum, so that the laser still runs multi-mode. The interference filter fixes the allowed wavelengths to an interval of ∼30 GHz (green) [99, 147]. As a result only one cavity mode (red) gets excited, which can be tuned with both, the diode current and the piezo. If only using the piezo, the mode-hop-free range is limited to about 2 GHz to 2.5 GHz, due to overlap with the external cavity's free spectral range. However, with a combination of piezo and current tuning, a mode-hop-free tuning range of several GHz is possible.

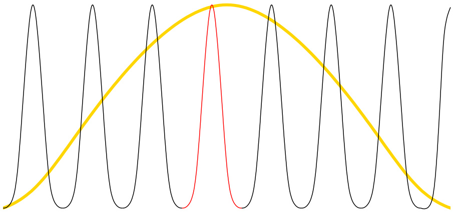

Figure 8.3.: Spectra of a laser diode without AR coated end faces: amplification profile of the active laser medium (yellow) and modes of the internal cavity (black). Not to scale!

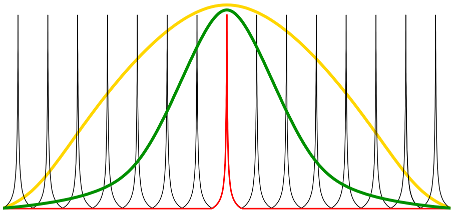

Figure 8.4.: Spectra of the active laser medium (yellow) and the external cavity (black). The free spectral range of the external cavity is significantly smaller without an additional frequency selective element, several modes would get excited. In combination with a interference filter (green) only one cavity mode is excited (red). Not to scale!

As a summary we can say, that this configuration has a superior stability, compared to grating-based ECDLs. Experiences at the ATLAS experiment showed, that with an additional temperature stabilisation for the aluminium chassis an ECDL can be run for several years without realignment. Even temporal loss of temperature stabilisation does not degrade the cavity alignment, although in some cases a realignment of the interference filter was needed.

Tapered Amplifiers

The presented ECDLs have an typical output power between 30 mW and 50 mW. Since operating a MOT or driving Raman transitions requires an overall laser output of some 100 mW, we have to amplify the laser fields using tapered amplifiers (TA). Tapered amplifiers are not too different from a laser diode with AR coated end facets. As in a laser diode, the layer structure of the semi-conductor forces a particular polarisation. Inserting light — the so-called seed light — of exactly this polarisation into the back facet induces avalanche-like emission of photons. Those photons, leaving the active medium through the front facet, have the same wavelength and phase as the seed light. To cope with the increasing light power from back facet towards the front facet, the active medium has a tapered shape like displayed in figure 8.5 (b). Thus, the power density can be kept below the damage threshold throughout the entire chip.

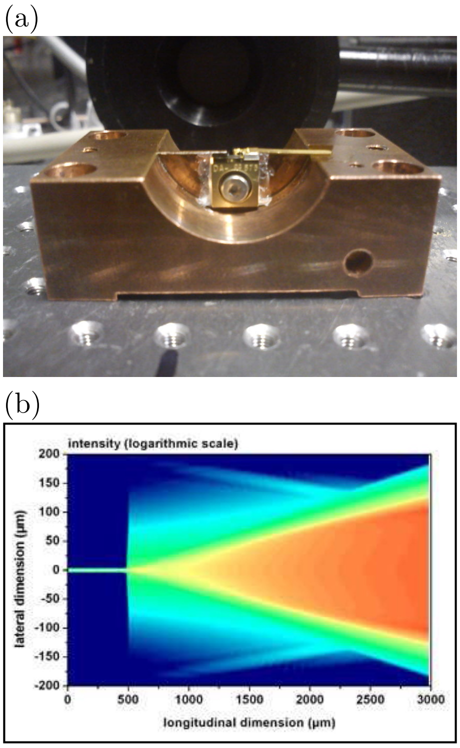

Figure 8.5.: (a) Tapered amplifier mounted to a solid copper block for heat dissipation. (b) Top view on a tapered amplifier with intensity distribution [147].

8.1.3. Master Oscillator Power Amplifier

In our setup the light from a ECDL is used as seed light for the TA. This combination of a master laser with a subsequent optical amplifier is also referred to as master oscillator power amplifier (MOPA). We often find setups using an optical fiber to connect the seed laser to the TA. Since the polarisation maintaining fiber is a single mode fiber, it acts as mode cleaner. Thus, the fiber output gives a good estimate of how much light power is actually available as seed light. Apart from that, the fiber decouples the amplifier from the master laser. Since the fiber acts like the eye of a needle, the setup in front of the fiber can be modified or even exchanged completely without affecting the beam alignment behind the fiber.

There are several possibilities of producing the two laser fields, needed for the operation of a Raman interferometer. In our reference setup, we use two disjunct ECDLs. It would be possible to combine the beams into one seed laser and amplify the combined seed light in a single TA [182]. The other possibility is to have two TAs and combine the two beams after being amplified. While the first solution allows a more compact setup, the latter one leaves a lot more flexibility and control over power, polarisation, and other parameters of the individual light fields. In either case the two laser fields are superimposed at a polarising beam splitter cube and coupled into a polarisation maintaining optical fibre. While one port of the beam splitter cube provides the light for the interferometer, the other port can be used for the optical beat detection within the OPLL. The developement of the laser system used within this thesis is well-documented in [99, 136, 109, 185, 97]. For a similar system see also [23].

8.2. Phase Detector

As the central component of our OPLL we designed a completely new phase detector board, from now on referred to as *the phase detector*. The key features are — apart from sufficient phase noise performance — a simple but efficient design, versatile applicability and inexpensive small series production. While Telle and Li [164] applied a double-balanced mixer as phase detector in their OPLL, since that time digital phase-frequency detectors have proved themselves in various experiments involving atom interferometers [19, 25, 90, 14, 144]. One advantage of digital phase-frequency detector chips is that they are applicable for both phase locking and frequency locking.

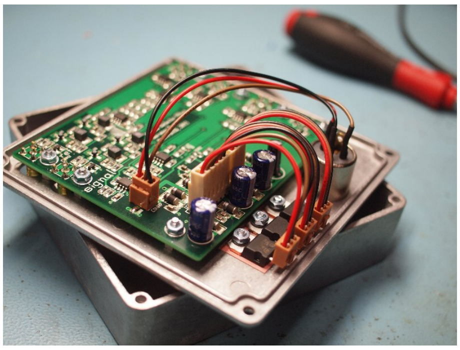

Figure 8.6.: Second generation phase detector, developed for the ATLAS experiment.

8.2.1. Phase Detector Types

There are basically two types of phase detectors [82]: multiplier circuits and sequential circuits.

Multiplier circuits In multiplier circuits the output is proportional to the product of the input amplitudes times the cosine of the phase difference between the input signals. Hence, a vanishing error signal corresponds to a phase difference of 90°. Although the output is sinusoidal, multiplier circuits have an approximately linear response in the range of small error signals, around the zero crossing of the sinusoid. One example of multiplier circuits is the double-balanced frequency mixer, also referred to as diode-ring phase detector. While the mixer is a passive device, it is also possible to design active multiplier circuits based on bipolar transistors, field effect transistors, opto-electronic devices or even mechanical switches.

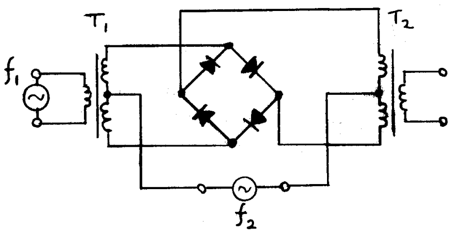

Figure 8.7.: Double balanced frequency mixer, suitable as a diode-ring phase detector. [29]

Sequential Circuits In a sequential circuit the output is a function of time between the zero crossings of the two input signals. Since it does only recognise zero crossings, other details of the waveform do not contribute to the output. Especially the amplitude of the input signals has no impact on the output signal. A drawback is, that sequential circuits are less tolerant of missing or extra crossings and thus less noise-tolerant than sequential ones. This is due to the fact, that in multiplier circuits the input waveform as a whole determines the output, while the zero-crossing itself has only minor influence. Sequential circuits are often composed of digital components like flip-flops and gates. Therefore they are sometimes called digital phase detectors. This is not to be confused with digital phase-locked loops, since the output of a digital phase detector is again an analog signal. The most important kind of sequential phase detectors is the phase-frequency detector (PFD), which will be introduced in the following section.

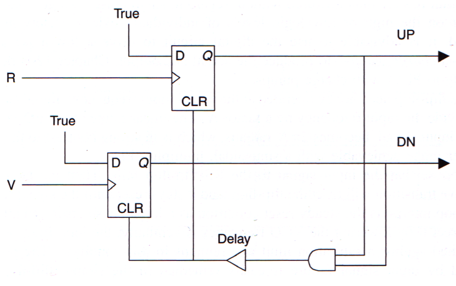

Figure 8.8.: Typical schematic of a phase-frequency detector. Taken from [82] p. 248.

8.2.2. Phase-frequency Detectors

Our *phase detector* is build around the `MCH12140` phase detector chip, which already proved suitable in [24]. It is suited for input frequencies up to 800 MHz. A phase-frequency detector has the great advantage, that it combines the functionality of a frequency-to-voltage converter and a phase detector: It generates a linear error signal proportional to the phase error, while the sign of the error signal is determined by the frequency deviation. Thus it provides also an suitable error signal for the frequency error, when the loop is not phase-locked. It can hence be applied for both, frequency and phase stabilisation.

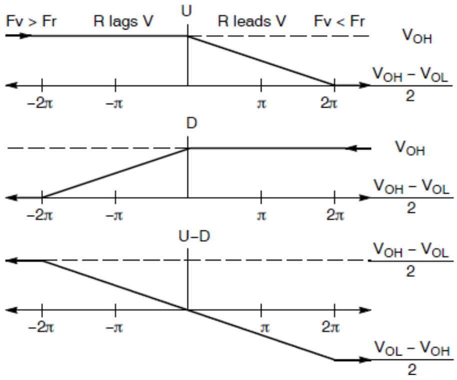

Figure 8.9.: Error signal generated by the MCH12140 chip. The duty ratios d_u, d_d and d are translated to voltage levels here. [129]

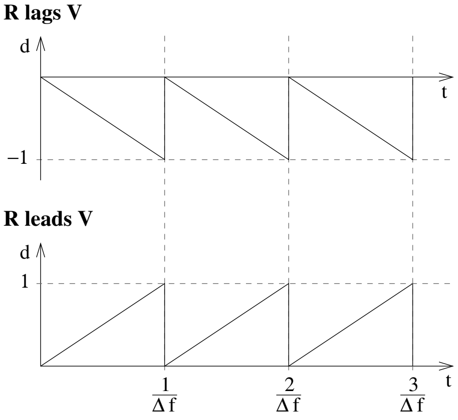

Figure 8.10.: Sawtooth-shaped output of the phase-freuqency detector if $f_R < f_V$ (top) or $f_R > f_V$ (bottom).

Figure 8.8 shows a schematic of a generic phase-frequency detector. It basically consists of two D flip-flops and a feedback circuit. The inputs are typically labeled R (for reference) and V (for VCO), the outputs are labeled U (for up) and D (for down). A zero-crossing on either R or V turns on the associated flip-flop. A following zero-crossing on the other input resets both flip-flops. Thus, a zero crossing on R followed by a zero crossing on V induces an output pulse on U, while a zero crossing on V leading a zero crossing on R turns on D for a while. The pulse on U indicates, that the VCO is lagging behind the reference signal and the frequency has to be increased. Opposed to that, the pulse on D tells the PLL to lower the VCO frequency, since it leads the reference signal. Thus, the sign of the phase error is indicated through wether output U or output D is active. The magnitude of the phase error is encoded in the pulse width. In this respect we define the duty ratios d_u and d_d, beeing the ratio of pulse width to signal period. The net duty ratio

$$d = d_u - d_d \tag{8.1}$$

is exactly proportional to the phase error. This is illustrated in figure 8.9, which shows the duty ratios d_u, d_d and d as functions of the phase error. The net duty ratio d is perfectly linear to the phase error within the interval of $[-2\pi, 2\pi]$.

However, how does frequency detection work in a PFD? We assume that the frequency at the R input f_R is slightly higher than f_V. Starting from zero phase difference V immediately lags R, activating the U flip-flop. As more and more periods evolve, the duty ratio d_u approaches 1. When the phase lag exceeds 2π, d_u drops back to zero and directly increases again. Meanwhile d_d constantly remains zero. This leads to the sawtooth-shaped output signal of the net duty ratio d, as depicted in figure 8.10. It is always positive as long as $f_R > f_V$ and always negative if $f_R < f_V$. The average duty ratio for frequency errors thus is 0.5 and -0.5 respectively. However, if $f_R \ll f_V$, several zero-crossings might occur on R before a zero-crossing on V. Since then U will remain active for several cycles of f_R, the average net duty ratio d exceeds one half [82]:

$$\bar{d} = \begin{cases} 1 - 0.5\frac{f_V}{f_R}, & f_R \gg f_V \\ 0.5\,\frac{f_R}{f_V} - 1, & f_R \ll f_V \end{cases} . \tag{8.2}$$

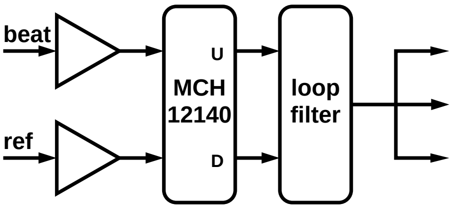

Figure 8.11.: Block diagram of the phase detector.

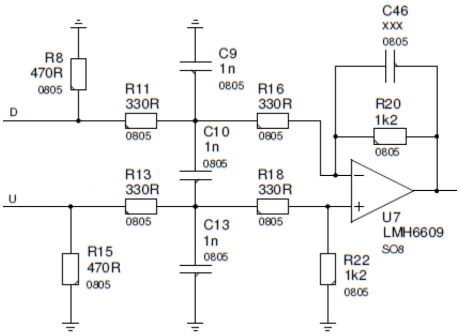

Figure 8.12.: The error signal encoded in the duty ratios of the U and the D output is converted to a DC voltage by a low pass filter followed by a differential amplifier.

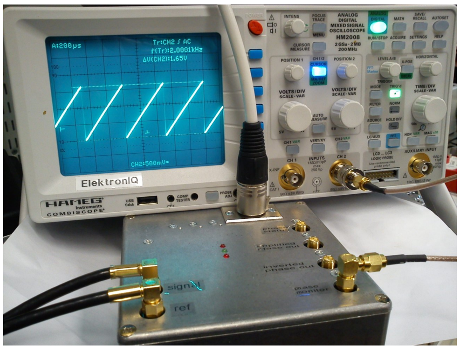

Figure 8.13.: Test setup for the phase detector using two synthesisers and an oscilloscope.

8.2.3. Layout

Figure 8.11 shows the block diagram of the phase detector. It has two inputs, corresponding to the inputs R and V of the phase-frequency detector chip. Each input provides the possibility of inserting up to two pre-amplifiers. Both input stages are identical, which allows to revert the sign of the error signal simply by swapping the inputs signals. Up to now the phase error is still encoded in the duty ratios d_u and d_d. To convert the pulsed output of the U and the D port of the `MCH12140` into a voltage, we apply the circuit from figure 8.12. Since the outputs can be interpreted as current sources, R8 and R15 are applied for current-to-voltage conversion. The pulses are averaged out by the following two-terminal low pass filter, while the differential amplifier is the technical counter piece of the minus sign in equation (8.2). The low pass filter then has a cutoff frequency of 482 kHz for common mode and 322 kHz for differential signals, as long as the inactive output of the `MCH12140` is open terminal. This is in fact the case, apart from that it is activated at zero crossings on the corresponding input. It is nearly immediately — limited only by the signal delay in inside the phase detector chip — turned off again, so that the effect is typically neglected. However, since the output is not open terminal when active, deviations of the two-terminal low pass filter's behaviour from the ideal low pass filter can not be precluded. The converted output voltage is finally distributed to three output ports; see the complete schematic and the board layout in appendix C.

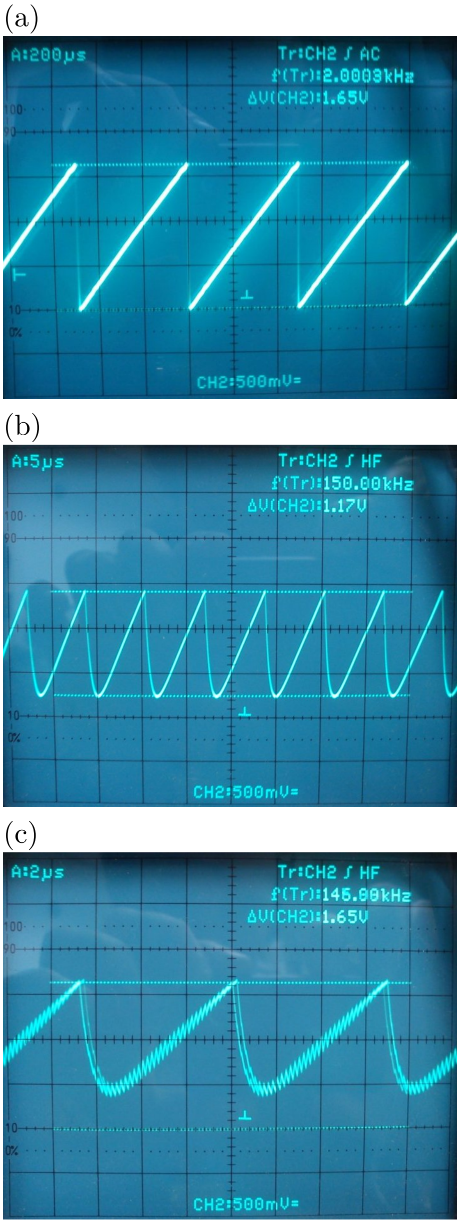

Figure 8.14.: Output of the phase detector for several operational conditions. (a) f_V = 100.000 MHz, f_R = 100.002 MHz, Δf = 2 kHz (b) f_V = 100.00 MHz, f_R = 100.15 MHz, Δf = 150 kHz (c) f_V = 5.00 MHz, f_R = 5.15 MHz, Δf = 150 kHz

8.2.4. Gain Factor K_{pd} and Transfer Function F_{pd}

A quick functional check of the phase detector can be done by using two slightly different frequencies. Figure 8.13 shows the test setup with f_V =100.000 MHz and f_R =100.002 MHz being connected to the two inputs of the phase detector and an oscilloscope connected to one of the outputs. The sawtooth-shaped error signal is also displayed in figure 8.14 (a). Its frequency corresponds to the frequency difference of the two input signals $\Delta f = 2\,\mathrm{kHz}$. The peak-to-peak voltage is $V_{pp} = 1.65\,\mathrm{V}$, which leads to the gain factor

$$K_{pd}^{DC} = \frac{V_{pp}}{2\pi} = 262\,\mathrm{mV/rad} \tag{8.3}$$

as defined in (7.5). K_{pd} is not a constant for Fourier frequencies above some tens of kHz, but is low passed by the filter from figure 8.12. Thus we have to define the full transfer function of the phase detector as

$$F_{pd}(s) = K_{pd} \cdot \frac{f_c}{f_c + s} \quad , \tag{8.4}$$

assuming a cut-off frequency $f_c \approx 322\,\mathrm{kHz}$. Figure 8.14 (b) shows, that the peak-to-peak voltage of the phase detector output in fact decreases with frequency. The lower f_c, the lower the possible bandwidth of the PLL. On the other hand, f_c can not be increased arbitrarily, but needs a careful consideration. The spike train from the `MCH12140` outputs will be in the range of the input signal frequency. Hence, we need f_c to be low enough to properly suppress the input frequency and to avoid ripples on the error signal like in figure 8.14 (c). However, ripples are sufficiently suppressed for input frequencies above 25 MHz. As the OPLL can still achieve a bandwidth of several MHz, the values of the components depicted in figure 8.12 (leading to f_c=322 kHz) can be considered a good compromise for a phase detector working at 65 MHz.

The most important characteristic of the phase detector is its inherent phase noise. This is treated separately in section 9.3.1. At this point we suffice to say, that the phase noise performance of the phase detector is by far sufficient for our purposes.

8.3. Low Phase Noise Frequency Reference

When working with the atomic isotope ^{87}Rb, the frequency difference between the two Raman lasers is 6.834 GHz, corresponding to the hyperfine transition between $|5S_{1/2}, F=1, m_f=0\rangle$ and $|5S_{1/2}, F=2, m_f=0\rangle$. Stabilising the beat of the Raman lasers at that frequency requires a frequency reference in the microwave band. Setups for that purpose have already been demonstrated in [85] and [24]. The generation of the microwave was done with an ultra-stable 100 MHz reference oscillator and a subsequent passive frequency multiplication, based on a step recovery diode. However, we want to pursue the question if the phase noise performance of the frequency reference can be improved further by utilising an active frequency multiplication. The performance of the above mentioned setups serves as the benchmark to get ahead of. With respect to the experiments of the QUANTUS family, compactness and serviceability for application in the drop tower and on sounding rockets have been specified as additional requirements.

The frequency reference for the OPLL reference setup is a combination of a 100 MHz frequency reference `Spectra Dynamics DLR-100`, a 100 MHz frequency synthesiser `Spectra Dynamics LNFS-100` and an active frequency multiplication chain `GMU69124LN`. In this section we will first of all give a technical overview over the setup and its components. The phase noise performance will be discussed in chapter 9.3.2.

8.3.1. Variable 100 MHz Frequency Synthesiser

Due to the atom's free fall during the interferometer sequence, we have account for the Doppler shift. Using contra-propagating Raman beams, it leads to a frequency shift of 25 MHz/s, or 5 MHz during 200 ms of free fall [97]. Furthermore we want to apply phase shifts to the laser phase in some measurement schemes. First-choice offering both operations is using a direct digital synthesiser (DDS) as variable frequency reference. We use the 100 MHz frequency synthesiser `Spectra Dynamics LNFS-100 OPT3`. It provides three independent DDS devices, whose output frequency can be varied between 1 μHz and 120 MHz with 1 μHz frequency resolution and 0.38 mrad phase resolution. It can be programmed via a RS 232 serial interface to perform — among other modulation functions — phase jumps and frequency shift keying. For time critical applications, like the cycle of the atom interferometer, these functions can

f	$\mathcal{L}(f)$
10 Hz	-130 dBc/Hz
100 Hz	-142 dBc/Hz
1 kHz	-150 dBc/Hz
>10 kHz	-155 dBc/Hz

Table 8.1.: Phase noise specification of the 100 MHz frequency synthesiser `Spectra Dynamics LNFS-100 OPT3` at 10 MHz output.

be triggered by an external TTL signal. For the detailed discussion of the `LNFS-100`'s phase noise properties see section 9.3.2.

8.3.2. Frequency Down Conversion

As already mentioned we have a laser beat frequency of 6.834 GHz. As a counterpart we have a phase detector suitable for frequencies up to 800 MHz and a DDS with a maximum output frequency of 120 MHz. Consequently the laser beat has to be down converted by a factor of 70. The easiest way would of course be a frequency divider. However, with respect to phase noise, down-conversion of the laser beat is equivalent to upconversion of the reference frequency. Phase noise is always referenced to the carrier frequency. To understand the conversion of phase noise during up- or down-conversion of the carrier frequency, it is easiest to treat phase noise as absolute timing jitter:

$$\delta t = \frac{\delta\phi}{2\pi f} \quad . \tag{8.5}$$

In a time interval of 5 ns a 100 MHz oscillation over-sweeps a phase of 1 mrad while a 200 MHz oscillation over-sweeps 2 mrad. The other way round, to oversweep a phase of 1 mrad at 100 MHz takes the same amount of time as 2 mrad at 200 MHz — and the same time as 70 mrad at 7 GHz. Hence the phase noise of the DDS would be multiplied by a factor of 70, corresponding to +37dB, when using a frequency divider. An alternative approach is provided by using a frequency mixer instead. We use a 6.9 GHz microwave frequency, to mix down the 6.834 GHz laser beat. The frequency mixer's output is ∼66 MHz, which can directly be compared with the DDS output. Thus, the phase noise of the DDS only contributes onefold, instead of 70-fold.

f	DLR-100	LNFR-100
1 Hz	-93 dBc/Hz	—
10 Hz	-126 dBc/Hz	-120 dBc/Hz
100 Hz	-135 dBc/Hz	-134 dBc/Hz
1 kHz	-159 dBc/Hz	-157 dBc/Hz
10 kHz	-173 dBc/Hz	-177 dBc/Hz
100 kHz	-174 dBc/Hz	-177 dBc/Hz

Table 8.2.: Phase noise specification of the 100 MHz frequency synthesiser `Spectra Dynamics DLR-100` [3] and `Spectra Dynamics LNFR-100`.

8.3.3. 6.9 GHz Microwave Generation

The 6.9 GHz generation is a combination of two devices: The commercially available `Spectra Dynamics DLR-100` 100 MHz frequency reference, followed by the custom-made device `GMU69124LN` for frequency up conversion to 6.9 GHz.

100 MHz frequency reference The `Spectra Dynamics DLR-100` contains a 5 MHz and a 100 MHz ultra-low noise ovenised oscillator, where the 100 MHz oscillator is phase locked to the 5 MHz oscillator. Thus, the phase of the 5 MHz oscillator is transferred to the 100 MHz oscillator within the bandwidth of the PLL. The 5 MHz oscillator in turn can be locked to an external reference (e.g. a MASER) to improve long term stability and phase noise at Fourier frequencies below 2 Hz (default PLL bandwidth of the reference input). The `DLR-100` is a version of the `Spectra Dynamics LNFR-100` (not listed separately in the catalogue), optimised for low phase noise at Fourier frequencies up to 100 Hz. It was also used as reference for the passive frequency multiplication in [85]. The phase noise specifications of both devices, the `DLR-100` and the `Spectra DynamicsLNFR-100` is listed in table 8.2. It provides three outputs at 100 MHz and one additional output at 10 MHz. It also serves as reference for the variable 100 MHz synthesiser.

Frequency Multiplication The 6.9 GHz microwave reference is generated within the `GMU69124LN`. It contains an 100 MHz oscillator `Pascall OCXOF` and a subsequent frequency multiplication, composed of several frequency mixers. The exact combination of mixers can be gathered from the block diagram in appendix F. To obtain the best phase noise performance in all frequency bands, we apply the same technique was already used internally in the `DLR-100`. The `OCXOF` is locked to the 100 MHz signal of the `DLR-100` with a bandwidth of 1 kHz. This was chosen with respect to the `Spectra Dynamics DLR-100`, whose phase noise is lower at Fourier frequencies below 1 kHz, than that of the `OCXOF`. Thus, the phase of the `DLR-100` is transfered to the `OCXOF` for Fourier frequencies below 1 kHz. For Fourier frequencies above 1 kHz, we benefit from the phase noise performance of the `OCXOF`, which is superior to the `DLR-100` in that frequency band. In this constellation, the `GMU69124LN` and the `Spectra Dynamics DLR-100` are combined in a complementary way, to provide low phase noise over the whole Fourier spectrum up to 100 kHz.

f	DLR-100	GMU69124LN
10 Hz	-88 dBc/Hz	-85 dBc/Hz
100 Hz	-104 dBc/Hz	-100 dBc/Hz
1 kHz	-114 dBc/Hz	-125 dBc/Hz
10 kHz	-135 dBc/Hz	-135 dBc/Hz
100 kHz	-135 dBc/Hz	-138 dBc/Hz

Table 8.3.: Phase noise specification of the 100 MHz frequency synthesiser `Spectra Dynamics DLR-100` transfered to 6.9 GHz and the 6.9 MHz frequency generation `GMU69124LN`. The values for the `GMU69124LN` assume that it is locked to the `DLR-100`.

8.4. OPLL Reference Setup

The purpose of our OPLL setup is the suppression of phase noise on the relative phase between a pair of lasers. Or in other words: The purpose of the OPLL setup is to transfer the phase of a reference frequency with superior phase noise properties to the laser phase. What does *superior* mean in this context? While for now

We will refer to the relative phase between the two lasers as the **laser phase**.

its sufficient to consider *superior* just qualitatively as *being much better than the lasers*, we will discuss it quantitatively in chapter 9.

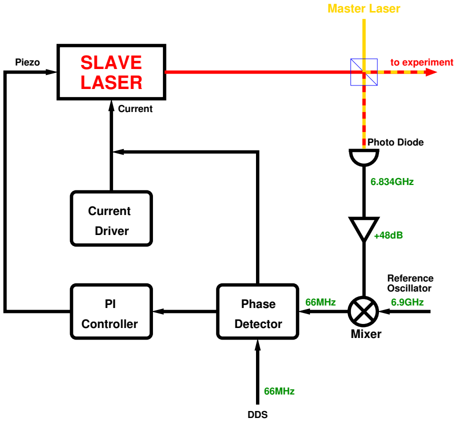

Figure 8.15.: Block diagram of the OPLL reference setup used within this thesis.

All OPLL measurements in this chapter and in chapter 9 were performed with the *reference setup* depicted in figure 8.15. It features two lasers, the *master laser* and the *slave laser*. While the master laser may be stabilised on a spectroscopy, on a reference laser or even be free running, the slave laser is the one controlled by the OPLL. Both lasers are superimposed on a polarising beam splitter cube. One part of the combined laser light is available for application in the atom interferometer. The other part is focused on a ultrafast GaAS photodetector `Hamamatsu G4176`, where the optical laser beat is transduced to an electrical signal. The photodetector is supplied with a bias voltage of 9 V via a bias-tee, which is not depicted in the figure. Fully exploiting the maximum allowed input power of 5 mW for CW light, typically yields a signal between -35 dBm and -30 dBm. To avoid continuous operation of the photo diode at absolute maximum ratings, it was typically operated at a beat power of -40 dBm. Since this is far too low for the phase detector, the signal is amplified by +48 dB in a low-phasenoise amplifier `AML67P4801`.

The reference setup is designed for use with the atomic isotope ^{87}Rb. Hence, the frequency difference between master and slave laser and thus the beat frequency is 6.834 GHz. To provide a signal that can be processed by the phase detector, the beat signal is mixed down with a reference frequency (6.9 GHz, 13 dBm) in a double balanced frequency mixer `Minicircuits ZMX-7GR`. With a conversion loss of typically 5 dB this yields between 5 dBm and 10 dBm for the mixed down signal at 66 MHz. It should be noted, that in principle also a lower signal power could be processed by the phase detector if the pre-amplifiers are configured appropriately. Finally, a variable frequency synthesiser `Spectra Dynamics LNFS-100` provides the reference frequency connected to the second input of the phase detector. The frequency down conversion using a mixer and the segmentation of the frequency reference to fixed reference frequency at 6.9 GHz and variable frequency around 66 MHz is mainly due to phase noise considerations. See section 9.3.2 for a detailed discussion.

As already discussed in section 7.3.1, the error signal v_e is distributed into two paths, the piezo path and the current path. In the piezo path we use a PI controller, configured to compensate DC offsets and long term drifts only. It was specifically designed for the use with ECDL lasers and is low passed with a cut-off frequency

f_c =800 Hz. Faster fluctuations are compensated by modulating the laser diode current. For the reference setup we intentionally stay with a zero order loop filter, featuring only a proportional term K_p. This simplest of all PLLs is a good starting point for the analysis of the loop, on whose basis an optimised (higher order) loop filter can be designed. It is implemented by the incoupling circuit shown in figure 8.16. The potentiometer R allows the adjustment of K_p. Since DC components of the error signal are compensated with the piezo path, the control signal is AC coupling to the laser current by means of the capacitor C_2. This prevents the phase detector from provoking mode hops of the laser, when the loop is not in lock. On the other end, the inductor L prevents the high frequency control signal from being back coupled into the laser diode driver. While the voltage from the laser diode driver is always positive, the control signal v_c coming from the loop filter is either positive or negative. The protective diode D keeps the net voltage from beeing too negative and thus protects the laser diode LD against being damaged by a reverse current.

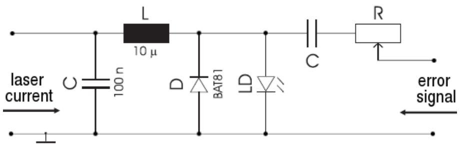

Figure 8.16.: Schematic of the incoupling circuit used to modulate the OPLL control signal onto the laser current.

8.4.1. Comissioning and Performance Check

The comissioning of the OPLL reference setup using a spectrum analyser is quite simple: The first step is to stabilise the laser frequency using the PI controller connected to the piezo. If the laser is frequency-locked, the second output of the phase detector can be connected to the incoupling circuit. Now the loop gain K_p has to be adjusted until a beat signal similar to that in figure 8.17 (a) shows up on the spectrum analyser. This is the power spectral density of the laser beat signal. It was shifted to the left by the carrier frequency so that the frequency axis shows the frequency offset from the carrier. The power is normalised to the carrier power, yielding units of decibel relative to the carrier (dBc). Different from the transfer function plots in chapter 7, which were one-sided spectral densities, this is a two sided spectral density. However, it can easily be transformed into a single-sided spectral density, by turning the negative negative semi-axis over to the positive semi-axis. Provided a symmetric noise distribution around the carrier, the resulting one-sided power spectral density is two times — +3 dB on the decibel scale — the two-sided power spectral density. However, we will stay with the two-sided display at this point, since that is what we see on the spectrum analyser.

The power spectral density as measured with a spectrum analyser is typically indicated in units of dBm/Hz. This is the power within a frequency interval of 1 Hz, normalised to a reference power of 1 mW and converted to a logarithmic scale:

$$S_{\text{dBm}} = 10 \log_{10} \left(\frac{S_{\text{mW}}}{1\,\text{mW}} \right) \text{dBm/Hz}$$

When analysing the noise in the edges of the carrier, it is useful to quantify the noise relative to the carrier. It is thence not normalised to 1 mW anymore, but to the carrier power, and is indicated in **decibels relative to the carrier (dBc)**:

$$S_{\text{dBc}} = 10 \log_{10} \left(\frac{S_{\text{mW}}}{P_{\text{carrier}}} \right) \text{dBc/Hz}$$

Under certain conditions the noise level in this plot is directly related to the phase noise power spectral density, as we will see in section 9.1.4. Thus we aim for a noise suppression as good as possible. To get a basic understanding for the influence of the loop gain, we look at the three additional plots with different values of K_p in figure 8.17 (b): With a low value of K_p (red), the overall loop gain decreases. The suppression of noise diminishes and the noise level near the carrier increases. On the other hand, if going to a high value of K_p (dark blue), the loop gain increases and noise suppression near the carrier gets better. While K_p increases we also see two resonance peaks arising near the gain crossover frequency, between 2 and 3 MHz from the carrier. This gets clear, when remembering the Bode stability criterion from section 7.4.4. Increasing K_p raises the loop gain for all Fourier frequencies. Thus, it shifts the gain crossover frequency to higher values. Since simultaneously the phase margin decreases, we get closer and closer to a resonance condition. If finally the gain crossover frequency exceeds the phase crossover frequency — the gain margin is negative now — the loop becomes unstable. We see a strong oscillation at the phase crossover frequency and strong increase of noise near the carrier (light blue).

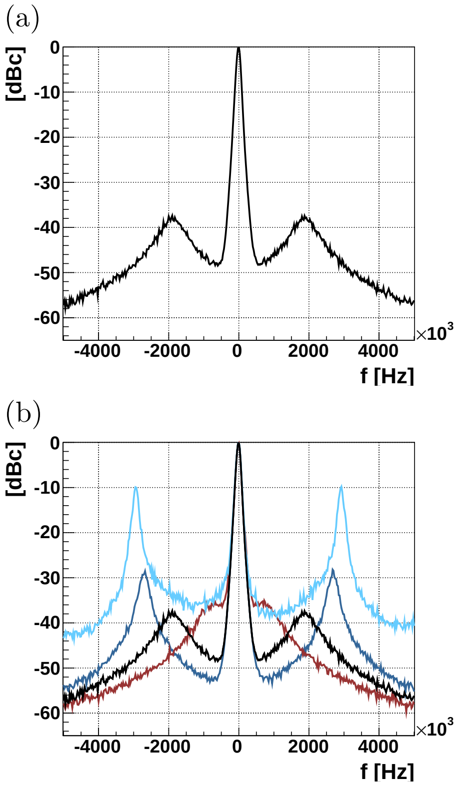

Figure 8.17.: (a) Two-sided power spectral density of the laser beat signal, measured with a spectrum analyser `Agilent E4405B`. (b) Laser beat signal with different settings of K_p: Low (red), medium (black), high (blue), too high (light blue).

This shows already the limitations of the first order PLL: It has only one adjustable parameter, K_p, which influences the loop gain for all Fourier frequencies. Increasing the noise suppression at lower Fourier frequencies does also increase the gain crossover frequency and thus leads to undamped oscillations. Corrective actions will be discussed in section 8.5.1. However, the setup has proven to be easy to implement, fail-safe to high degree and might even be considered *plug-and-play*. Despite its limitations, it has a phase noise level, which is quite sufficient for basic atom interferometer operation (see chapter 9) since it is significantly below vibration induced phase noise [97].

8.4.2. Some Remarks on Control Bandwidth

Before proceeding with the analysis of the OPLL, we should spend some clarifying lines on the term *control bandwidth*, which is often used in a misleading way. We define the control bandwidth of a OPLL as the Fourier frequency up to which the OPLL is able to suppress noise. It should be stressed that the control bandwidth is not identical to the frequency offset of the resonance peaks to the carrier! These peaks occur due to resonance near the loop's natural frequency, when increasing the loop gain K_p. The noise power level around the resonance peaks is higher than that of the free running laser. This is clearly visible in figure 8.17 (b), where the black curve has a lower noise level near the carrier than the red curve, but a higher noise level at the resonance peaks. Following the definition above, the resonance peaks are obviously outside the control bandwidth. It is not possible to extract a precise value for the control bandwidth from figure 8.17, since it is not possible to measure a power spectral density of the laser beat when the lasers are not locked. Nevertheless, the control bandwidth is correlated to the position of the resonance peaks. If the resonance peaks move outwards, also the bandwidth within which noise is suppressed increases. In the setup used for the plots in figure 8.17 the control bandwidth is limited by signal propagation delay. The setup contains 5 m of cables and 65 cm of free space between laser and photodetector. Assuming an inverse signal velocity of 3 ns/m for laser light and 5 ns/m for electrical signals we get a delay of δt=27 ns. At 3 MHz this already yields an additional phase lag of

$$\Delta\phi \quad = \quad 2\pi f \delta t = \frac{2\pi\delta t}{T} = 32^\circ \quad , \tag{8.6}$$

not including delays caused by operational amplifiers and other electronic components. Having the resonance peaks at e.g. 6 MHz, like demonstrated in [14], is only possible with a setup optimised for small signal propagation delay. That is to say, components being arranged together as close as possible and cables being as short as possible.

After all, control bandwidth is not our major concern. The crucial parameter for the performance of the atom interferometer is noise suppression. However, control bandwidth is not a valid measure for the suppression of phase noise. As we will see in section 9.2, we need noise being suppressed up to 100 kHz only. Thus, even the bandwidth of an OPLL not optimised for low signal propagation delay is sufficient straightaway. Can information on noise suppression be extracted from the spectrum analyser's signal at all? We look again at the dark blue line in figure 8.18. The noise suppression level near the carrier is obviously better than 50 dB. Unfortunately, this plot doesn't help evaluating the suppression of phase noise, since the noise floor at -50 dBc is limited by the inherent noise of the spectrum analyser. Hence, it does not represent the actual noise suppression, but can only give an upper bound. Furthermore the minimal resolution bandwidth of the spectrum analyser is 10 kHz. That means, for Fourier frequencies below 10 kHz the plot does not provide any information at all. Hence, we will introduce another method for the quantification of phase noise in chapter 9.

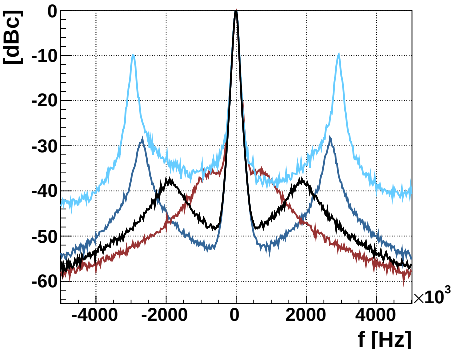

Figure 8.18.: Replication of figure 8.17 (b).

8.5. Theoretical Model of the OPLL's Transfer Function

As was already mentioned, the performance of the zero order OPLL is sufficient for now, since vibrations are much stronger [97]. However, laser phase noise might become the limiting factor for the interferometer's sensitivity, when other noise sources are eliminated. To analyse the potential for improvement, we need to know the OPLLs actual open loop transfer function $G(s)$. Setting up a Laplace representation of the OPLL and all its individual components will enable us to make a statement about how good the loop suppresses disturbances at specific frequencies. Knowing $G(s)$ thus also allows a concerted modification of the loop filter.

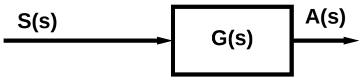

Figure 8.19.: Direct measurement of the open loop transfer function $G(s)$, while the loop is open. This is not possible with our OPLL, since the loop is in a non-linear state if not locked.

8.5.1. Measurement of the Open Loop Transfer Function

Since we have no knowledge about the laser's frequency and phase response, the only way of obtaining the open loop transfer function is to measure it. Usually we would perform a direct measurement by opening up the loop and connecting it to a network analyser (see figure 8.19). The network analyser's source output $S(s)$ would be connected to the opened loop and the loop output $A(s) = S(s) \cdot G(s)$ fed back to the network analysers measurement input. The open loop transfer function then simply is $G(s) = A(s)/S(s)$. Unfortunately the loop has to be in a linear state during this measurement. That is, the laser has to be phase-locked and that again means, the loop has to be closed. Hence, the direct measurement scheme cannot be used. To measure $G(s)$ while the loop is closed and locked, we apply an indirect measurement scheme [98]. By means of figure 8.20 (a), we immediately see that

$$
\begin{aligned}
B(s) &= S(s) + A(s) \quad \text{and} && (8.7)\\
A(s) &= G(s) \cdot B(s) \quad . && (8.8)
\end{aligned}
$$

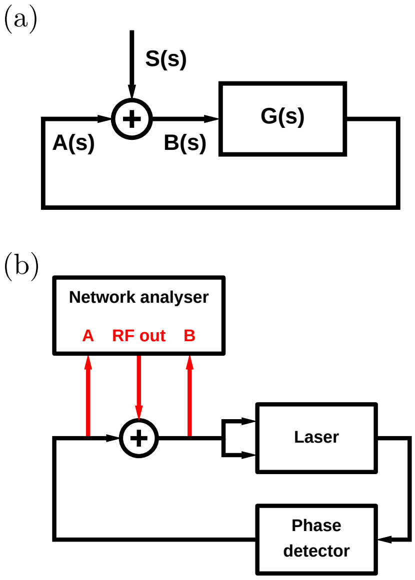

Figure 8.20.: (a) Indirect measurement of the open loop transfer function $G(s)$, while the loop is closed and locked. (b) Setup using a the network analyser in combination with the adder circuit from appendix E.

This yields

$$G(s) = \frac{A(s)}{B(s)} \quad . \qquad (8.9)$$

It can be measured with the network analyser, using the setup from figure 8.20 (b). In doing so, the output signal of the network analyser has to be electrically added to the control signal. Combination and distribution of the signals is done using the adder circuit from appendix E, provided by Tobias Eberle, Albert Einstein Institut Hannover.

The network analyser `HP4395A` can directly output a Bode plot for A/B. The result is depicted in figure 8.21. During the measurement the output power of the network analyser's source was set to $P_s = 5$ dB. Unfortunately it was not possible to find a value for P_s applicable for the complete frequency band. At frequencies below 10 kHz the signal is on the edge the network analyser's sensitivity range. This leads to a noisy amplitude signal, while the phase signal isn't significant at all. Increasing the source power P_s yielded a clear signal, but unfortunately drove the OPLL into a nonlinear state. Such a signal does not represent the actual behaviour of the locked OPLL.

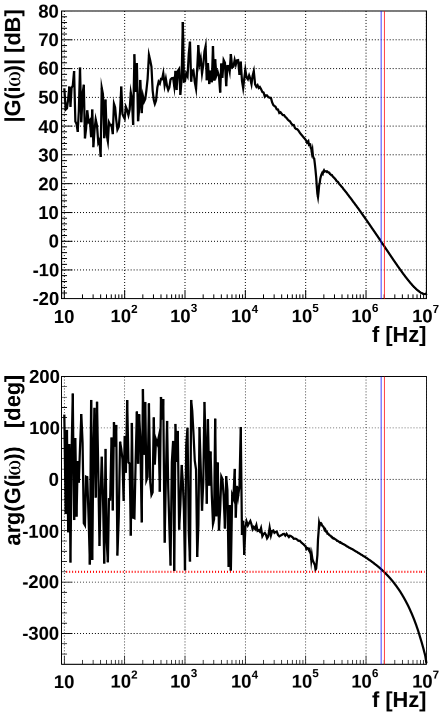

Figure 8.21.: Open loop transfer function of the OPLL reference setup, measured with the setup from 8.20 (b). With the chosen setting of K_p the gain crossover frequency (blue vertical line) and the phase crossover frequency (red vertical line) are very close together.

To understand the shape of the signal in figure 8.21, we will now setup a model of the open loop transfer function. Moreover, this will enable us to simulate the impact of different loop filter designs on the OPLL's performance. The theoretical model developed on the following pages was implemented in `Mathematica`. The complete script can be found in appendix D.

Unfortunately, we do not know the exact amplitude and phase characteristic of all components within the loop. However, we can at least perform a subtle guess. The main difference to the generic open loop transfer function 7.33 is, that we now have two parallel control paths:

$$G(s) = K_{beat} F_{pd}(s) \left[F_{pi}(s) F_{pzt}(s) + K_{p2} F_{cur}(s) F_{\delta} \right] . \tag{8.10}$$

Starting with the optical beat, we assume the photo detector to be completely linear, since the Fourier interval of interest (<10 MHz) is small compared to the absolute frequency (∼6.8 GHz). The photo detector thus contributes only with a proportional factor K_{beat}. The second device on our way through the control loop is the phase detector

$$F_{pd}(s) = K_{pd} \cdot \frac{f_c}{f_c + s} \tag{8.4}$$

with $f_c \approx 322$ kHz. Afterwards the signal splits up into a term for the piezo path, $F_{pi}(s)F_{pzt}(s)$, and a term for the current path, $K_{p2}F_{cur}(s)F_{\delta}$. Since the output of the PI controller in the piezo path is low passed with $f_c = 800$ kHz, its transfer function is

$$F_{pi}(s) = (K_p + \frac{K_i}{s}) \frac{f_c}{f_c + s} , \quad \text{with } f_c = 800\,\text{Hz} \quad . \tag{8.11}$$

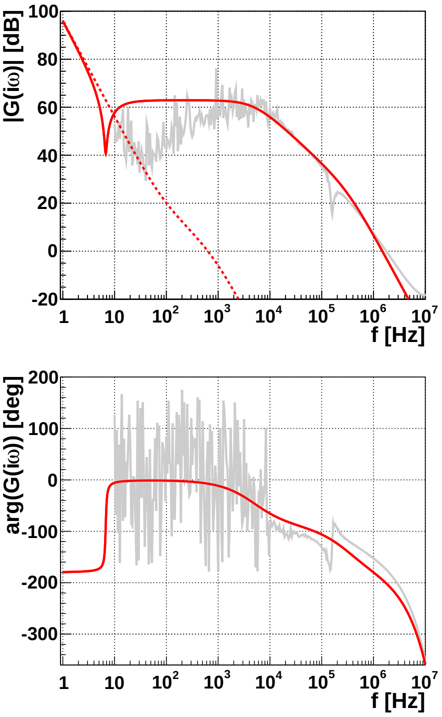

Figure 8.22.: Theoretical model of the open loop transfer function $G(s)$ (function `G[s_]` in appendix D). The measured open loop transfer function from figure 8.21 is plotted in gray.

We assume, that the control voltage for the piezo is translated linearly into change of the cavity length and thus into a frequency shift. The laser transfer function for the piezo path then is

$$F_{pzt} \quad = \quad \frac{K_{pzt}}{s} \quad . \tag{8.12}$$

The contribution of the piezo path is represented by the dashed red line in figure 8.22. This yields the -6 dB/octave slope in the amplitude plot below 400 Hz.

Some more thoughts have to be spend on the current path. The first order loop filter contributes with a proportional factor K_{p2} only. At the set point the laser diode has a resistance of $R_{ld} \approx 20\,\Omega$. Since the control signal in the current path is small compared to the laser diode current, we treat the laser diode as ohmic load. Together with the capacitor, $C = 1\mu$F, in the incoupling circuit it forms a high pass filter with 5 kHz cutoff frequency:

$$F_{cur}(s) \quad = \quad \frac{s}{f_c + s} \quad \text{with } f_c = 5\,\text{kHz} \quad . \tag{8.13}$$

Considering Fourier frequencies in the MHz regime, we have to include signal propagation delay

$$F_\delta = e^{-2\pi s \cdot \delta t} \quad . \tag{8.14}$$

As was pointed out in section 8.4.2 there is already 27 ns delay in cables and by free laser propagation. To account also for delay in the electronic components, we initially assume a overall delay of $\delta t = 50\,$ns. With this assumptions the overall open loop transfer function $G(s)$ results in the red line in figure 8.22. The plot already gives a good approximation for amplitude and phase at Fourier frequencies above 10 kHz, but it does not explain the data below 10 kHz. To improve the consistency with measured data, we apply the following corrections to our model, with result plotted in figure 8.23:

1. Obviously there is another part contributing high pass behaviour, supposedly originating from parasitic capacitances of the laser diode. Hence we multiply a high pass term $F_{hp}(s)$ with cutoff frequency of 800 Hz to the open loop transfer function $G(s)$. The green plot in figure 8.23 shows, that the corrected $G(s)$ does now fit to the 6 dB/octave slope between 40 Hz and 1 kHz.

2. The data shows a dip at 160 kHz. It has been traced back to the incoupling circuit, depicted in figure 8.16. The inductor

L and the capacitor C have to be considered a series LC circuit, dissipating some of the control signals power. Using the actual values, $C = 1\,\mu\text{F}$ and $L = 1\,\text{mH}$, leads to a resonance frequency of 160 kHz. This is exactly the frequency of the dip observed in the data. The amplitude and phase response can be reproduced by including a notch filter $F_{notch}(s)$ into the theoretical model. Although the dip does not affect the phase noise performance of the OPLL reference setup, it could be removed by inserting additional resistors between inductor L and capacitor C.

3. Finally we can achieve a better consistency with the data above 100 kHz by slightly changing the high-frequency behaviour of the phase detector; i.e. replacing the low pass filter in the phase detector's transfer function (8.4) with a lead-lag network

$$F_{pd}(s) \quad = \quad K_{pd} \cdot \frac{1 + s/f_l}{1 + s/f_h} \quad . \tag{8.15}$$

   The corner frequencies are $f_l = 322\,\text{kHz}$ and $f_h = 2\,\text{MHz}$. Best fitting of the high frequency behaviour was achieved with signal propagation delay increased to $\delta t = 75\,\text{ns}$.

The corrected open loop transfer function finally reads

$$\begin{aligned} G(s) \quad = \quad & K_{beat} F_{pd}(s) \left[F_{pi}(s) F_{pzt}(s) \right. \\ & \left. + K_{p2} F_{cur}(s) F_{hp}(s) F_{notch}(s) F_{\delta} \right] \quad . \end{aligned} \tag{8.16}$$

However, as the modifications in item 2. and 3. take effect way above 100 kHz it does not affect the phase noise performance of the atom interferometer, but essentially serve as a sanity check.

8.5.2. Closed Loop Transfer Function

Now that we have a theoretical model of our OPLL, we can calculate the closed loop transfer function $H(s)$ and the error transfer function $E(s)$. Figure 8.24 shows an amplitude plot of $E(s)$, derived from the open loop transfer function plotted in figure 8.23. Since $E(s)$ is the measure for the suppression of inherent laser phase noise, we will use it again in section 9.4.

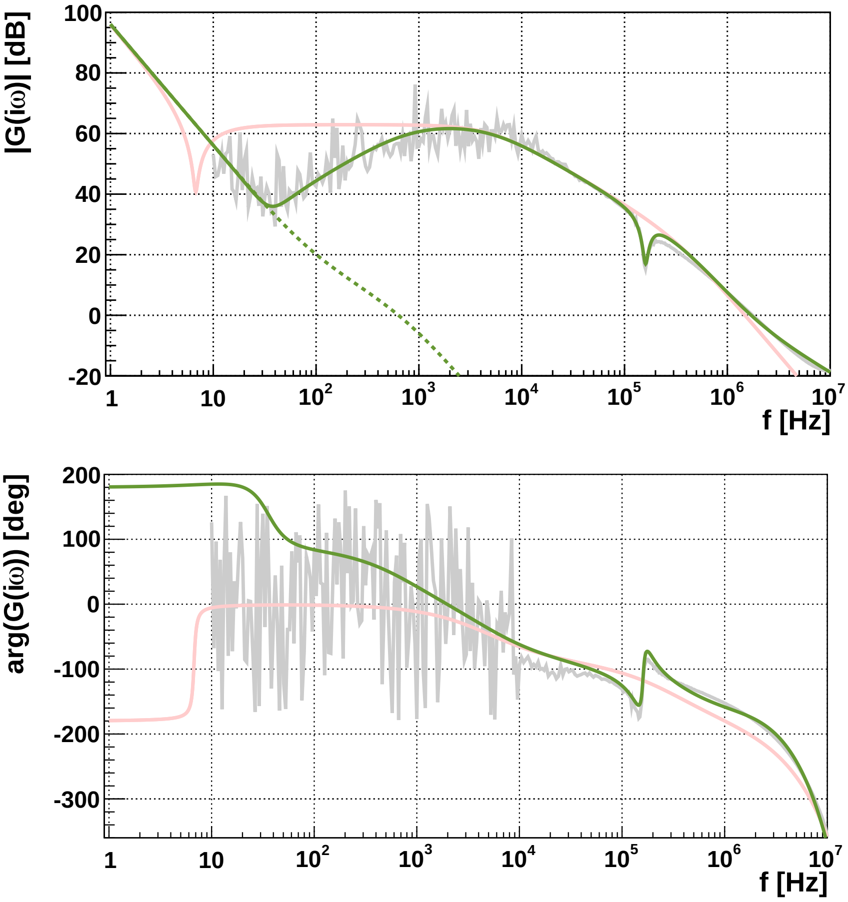

Figure 8.23.: Introducing some modifications into the theoretical model of the open loop transfer function $G(s)$, allows reproducing the measured data (function `GC2[s_]` in appendix D). The unmodified version from figure 8.22 and the measured open loop transfer function from figure 8.21 is plotted palish.

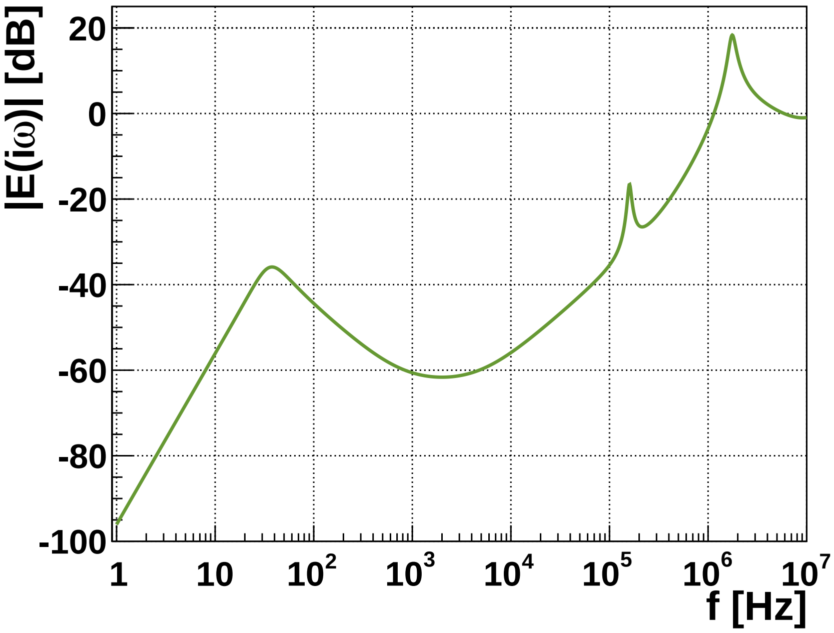

Figure 8.24.: Theoretical model of the error transfer function $E(s)$ (function `ErC2[s_]` in appendix D), derived from the open loop transfer function $G(s)$ as plotted in figure 8.23.

9. Suppression of Laser Phase Noise

The purpose of the OPLL setup is the suppression of phase noise on the relative phase between a pair of lasers. Or in other words: The purpose of the OPLL setup is to transfer the phase of a reference frequency with superior phase noise properties to the lasers. When using the phase detector for frequency and phase stabilisation, the laser beat is compared to a frequency reference. Thus the phase detector will transfer any phase noise present in the frequency reference to the laser. For the MOT lasers, where phase stability is not required, the reference frequency can be delivered by a simple synthesiser or even a voltage controlled oscillator. However, the requirements on phase stability of the Raman lasers demand for an ultra-stable reference oscillator, optimised for low phase noise.

Before discussing the phase noise performance of the OPLL reference setup, there are some basic questions:

- What is phase noise?
- What is its impact on the atom interferometer?

These questions will be answered in sections 9.1 and 9.2, respectively. The low phase noise reference frequency will be described in section 8.3. In section 9.3 we will finally measure the phase noise of the OPLL reference setup. We will identify the noise contributions of the different OPLL components and suggest some possibilities for optimization.

9.1. What is Phase Noise?

This section gives a short introduction into the vocabulary of noise, essentially inspired by [30, 104]. We will learn how noise can be characterised and what are the measures to quantify noise.

9.1.1. What is Noise?

Noise, sometimes called *jitter*, is a random process. Thus it is un-

Although noise is a **random process**, we often have to face also non-random perturbations. This might be 50 Hz line noise or other cross feed with discrete frequency. However, also longtime drifts with periodic pattern on the timescale of seconds, minutes or hours might disturb precision measurements. Those autocorrelated perturbations can be identified using two-sample variances, also known Allan variance. Some examples, where periodic longterm drifts in the CAPRICE atomic gravimeter have been identified can be found in [97].

correlated per definition. An example from nature is the sound of a waterfall. The innumerable number of water drops create a sound, whose frequency spectrum is that broad that no specific pitch could be identified. These processes can no longer be described analytically, but by statistical methods only. That is, the exact value of a noisy voltage U can not be predicted, but we can identify some characteristics: the stochastic distribution of occurring frequencies and the amplitude characteristic.

Frequency Distribution To specify the frequency distribution, different kinds of noise are assigned different *colors*. **White noise** is uniformly distributed over all frequencies. The frequency characteristic is hence $1/f^0 \equiv 1$. **Pink noise** is noise with a $1/f$ characteristic. It has some characteristics worth mentioning: The carried energy is equal in every octave, so that the 100-200 Hz band has equal total noise power as the the 1-2 kHz band. The noise power spectral density decreases at 3 dB/octave. Thereby, the frequency characteristic is complementary to the sensitivity of the human ear and appears equally loud over all frequencies. Sometimes, the term pink noise is also found in a more general sense for noise with $1/f^\alpha$ frequency distribution. Also in use is the term **red noise**, which refers to $1/f^2$ noise. However, our primary concern is, wether noise has a flat frequency distribution or not. Also in time-domain the mentioned noise colours can be distinguished, as can be seen in figure 9.1.

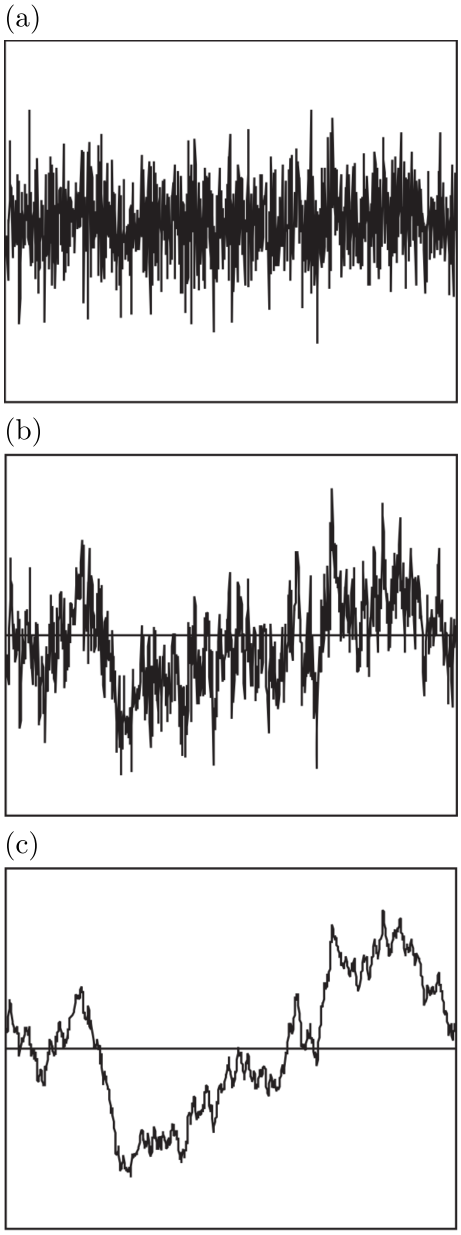

Figure 9.1.: Time-domain signal (amplitude over time with arbitrary units) of (a) white noise with flat spectrum, (b) pink noise with $1/f$ spectrum and (c) red noise with $1/f^2$ spectrum. [135]

9.1.2. Power Spectral Densities & Decibels

Although it is possible to specify the total noise power, this is in many cases not very helpful. If we want to evaluate noise, we need to know the noise intensity as a function of Fourier frequency. At that point we can apply the concept of power spectral densities. This is basically the information of how much noise is in a 1 Hz Fourier interval. It usually has dimensions of power per Hertz or energy per Hertz. For electrical signals this is either W/Hz or V^2/Hz. Similarly, also the fluctuation of a phase measured in $\mathrm{rad}^2/\mathrm{Hz}$ results in a power spectral density. Sometimes the amplitude spectral density is used, which is the square root of the power spectral density in units $\mathrm{V}/\sqrt{\mathrm{Hz}}$ and $\mathrm{rad}/\sqrt{\mathrm{Hz}}$. However, we will stay with power spectral densities.

With a spectrum analyser the power spectral density can often not be measured in a 1 Hz frequency interval, but the bandwidth is determined technically. The bandwidth used in the measurement is called the resolution bandwidth (RBW). When processing measured data, we have to take care wether it is referenced to the resolution bandwidth or the spectrum analyser has already converted it to a 1 Hz bandwidth. Furthermore it is noticeable that spectrum analysers usually don't have rectangular window functions, to fix the measurement band. However, there is such a large quantity of window functions — Blackman, flat top, Hamming, Hanning, to name only a few — that we have to consult the spectrum analyser's manual if the kind of window function has to be considered during data analysis.

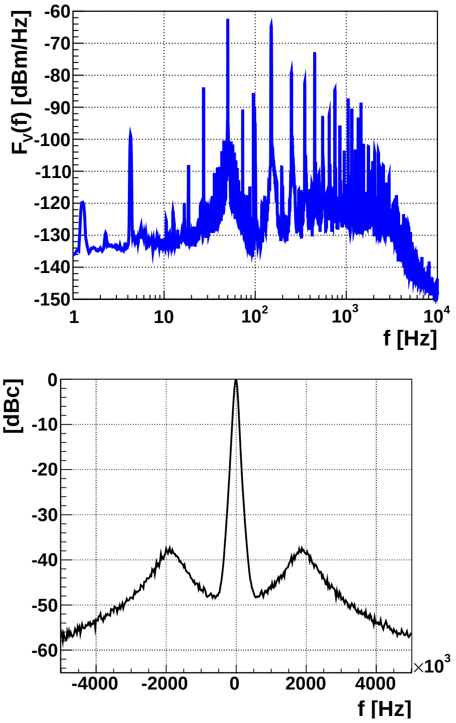

Figure 9.2.: One-sided (top) and two sided (bottom) noise power spectral density.

One-sided and two-sided Power Spectral Densities

Figure 9.2 shows two examples of power spectral densities. We can spot a noticeable difference in the frequency axis: The black plot (bottom) is a two-sided spectral density. It is defined for Fourier frequencies $-\infty < f < \infty$, so that the frequency axis extends to both the positive and negative side of the frequency spectrum. This is used, when the signal is a wave at a certain frequency. In figure 9.2 the x-axis has been shifted such that the carrier is at $f = 0\,\mathrm{Hz}$. The Fourier frequency f thus determines the distance from the carrier. The blue plot (top) is a noise spectrum without a carrier signal being present. It is a a one-sided power spectral density, which is only defined for Fourier frequencies $0 \leq f < \infty$. Provided the noise spectrum is symmetrical around the carrier, the two-sided power spectral density can be converted to a one-sided power spectral density by [135]:

$$S_{\mathrm{one-sided}}(f) \;=\; 2 \cdot S_{\mathrm{two-sided}}(f) \quad . \tag{9.1}$$

Decibel

If the dynamic range of the signal stretches across several orders of magnitude, it is convenient to indicate the power spectral density on a logarithmic scale. Prevalent is the logarithmic pseudo-unit (dimensionless) decibel (dB). It indicates the signal power relative to a specified reference level:

$$L_P \;=\; 10 \cdot \log_{10}\left(\frac{P_1}{P_0}\right)\,\mathrm{dB} \quad . \tag{9.2}$$

P_1/P_2	U_1/U_2	dB
0.001	0.03162	-30
0.01	0.1	-20
0.1	0.3162	-10
0.551	0.708	-3
1	1	0
1.995	1.413	3
10	3.162	10
100	10	20
1000	31.62	30
10000	100	40

Table 9.1.: Conversion between power ratios and decibels.

P	U	dBV/dBm
1 μW	31.62 mV	-30
10 μW	100 mV	-20
100 μW	316.2 mV	-10
551 μW	708 mV	-3
1 mW	1 V	0
1.995 mW	1.413 V	3
10 mW	3.162 V	10
100 mW	10 V	20
1 W	31.62 V	30
10 W	100 V	40

Table 9.2.: Conversion from power to dBm and voltage to dBV respectively.

For data in W this is indicated by the symbol **dBm** (sometimes dBmW), refering to the power in decibel referenced to 1 mW,

$$L_P(\text{dBm}) \;=\; 10 \cdot \log_{10}\left(\frac{P}{1\ \text{mW}}\right) \quad . \tag{9.3}$$

In communications engineering the unit **dBc** is rampant. It is used to specify the noise of oscillators relative to the carrier power:

$$L_P(\text{dBc}) \;=\; 10 \cdot \log_{10}\left(\frac{P}{P_\text{carrier}}\right) \quad . \tag{9.4}$$

According to the logarithmic identities it can be converted to dBm by adding the carrier power P_carrier in dBm:

$$L_P(\text{dBm}) \;=\; L_P(\text{dBc}) + L_{P_\text{carrier}}(\text{dBm}) \quad . \tag{9.5}$$

If dealing with voltages, we use **dBV**, which is the squared voltage referenced to 1 V:

$$L_V(\text{dBV}) \;=\; 10 \cdot \log_{10}\left(\frac{U^2}{(1\,\text{V})^2}\right) \;=\; 20 \cdot \log_{10}\left(\frac{U}{1\,\text{V}}\right) \quad . \tag{9.6}$$

It should we noted that this is mathematically correct only if the argument of the logarithm is dimensionless. Strictly speaking this means that we may not use the dB units with power spectral densities, since the argument of the logarithm then has units of 1/Hz. In praxis, we ignore this objection. Sometimes this is denoted by dBV/Hz, but the 1/Hz is often omitted completely.

9.1.3. The Origin of Noise

When dealing with electronics we can classify noise by the underlying process. Essentially, we can name thermal noise, flicker noise and shot noise, which will be introduced in the following pages. There are other sources of noise, such as generation-recombination noise, burst noise or quantisation noise in digital-to-analog converters (DAC) and analog-to-digital converters (ADC), which we will not discuss within this scope.

Thermal noise was first measured in 1928 by **John B. Johnson** at Bell Labs. A thermodynamic model, that explained the results, was developed by **Harry Nyquist**, also at Bell Labs. [30]

Thermal noise Thermal noise has a (nearly) flat spectrum — white noise — and is also refered to as Johnson-Nyquist noise. It is irreducible form of noise, caused by the thermal movement (Brownian motion) of the charge carriers — usually electrons —

in all electrical conductors. The cheapest of all resistors exhibits exactly the same thermal noise, as the most expensive high-quality amplifier of equal source impedance. Different from shot noise and flicker noise thermal noise is always there, regardless of wether there is any voltage applied or not. Connecting an ideal voltmeter to the pins of a resistor R, we would measure an randomly distributed open-circuit voltage. It has Gaussian distribution and its spectral density is

$$S_V = \sqrt{4\mathrm{k_B}TR} \quad , \tag{9.7}$$

where $\mathrm{k_B}$ is Boltzmann's constant in joules per kelvin, T is the absolute temperature in Kelvin. When shorting the ends of the resistor, it dissipates power with the spectral density

$$S_P = \frac{S_V^2}{R} \quad . \tag{9.8}$$

Since thermal noise is white noise, the absolute values within a given frequency interval can be obtained by multiplying with the bandwidth Δf:

$$P_{short}(\Delta f) = \frac{S_V^2}{R}\Delta f \quad . \tag{9.9}$$

If connecting a second resistor of equal resistance, each of the resistors dissipates

$$P(\Delta f) = \frac{S_V^2}{4R}\Delta f = \mathrm{k_B}T\Delta f \tag{9.10}$$

into the other. In impedance matched systems, the dissipated power is thus independent of R, but is determined thermodynamically only! At room temperature (290 K) this yields a noise power spectral density of S_P=-174 dBm/Hz. Although this is quite small, it may become important if the signals are as well small — for instance an optical beat measured with a high frequency photo detector. Additionally we have to bear in mind that when amplifying a small signal, the thermal noise is lifted by the same factor. Amplification by 50 dB already yields S_P=-124 dBm/Hz.

Shot Noise The concept of shot noise was first introduced in 1918 by Walter Schottky who studied fluctuations of current in vacuum tubes [145]. Shot noise exists because energy appears in quantised packets only. It occurs only in the presence of a direct-current (DC) and if the flow of charge carriers is constrained to a single direction.

Walter Hermann Schottky (* 23 July 1886, Zürich, Switzerland, † 4 March 1976, Pretzfeld, Germany) was a German physicist.

This might be an electric DC current in a pn-junction within diodes and transistors, but it also applies to light, being a directed stream of photons and even to the number of atoms in a certain hyperfine level at the end of an interferometer cycle. Shot noise get's relevant, when single particles can produce a relevant contribution to a signal. The number of electrons (or photons) within a certain time interval follows Poisson statistics. When counting N particles, the signal-to-noise ratio is

$$\mathrm{SNR} = N/\sqrt{N} = \sqrt{N} . \tag{9.11}$$

Following *Schottky's theorem*, the power spectral density of electric current shot noise,

$$S_{shot} = 2\mathrm{e}I \quad , \tag{9.12}$$

is flat (white), where e is the charge of an electron and I is the direct current flowing. However, the noise level falls of for frequencies greater than τ^{-1} with τ being the mean transit time of the carriers through the junction's depletion zone. Whether shot noise has a relevant contribution in electronic circuits, depends essentially on the current and the time scale. In electrical conductors it is usually not significant. However, it might get relevant in solid state electronic components, particularly in amplifiers with very small transistor base current.

Flicker Noise As shot noise, flicker noise is always associated with a direct current flowing. It is found in all active devices and hence in semi-conductor devices like amplifiers. The cause of flicker noise are manifold and to some extent not universally explained. Flicker noise is pink noise with a $1/f$ characteristic in its power spectral density

$$S_{flicker} = K\frac{I^a}{f^b} \quad , \tag{9.13}$$

where K, a and b are device-dependent constants; usually $0.5 \leq a \leq 2$ and $b \approx 1$. The amplitude distribution is in many cases non-Gaussian. Flicker noise depends to high degree on the specific design of a circuit. It can not be calculated theoretically, but has to be measured or taken from the data sheet.

For further reading on phase noise refer to e.g. [135, 30, 82].

9.1.4. Phase Noise

The basic relation between phase and frequency of a harmonic oscillator running at the center frequency ν_0 is

$$\phi(t) \;=\; \int \mathrm{dt}\; 2\pi\nu_0 \;=\; \int \mathrm{dt}\; \omega_0 \;=\; \omega_0 t + \phi_0 \quad . \tag{9.14}$$

This simple relation already tells us that there is a relation between phase and frequency noise. When considering phase modulations or phase noise we have to add another term, $\phi_m(t)$, describing the modulation:

$$\phi(t) \;=\; \omega_0 t + \phi_0 + \phi_m(t) \quad . \tag{9.15}$$

The other way round, the instantaneous frequency can be derived from phase by

$$\omega(t) \;=\; \partial_t \phi(t) \;=\; \omega_0 + \delta\omega(t) \quad , \tag{9.16}$$

where

$$\delta\omega(t) \;=\; \dot{\phi}_m(t) \tag{9.17}$$

represents the deviation of the instantaneous frequency from the centre frequency ω_0.

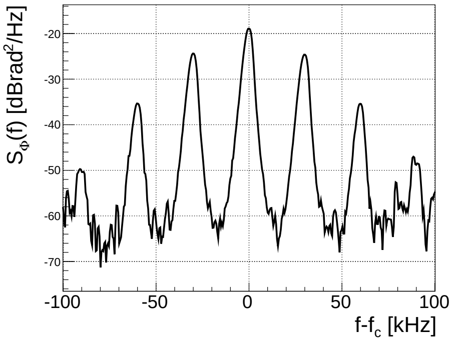

Figure 9.3.: Power spectral density of a laser beat at 6,835 GHz and 30 kHz phase modulation sidebands.

Phase and Frequency Modulation

Introducing a harmonic modulation of the phase $\phi_m(t) = \mathrm{A}_m \cdot \cos(\omega_m t)$ equation (9.15) becomes

$$\phi(t) = \omega_0 t + \phi_0 + \mathrm{A}_m \cos(\omega_m t) \quad . \tag{9.18}$$

Using (9.16) we get

$$\omega(t) = \omega_0 - A_m \omega_m \sin(\omega_m t) \quad . \tag{9.19}$$

In a PLL, this occurs by a spurious, sinusoidal contamination of the signal controlling the VCO — or the laser in an OPLL. Radio engineers distinguish frequency modulation (FM), where $A_m\omega_m =$ const., and phase modulation (PM) with $A_m =$ const. Looking at the spectrum of $\omega(t)$ we'll in either case find the carrier frequency ω_0 accompanied by a infinit number of side bands at frequencies $\omega_0 \pm n\omega_m$. The amplitude of those sidebands depends on the modulation index and are given by the Bessel functions $J_{|n|}(A_m)$. We do of course not intend to imprint something like this onto our laser phase. However, recognising sidebands like the ones in figure 9.3 might help to isolate the source of disturbances.

Bessel functions of the first kind are usually denoted by their Taylor series expansion:

$$J_\alpha(x) = \sum_{m=0}^{\infty} \frac{(-1)^m}{m!\,\Gamma(m+\alpha+1)} \left(\tfrac{1}{2}x\right)^{2m+\alpha}$$

They are canonical solutions of Bessel's differential equation

$$x^2 \frac{d^2y}{dx^2} + x\frac{dy}{dx} + (x^2 - \alpha^2)y = 0.$$

They were defined by the Swiss mathematician and physicist Daniel Bernoulli (* 8 February 1700, † 17 March 1782) and later generalised by the German mathematician and astronomer Friedrich Bessel (* 22 July 1784 - † 17 March 1846).

Frequency Domain Description of Phase Fluctuations

In the more general case, our oscillator — especially when it's about a laser — won't be that honest to produce only harmonic modulations of the phase, but the variation of phase will be a random process: Noise! We use again (9.15) as starting point for our description, but now assume a small (random) perturbation of the phase $\delta\phi(t)$:

$$\phi(t) \;=\; \omega_0 t + \delta\phi(t) \quad . \tag{9.20}$$

When comparing phase noise at different carrier frequencies it can be helpful to define the phase time

$$x(t) \;=\; \frac{\delta\phi(t)}{\omega_0} \quad , \tag{9.21}$$

which is basically the phase fluctuation $\delta\phi(t)$ normalised to the carrier frequency ω_0. The phase time $x(t)$ has units of s and can be considered as a measure for absolute timing jitter: When regarding e.g. the zero-crossing of an oscillation the absolute timing error for $\omega_0 = 1\,\mathrm{MHz}$ and $\delta\phi = 1\,\mathrm{rad}$ is the same as for $\omega_0 = 2\,\mathrm{MHz}$ and $\delta\phi = 2\,\mathrm{rad}$. This is accordingly indicated by $x(t)$. Analogously we can define a normalised version of the instantaneous frequency (9.17):

$$y(t) \;=\; \partial_t x(t) = \frac{\delta\omega(t)}{\omega_0} \quad . \tag{9.22}$$

Phase Noise Power Spectral Densities

When looking at the spectral distribution of frequency and phase fluctuations, we can find several measures in literature [135]:

1. The power spectral density of the frequency fluctuations $\delta\omega(t)$, measured in units of $\mathrm{Hz}^2/\mathrm{Hz}$, is typically denoted with

   $$S_{\delta\nu}(f), \quad f \in [0, \infty] \quad , \tag{9.23}$$

   where f is the distance from the carrier frequency.

2. The power spectral density of the normalised frequency fluctuations $y(t)$, measured in units of $1/\mathrm{Hz}$, is related to $S_{\delta\nu}(f)$ by

   $$S_y(f) = \frac{1}{\nu_0^2} S_{\delta\nu}(f), \quad f \in [0, \infty] \quad . \tag{9.24}$$

3. Finally the one-sided power power spectral density of phase fluctuations, measured in units of $\mathrm{rad}^2/\mathrm{Hz}$, is

   $$S_{\delta\phi}(f) = \frac{\nu_0^2}{f^2} S_y(f) = \frac{1}{f^2} S_{\delta\nu}(f), \quad f \in [0, \infty] \quad . \tag{9.25}$$

   We will mostly use it on a decibel scale:

   $$S_{\delta\phi}^{\mathrm{dB}}(f) = 10 \cdot \log_{10}\big(S_{\delta\phi}(f)\big) \quad . \tag{9.26}$$

   It is denoted with the pseudo-unit dB $\mathrm{rad}^2/\mathrm{Hz}$.

4. However, the most common measure used in industry is a two-sided power spectral density: the normalised frequency-domain representation of phase fluctuations [149],

   $$\mathcal{L}(f),\, f \in [-\infty, +\infty] \quad , \tag{9.27}$$

   which is usually also used on a decibel scale:

   $$\mathcal{L}^{\mathrm{dB}}(f) = 10 \cdot \log_{10}\big(\mathcal{L}(f)\big) \quad . \tag{9.28}$$

For small phase fluctuations $\int_f^\infty df' \ll 1 S_{\delta\phi}(f')\,\mathrm{rad}^2$, we can apply the relations

$$\begin{aligned} \mathcal{L}(f) &= \frac{1}{2} \cdot S_{\delta\phi}(f) \qquad \text{and} \\ \mathcal{L}^{\mathrm{dB}}(f) &= S_{\delta\phi}^{\mathrm{dB}}(f) - 3\,\mathrm{dB} \end{aligned} \tag{9.29}$$

to convert between the one-sided and the two-sided power spectral density of phase fluctuations.

9.1.5. Noise Equipartition

We will sometimes face the case that we have a power spectral density in frequency domain without a carrier to present. How does it convert to phase fluctuations? For the general case this is in fact a non-trivial question, which we will not deepen at this point. However, for the special case of white noise, we can adopt the theorem of noise equipartition [30]:

> Purely random white noise goes into amplitude and phase noise in equal parts.

It can be derived from statistical thermodynamics and stochastic process theory.

9.2. Sensitivity of an AI to Phase Noise

How can we calculate the actual atomic phase noise from laser phase noise? For components in the OPLL, we have defined the complex transfer functions $F(s)$ to link the output signal with the input signal. We can do a similar thing for the atom interferometer and define the transfer function

$$H(\omega) = \frac{S_\Phi(\omega)}{S_\phi(\omega)} \quad . \tag{9.30}$$

It links the noise power spectral density $S_\phi(\omega)$ of laser phase to the noise power spectral density $S_\Phi(\omega) = H(\omega)S_\phi(\omega)$ of the interferometer phase.

Since we now have to distinguish between **laser phase** and **interferometer phase**, we will use the following **convention**: Uppercase Φ denotes the interferometer phase, while lowercase ϕ is the laser phase.

9.2.1. Transfer Function for the Mach-Zehnder Interferometer

For a complete derivation of the transfer function for the atomic Mach-Zehnder interferometer see [24, 25]. We will only give a brief summary of the results. The starting point is the response function for infinitesimal phase jumps:

$$g(t) = 2 \lim_{\delta\phi \to 0} \frac{\delta P(\delta\phi, t)}{\delta\phi} \quad . \tag{9.31}$$

This is basically the relative change of the transition probability P (4.19) related to a phase jump $\delta\phi$ of the Raman phase ϕ at time t.

For the atomic Mach-Zehnder interferometer, we assume that the laser waves are plane waves, the atomic motion is quantised in the direction parallel to the laser and the Rabi frequency is considered to be constant (square pulses). Then the result for $t > 0$ — $t = 0$ is chosen to be in the middle of the second Raman pulse — is:

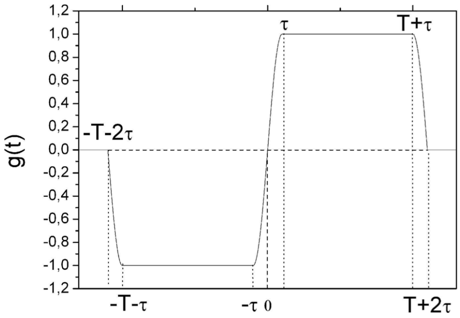

Figure 9.4.: Time-domain representation of the response function for infinitesimal phase jumps $g(t)$. Taken from [24].

$$g(t) = \begin{cases} \sin(\Omega_R t), & 0 < t < \tau_R \\ 1, & \tau_R < t < T + \tau_R \\ \sin\left(\Omega_R (T/t)\right), & T + \tau_R < t < T + 2\tau_R \\ 0, & t > T + 2\tau_R \end{cases} \quad . \tag{9.32}$$

Respective for $t < 0$ since (9.32) is an odd function. The result has been confirmed experimentally in [25].

A real laser does not perform well-arranged phase jumps, but its phase fluctuates with arbitrary phase noise $\phi(t)$. In time-domain we have to perform an integration:

$$\delta\Phi \;=\; \int\limits_{-\infty}^{+\infty} d\phi(t)\, g(t) \;=\; \int\limits_{-(T+2\tau_R)}^{+(T+2\tau_R)} dt\, \dot{\phi}(t) g(t) \quad . \tag{9.33}$$

This gets much simpler again if using the Fourier transform of the response function $g(t)$:

$$\begin{aligned} G(\omega) \;&=\; \int\limits_{-\infty}^{+\infty} dt\, \mathrm{e}^{-\mathrm{i}\omega t} g(t) \qquad\qquad (9.34) \\ &=\; \frac{4\mathrm{i}\Omega_R}{\omega^2-\Omega_R^2} \sin\left(\frac{\omega T+2\tau_r}{2}\right) \\ &\qquad \cdot \left[\cos\left(\frac{\omega T+2\tau_r}{2}\right) + \frac{\Omega_R}{\omega}\sin\left(\frac{\omega T}{2}\right)\right] \quad . \end{aligned}$$

The transfer function in the sense of (9.30) for the Mach-Zehnder interferometer is

Please note that [24] uses the symbol $H(\omega)$ instead of $\omega G(\omega)$.

$$H_{\mathrm{MZ}}(\omega) \;=\; |\omega G(\omega)|^2 \quad . \tag{9.35}$$

Characteristics of the Transfer Function $H_{\mathrm{MZ}}(\omega)$

Due to the symmetric Mach-Zender sequence, the interferometer is blind for phase fluctuations at $f = 1/T$ and higher harmonics $f_i = i \cdot 1/T$. It is clearly visible in figure 9.5 that the transfer function has multiple zeros at that frequencies. By adjusting T, this can for instance be used to suppress 50 Hz line noise, as we will see in 9.3.7. Another property of $H_{\mathrm{MZ}}(\omega)$ that can be influenced by experimental parameters is the drop-off at high frequencies. It is a low-pass filter with cut-off frequency $f_c = \Omega_R/\pi$, determined by the Rabi frequency Ω_R.

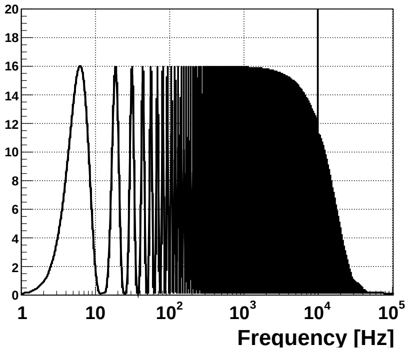

Figure 9.5.: Transfer function $H_{\mathrm{MZ}}(2\pi f)$ for a Mach-Zehnder interferometer.

9.2.2. Calculation of Atomic Phase Noise

According to the definition of the transfer function (9.30), we can calculate the power spectral density of the interferometer phase by

$$S_\Phi(\omega) \;=\; H_{\mathrm{MZ}}(\omega) S_\phi(\omega) \quad , \tag{9.36}$$

given a (measured) power spectral density of laser phase fluctuations $S_\phi(\omega)$. The standard deviation of the atomic phase for one measurement — often referred to as the atom interferometer's single shot sensitivity — then is

$$\sigma_\Phi^{\mathrm{rms}} = \sqrt{\int d\omega\, S_\Phi(\omega)} \;=\; \sqrt{\int d\omega\, H_{\mathrm{MZ}}(\omega) S_\phi(\omega)} \quad . \tag{9.37}$$

For long averaging times we can also use the Allen variance [25],

$$\sigma_\Phi^2(\tau) \;=\; \frac{1}{\tau} \sum_{n=1}^{\infty} H_{\mathrm{MZ}}(2\pi n f_c) S_\phi(2\pi n f_c) \quad , \tag{9.38}$$

where $f_c = 1/T_c$ is the repetition rate of the interferometer sequence. Thus, $\tau = nT_c$ can only be a multiple of T_c.

Transfer Function for Vibrations

From (9.35) it is only a small step to a transfer function for vibrations. Displacing the retroreflecting mirror by δz leads to a displacement of the Raman phase fronts relative to the free falling atoms. This acts like a phase shift $k_{\mathrm{eff}}\delta z$ of the Raman phase. Putting this into (9.38) yields

$$\sigma_\Phi^2(\tau) = \frac{k_{\mathrm{eff}}^2}{\tau} \sum_{n=1}^{\infty} H_{\mathrm{MZ}}(n\omega) S_z(n\omega) \quad , \tag{9.39}$$

where $S_z(\omega)$ is the spectral density of the retroflection mirror's position fluctuation. Using the power spectral density of acceleration noise $S_a(\omega)$ instead, this becomes:

$$\sigma_\Phi^2(\tau) = \frac{k_{\mathrm{eff}}^2}{\tau} \sum_{n=1}^{\infty} \frac{H_{\mathrm{MZ}}(n\omega)}{(n\omega)^4} S_a(n\omega) \quad . \tag{9.40}$$

The influence of vibration noise to the CAPRICE atom interferometer is treated in detail in [97]. In a similar manner, the formalism can also be used to calculate phase shifts that arise from light shifts, magnetic field gradients, cold atom collisions and other systematic effects [25].

9.3. Phase Noise in the OPLL Reference Setup

Finally, we have made it through a lot of introductory stuff to our actual task: We will measure the phase noise of the OPLL reference setup, as presented in chapter 8. This especially includes the phase detector, as well as the low phase noise frequency reference, since they are the key components with respect to phase noise. The goal of the following analysis is to identify as much individual contributions to the overall phase noise as possible and to sound out the potential for improvements.

9.3.1. Phase Noise of the Phase Detector

To measure the phase noise of our phase detector, we employ the scheme from figure 9.6 (a). The idea is to distribute a common oscillation, provided by a 100 MHz reference oscillator and a subsequent power splitter to the two inputs of the phase detector. Thus the output of the phase detector only dumps the internal noise of the phase detector and the phase noise due to thermal effects in the cables between power splitter and phase detector. The phase shifter can be used to adjust the phase difference at the input ports of the phase detector. Since this is the usual operating condition we set it to zero, which corresponds to a zero DC offset at the phase detector's output.

The output is measured by a Dynamic Signal Analyser `HP 35670A`. Its input is set to AC coupling and floating ground to avoid unintended line noise due to ground loops in the measurement setup. The maximum resolution of the `HP 35670A` is 1600 lines, which would yield a bandwidth of 64 Hz at a span of 102.5 Hz. To provide a sufficient resolution also in the lower frequency bands, we'll take spectra with spans of 102.5 kHz, 51.25 kHz, 12.5 kHz, 6.125 kHz, 1600 Hz, 800 Hz, 100 Hz and optionally 50 Hz, where the particular values are determined by the technical properties of the `HP 35670A`. The single spectra can be combined to a continuous spectrum by normalising to the respective resolution bandwidth.

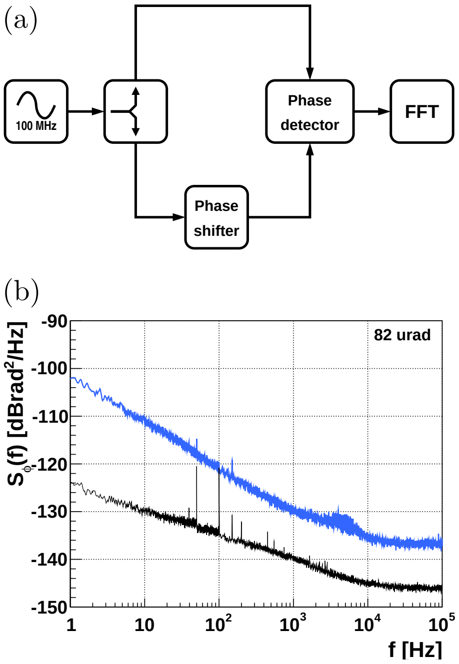

Figure 9.6.: (a) Measurement scheme for the measurement of the phase noise of the phase detector. (b) Inherent phase noise power spectral density of the phase detector (blue) and background phase noise of the measurement setup (black).

The thus obtained spectrum is an amplitude noise power spectral density $P_V(f)$, measured in units of V^2/Hz. By multiplying with the phase detector's gain factor K_{pd}, we obtain the phase noise power spectral density,

$$S_{\delta\phi}(f) = K_{pd} \cdot P_V(f) \quad , \tag{9.41}$$

measured in units of $\mathrm{rad}^2/\mathrm{Hz}$. Figure 9.6 (b) shows $S_{\delta\phi}(f)$ converted to units of $\mathrm{dBrad}^2/\mathrm{Hz}$ (blue). To ensure that this is actually the noise coming from the phase detector and not e.g. the internal noise of the `HP 35670A` we perform a background measurement, using a frequency mixer in place of the phase detector. The corresponding measurement is depicted by the black spectrum in figure 9.6 (b) and is considered neglectable.

9.3.2. Phase Noise of the Frequency Reference

100 MHz frequency reference

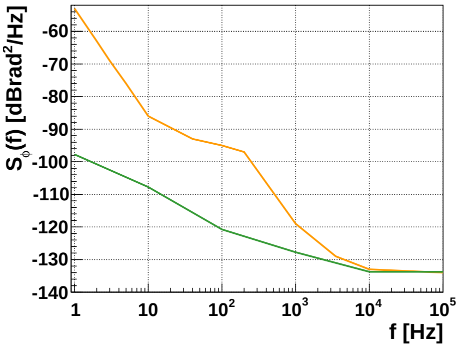

Figure 9.7.: Straight line templates of the phase noise power spectral density of the 100 MHz reference oscillator (yellow) and the DDS (green).

Since the 100 MHz frequency reference `Spectra Dynamics DLR-100` is the central component of the frequency generation, we have to pay special attention to its phase noise characteristics. Figure 9.7 shows a straight line template of the `DLR-100`'s phase noise, measured with a `Spectra Dynamics ND-1` noise detector [3]. For comparability with the plots following on the next pages, it has been upconverted to 6.9 GHz; the actual phase noise at 100 MHz is 37 dB lower.

100 MHz frequency synthesiser

The phase noise of the variable 100 MHz frequency synthesiser `Spectra Dynamics LNFS-100` has not been measured. We will use the specification from the data sheet for further calculations, assuming that the actual phase noise is sufficiently approximated by the straight line template plotted in figure 9.7 (green).

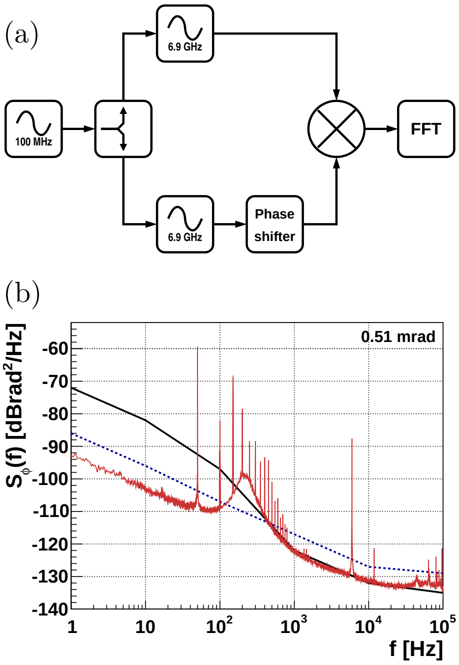

Figure 9.8.: (a) Setup for the phase noise measurement of the 6.9 GHz reference oscillator (b) Phase noise of the 6.9 GHz reference oscillator (red), valid for Fourier frequencies above 200 Hz. The specification according to the data sheet is plotted in black. For comparison the phase noise of the CASI reference multiplication chain at 7 GHz is depicted by the dashed blue line [174].

6.9 GHz frequency multiplication stage

Figure 9.8 (a) shows the setup employed to measure the phase noise of the 6.9 GHz reference oscillator `GMU69124LN` described in section 8.3. Two identical devices are connected to a common 100 MHz signal. The output of both devices is connected to a frequency mixer in order to measure the phase difference between them. Using a phase shifter the relative phase between both signals is offset to 90° so that the DC part of the frequency mixer's output is zero. The power spectral density $P_V^{pair}(f)$ of the frequency mixer's output signal is measured in units of V^2/Hz using again the `HP 35670A`. By multiplying with the mixer's gain factor $K_\otimes = 455\,mV/rad$ we obtain the power spectral density of phase fluctuations for a pair of devices:

$$S_{\delta\phi}^{pair}(f) = K_\otimes \cdot P_V^{pair}(f) \quad . \tag{9.42}$$

Assuming a Gaussian distribution for the phase noise in $S_{\delta\phi}(f)$ we can calculate the phase noise power spectral density for a single device by

$$S_{\delta\phi}(f) = \frac{1}{\sqrt{2}} \cdot S_{\delta\phi}^{pair}(f) \quad . \tag{9.43}$$

The result is plotted in red in figure 9.8 (b). Comparison with the data sheet (black line) shows that the device basically meets the developers simulations. The bump at 200 Hz is caused by the transition from the external 100 MHz reference signal on the left to the internal 100 MHz oscillator on the right. Since both devices share a common reference signal, phase noise below the transition frequency cancels out. The plot is hence only valid for Fourier frequencies above 200 Hz.

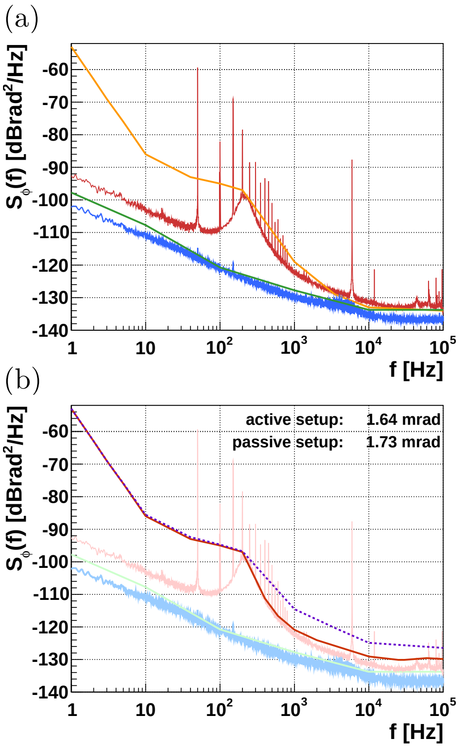

Figure 9.9.: (a) Phase noise of the 7 GHz reference oscillator (red), the phase detector (blue), the DDS (green) and the 100 MHz reference oscillator (yellow) [3]. (b) Overall phase noise power spectral density of the active `GMU69124LN`-based frequency generation (red). The total phase noise of a setup based on a passive frequency multiplication stage (dashed, violet) is added for comparison.

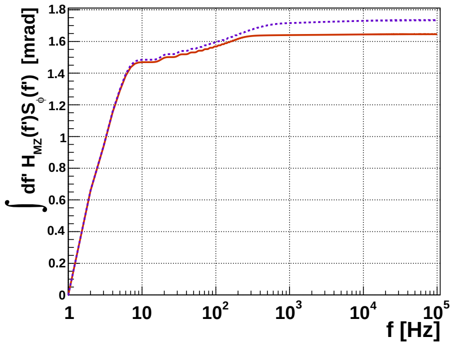

Figure 9.10.: Standard deviation of the atomic phase (T=80 ms) as a function of the upper integration bound for the active (red) and the passive (dashed, violet) frequency multiplication stage.

Combined Phase Noise

Figure 9.9 (a) shows additional phase noise contributions: The yellow line shows again the phase noise of the 100 MHz frequency reference `Spectra Dynamics DLR-100` upconverted to 6.9 GHz. For comparison we also include the phase noise of the phase detector from figure 9.6 (b) (blue) and of the DDS `Spectra Dynamics LNFR-100` as specified in the data sheet (green). Both lines show the phase noise at 65 MHz. However, due to the frequency down conversion based on a frequency mixer (see figure 7.10) the phase noise power spectral densities of DDS and phase detector must not be upconverted to 6.9 GHz, but contribute onefold only. Thus we see that they are well below the red and the yellow line and the system performance is limited by the oscillators. The red line in figure 9.9 (b) shows the combined noise contributions of the 100 MHz reference oscillator, the active 6.9 GHz frequency multiplication stage, the DDS and the phase detector. It yields a standard deviation of the atomic phase of 1.64 mrad, when folded with the interferometer's transfer function (T=80 ms, $t_{\pi/2}$=25 µs) according to (9.37).

Comparison of active and passive Microwave Generation

Finally we come back to the question if the design of an active 6.9 GHz frequency multiplication stage was worth the effort. In comparison to the active setup the dashed violet line 9.9 (b) is the calculated overall phase noise of a setup without the active frequency multiplication stage. It is identical to the one represented by

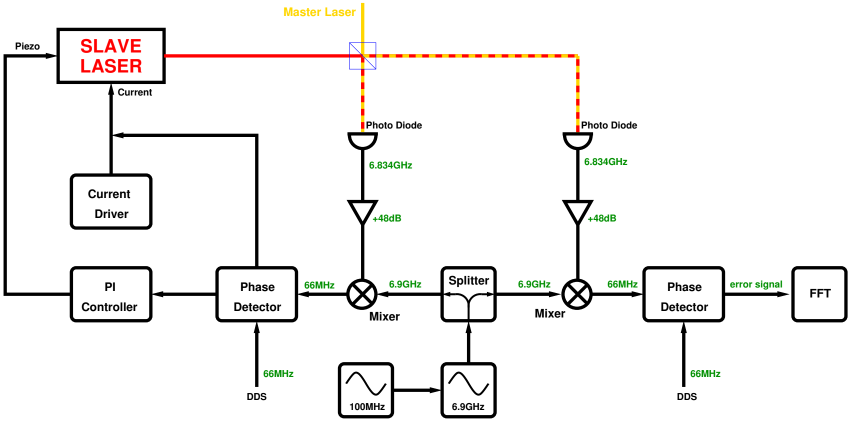

Figure 9.12.: Measurement setup to perform an out-of-loop phase noise measurement of the OPLL reference setup. An independent phase measurement is performed on the combined laser light, that is usually fed to the experiment.

the red line, except that it uses the passive frequency multiplication stage from [174]. As the phase noise at Fourier frequencies below 200 Hz is in both cases governed by the 100 MHz reference oscillator, there is only a small difference between the two setups in that interval. On the other hand at Fourier frequencies above 200 Hz the oscillator `Pascall OCXOF` used in the `GMU69124LN` proves its superior phase noise characteristics. However, weighting the phase noise power spectral density with the transfer function (9.35) and integrating from 1 Hz to 100 kHz reveals only a minor improvement on the overall phase noise: 1.6 mrad for the active setup compared to 1.7 mrad for the passive setup.

This finding gets clear immediately, when looking at figure 9.10. It shows the integrated phase noise as a function of the upper integration bound, again for the active (red) and the passive (dashed, violet) setup. Reminding ourselves that on a dB scale 10 dB correspond to one order of magnitude, it's no wonder that most of the phase noise is already collected at Fourier frequencies below 10 Hz and that the interval above 1 kHz — with more than three orders of magnitude less phase noise — has only a minor contribution. Considering furthermore the phase noise contributions from other sources (see the following sections) a passive frequency multiplication stage should be sufficient in most cases. For the `GMU69124LN` sparing the internal oscillator would save roughly € 2000 per unit.

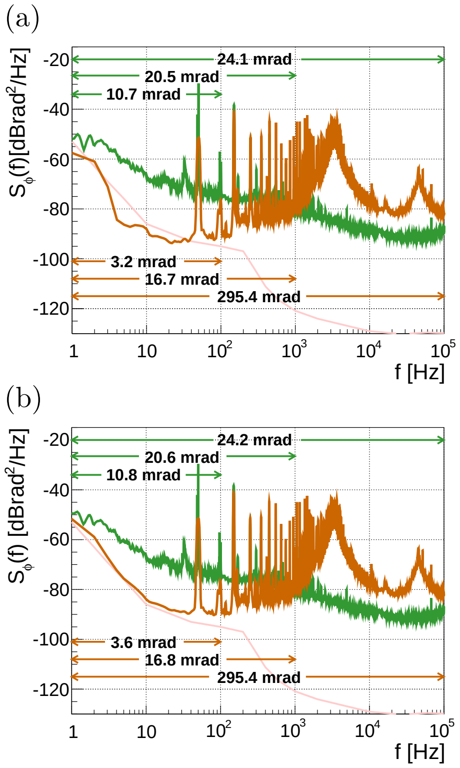

Figure 9.11.: (a) Phase noise power spectral densities S_ϕ of two OPLL setups, obtained with the measurement scheme from figure 9.12. The frequency reference's phase noise is added for comparison (light red). (b) Combined phase noise power spectral densities of the OPLL measurement and the frequency reference.

9.3.3. Measurement of residual OPLL Phase Noise

To obtain the overall phase noise of the OPLL we need to measure the phase error of the combined laser light, that is feed from the OPLL laser setup to the experiment. The simplest possibility would be to take the auxiliary output from the phase detector of the OPLL. However, in this kind of in-loop-measurement certain sources of phase noise are – at least partially – canceled out, since they are compensated by the OPLL.

To get an out-of-loop measurement, we start with an independent phase measurement on the combined laser light, that is usually fed to the experiment, as depicted in figure 9.12. Thus, the measured phase noise spectral densities in figure 9.11 (a) consist of the OPLL's residual phase noise plus the phase noise of the photodetector, the amplifier and the phase detector. Since this measurement is referenced to the same 100 MHz oscillator, the same frequency multiplier (`GMU69142LN`) and the same DDS as the OPLL, the phase noise contribution of those devices is still canceled out and this is not a complete out-of-loop measurement.

To calculate the the overall phase noise of the outgoing laser light, the phase noise contribution of the 100 MHz reference oscillator, the frequency multiplier and the DDS has to be added to the measured phase noise spectral density, resulting in the plots depicted in figure 9.11 (b). They will be discussed in section 9.4.

9.3.4. Thermal Noise

As was already mentioned, the thermal noise of an impedance matched system at room temperature is -174 dBm/Hz. Due to noise equipartition half of the noise power contributes to phase noise, so that the phase noise power spectral density originating from thermal noise is -177 dBm/Hz. At first glance this seems too small to be relevant for the phase noise in our frequency generation system. However, when processing the beat signal from a photodiode, we're dealing with small signal amplitudes. To check if it has a significant contribution, we will calculate the phase noise originating from thermal noise. We calculate the two-sided spectral density,

$$\mathcal{L}(f) = \frac{1}{2} P_{\text{thermal}} - P_{\text{carrier}}, \tag{9.44}$$

as a function of signal carrier power P_{carrier}. To convert from $\mathcal{L}(f)$ to the single-sided spectral density $S_{\delta\phi}(f)$ we have to add another 3 dB. Figure 9.13 shows the phase noise contribution from thermal noise for different powers P_{carrier} of the beat signal coming from

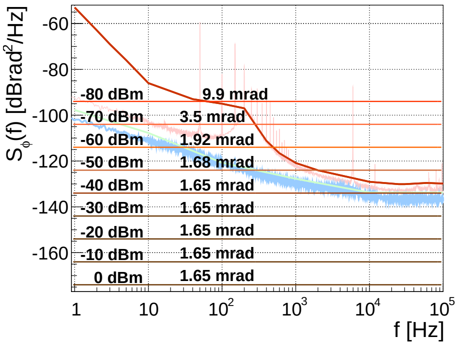

Figure 9.13.: The thermal noise of an impedance matched system at room temperature is - 174 dBm/Hz. Due to noise equipartition it also contributes to phase noise. It has been converted to units of dBrad^2/Hz with respect to the carrier power, which is the beat signal coming from the photo diode. The values in dBm label the thermal noise at the corresponding carrier power. The values in mrad label the corresponding standard deviation of the atomic phase resulting from the combined phase noise of the frequency reference and thermal noise.

the photo diode. When illuminating a `Hamamatsu G4176` photo diode with the maximum allowed laser power of 5 mW equally distributed to both lasers, this results in a beat power of -30 dBm. However, calculating the standard deviation of the atomic phase (T=80 ms, $t_{\pi/2}$=25 µs) phase noise including thermal noise does lead to theoretical values of 1.9 mrad and 3.5 mrad with a beat powers of -60 dBm and -70 dBm respectively. The contribution of thermal noise to the standard deviation of the atomic phase vanishes if thermal noise is kept below the noise floor of the frequency reference. Thus thermal noise can be considered insignificant, as long as the power of the beat signal is -40 dBm or higher. Furthermore, when using a `Hamamatsu G4176` photo diode, thermal noise is much smaller than the noise due to the photo detector, as we will see in section 9.3.6.

9.3.5. Amplifier Noise

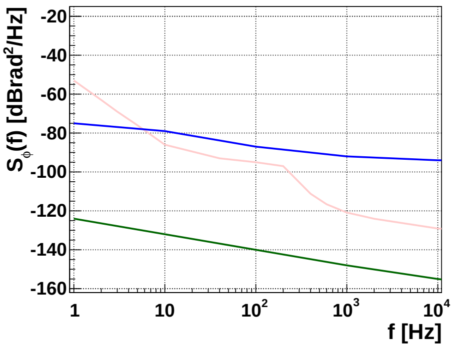

Figure 9.14.: Phase noise of the amplifiers `MiniCircuits ZJL7G` (blue) and `aml67P4801` (green). Combined phase noise of the references (violet) and the `ZJL7G` leads to 13.7 mrad of integrated phase noise.

During the development of the OPLL reference setup, different amplifiers have been used. First versions were setup using several low-cost amplifier `MiniCircuits ZJL7G` (∼50€), which gain ∼8 dB at 6.8 GHz. In the final version they have been replaced by a single ultra-low phase noise amplifier `aml67P4801` (∼1800€), gaining 48 dB at 6.8 GHz. Figure 9.14 compares the inherent phase noise of both amplifier types. The green line for the `aml67P4801` has been provided by the manufacturer. The `MiniCircuits ZJL7G` is represented by the blue line. Since no phase noise specifications were available for the `MiniCircuits ZJL7G`, it has been measured using a measurement scheme similar to figure 9.7 (a), but with an input frequency of 6.9 GHz. The phase noise of the frequency reference has again been added in light red for comparison. It is clearly visible that the phase noise contribution of `MiniCircuits ZJL7G` amplifiers within the OPLL will become significant at some point, while the contribution of `aml67P4801` can be neglected. Since the phase noise of the `aml67P4801` is more than 2 orders of magnitude below the phase noise of the frequency reference, it does not contribute to the OPLL's overall phase noise.

9.3.6. Photo Detector Noise

A significant source of phase noise is the photo detector, used to detect the laser beat. It is caused by dark current, noise from the photo detector's bias voltage and straw light. At the maximum

Dark current is a small electric current flowing in photosensitive devices and also non-optical devices like diodes. In photosensitive semiconductors it is caused by spontaneous production of free charge carriers. It is caused by the thermal motion of the crystal lattice and has a Poissonian pattern (shot noise). In non-optical diodes dark current is referred to as *reverse bias leakage current.*

allowed continuous light irradiation of 5 mW the `Hamamatsu G4176` yields an electrical beat signal of -30 dBm. During the measurements the photo diode yielded -40 dBm, as during usual operation of the experiment. Figure 9.15 (a) shows the noise power spectral density from the `Hamamatsu G4176` photodetector, measured with a Dynamic Signal Analyser `HP 35670A`. It was found regardless of wether there was light irradiated to the photo detector or not.

The spectrum shows a multitude of discrete peaks and a noise floor around -130 dBm, which drops off above ~3 kHz. According to noise equipartition, white noise equally contributes to both, amplitude noise and phase noise. Since the noise floor is approximately flat before and after it drops off, we assume noise equipartition for the noise floor to be valid. With this assumption the power spectral density can be transferred to the dBc scale by subtracting the carrier power and to the dBrad^2/Hz scale by subtracting another 3 dB. Although the discrete peaks of the noise spectrum are also transferred to the phase noise plot, we stress again that the quantitative result in dBrad^2/Hz is not valid for the discrete peaks, but only for the noise floor!

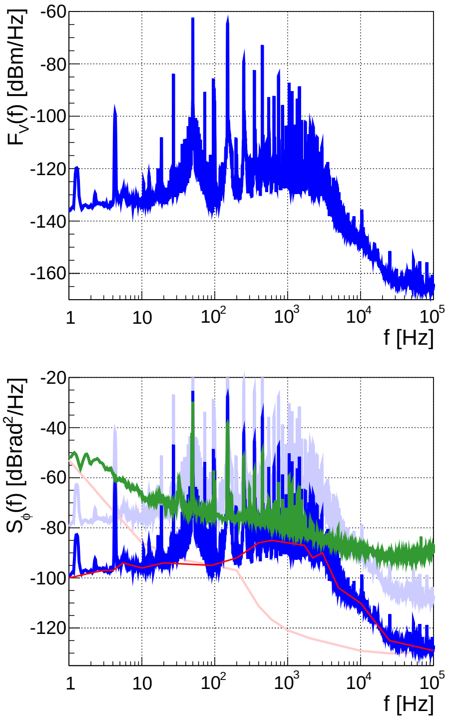

Figure 9.15.: (a) Noise power spectral density of the photo detector `Hamamatsu G4176` (blue), including contributions from the bias voltage. (b) Conversion of the photo detector noise to phase noise, assuming a flat distribution for the noise floor and a beat signal at -40 dBm (blue). It hardly limits the OPLL phase noise power spectral density (green). This is different with a -60 dBm beat signal, since then the signal-to-noise ratio would be reduced (light blue).

Noise floor

For comparison we have plotted a phase noise power spectral density taken from the OPLL (green) in figure 9.15 (b). At a carrier power of -40 dBm the photo detector's noise floor is hardly below the OPLL phase noise. When assuming a beat power of only -60 dBm (light blue), we can expect a significant aggravation of the OPLL's phase noise power spectral density due to photo detector noise. For comparison we have again plotted the well-known phase noise power spectral density of the frequency reference (light red). At Fourier frequencies above ~20 Hz the photo detector noise floor is above the frequency reference's phase noise power spectral density. As noise equipartition is not valid for the discrete peaks, we apply a straight line fit to the noise floor of the photo diodes phase noise spectral density (red line). Using the atom interferometers transfer function (T=80 ms, $t_{\pi/2}$=25 µs) it leads to a standard deviation of the atomic phase of 5.8 mrad, as compared to 1.64 mrad for the frequency reference. Thus, the superior phase noise performance of the frequency reference is of no advantage, as long as photo detector noise is at that level. The photo detector's contribution to the standard deviation of the atomic phase could be reduced to 1.8 mrad at a carrier power of -30 dBm, but increases as much as 18 mrad and

56 mrad for carrier powers of -50 dBm and -60 dBm respectively. To keep the photo detectors contribution to phase noise as low as possible, the allowed light irradiation power should always be fully exploited.

Discrete peaks

Since noise equipartition is only valid for white noise, we can not apply it to convert the discrete peaks in the photo detector power spectral density to phase noise. However, we already find some hints for the peak's influence on phase in figure 9.15 (a). Especially the harmonics of the 50 Hz peak show the frequency domain side band pattern typical for phase modulation at 50 Hz (see figure 9.3). This is confirmed by figure 9.15 (b). The majority of peaks from the photo detector's noise power spectral density (blue) also show up in the OPLL's phase noise power spectral density (brown).

9.3.7. Suppression of 50 Hz Line Noise

Most of the discrete peaks in figure 9.15 are harmonics of the 50 Hz line frequency. Fortunately the AI transfer function (9.35), has notches at

$$f_i \;=\; i \cdot \frac{1}{T} \quad , i \in \mathbb{N} \quad . \tag{9.45}$$

Both, the line noise peaks as well as the notches in the transfer function, are equally spaced. Hence, we can suppress 50 Hz line noise simply by overlaying the transfer function notches with the line noise peaks. This can be done by adjusting T:

$$\begin{aligned} f_i &= i \cdot \frac{1}{T} = 50\,\mathrm{Hz} \\ \Leftrightarrow \quad T &= i \cdot 20\,\mathrm{ms}, \quad i \in \mathbb{N} \quad . \end{aligned} \tag{9.46}$$

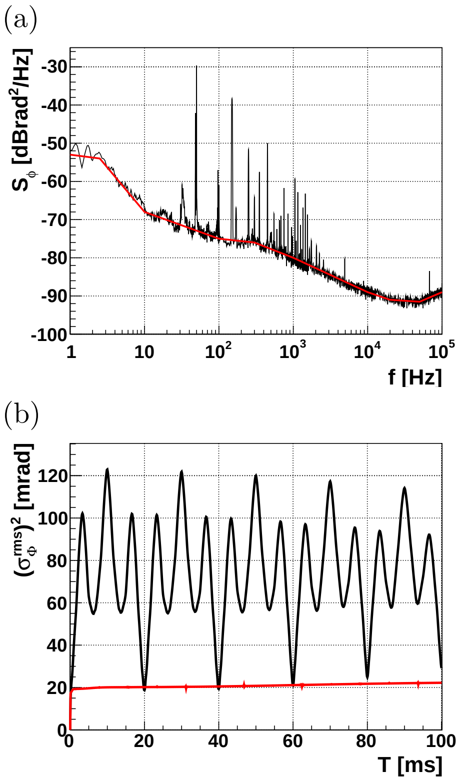

Figure 9.16.: (a) Phase noise power spectral density of the OPLL (black) and corresponding straight line fit, where the discrete peaks have been removed (red). (b) Standard deviation of the atomic phase as a function of evolution time T for the measured phase noise spectral density (black) and the straight line fit (red).

Figure 9.16 (a) shows a phase noise power spectral density of the OPLL (black). For comparison we have added a straight line fit, where all discrete peaks have been removed (red). Figure 9.16 (b) shows the resultant standard deviation of the atomic phase (9.37) as a function of free evolution time T. Comparison with the corresponding plot for the straight line fit (red) confirms that 50 Hz line noise can be completely suppressed when choosing T according to (9.46).

9.4. Dimensioning the Loop Filter

9.4.1. AC vs. DC coupling

The phase noise power spectral density plot in figure 9.17 (a) shows two different versions of the OPLL setup. The values of the standard deviation of the atomic phase are denoted for different integration intervals. While the green spectrum is taken from the final OPLL reference setup, as introduced in chapter 8, the brown spectrum was taken from an earlier version. The early version exhibits some issues, which could be removed in the final version; e.g. the resonances at 3 kHz and 45 kHz causing a quite large standard deviation of the atomic phase. However, the crucial point is another: Although the early version has a much higher overall phase noise, it has significantly less phase noise at Fourier frequencies below 1 kHz. Below 100 Hz it even hits the ground of the frequency reference (light red). Thus, in this frequency band it features the best performance that is possible at all.

The reason for this difference is that the current path of the early version was DC coupled to the laser diode, while in the final version it is AC coupled by inserting the capacitor C to the incoupling circuit (figure 8.16): Together with the laser diode the capacitor acts as a high pass filter, as was already pointed out earlier. The effect can also be seen in the amplitude plot of the open loop transfer function G in figure 9.17 (b): At Fourier frequencies below 2 kHz the high pass term causes a 6dB/octave slope, dragging down the gain to the level of the piezo path (dashed green line). It thus leads to a considerable reduction of loop gain for Fourier frequencies between 10 Hz and 10 kHz. This also affects the error transfer functions E, figure 9.17 (c), where the noise suppression is reduced by more than 20 dB at Fourier frequencies between 10 Hz and 1 kHz. This eventually corresponds with the frequency band of increased phase noise in the green power spectral density plot. Thus, we have traced back the increased phase noise below 1 kHz to the AC coupling or rather the capacitor C in the current path.

Nonetheless, we have not introduced AC coupling for nothing. Firstly it protects the laser diode from uncontrolled currents from the phase detector. Secondly it has proven to drastically reduce the risk of laser mode hops, in case the OPLL gets unlocked, and enables automatic relock in many cases. It is thus desirable to keep the AC coupling, despite its negative effect on phase noise performance.

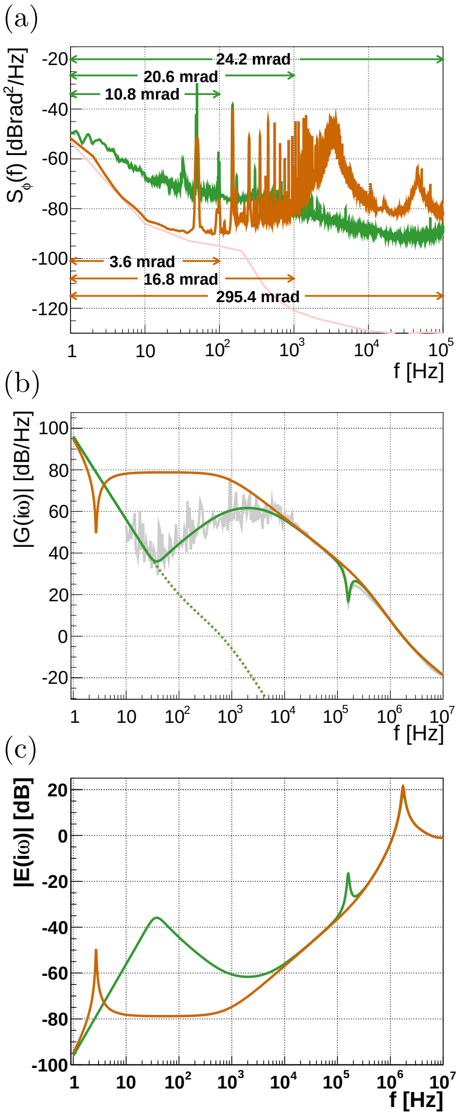

Figure 9.17.: (a) Phase noise power spectral densities S_ϕ of two OPLL setups: AC coupling (green) and DC coupling (brown). The high pass behavior of the AC coupling leads to increased phase noise in the low frequency band. The standard deviation of the atomic phase for $T = 80\,\text{ms}$ is denoted for several integration intervals. The phase noise of the frequency reference is included for comparison (red). (b) The increased phase noise in S_ϕ is due to the reduced gain in the open loop transfer function G (dashed green line = piezo path). (c) This corresponds to a reduced noise suppression in the error transfer function E.

9.4.2. Limits of the First-Order OPLL

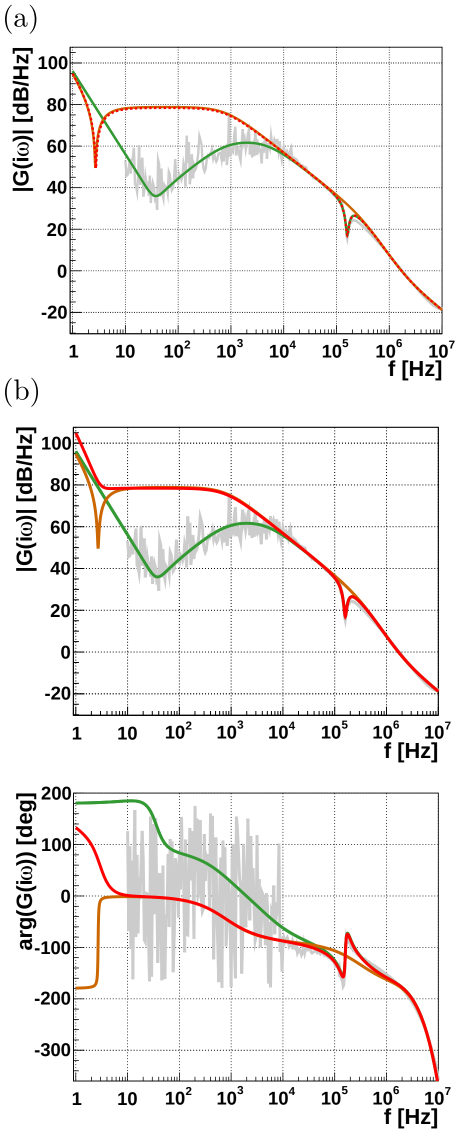

Figure 9.18.: Open loop transfer functions of the AC coupled setup (green) and the DC coupled setup (orange) as was depicted in figure 9.17. (a) Including an additional integrator in the AC coupled setup (dashed red) compensates the loss in loop gain below 1 kHz. (b) Shows loop gain and phase of a setup, where the bandwidth of the piezo path has been limited to 1 Hz. This removes the notch at 2,5 Hz, that is caused by the overlap of the control bands of piezo path and current path.

Using the Laplace model of the transfer function, it is easy to identify a possibility to compensate the loss of performance due to AC coupling. We look at the AC coupled setup (green) in figure 9.17: 80% of the overall atomic phase noise are caused by laser phase noise below 1 kHz. This is exactly the frequency band, where the AC coupling reduces noise suppression. The AC coupling acts like a high pass filter, which has a 6 dB/octave slope. On the other hand, in section 7.2.3 we have noticed that an integrator has a -6 dB/octave slope.

Therefore, the solution is a second-order loop filter. Figure 9.18 (a) shows the open loop transfer functions of the AC coupled setup (green) and the open loop transfer function of the DC coupled setup (orange). Additionally the transfer function of the AC coupled setup with second order loop filter (additional integrator) is plotted as dashed red line: In fact, the damping of the AC coupling can be compensated completely by adding an integrator to the loop filter, while the superior stability of the AC coupling is preserved.

At this point, we should address the notch at 2.5 Hz. It is caused by the overlapping frequency bands of piezo path and current path. Metaphorically speaking, the two control paths are working against each other, thus degrading loop performance. This can be avoided by limiting the bandwidth of the piezo path. The red plot in 9.18 (b) shows the AC coupled transfer function with integrator and the bandwidth of the piezo path limited to 1 Hz. The notch has completely vanished. Figure 9.18 (b) provides also the phase plot. It confirms that the integrator does neither change gain crossover frequency nor phase crossover frequency. Due to its -6 dB/octave slope, the integrator's contribution to the open loop transfer function G immediately diminishes towards higher frequencies. Thus, the loop stability is not affected, while loop gain is increased — as required — for Fourier frequencies below 10 kHz.

Expected Improvement of a Second-Order OPLL

Figure 9.19 shows the associated error transfer functions E for all three setups:

- DC coupled first-order setup (orange),
- AC coupled first-order reference setup (green) and
- AC coupled second-order setup with additional integrator (red).

The second-order setup featuring the additional integrator (red) improves the noise suppression below 1 kHz up to 20 dB, compared to the first-order setup (green).

We will now use the simulation of the error transfer function to calculate the expected effect of the second-order loop filter. Figure 9.20 shows the measured phase noise power spectral density of the OPLL reference setup without integrator (green). In section 7.4 we learned, that the error transfer function quantifies the suppression of noise. Therefore, we only have to subtract the improvement observed in the error transfer function in figure 9.19 from the measured phase noise power spectral density. However, the OPLL can only suppress self noise of the laser. Therefore, we account for the frequency reference (light red) and the photo detector noise (light blue), since they cannot be suppressed by the OPLL.

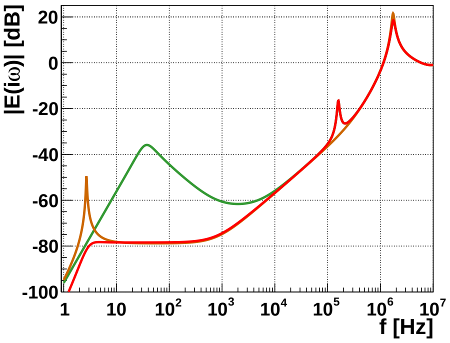

Figure 9.19.: (a) Error transfer function E of the DC coupled early setup (orange), the AC coupled OPLL reference setup (green) and the improved setup with additional integrator (red).

The result is the phase noise power spectral density plotted in red in figure 9.20. Figure 9.20 (a) shows the resulting power spectral density including photo detector noise, while photo detector noise has been left out in figure 9.20 (b). The OPLL's impact on the standard deviation of the atomic phase (assuming T=80 ms) would be reduced from 25 mrad to 11.4 mrad or rather 9.9 mrad if eliminating photo detector noise (see table 9.3 for a conversion to σ_η). Since the limit with respect to loop stability is not yet reached, the strength of the integrator could be increased and the phase noise at low Fourier frequencies could be reduced further. However, the comparison of both plots suggests that photo detector noise will become the limiting factor of the improved setup.

9.4.3. Increasing Loop Gain

A further improvement of noise suppression can be achieved by increasing the open loop gain. However, increasing loop gain reduces the phase margin and finally leads to resonance in the OPLL, as we have seen in section 8.4.1. When the open loop transfer function $G(s)$ (green fit in 9.18) had been taken, the OPLL was already adjusted to maximum possible gain. According to the Bode stability criterion increasing overall loop gain is only possible if shifting the phase crossover frequency towards higher frequencies. As the phase crossover frequency of the OPLL reference setup is currently governed by signal delay within the loop, this can be achieved by reducing the physical dimension of the loop — i.e. the length of cables and laser beams. The more compact setup in [14] confirms, that by using shorter cables the loop delay can be reduced significantly, indicated by a higher control bandwidth of 6.2 GHz in [14] compared to ~3 GHz in our case.

Figure 9.21 shows the computed phase noise power spectral density for the second-order loop filter with additional +10 dB loop gain. At Fourier frequencies up to 100 Hz the performance is now limited by the frequency reference, while at Fourier frequencies above 100 Hz the impact of photo detector noise gets evident. The overall standard deviation of the atomic phase (T=80 ms) would be reduced to 3.5 mrad if leaving out photo detector noise (figure 9.21 (b)), but would be 6.7 mrad if accounting for photo detector noise (figure 9.21 (a)).

Noise from the photo detector ultimately limits the performance of the OPLL reference setup, no matter to which abysses the error transfer function E might be pushed. To fully exploit the room for improvement offered by the improved setup, presumably some efforts will have to be made with the photo detectors, since they would pose the new limit to the overall phase noise performance.

	σ_Φ	σ_η
Measurement (first-order loop filter)	24.8 mrad	$2.5\cdot10^{-8}$
2nd-order loop filter	11.4 mrad	$1.1\cdot10^{-8}$
2nd-order loop filter (w/o p.d. noise)	9.9 mrad	$9.8\cdot10^{-9}$
2nd-order loop filter, +10 dB	6.7 mrad	$6.6\cdot10^{-9}$
2nd-order loop filter, +10 dB (w/o p.d. noise)	3.5 mrad	$3.5\cdot10^{-9}$
frequency reference	1.6 mrad	$1.6\cdot10^{-9}$
shot noise (10^6 atoms, 100% contrast)	1.0 mrad	$9.9\cdot10^{-10}$

Table 9.3.: Conversion of the standard deviation of the atomic phase σ_Φ to uncertainty of the Eötvös ratio η for the discussed optimisation measures. (With and without photo detector noise and assuming T=80 ms, g=9,81 m/s^2 and $k_{\mathrm{eff}}^{\mathrm{Rb}}$ from page 51.)

(a)

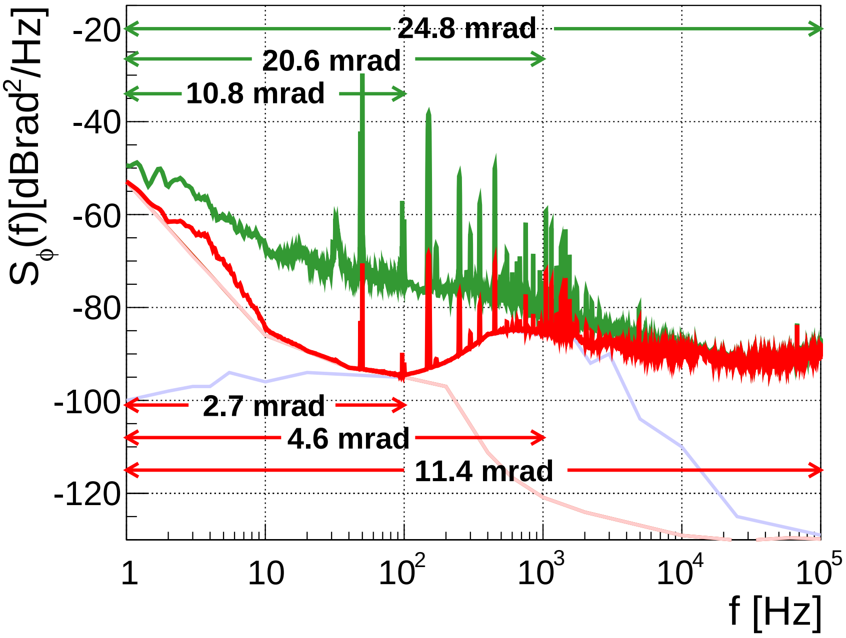

(b)

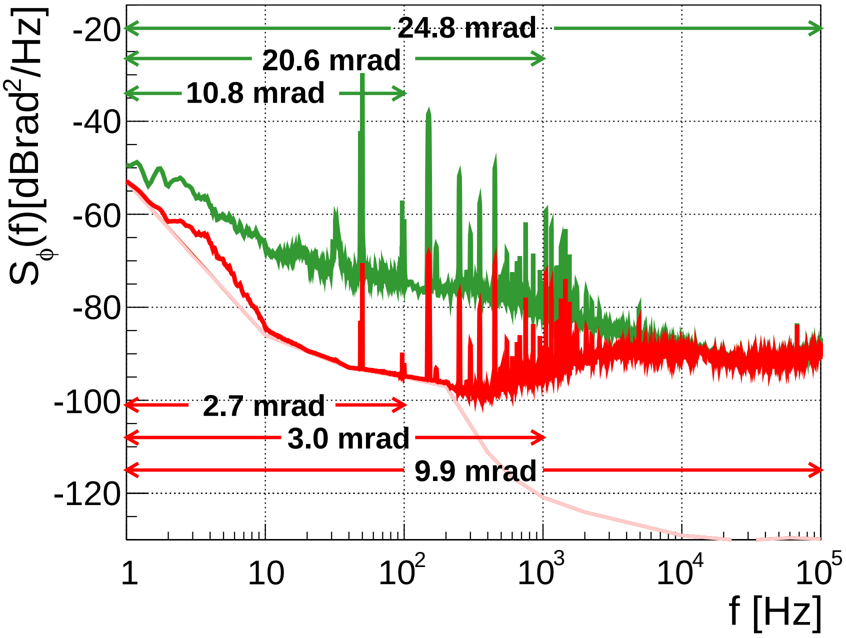

Figure 9.20.: **Measured** phase noise power spectral density of the first-order OPLL reference setup (green) and **computed** phase noise power spectral density of the improved second-order setup with additional integrator (red). Photo detector noise (light blue) is included in (a), but disregarded in (b). The performance of the frequency reference is included for comparison (light red). The integrated phase noise of the atomic phase (T=80 ms) is indicated for frequency intervals [1 Hz,100 Hz], [1 Hz,1 kHz] and [1 Hz,100 kHz] respectively.

(a)

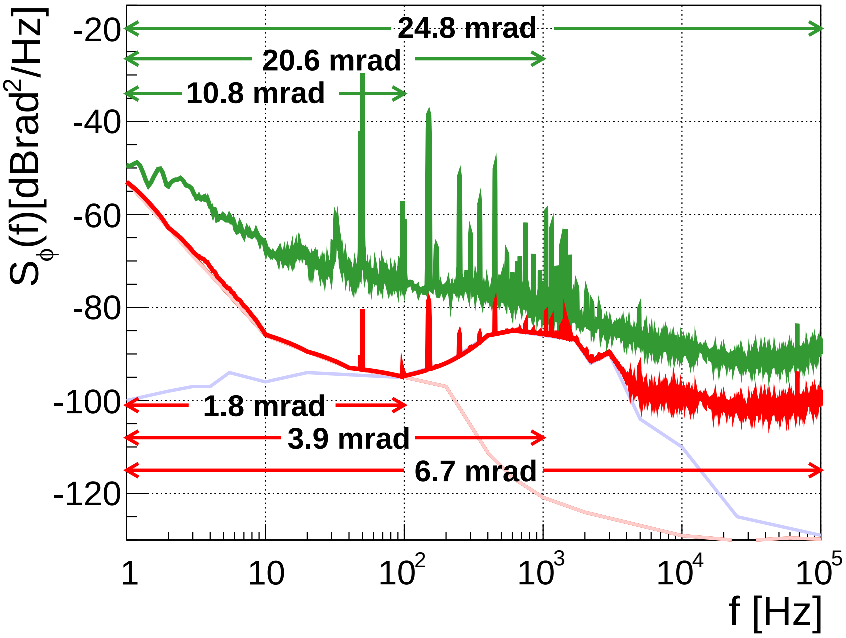

(b)

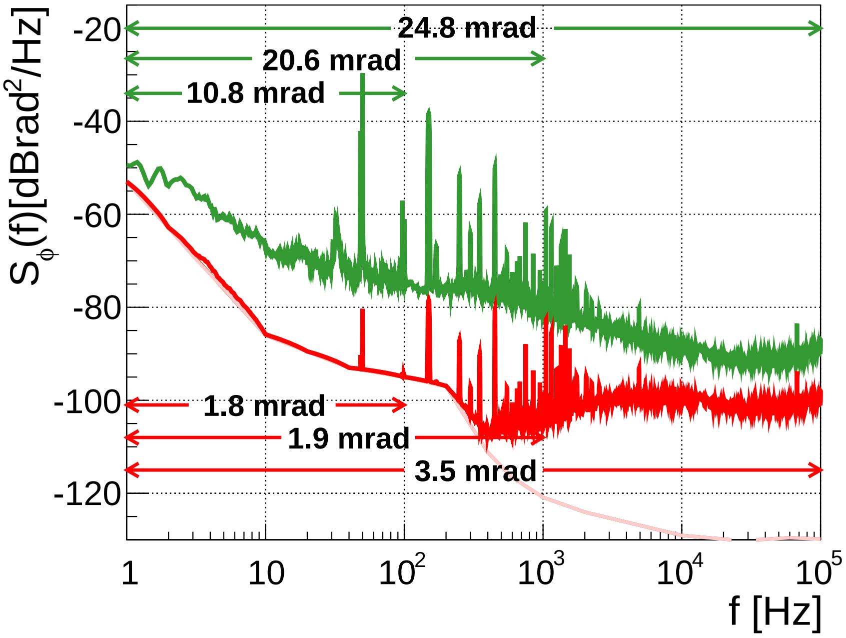

Figure 9.21.: **Measured** phase noise power spectral density of the first-order OPLL reference setup (green) and **computed** phase noise power spectral density of the improved second-order setup with additional integrator (red) and +10 dB overall loop gain. Photo detector noise (light blue) is included in (a), but disregarded in (b). The performance of the frequency reference is included for comparison (light red). The integrated phase noise of the atomic phase (T=80 ms) is indicated for frequency intervals [1 Hz,100 Hz], [1 Hz,1 kHz] and [1 Hz,100 kHz] respectively.

9.5. Summary & Discussion

The ^{87}Rb and ^{39}K dual species atom interferometers envisaged for the CAPRICE and QUANTUS II experiments required the construction of an optical phase-locked loop (OPLL) for the stabilisation of the Raman laser pairs. This included the design of a phase detector board and a low-phase noise frequency reference, as described in chapter 8. An OPLL reference setup, which eventually serves as the OPLL of the CAPRICE atom interferometer, was constructed as a defined test bed. OPLLs demonstrated at other atom interferometers [23, 14, 144] served as a blueprint for the setup.

The scope of part III of this thesis is understanding OPLLs and the impact of their design on their phase noise performance. The contents of chapters 7 through 9 can be summarised as follows:

1. Understanding, measuring and mathematically modelling the OPLL's transfer function using Laplace transforms.
2. Understanding and measuring phase noise of the overall loop and assessing the phase noise contribution of the individual components.
3. Demonstrating how the Laplace representation of the loops transfer function can help optimising the loop filter to systematically reduce phase noise.

While it is possible to optimise a loop filter through trial and error, in this case we decided to apply a different approach, based on prior understanding of the OPLLs function and modelling of the transfer function. Therefore, chapter 7 provides a general overview of the underlying techniques of phase-locked loops, including the essentials about control theory and the concept of transfer functions.

Chapter 8 describes the technical and experimental setup, including the above mentioned phase detector board and the low-phase noise frequency reference. In section 8.5 we demonstrate how to measure the open loop transfer function while the loop is actually locked and how to simulate it with the Laplace representation.

Chapter 9 starts with a theoretical introduction of phase noise in section 9.1. Section 9.3 contains the description of the measurement scheme and discusses the results of the phase noise measurement. In section 9.4 we finally apply the Laplace representation of the transfer function and demonstrate how to optimise the loop filter to systematically reduce phase noise in specific frequency bands.

Understanding OPLLs: The mathematical Model

In the previous chapters we learned about the relevance of transfer functions for understanding the phase noise performance of OPLLs. The two relevant transfer functions are the transfer function of the OPLL describing the transfer of the frequency reference's phase to the lasers and the transfer function of the Mach-Zehnder atom interferometer describing the transfer of the laser phase to the atomic phase. We only gave a summary of the results from previous works [23, 25] for the latter one in section 9.2, but concentrated on the theoretical derivation and application of the OPLL's transfer function.

There are actually three relevant transfer functions when describing OPLLs: Initial point is the open loop transfer function $G(s)$, describing the laser's frequency and phase response to phase errors. There are two closed loop transfer functions, that can be deduced from the open loop transfer function $G(s)$: the system transfer function $H(s)$ relating laser phase to the phase of the frequency reference and the error transfer function $E(s)$ as a measure for the suppression of phase noise.

The mathematical model of the transfer function was constructed using the concept of Laplace transforms and was implemented in `Mathematica`. Each component included in the loop is represented by an individual term. Chaining all the individual Laplace transforms together leads to the generic transfer function for the complete loop, described in sections 7.4 and 8.5. The set of corresponding `Mathematica` expressions is included in appendix D.

How do we know, the theoretical transfer function does represent the OPLLs actual behaviour? To get hold of the OPLL's actual open loop transfer function we need to measure it. The usual approach would be to perform a direct measurement by opening up the loop and connecting it to a network analyser. However, if the loop is opened, i.e. the lasers are not locked, it is in a non-linear state, while the measurement requires the loop to be in a linear, i.e. locked, state. Therefore we applied the indirect measurement scheme provided in [98] to measure the open loop transfer function, while the loop is actually locked.

The comparison of the theoretically deduced open loop transfer function to the measurement showed a good agreement: By adding another frequency selective Laplace term and a slight adjustment of parameters the measured open loop transfer function could be reproduced astonishingly well. Thus, we showed that the phase response and the frequency response of the OPLL reference setup can be fully understood with the theoretical model. It helps to trace down the loop's behaviour to its individual elements and allows quantifying their impact on the interferometer's output data. Conversely, we demonstrated that we can simulate the impact of optimisation measures. Doing so prior to implementation allows for more targeted, systematic design and optimisation of the loop. The recommendations for optimisation made in section 9.4 are the result of this.

Development and Performance of the Phase Detector

The phase detector developed within this thesis — colloquially known as *phase detector ATLAS* — is described in section 8.2. Primary requirements for the phase detector were defined by the needs of the CAPRICE experiment. As auxiliary requisite it should be versatile so that it can serve in other experiments.

While early demonstrations of phase-locked diode lasers employed double-balanced mixers [156, 164], the use of digital phase-frequency detector chips has proved its worth in various experiments involving atom interferometers [19, 25, 90, 14, 144]. They allow not only the use in OPLLs, but also as replacement for frequency-to-voltage converters if frequency stabilisation is sufficient. While the inputs can optionally be equipped with various amplifiers to fit the detector to the level of the input signal, the phase detector can process input frequencies between 10 MHz and 800 MHz, depending on the population of the output filter. The phase noise measurement described in section 9.3 showed that the phase detectors intrinsic noise can be neglected, because it is more than one order of magnitude below the phase noise of the frequency reference. Also, the demand on versatility paid off: To date the phase detector board has been built more than 20 times and successfully utilised in various other experiments.

Development and Performance of the Frequency Reference

The frequency reference developed within this thesis is described in section 8.3. In contrast to the multi-purpose phase detector, the frequency reference is a highly specialised device designed for the envisaged application in atom interferometers based on ^{87}Rb and ^{39}K. It provides outputs at 400 MHz and 6.9 GHz corresponding to the relevant ^{87}Rb and ^{39}K hyperfine transitions. The specifications included not only requirements of the CAPRICE atom interferometer, but also took into account requirements of the QUANTUS experiments, namely compactness and 50 g shock resistance. The frequency reference is a combination of a commercially available 100 MHz frequency reference, `Spectra Dynamics DLR-100`, and a custom-made frequency multiplier, `GMU69124LN`, designed by an engineering consultant. Opposed to the passive step-recovery design used in e.g. [23, 90, 14, 144], the `GMU69124LN` is an active device. It provides an additional 100 MHz oscillator lowering the noise floor for Fourier frequencies above 1 kHz. Finally, the fixed-frequency output is supplemented by a variable Direct Digital Synthesiser (DDS), `Spectra Dynamics LNFS-100 OPT3`.

The phase noise measurements described in section 9.3 confirmed that the combined frequency reference meets the specifications, contributing 1.6 mrad to the standard deviation of the atomic phase (T=80 ms, $t_{\pi/2}$=25 µs). This corresponds to the shot noise level of an atom interferometer featuring $3.5 \cdot 10^5$ atoms at 100 % contrast or 10^6 atoms at 59 % contrast.

The comparison with the passive setup in section 9.3.2 showed that the active design constitutes only a minor improvement over the passive design (1.6 mrad vs. 1.7 mrad). A definite result of the phase noise measurements is, that the frequency reference's main contribution to phase noise arises from Fourier frequencies below 100 Hz. However, the frequency reference's phase noise below 100 Hz is not determined by the `GMU69124LN`, but by the 100 MHz frequency reference `Spectra Dynamics DLR-100`. Also the DDS's phase noise is not an issue since it contributes onefold only, while the phase noise of the 100 MHz frequency reference contributes 69-fold due to the frequency up-conversion. Improvements of the 6.9 GHz output can, thus, only be made by improving the 100 MHz source. For the same reason, the *active* frequency up-conversion cannot display its strength. For future setups it should therefore be assessed if the additional oscillator inside the `GMU69124LN` could be spared. Besides the cost reduction (∼€2000) this would eliminate a potential cause of defect, which is expedient especially in unattended space-borne devices.

In conclusion we can say that the frequency reference is sufficient for operating a Mach-Zehnder atom interferometer at T=80 ms, since its contribution to the standard deviation of the atomic phase is in the order of shot noise. Concerning atom interferometers operated at $T \gg$100 ms, see the remarks on space-borne missions below.

Performance of the OPLL

To assess the performance of the developed devices, we needed a defined test environment. This was implemented by the *OPLL reference setup*, described in section 8.4. Since it turned out to be inherently stable with a passive first-order loop filter, it can serve as a general starting point for OPLLs at other experiments and for further optimisation.

In section 9.3 we studied the phase noise performance of the OPLL reference setup. A summary of the phase noise contributions of individual loop components is given in table 9.4. The relevant results are the following:

- The frequency reference contributes 1.6 mrad to the standard deviation of the atomic phase (T=80 ms). The major contribution originates from the 100 MHz oscillator `Spectra Dynamics DLR-100`, while the frequency upconversion `GMU69124LN` only contributes 0.1 mrad.
- The inherent phase noise of the phase detector is sufficiently below the phase noise of the frequency reference and can, thus, be neglected.
- Thermal noise can be neglected if the laser beat yields -40 dBm or higher at the photo detector output.
- Amplifier noise can be neglected if sticking with low phase noise amplifiers.
- A special case is 50 Hz line noise, whose impact strongly depends on the free evolution time T. If operated at multiples of 20 ms, the interferometer is effectively blind to 50 Hz spurious frequencies and higher harmonics.
- The 3.2 mrad originating from the photo detector was identified as the greatest contribution to phase noise resulting from a single component.

The phase noise contributions of the loop components from table 9.4 sums up to 4.9 mrad. Even if adding 1 mrad for phase noise originating from optical fibres [23], this leaves ∼19 mrad of residual noise, not sufficiently suppressed by the OPLL. This is due to a lack of loop gain, for a most part at Fourier frequencies below 1 kHz. For the time being the main contribution to noise of the atomic phase was due to vibrations [97] and the phase noise performance of the OPLL is sufficing for the operation of the CAPRICE atom interferometer. However, setups using similar components [14, 90,

OPLL (first-order loop filter)	24.8 mrad
Phase Detector	0.1 mrad
100 MHz Frequency Reference (<100 MHz)	1.5 mrad
6.9 GHz Frequency Reference (>100 MHz)	0.1 mrad
Photo Detector Noise	3.2 mrad[1]
Thermal Noise	negligible[1]
Amplifier Noise (Low-Noise Amplifiers)	negligible
50 Hz Line Noise	negligible[2]

Table 9.4.: Phase noise contributions of individual loop components to the atomic phase Φ.
— [1] -40 dBm electrical beat signal at the photo diode output
— [2] provided T is a multiple of 20 ms

144] demonstrated, that residual noise of the OPLL can be further reduced by one order of magnitude.

If at some point the laser phase noise becomes the limiting factor, the performance can be improved by the optimisation measures discussed in section 9.4. Basically the OPLL's frequency response can be adjusted with the loop filter. The key to understanding and tuning the loop filter was again the theoretical model of the transfer function. The simulation showed that the lack of loop gain below 1 kHz can be compensated by either switching to DC coupling or by replacing the first-order loop filter with a second order loop filter. As the AC coupled loop filter is desirable with respect to loop stability, we recommend to stay with the AC coupled device. Adding an integrator would fully compensate the setback of loop gain below 1 kHz, while preserving loop stability. Doing so would reduce the OPLL's contribution to atomic phase noise (T=80 ms) from σ_Φ=25 mrad (corresponds to σ_η=2.5·10^{-8}) to less than σ_Φ=11.4 mrad (σ_η=1.1·10^{-8}) or rather σ_Φ=9.9 mrad (σ_η=9.8·10^{-9}) if disregarding photo detector noise.

Further increasing the strength of the integrator to a certain extent should be possible without affecting loop stability, but merely affects Fourier frequencies below 1 kHz. In contrast, the overall loop gain is frequency independent. However, its increase currently results in a resonance condition, because the loop's phase margin is exhausted. According to the Bode stability criterion increasing overall loop gain is only possible if shifting the phase crossover frequency towards higher frequencies. From the mathematical model we deduced, that the phase crossover frequency is currently determined by loop delay, i.e. length of cables and laser beams. Lowering loop delay, thus, would allow increasing overall loop gain. As was demonstrated in [14] a more compact setup leads to significant reduction of signal delay, indicated by a higher control bandwidth of 6.2 GHz vs. ~3 GHz in our case.

With the second-order loop filter and +10 dB loop gain the OPLL's performance will be limited by the photo detector: The simulation yields σ_Φ=3.2 mrad for the standard deviation of the atomic phase (σ_η=3.5·10^{-9}) without photo detector noise, but σ_Φ=6.7 mrad (σ_η=6.6·10^{-9}) if including photo detector noise. Thus, the noise of the currently used photo detector frustrates fully exploiting the phase noise performance of the frequency reference (σ_Φ=1.6 mrad, σ_η=1.6). It remains unclear, whether this is a general feature of the photo diode, since photo detector noise was canceled out in the phase noise measurements published for similar setups [90, 144]. The influence of stray light and the possibility of so far undetected reflections within the laser setup has not been analysed. Another possibility would be a damage of the particular photo diode used during the measurements, since it once was accidentally irradiated with more than the allowed 5 mW of laser power for a few minutes. Therefore a closer investigation of the photo detector's noise contribution is recommended.

Impact on space-borne missions

We closed our assessment of the frequency reference with the statement, that it is sufficient for operating a Mach-Zehnder atom interferometer at T=80 ms. However, this statement is not valid for atom interferometers operated at $T \gg$100 ms! The transfer function of the Mach-Zehnder atom interferometer (9.36) shifts to the left as T is increased. Figure 9.22 shows the transfer function for T=80 ms (black), T=1 s (red) and T=5 s (light blue); other parameters of the atom interferometer kept constant. The consequence is that the impact of phase noise at low Fourier frequencies gets even bigger.

Extrapolating the phase noise of the 100 MHz frequency reference `Spectra Dynamics DLR-100` (see figure) 9.22 (b) to the sub-Hertz regime and using the transfer function from figure 9.22 (a) yields σ_Φ=28.6 mrad for T=1 s and even σ_Φ=176.0 mrad for T=5 s ($t_{\pi/2}$=25 µs assumed for all given values). This is particularly critical, since there are hardly any oscillator-based frequency references commercially available, that could outperform the `Spectra Dynamics DLR-100`. The impact of the sub-Hertz phase noise is so severe that even locking the frequency reference to a MASER is not sufficient to reach the shot noise limit of σ_Φ=1.0 mrad (10^6 atoms).

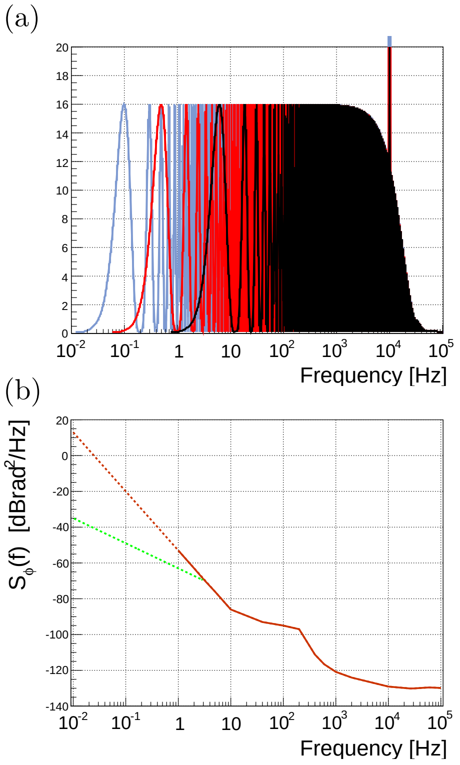

Figure 9.22.: (a)Transfer functions of the Mach-Zehnder atom interferometer for T=80 ms (black), T=1 s (red) and T=5 s (light blue). (b) Phase noise of the frequency reference (brown) and possible improvements using a MASER (green).

Using the exemplary performance of a MASER from figure 9.22 (green line) still leads to σ_Φ=3.7 mrad for T=1 s and σ_Φ=5.4 mrad for T=5 s.

This would be a show-stopper for space-borne missions like QUEST, were it not for the Microwave-Optical Local Oscillator (MOLO) (see section 5.4) and countermeasures like e.g. double diffraction [114] or the composite-light-pulse technique [13], which comprise inherent cancellation of laser phase noise. To keep the device as simple as possible, it would be advantageous to use a frequency reference based on quartz oscillators like employed in the `Spectra Dynamics DLR-100`. Due to the strong impact of sub-Hertz phase noise, using quartz oscillators requires the double diffraction scheme to suppress laser phase noise by more than 20 dB to reach the shot-noise limit. Therefore the suppression capabilities of double diffraction should be assessed in detail. The definition of requirements for the frequency reference and the further development of counter measures coping with clock noise is strongly advisable for the continuing assessment of QUEST-like missions.

Part IV.

Conclusion

10. The long way into space

Today, the test of the universality of free fall is more than ever in the focus of fundamental physics. While the historical examples *just* tested the universality of free fall in itself, todays tests evolved into a test of general relativity or even our understanding of cosmology in general. To that effect applying atom interferometers for a test of the universality of free fall covers an extraordinary range of fields in physics. While on the technical side it is on the cutting-edge between applied physics and engineering, the motivation for those measurements touches the most fundamental questions of physics.

Finding a violation of the equivalence principle implies either that Einstein's theory of general relativity is wrong or that there is new physics. A new, so far unknown interaction acting on similar length scales as gravity would in fact become visible as an apparent violation of the universality of free fall. Despite their theoretical nature, many of the beyond-Standard-Model theories predict a violation of the universality of free fall caused by such a new long-range interaction. This renders the search for violations of the equivalence principle an important topic in modern cosmology.

Applying the framework of Blaser and Damour showed that alkaline and alkaline earth metals offer an even big potential in maximising the covered volume in the phase space of possible charges, when compared with materials, that can be formed into macroscopic test masses. Also beyond the framework of Blaser and Damour atomic test masses might access effects, that aren't accessible with macroscopic test masses at all, e.g. spin-dependence or spacetime fluctuations.

T [s]	σ_a [m/s^2]	
	$N_{\text{tot}} = 10^5$	$N_{\text{tot}} = 10^6$
0.1	$2.0 \cdot 10^{-8}$	$6.0 \cdot 10^{-9}$
1	$2.0 \cdot 10^{-10}$	$6.0 \cdot 10^{-11}$
5	$0.8 \cdot 10^{-11}$	$2.4 \cdot 10^{-12}$

Table 10.1.: The influence of atom number N_{tot} and free evolution time T on the shot noise limit: While increasing the number of atoms by one order of magnitude improves the sensitivity by a factor 3.25, increasing the free evolution time by one order of magnitude yields a factor 100. All values are calculated for 100% contrast.

If we look at the level of precision we can say that — with consequent further development of the experimental techniques — atom interferometers offer the potential of significantly outperforming the precision reached with classical tests of about $\eta \approx 10^{-13}$. Based on experiences from experiments already being carried out, the extension of the free evolution time T holds the greatest potential of improving the sensitivity, since doubling T leads to the same improvement of the sensitivity as increasing the atom number by a factor of eight! Some example values are given in table 10.1.

However, due to the free fall character of the experimental method also the drop distance grows quadratically with T, soon going beyond the dimensions of the common table top experiments. It is thus reasonable to go ahead and pave the way into space. Going to space allows a small and compact experimental setup, since in a zero-g environment T is not limited by the dimension of the experimental chamber anymore, but only by temperature and expansion rate of the atomic cloud. As the atomic cloud is shielded from environmental influences (atmospheric drag, solar wind) by the satellite, it moves on a geodetic. A violation of the EP then becomes manifest in deviation from the geodetic, as depicted in figure 10.1.

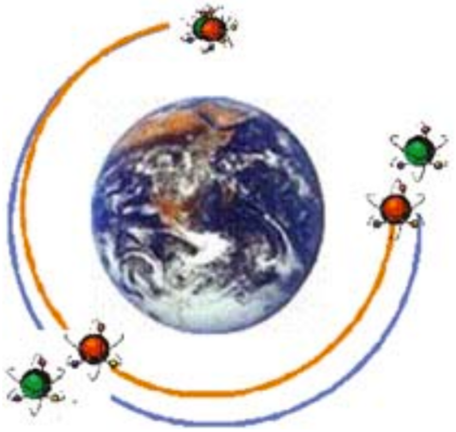

Figure 10.1.: Atoms deviating from a geodetic trajectory due to a composition dependent violation of the universality of free fall. [46]

A space-borne atom interferometer, the *HYPER-precision cold atom interferometry in space* (HYPER) mission, had already been proposed in January 2000 within ESA's Horizons 2000 programme (now Cosmic Vision 2005-2015) [47, 50]. A mission testing the universality of free fall, the *Matter Wave eXplorer of Gravity* (MWXG), was first proposed in 2008 [46].

However, preparing a spaceborne scientific apparatus is completely different from developing experiments in the lab. A spaceborne device requires being compact and extremely energy-efficient. It must be that robust to stand a rocket launch without the need for any subsequent adjustment. Moreover, after being suffering accelerations and vibrations dwarfing every earthquake, it must be self-sustained over the whole mission lifetime, quite often several years.

Since there is absolutely no possibility for hardware modifications or repairs after launch, the topmost criterion for space-borne missions is technology readiness level (TRL). Going this path requires a high degree of perseverance. The dry spell of engineering consecutive experiments, that are rather technology demonstrators than experiments yielding a scientific output, demands stable funding and is not exactly eased by *evaluitis*. Nevertheless, this cumbersome path is treaded by the QUANTUS collaboration, significantly triggered by the *Atom Optics and Quantum Sensors* group, Institute of Quantum Optics at Leibniz Universität Hannover.

A first approximation of spaceborne missions are experiments carried out in reduced gravity aircrafts (e.g. ICE) and at drop towers. The 110 m drop tower at ZARM (Zentrum für Angewandte Raumfahrttechnologie und Mikrogravitation) in Bremen allows drop times of 4 s (drop mode) or 9 s (catapult mode). This already poses remarkable challenges on compactness and robustness of the experimental setup. The feasibility of this concept was successfully demonstrated by the QUANTUS I (QUANtengase Unter Schwerelosigkeit) experiment in 2007 [170, 171]. While QUANTUS I was dedicated to the creation of a BEC under zero-g conditions, the second generation experiment, QUANTUS II, demonstrates the operation of an atom interferometer in a drop tower [100]. With the implementation of a dual atom interferometer for Rubidium and Potassium, it will be able to perform a test of the UFF [159].

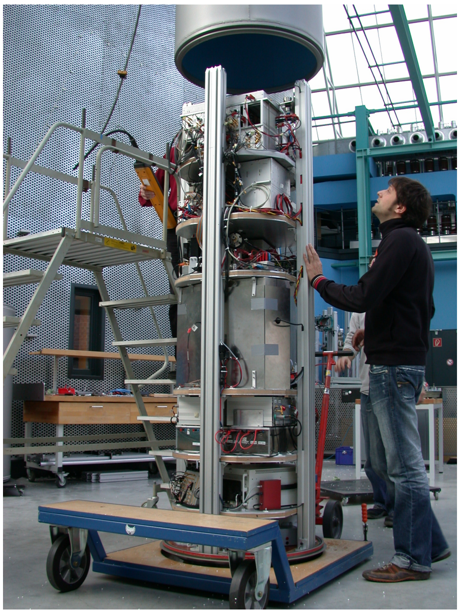
Figure 10.2.: Capsule of the QUANTUS I experiment.

The handicap of the drop tower experiments is their limited repetition rate; for instance the operation of the drop tower at ZARM does only allow three measurements per day. Inter alia on that account the long term strategy envisages a space-borne mission. As a successor of QUANTUS II the sounding rocket mission MAIUS (MAteriewellen-Interferometer Unter Schwerelosigkeit) will be the next step on the way into space. The VSB-30 rocket poses even higher demands on compactness than the ZARM drop capsules. And while the drop tower experiments can be adjusted prior to drop and without being exposed to noteworthy mechanical stress, the MAIUS apparatus has to survive a rocket launch without subsequent possibility of human intervention — another analogy to spaceborne missions. MAIUS was successfully launched on 23 January 2017 within the TEXUS (Technologische EXperimente Unter Schwerelosigkeit) program of DLR (Deutsches Zentrum für Luft- und Raumfahrt) from Esrange Space Center near Kiruna in northern Sweden [81].

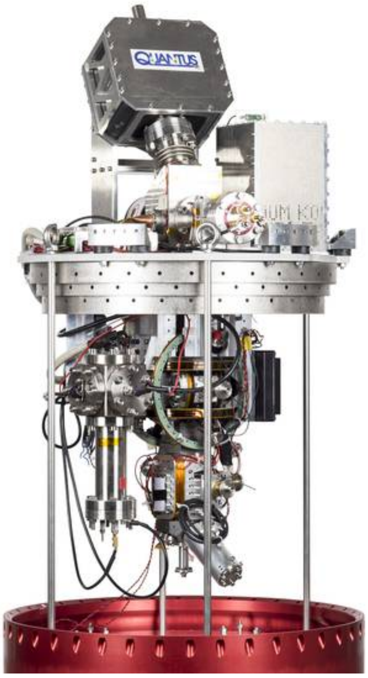

Figure 10.3.: The MAIUS-1 physics package. [79]

Those experiments are indispensable technology demonstrations required to achieve the technology readiness level (TLR) called for by spaceborne missions, like **QUEST** (Quantum Equivalence Principle Space Test). As part of the joint mission STE-QUEST it was one of four class M candidate missions within the Cosmic Vision program of the European Space Agency between 2010 and 2014. Since it provides uninterrupted zero-g conditions, it allows a free evolution time T of up to 5 s, only limited by the thermal expansion of the atomic cloud. Those long expansion times are actually not feasible with thermal atoms, but only by using a Bose-Einstein condensate (BEC).

Although in 2014 the PLATO mission was finally selected out of the four candidate mission planned for launch in 2022, the STE-QUEST assessment phase was a major step forward. What had just left behind the stage of a rough sketch in the 2010 proposal has meanwhile evolved into a well-engineered blueprint. During this study phase many parts of the mission were assessed to much higher extent than before. As part of this assessment process the examination of the relation between sensitivity and orbit design performed within this thesis confirmed that a space-borne test of the UFF based on atom interferometers is — despite its present shortcomings in TLR — definitely feasible.

A secondary result of the orbit simulation is that a well-thought-out orbit geometry might allow optimisation of the mission's overall sensitivity if not conducted as a joint-mission like STE-QUEST. Although the integrated sensitivity depends on the shape of the satellite orbit, it is much more independent of altitude than originally thought. This opens up the possibility of departing from the circular orbit proposed for MWXG. Since a slightly elliptical orbit leads to a variation of local g, it might allow identifying systematic effects or even the detection of a g dependence of the UFF violating effect. For instance the question whether the effect scales with $1/r^2$ or not can only be answered with an elliptical orbit. Therefore orbit-optimisation with respect to integrated sensitivity, susceptibility to systematic effects and the scaling of possible UFF violating effects should be performed during the further development of QUEST.

Despite those basic questions of mission design, the primary challenge for further development is of course technology readiness level. Our example of the optical phase locked loop showed that building an OPLL is pretty simple using common technology, but that there is no out-of-the box design, fulfilling the requirements posed by a high-precision experiment like QUEST. Nevertheless, a solution seems accomplishable; be it by the Microwave-Optical Local Oscillator (MOLO) or by the technique of double diffraction, comprising inherent suppression of laser phase noise.

However, any non-perfect common-mode noise suppression by double diffraction would still pose a fierce requirement on the phase noise of the frequency reference. To keep the device as simple as possible, it would be advantageous to use a frequency reference based on quartz oscillators like employed in the `Spectra Dynamics DLR-100`. Due to the strong impact of sub-Hertz phase noise, using quartz oscillators requires a further suppression of laser phase noise better than 20 dB to reach the shot-noise limit. Therefore the suppression capabilities of techniques like double diffraction should be assessed in detail.

Experiences from other fundamental physics mission like LISA show that clock noise, if posing a limit to the sensitivity, is not easy to overcome. Defining the requirements for the frequency reference at an early stage and further development of counter measures coping with clock noise in good time is strongly advisable for the continuing assessment of QUEST-like missions.

Figure 10.4.: Launch of a VSB-30 sounding rocket from ESRANGE (European Space and Sounding Rocket RANGE) near Kiruna, Lapland. [80]

Part V.

Acronyms, Lists & References

Acronyms

A

ACES	Atomic Clock Ensemble in Space
ALPS	Axion-Like Particle Search
AOCS	Attitude and Orbit Control System
ATLAS	ATom LASer

B

BEC	Bose-Einstein Condensate

C

CAPRICE	Cold Atom test of the PRInCiple of Equivalence
CAST	CERN Axion Solar Telescope
CERN	Conseil Européen pour la Recherche Nucléare
CMB	Cosmic Microwave Background
CNES	Centre national d'études spatiales

D

DESY	Deutsches Elektronen-SYnchrotron
DFB laser	Distributed FeedBack laser
DLR	Deutsches Zentrum für Luft- und Raumfahrt

E

ECDL	Extended Cavity Diode Laser
EP	Equivalence Principle
EEP	Einstein Equivalence Principle
ESA	European Space Agency
ESRANGE	European Space and sounding rocket RANGE
ESTEC	European Space research and TECnology Centre

F

FORT	Far Off-Resonant Trap
FVC	Frequency-to-Voltage Converter

G

GNSS	Global Navigation Satellite System

GTR	General Theory of Relativity
GUT	Grand Unification Theory

H

HYPER	HYPER precision cold atom interferometry in space

I

ICE	Interférometrie atomique à sources Cohérentes pour l'Espace
ICU	Instrument Control Unit

K

K	Potassium

L

LASUS	LASer Unter Schwerelosigkeit
LCT	Laser Communication Terminal
LHC	Large Hadron Collider
LISA	Laser Interferometer Space Antenna
LLI	Local Lorentz Invariance
LPI	Local Position Invariance
LSP	Lightest Supersymmetric Particle
LTI	linear, time-invariant

M

MAIUS	MAteriewellenInterferometrie Unter Schwerelosigkeit
MICROSCOPE	MICROSatellite pour l'Observation de Principe d'Equivalence
MOND	Modified Newtonian Dynamics
MOLO	Microwave-Optical Local Oscillator
MOPA	Master Oscillator Power Amplifier
MOT	Magneto Optical Trap
MSD	Microwave Synthesis and frequency Distribution
MSSM	Minimal Supersymmetric Standard Model

N

NPL	National Physical Laboratory

O

ONERA	Office National d'Etudes et de Recherches Aérospatiales

P

PHARAO	Projet d'Horloge Atomique par Refroidissement d'Atomes en Orbite
PID controller	Proportional-Integral-Derivative controller
PLATO	PLAnetary Transits and Oscillations fo stars

PTB	Physikalisch Technische Bundesanstalt

Q

QUANTUS	QUANTengase Unter Schwerelosigkeit
QCD	Quantum Chromo Dynamics
QED	Quantum Electro Dynamics
QFT	Quantum Field Theory
QUEST	QUantum Equivalence principle Space Test

R

Rb	Rubidium

S

SEP	Strong Equivalence Principle
SLAC	Stanford Linear Accelerator Center
SM	Standard Model
STR	Special Theory of Relativity
STE	Space Time Explorer
STEP	Satellite Test of the Equivalence Principle
SSS	Static Spherically Symmetric
SUGRA	SUPerGRAvity
SUSY	SUperSYmmetry
SQL	Standard Quantum Limit

T

TEXUS	Technologische EXperimente Unter Schwerelosigkeit
TOE	Theory Of Everything
TRL	Technology Readiness Level
TTL	Transistor-Transistor Logic

U

UFF	Universality of Free Fall
UGR	Universality of Gravitational Redshift
ULE	Ultra Low Expansion

V

VCO	Voltage Controlled Oscillator
VHF	Very High Frequency (30 to 300 MHz)

W

WEP	Weak Equivalence Principle
WMAP	Wilkinson Microwave Anisotropy Probe

Z

ZARM	Zentrum für Angewandte Raumfahrttechnologie und Mikrogravitation

List of Figures

List of Tables

Listings

Bibliography

[1] E. G. Adelberger and B. R. Heckel. Searches for new macroscopic forces. *Annu. Rev. Nucl. Part. Sci.*, 41:269–320, 1991. Cited on pages 3, 20, 21, 23, and 25.

[2] Jonathan Allday. *Quarks, Leptons and the Big Bang.* Taylor & Francis Group, New York, 2 edition, 2002. ISBN 0-7503-0806-0. Cited on page 1.

[3] Franklin Ascarrunz. Pair measurement of the phase noise power spectral density of the dlr-100b w/ fs010-100. private communication. Cited on pages 128, 154, 155, 194, and 198.

[4] Daniel Mader at the English Wikipedia project. `http://en.wikipedia.org/wiki/File:Mach-zender-interferometer.png`. This file is licensed under the Creative Commons Attribution-Share Alike 3.0 Unported license. Accessed 17 February 2013. Cited on pages 47 and 188.

[5] Lasunncty at the English Wikipedia project. `https://commons.wikimedia.org/wiki/File:Orbit1.svg`. This file is licensed under the Creative Commons Attribution-Share Alike 3.0 Unported license. Accessed 13 February 2013. Cited on pages 82 and 190.

[6] Metacomet at the English Wikipedia project. `http://en.wikipedia.org/wiki/File:LTI.png`. This work has been released into the public domain by its author. Accessed 18 February 2013. Cited on pages 107 and 191.

[7] ScottAlanHill at the English Wikipedia project. `http://commons.wikimedia.org/wiki/File:OrbitalEccentricityDemo.svg`. This work has been released into the public domain by its author. Accessed 13 February 2013. Cited on pages 81 and 190.

[8] S.fonsi at the German Wikipedia project. `https://commons.wikimedia.org/wiki/File:Axialtilt.svg`. This file is licensed under the Creative Commons Attribution-Share Alike 3.0 Unported license. Accessed 12 November 2012. Cited on pages 83 and 190.

[9] Various authors. Session electroweak interactions and unified theories. In *Proceedings of the 48th Rencontre de Moriond*, 2013. `http://moriond.in2p3.fr/Proceedings/2013/Moriond_EW_2013.pdf`. Cited on page 4.

[10] X. Baillard, A. Gauguet, S. Bize, P. Lemonde, Ph. Laurent, A. Clairon, and P. Rosenbusch. Interference-filter-stabilized external-cavity diode lasers. *Optics Communications*, 266:609–613, 2006. Cited on pages 120 and 121.

[11] Jacob D. Bekenstein. Fine-structure constant: Is it really constant? *Physical Review D*, 25(6):1527–1539, 1982. Cited on pages 3 and 24.

[12] Jacob D. Bekenstein. Fine-structure constant variability, equivalence principle, and cosmology. *Physical Review D*, 66:123514, 2002. Cited on page 24.

[13] P. Berg, S. Abend, G. Tackmann, C. Schubert, E. Giese, W. P. Schleich, F. A. Narducci, W. Ertmer, and E. M. Rasel. Composite-light-pulse technique for high-precision atom interferometry. *Physical Review Letters*, 114(6):063002, 2015. Cited on pages 56 and 174.

[14] Peter Berg. Analyse und unterdrückung von phasenrauschen in der atominterferometrie. Master's thesis, Universität Hannover, 2009. Cited on pages 119, 123, 133, 163, 164, 167, 169, 170, and 172.

[15] G. W. Biedermann, X. Wu, L. Deslauriers, K. Takase, and M. A. Kasevich. Low-noise simultaneous fluorescence detection of two atomic states. *Optics Letters*, 34(347-349):1527–1539, 2009. Cited on page 56.

[16] J.P. Blaser. Test mass material selection for equivalence principle experiments. *Classical and Quantum Gravity*, 18:2515–2520, 2001. Cited on pages 21, 32, and 66.

[17] Felix Bloch. Leonard isaac schiff. *Biographical Memoirs*, 54:300–323, 1983. Cited on page 19.

[18] A. Bonnin, N. Zahzam, Y. Bidel, and A. Bresson. Simultaneous dual-species matter-wave accelerometer. *Physical Review A*, 88:043615, 2013. Cited on pages 6, 7, and 33.

[19] L. Cacciapuoti, M. de Angelis, M. Fattori, G. Lamporesi, T. Petelski, M. Prevedelli, J. Stuhler, and G. M. Tino. Analog + digital phase and frequency detector for phase locking of diode lasers. *Review of Scientific Instruments*, 76:053111, 2005. Cited on pages 119, 123, and 169.

[20] Luigi Cacciapuoto. private communication, 3 June 2016. Cited on page 99.

[21] Sean M. Caroll, Sonny Mantry, Michael J. Ramsey-Musolf, and Christopher W. Stubbs. Dark-matter-induced violation of the weak equivalence principle. *Physical Review Letters*, 103:011301, 2009. Cited on pages 3 and 26.

[22] Riccardo Catena and Jan Möller. Axion-dilaton cosmology and dark energy. *arXiv:0709.1931*, 2007. Cited on pages 3 and 23.

[23] P. Cheinet, F. Pereira Dos Santos, T. Petelski, J. Le Gouët, J. Kim, K.T. Therkildsen, A. Clairon, and A. Landragin. Compact laser system for atom interferometry. *Appl. Phys. B*, 84:643–646, 2006. Cited on pages 119, 123, 167, 168, 170, and 171.

[24] Patrick Cheinet. *Conception et Réalisation d'un Gravimètre à Atomes Froids*. PhD thesis, Université Paris IV, 2006. Cited on pages 52, 56, 60, 124, 127, 150, 151, and 193.

[25] Patrick Cheinet, Benjamin Canuel, Franck Pereira Dos Santos, Alexandre Gauguet, Florence Yver-Leduc, and Arnaud Landragin. Measurement of the sensitivity function in a time-domain atomic interferometer. *IEEE Transactions on Instrumentation and Measurement*, 57:1141–1148, 2008. Cited on pages 60, 119, 123, 150, 152, 168, and 169.

[26] CNES. This document is taken from the CNES Web site cnes.fr. Protected information. All rights reserved © CNES 2016. Accessed 20 October 2016. Cited on pages 66 and 189.

[27] CNES. Cnes onera cooperation first ultra-precise measurements from microscope. `https://presse.cnes.fr/en/cnes-onera-cooperation-first-ultra-precise-measurements-microscope`. Accessed 3 October 2016. Cited on pages 66 and 67.

[28] R. Colella, A. W. Overhauser, and S. A. Werner. Observation of gravitationally induced quantum interference. *Physical Review Letters*, 34:1472–1474, 1975. Cited on page 6.

[29] Wikimedia Commons. `http://en.wikipedia.org/wiki/File:Diode_DBM.png`. This file is licensed under the Creative Commons Attribution-Share Alike 3.0 Unported license. Accessed 16 February 2013. Cited on pages 123 and 192.

[30] James A. Crawford. *Advanced phase-lock techniques.* Artech House, 2008. Cited on pages 117, 141, 144, 146, and 149.

[31] T. Damour and J.-P. Blaser. Optimizing the choice of materials in equivalence principle experiments. In *Proceedings of the 29th Rencontre de Moriond, 14th Moriond Workshop: Particle astrophysics, atomic physics and gravitation,*, volume 29, pages 433 – 440, 1994. `http://adsabs.harvard.edu/abs/1994paap.conf..433D`. Cited on pages 23, 25, 28, 29, 30, 31, 32, 38, 42, 66, 187, and 188.

[32] T. Damour and J.P. Blaser. Selection of test mass materials for equivalence principle experiments. *Adv. Space Res.*, 32(7):1335 – 1338, 2003. Cited on page 32.

[33] T. Damour, F. Piazza, and G. Veneziano. Violations of the equivalence principle in a dilaton-runaway scenario. *PHYSICAL REVIEW D*, 66:046007, 2002. Cited on pages 3 and 23.

[34] Thibault Damour. Gravitation, experiment and cosmology. `http://arxiv.org/pdf/gr-qc/9606079v1.pdf`. Accessed 17 February 2014. Cited on pages 3 and 23.

[35] Thibault Damour. Testing the equivalence principle: Why and how? *Classical and Quantum Gravity*, 13:A33–A41, 1996. Cited on pages 21, 32, 34, and 66.

[36] R. H. Dicke. Eötvös experiment and the gravitational red shift. *Am. J. Phys.*, 28:344, 1960. Cited on page 19.

[37] R. H. Dicke, P. J. E. Peebles, P. G. Roll, and D. T. Wilkinson. Cosmic black-body radiation. *Astrophysical Journal*, 142:414–419, 1965. Cited on page 24.

[38] Savas Dimopoulus, Peter W. Graham, Jason M. Hogan, and Mark A. Kasevich. Testing general relativity with atom intererometry. *PRL*, 98:111102, 2007. Cited on pages 55 and 92.

[39] W. G. Dixon. Dynamics of extended bodies in general relativity. i. momentum and angular momentum. *Proceedings of the Royal Society A*, 314:499–527, 1970. Cited on page 25.

[40] Norbert Dragon. Anmerkungen zur quantenmechanik. `http://www.itp.uni-hannover.de/~dragon/stonehenge/qm.pdf`. Accessed 17 February 2014. Cited on page 52.

[41] Xiao-Chun Duan, Xiao-Bing Deng, Min-Kang Zhou, Ke Zhang, Wen-Jie Xu, Feng Xiong, Yao-Yao Xu, Cheng-Gang Shao, Jun Luo, and Zhong-Kun Hu. Test of the universality of free fall with atoms in different spin orientations. *Physical Review Letters*, 117:023001, 2016. Cited on page 7.

[42] Albert Einstein. über den einflußder schwerkraft auf die ausbreitung des lichtes. *Annalen der Physik*, 35:898–908, 1916. Cited on page 69.

[43] Albert Einstein. *Über die spezielle und die allgemeine Relativitätstheorie.* Springer, Berlin, 23 edition, 1988. ISBN 3-540-42452-0. Cited on page 69.

[44] Albert Einstein. *Mein Weltbild/Albert Einstein.* Ullstein, Berlin, 26 edition, 1997. ISBN 3-540-42452-0. Cited on pages 3 and 16.

[45] R.v. Eötvös. über die anziehung der erde auf verschiedene substanzen. *Mathematische und Naturwissenschaftliche Berichte aus Ungarn.*, 8:65–68, 1890. Cited on page 6.

[46] W. et al. Ertmer. Matter wave explorer of gravity (mwxg). *Axp Astron*, 23:611–649, 2009. Cited on pages 8, 65, 67, 68, 69, 76, 178, 189, and 196.

[47] W. et al. Ertmer. Hyper: Hyper precision atom interferometry in space – a proposal for flexi-mission f2 or f3 in fundamental physics. Technical report, HYPER Science Team, January 2000. Cited on pages 8, 67, 178, and 189.

[48] ESA. Esa science & technology: Plato. `http://http://sci.esa.int/plato/`. Accessed 29 March 2014. Cited on pages 77 and 100.

[49] ESA. Ste-quest mission status. `http://sci.esa.int/ste-quest/49263-status/`. Accessed 24 February 2014. Cited on pages 77 and 100.

[50] ESA. Hyper: Hyper precision atom interferometry in space - assessment study report. Technical Report ESA-SCI(2000), European Space Agency, 10, July 2000. Cited on pages 67 and 178.

[51] ESA. Space-time explorer assessment study. Technical report, Euroepan Space Agency, 2010. Cited on page 76.

[52] ESA. Ste-quest (space-time explorer and quantum equivalence principle space test: A class m mission proposal for cosmic vision 2015-2025. Technical report, STE-QUEST Team, December 2010. Cited on pages 8, 65, 67, 69, 72, 73, 76, 95, and 189.

[53] ESA. Ste-quest: Concurrent design facility (cdf). Technical report, European Space Agency, 2011. Cited on pages 65, 70, 71, and 189.

[54] ESA. Ste-quest: Technology readiness review for atom interferometry in space (trr). Technical report, STE-QUEST Science Team, 2011. Cited on pages 65 and 73.

[55] ESA. Ste-quest: Mission analysis guidlines (mag). Technical Report Issue1, Revision 2, European Space Agency, January 2012. Cited on pages 65, 75, 76, 77, 190, and 197.

[56] ESA. Ste-quest: Mission requirements document (mrd). Technical report, European Space Agency, 2012. Cited on page 65.

[57] ESA. Ste-quest: Payload definition document (pdd). Technical report, European Space Agency, 2012. Cited on pages 65, 71, 72, 74, 189, and 190.

[58] ESA. Ste-quest: Science requirements document (srd). Technical report, European Space Agency, 2012. Cited on pages 65, 70, 76, 99, and 197.

[59] ESA. Ste-quest: Assessment study report (yellow book). Technical report, STE-QUEST Team, 2013. Cited on pages 65, 74, 75, and 197.

[60] A. M. Nobili et al. 'galileo galilei' (gg): space test of the weak equivalence principle to 10^{-17} and laboratory demonstrations. *Class. Quantum Grav.*, 29, 2012. Cited on pages 66 and 67.

[61] A. Peters et al. Measurement of gravitational acceleration by dropping atoms. *Nature*, 400:849–852, 2004. Cited on pages 6, 7, 48, and 59.

[62] A. Vogel et al. Bose-einstein condensates in microgravity. *Applied Physics B: Lasers and Optics*, 84:663, 2006. Cited on page 68.

[63] G. Hinschaw et al. Nine-year wilkinson microwave anisotropy probe (wmap) observations: Cosmological parameter results. *The Astrophysical Journal*, 208(2):19, 2013. Cited on page 1.

[64] G. Stern et al. Light-pulse atom interferometry in microgravity. *Eur. Phys. J. D*, 53:353–357, 2009. Cited on page 63.

[65] G.M. Tino et al. Precision gravity tests with atom interferometry in space. *Nuclear Physics B (Proc. Suppl.)*, 243–244:203–214, 2013. Cited on page 67.

[66] H. Müntinga et al. Interferometry with bose-einstein condensates in microgravity. *Physical Review Letters*, 110:093602, 2013. Cited on page 68.

[67] J. Rudolph et al. Degenerate quantum gases in microgravity. *Microgravity Science and Technology*, 23:287, 2011. Cited on page 68.

[68] J. Rudolph et al. A high-flux bec source for mobile atom interferometers. *New Journal of Physics*, 17:065001, 2015. Cited on page 68.

[69] K. Bongs et al. Realization of a magneto-optical trap in microgravity. *Journal of Modern Optics*, 54:2513, 2007. Cited on page 68.

[70] R. Pegna et al. Abatement of thermal noise due to internal damping in 2d oscillators with rapidly rotating test masses. *Physical Review Letters*, 107:200801, 2011. Cited on page 67.

[71] T. Könemann et al. A freely falling magneto-optical trap drop tower experiment. *Applied Physics B: Lasers and Optics*, 89:431, 2007. Cited on page 68.

[72] W. Ertmer et al. Towards atomic quantum sensors in microgravity. *Nuclear Physics B - Proceedings Supplements*, 166:307, 2007. Cited on page 68.

[73] P. Fayet. Theoretical motivations for equivalence principle tests and searches for new long-range forces. *Proceedings of the 31. Rencontres de Moriond, Dark Matter in Cosmology, Quantum Measurement and Experimental Gravitation*, 31:379, 1996. Cited on pages 3, 23, and 31.

[74] Walter Fichter, Ulrich Johann, Giorgio Bagnasco, and Phil Airey. Spacecraft design for cold atom interferometry in space. Technical report, European Space Agency, 1 December 2003. Cited on page 67.

[75] Ephraim Fischbach, Daniel Sudarsky, Aaron Szafer, Carrick Talmadge, and S. H. Aronson. Reanalysis of the eötvös experiment. *Physical Review Letters*, 56:1427, 1986. Cited on pages 20 and 22.

[76] Nobel Foundation. All nobel prizes in physics. `http://www.nobelprize.org/nobel_prizes/physics/laureates/`. Accessed 12 February 2014. Cited on pages 3, 4, 22, and 49.

[77] Sebastian Fray, Cristina Alvarez Diez, Theodor W. Hänsch, and Martin Weitz. Atomic interferometer with amplitude gratings of light and its applications to atom based tests of the equivalence. *Phys.Rev.Lett.*, 93:240404, 2004. Not cited.

[78] Sebastian Fray, Cristina Alvarez Diez, Theodor W. Hänsch, and Martin Weitz. Atomic interferometer with amplitude gratings of light and its applications to atom based tests of the equivalence principle. *Physical Review Letters*, 93:240404, 2007. Cited on pages 6 and 7.

[79] Zentrum für angewandte Raumfahrttechnologie und Mikrogravitation (ZARM). Quantus iv – maius. `https://www.zarm.uni-bremen.de/en/research/space-technologies/fundamental-physics-tests-in-space/projects/quantus-iv-maius.html`. Accessed 24 January 2017. Cited on pages 179 and 196.

[80] Deutsches Zentrum für Luft-und Raumfahrt (DLR). Forschung unter schwerelosigkeit. `http://www.dlr.de/dlr/desktopdefault.aspx/tabid-10212/332_read-2153/year-2011/#/gallery/4142`. Accessed 24 January 2017. Cited on pages 180 and 196.

[81] Deutsches Zentrum für Luft-und Raumfahrt (DLR). Maius 1: Erstes bose-einstein-kondensat im all erzeugt. `http://www.dlr.de/dlr/desktopdefault.aspx/tabid-10081/151_read-20337/#/gallery/25194`. Accessed 24 January 2017. Cited on page 179.

[82] Floyd M. Gardner. *Phaselock techniques.* John Wiley & Sons, Inc., 2005. Cited on pages 118, 123, 124, 125, 146, and 192.

[83] A. Gauguet, B. Canuel, T. Lévèque, W. Chaibi, and A. Landragin. Characterization and limits of a cold-atom sagnac interferometer. *Physical Review A*, 80(6):063604, 2009. Cited on page 56.

[84] M. Gilowski, Ch. Schubert, M. Zaiser, W. Herr, T. Wübbena, T. Wendrich, T. Müller, E.M. Rasel, and W. Ertmer. Narrow bandwidth interference filter-stabilized diode laser systems for the manipulation of neutral atoms. *Optics Communications*, 280:443–447, 2007. Cited on pages 120, 121, and 192.

[85] Michael Gilowski. Aufbau und charakterisierung eines raman-lasersystems zur sagnac-interferometrie mit kalten atomen. Master's thesis, Leibniz Universität Hannover, 2005. Cited on pages 127 and 129.

[86] Michael Gilowski. *Quantitative Analyse der Auflösungsbegrenzung eines atomaren Gyroskops.* PhD thesis, Leibniz Universität Hannover, 2010. Cited on pages 52 and 53.

[87] Domenico Giulini. Equivalence principle, quantum mechanics, and atom-interferometric tests. *arXiv:1105.0749v2*, 2011. Cited on pages 17, 18, and 20.

[88] Ertan Göklü and Claus Lämmerzahl. Metric fluctuations and the weak euqivalence principle. *Classical and Quantum Gravity*, 25:105012 (10pp), 2008. Cited on pages 3 and 26.

[89] J. Le Gouët, P. Cheinet, J Kim, D. Holleville, A. Clairon, A. Landragin, and F. Pereira Dos Santos. Influence of lasers propagation delay on the sensitivity of atom interferometers. *The European Physikal Journal D*, 44:419–425, 2007. Cited on pages 61 and 119.

[90] J. Le Gouët, J. Kim, C. Bourassin-Bouchet, M. Lours, A. Landragin, and F. Pereira Dos Santos. Wide bandwidth phase-locked diode laser with an intra-cavity electro-optic modulator. *Optics Communications*, 282:977–980, 2009. Cited on pages 119, 123, 169, 170, 172, and 173.

[91] Julien Le Gouët. *Etude des Performances d'un Gravimètre Atomique Absolu: Sensibilitè Limite et Exactitude Préliminaire.* PhD thesis, Université Paris XI, 2008. Cited on pages 60 and 61.

[92] Peter W. Graham, Igor G. Irastorza, Steven K. Lamoreaux, Axel Lindner, and Karl A. van Bibber. Experimental searches for the axion and axion-like particles. *Annual Review of Nuclear and Particle Science*, 65:485–514, 2015. Cited on page 23.

[93] Domenico Guilini. Ergänzungen zur klassischen physik: Einführung in die allgemeine relativitätstheorie, Vorlesung Wintersemester 2009/2010. Cited on pages 3, 4, 13, and 16.

[94] P. Hamilton, T. Barter, G. Kim, B. Mukherjee, and H. Müller. Progress towards a test of the universality of free fall using a ˆ6Li-ˆ7Li atom interferometer. In *APS Division of Atomic, Molecular and Optical Physics Meeting Abstracts*, 2012. Cited on pages 33 and 36.

[95] William Happer, James Peebles, and David Wilkinson. Obituary: Robert henry dicke. *Physics Today*, 50:92–94, 1997. Cited on page 19.

[96] J. Hartwig, S. Abend, C. Schubert, D. Schlippert, H. Ahlers, K. Posso-Trujillo, N. Gaaloul, W. Ertmer, and E. M. Rasel. Testing the universality of free fall with rubidium and ytterbium in a very large baseline atom interferometer. *New Journal of Physics*, 17:035011, 2015. Cited on page 33.

[97] Jonas Hartwig. *Analyse eines Atomaren Gravimeters hinsichtlich eines Quantentest des Äquivalenzprinzips.* PhD thesis, Leibniz Universität Hannover, 2013. Cited on pages 56, 60, 61, 63, 66, 123, 127, 132, 134, 141, 152, and 171.

[98] Gerhard Heinzel. Resonant sideband extraction – neuartige interferometrie für gravitationswellendetektoren. Master's thesis, Universität Hannover, 1995. Cited on pages 134 and 168.

[99] Waldemar Herr. Realisierung eines schmalbandigen diodenlasersystems hoher ausgangsleistung zur rauscharmen detektion und manipulation von ^{87}rb-atomen mit hilfe der atom-licht-wechselwirkung. Master's thesis, Universität Hannover, 2007. Cited on pages 120, 121, and 123.

[100] Waldemar Herr. *Eine kompakte Quelle quantenentarteter Gase hohen Flusses für die Atominterferometrie unter Schwerelosigkeit.* PhD thesis, Leibniz Universität Hannover, 2013. Cited on pages 68, 73, and 179.

[101] Jason M. Hogan, David M. S. Johnson, and Mark A. Kasevich. Light-pulse atom interferometry. *arXiv:0806.3261*, 2008. Cited on page 59.

[102] Michael A. Hohensee and Holger Müller. Precision tests of general realtivity with matter waves. *Journal of Modern Optics*, 58(21):2021–2027, 2011. Cited on pages 3, 25, and 35.

[103] Michael A. Hohensee and Holger Müller. Equivalence principle and bound kinetic energy. *Physical Review Letters*, 111:151102, 2013. Cited on page 25.

[104] Paul Horowitz. *The art of electronics.* Cambridge University Press, 1980. Cited on page 141.

[105] Onur Hosten, Nils J. Engelsen, Rajiv Krishnakumar, and Mark A. Kasevich. Measurement noise 100 times lower than the quantum-projection limit using entangled atoms. *Nature*, 529(7587):505–508, 2016. Cited on page 57.

[106] IAEA. Live chart of nuclides, nuclear structure and decay data. `https://www-nds.iaea.org/relnsd/vcharthtml/VChartHTML.html`. Accessed 3 October 2012. Cited on pages 33 and 197.

[107] Perimeter Institute. Smolin's faculty page. `http://www.perimeterinstitute.ca/people/Lee-Smolin`. Accessed 13 February 2017. Cited on page 2.

[108] Agenzia Spaziale Italiana and Instituto Nationale di Fisica Nucleare. Phase a-2 study report – galileo galieli (gg) – a small satellite to test the equivalence principle of galilei, newton and einstein. Technical report, Agenzia Spaziale Italiana, April 2009. Cited on pages 66 and 67.

[109] Stefan Jöllenbeck. Realisierung einer kalten atomquelle zum beladen einer optischen dipolfalle. Master's thesis, Universität Hannover, 2008. Cited on page 123.

[110] David Kaplan and Mark B. Wise. Couplings of a light dilaton and violations of the equivalence principle. *JHEP*, 08(037), 2000. Cited on page 23.

[111] Stephen Kemble. Hyper initial feasibility study – orbit trade-off report. Technical Report HYP-1-01, Astrium Ltd, 19 March 2003. Cited on page 68.

[112] T. Kovachy, P. Asenbaum, C. Overstreet, C. A. Donnelly, S. M. Dickerson, A. Sugarbaker, J. M. Hogan, and M. A. Kasevich. Quantum superposition at the half-metre scale. *Nature*, 528:530–533, 2015. Cited on page 60.

[113] Shau-Yu Lan, Pei-Chen Kuan, Brian Estey, Philipp Haslinger, and Holger MÃ$\frac{1}{4}$ller. Influence of the coriolis force in atom interferometry. *Physical Review Letters*, 108:090402, 2012. Cited on page 59.

[114] T. Lévèque, A. Gauguet, F. Michaud, F. Pereira Dos Santos, and A. Landragin. Enhancing the area of a raman atom interferometer using a versatile double-diffraction technique. *Physical Review Letters*, 103:080405, 2009. Cited on page 174.

[115] Karl H. Lieser. *Einführung in die Kernchemie*. Wiley-VCH, 2001. Cited on page 31.

[116] John Maushammer. `http://en.wikipedia.org/wiki/File:Laser_diode_with_the_case_and_window_removed-powered_off.jpg`. This file is licensed under the Creative Commons Attribution-Share Alike 3.0 Unported license. Accessed 17 February 2013. Cited on pages 119 and 192.

[117] J. M. McGuirk, G. T. Foster, J. B. Fixler, M. J. Snadden, and M. A. Kasevich. Sensitive absolute-gravity gradiometry using atom interferometry. *Physical Review A*, 65:033608, 2002. Cited on page 61.

[118] S. Merlet, Q. Bodart, N. Malossi, A. Landragin, F. P. D. Santos, O. Gitlein, and L. Timmen. Comparison between two mobile absolute gravimeters: optical versus atomic interferometers. *Metrologia*, 47:L9–L11, 2010. Cited on pages 6 and 7.

[119] Ernst Messerschmid and Stefanos Fasoulas. *Raumfahrtsysteme: eine Einführung mit Übungen und Lösungen*. Springer, Berlin, 4 edition, 2011. ISBN 978-3-642-12816-5. Not cited.

[120] J. E. Moody and Frank Wilczek. New macroscopic forces? *Physical Review D*, 30:130, 1984. Cited on pages 3 and 25.

[121] Tobias Müller. *Realisierung eines Atominterferometers zur hochauflösenden Inertialsensorik mit kalten Rubidiumatomen*. PhD thesis, Universität Hannover, 2006. Cited on page 52.

[122] Vitali Müller. *Orbit Simulation Toolkit - OSTK - Documentation of Models, Methods and Implementation*. Bsc. thesis, Leibniz Universität Hannover, 2010. Cited on page 83.

[123] NASA. `https://www.nasa.gov/centers/goddard/news/topstory/2007/lsso2.html`. This file is in the public domain in the United States because it was solely created by NASA. NASA copyright policy states that "NASA material is not protected by copyright unless noted". Accessed 15 February 2017. Cited on pages 7 and 187.

[124] NASA. `http://www.hq.nasa.gov/office/pao/History/alsj/a11/AS11-40-5952.jpg`. This file is in the public domain in the United States because it was solely created by NASA. NASA copyright policy states that "NASA material is not protected by copyright unless noted". Accessed 15 February 2017. Cited on pages 7 and 187.

[125] NASA. `http://www.nasa.gov/mission_pages/calipso/multimedia/cloud_calip_mm.html`. Accessed 1 September 2012. Cited on pages 65 and 189.

[126] M. Novara and R. Reinhard. Hyper: Hyper precision cold atom interferometry in space – report of the concurrent design facility session at esa/estec. Technical Report ESA document number CDF-09, European Space Agency, September 2000. Cited on page 67.

[127] John J. O'Connor and Edmund F. Robertson. Biography of oskar klein at mactutor history of mathematics archive. `http://www-history.mcs.st-andrews.ac.uk/Biographies/Klein_Oskar.html`. Accessed 3 October 2016. Cited on page 23.

[128] Institute of Quantum Optics. Quantum gases in microgravity. `https://www.iqo.uni-hannover.de/quantus.html`. Accessed 20 October 2016. Cited on page 68.

[129] ON Semiconductor. *MCH12140, MCK12140 – Phase-Frequency Detector, Datasheet*, July 2006. Cited on pages 124 and 192.

[130] James Overduin, Francis Everitt, Paul Worden, and John Mester. Step and fundamental physics. *Class. Quantum Grav.*, 29, 2012. Cited on pages 66 and 67.

[131] Torsten Petelski. *Atom Interferometers for Precision Gravity Measurements.* PhD thesis, Université Paris VI, 2005. Not cited.

[132] Achim Peters. *High precision Gravity Measurements using Atom Intereromerty.* PhD thesis, Stanford University, 1998. Cited on pages 54, 55, and 59.

[133] R.V. Pound and J.L. Snider. Effect of gravity on nuclear resonance. *Physical Review Letter*, 13(18):539–540, 1964. Cited on page 70.

[134] C. V. Raman. A new radiation. *Indian Journal of Physics*, 2:387, 1928. Cited on page 49.

[135] Fritz Riehle. *Frequency Standards: Basics and Applications.* WILEY-VCH Verlag, Weinheim, 1st edition, 2004. Cited on pages 142, 143, 146, 148, and 193.

[136] Christina Rode. Aufbau eines kompakten lasersystems zur kühlung der isotope von rubidium und kalium. Master's thesis, Universität Hannover, 2009. Cited on pages 120, 123, and 192.

[137] P. G. Roll, R. Krotkov, and R. H. Dicke. The equivalence of inertial and passive gravitational mass. *Annals of Physics*, 26(26):442–517, 1964. Cited on page 6.

[138] Georges Sagnac. L'éther lumineux démontré par l'effet du vent relativ d'éther dans un interféromètre en rotation uniforme. *Comptes Rondus*, 157:708–710, 1913. Cited on page 48.

[139] Georges Sagnac. Sur la preuve de la réalité de l'éther lunineux par l'expérience de l'interférographie tournant. *Comptes Rondus*, 157:1410–1413, 1913. Cited on page 48.

[140] L. I. Schiff. On experimental tests of the general theory of relativity. *Am. J. Phys.*, 28:349, 1960. Cited on page 19.

[141] S. Schlamminger, K.-Y. Choi, T. A. Wagner, J. H. Gundlach, and E. G. Adelberger. Test of the equivalence principle using a rotating torsion balance. *Physical Review Letters*, 100:041101, 2008. Cited on page 6.

[142] D. Schlippert, J. Hartwig, H. Albers, L. L. Richardson, C. Schubert, A. Roura, W. P. Schleich, W. Ertmer, and E. M. Rasel. Quantum test of the universality of free fall. *Physical Review Letters*, 112:203002, 2014. Cited on pages 6, 7, 8, 33, and 36.

[143] Dennis Schlippert. *Quantum Tests of the Universality of Free Fall.* PhD thesis, Leibniz Universität Hannover, 2014. Cited on page 60.

[144] M. Schmidt, M. Prevedelli, A. Giorgini, G.M. Tino, and A. Peters. A portable laser system for high-precision atom interferometry experiments. *Applied Physics B*, 102:11–18, 2011. Cited on pages 119, 123, 167, 169, 170, 172, and 173.

[145] Walter Schottky. über spontane stromschwankungen in verschiedenen elektrizitätsleitern. *Annalen der Physik*, 57:541–567, 1918. Cited on page 145.

[146] C. Schubert, J. Hartwig, H. Ahlers, K. Posso-Trujillo, N. Gaaloul, U. Velte, A. Landragin, A. Bertoldi, B. Battelier, P. Bouyer, F. Sorrentino, G. M. Tino, M. Krutzik, A. Peters, S. Herrmann, C. Lämmerzahl, L. Cacciapouti, E. Rocco, K. Bongs, W. Ertmer, and E. M. Rasel. Differential atom interferometry with ^{87}rb and ^{85}rb for testing the uff in ste-quest, 2013. Cited on pages 34 and 99.

[147] Christian Schubert. Realisierung eines schmalbandigen diodenlasersystems hoher ausgangsleistung für präzisionsmessungen an 87-rb atomen. Master's thesis, Leibniz Universität Hannover, 2007. Cited on pages 121, 122, and 192.

[148] Christian Schubert. personal communication, 2012. Cited on page 93.

[149] S.H. Shoaf. Frequency stability specification and measurement: High frequency and microwave. Technical Report NBS Technical Note 632, National Bureau Of Standards, 1973. Cited on page 149.

[150] J. Simmons. *The Scientific 100*. Citadel Press Book, 1996. Cited on page 3.

[151] K. Simonyi. *Kulturgeschichte der Physik*. Verlag Harri Deutsch, 2001. Cited on pages 3, 5, 6, 31, 47, 79, and 187.

[152] A. Smekal. Zur quantentheorie der dispersion. *Die Naturwissenschaften*, 11(43):873–875, 1923. Cited on page 49.

[153] G. Smith, E. G. Adelberger, B. R. Heckel, and U. Su. Test of the equivalence principle for ordinary matter falling towards dark matter. *Physical Review Letters*, 70:123–126, 1993. Cited on page 26.

[154] Lee Smolin. *The trouble with physics*. Houghton Mifflin Company, 2006. Cited on page 2.

[155] Daniel Adam Steck. Rubidium 87 d line data. Technical Report Revision 2.1.4, Oregon Center for Optics and Department of Physics, University of Oregon, 2010. Cited on page 120.

[156] R. C. Steele. Optical phase-locked loops using semiconductor laser diodes. *Electronic Letters*, 19(2):69–70, 1983. Cited on pages 119 and 169.

[157] Felix Steinebach. Interferenzfilterstabilisierte diodenlaser für licht bei 780 nm. Master's thesis, Technische Universität Darmstadt, 2007. Cited on page 120.

[158] J. K. Stockton, K. Takase, and M. A. Kasevich. Absolute geodetic rotation measurement using atom interferometry. *Physical Review Letters*, 107(13):133001, 2011. Cited on page 56.

[159] Claus Lämmerzahl Sven Herrmann, Hansjörg Dittus. Testing the equivalence principle with atomic interferometry. *Class. Quantum Grav.*, 29:184003–184015, 2012. Cited on page 179.

[160] Laszlo Szerdahelyi, Walter Fichter, and Alexander Schleicher. Hyper – secondary aocs design. Technical Report HYP-2-01, Astrium Ltd, 28 May 2003. Cited on page 68.

[161] M. Niebauer T. P. McHugh M. and J.Ė. Faller. Galilean test for the fifth force. *Physical Review Letters*, 59:609, 1987. Cited on page 6.

[162] M. G. Tarallo, T. Mazzoni, N. Poli, D. V. Sutyrin, X. Zhang, and G. M. Tino. Test of einstein equivalence principle for 0-spin and half-integer-spin atoms: Search for spin-gravity coupling effects. *Physical Review Letters*, 113:023005, 2014. Cited on pages 6, 7, and 33.

[163] T. R. Taylor and G. Veneziano. Dilaton couplings at large distances. *Physics Letters B*, 213:450–454, 1988. Cited on page 23.

[164] H. R. Telle and H. Li. Phase-locking of diode lasers. *Electronic Letters*, 26(13):858–859, 1990. Cited on pages 119, 123, and 169.

[165] P. Touboul, G. Métris, V. Lebat, and A. Robert. The microscope experiment, ready for the in-orbit test of the equivalence principle. *Classical and Quantum Gravity*, 29(18), 2012. Cited on page 66.

[166] Eötvös Loránd University. Brief history of ELTE. `http://www.elte.hu/de/elte_brief_history`. Accessed 12 February 2014. Cited on page 6.

[167] Jean-Philippe Uzan. The fundamental constants and their variations: observational status and theoretical motivations. *arXiv:hep-ph/0205240v1*, 2002. Cited on pages 2 and 24.

[168] R. v. Eötvös, D. Pekár, and E. Fekete. Beiträge zum gesetze der proportionalität von trägheit und gravität. *Annalen der Physik (Leipzig)*, 68:11, 1922. Cited on page 6.

[169] David A. Vallado and Wayne D. McClain. *Fundamentals of astrodynamics and applications*, volume 21 of *Space technology library.* Microcosm Press [u.a.], Hawthorne, Calif., 3. ed. edition, 2007. Cited on page 83.

[170] Tim van Zoest. *Realiserung erster quantenentarteter Gase unter Schwerelosigkeit.* PhD thesis, Leibniz Universität Hannover, 2008. Cited on pages 68 and 179.

[171] T. van Zoest et al. Bose-einstein condensation in microgravity. *Science*, 328:1540–1543, 2010. Cited on pages 68 and 179.

[172] Gaël Varoqaux. *Sources atomiques pour senseur inertiels interféromt́riques à long temps d'interrogation.* PhD thesis, Université Paris 11, 2006. Not cited.

[173] R. F. C. Vessot, M. W. Levine, E. M. Mattison, E. L. Blomberg, T. E. Hoffman, G. U. Nystrom, B. F. Farrel, R. Decher, P. B. Eby, C. R. Baugher, J. W. Watts, D. L. Teuber, and F. D. Wills. Test of relativistic gravitation with a space-borne hydrogen maser. *Phys. Rev. Lett.*, 45:2081–2084, Dec 1980. Cited on page 70.

[174] Thijs Wendrich. *High resolution rotation sensor based on cold atom interferometry.* PhD thesis, Leibniz Universität Hannover, 2010. Cited on pages 154, 156, and 194.

[175] C. Wetterich. Cosmology and the fate of dilaton symmetry. *Nuclear Physic B*, 302:668, 1988. Cited on pages 2 and 24.

[176] C. Wetterich. Conformal fixed point, cosmological constants and quintessence. *hep-th/0210156*, 2003. Cited on page 24.

[177] C. Wetterich. Crossover quintessence and cosmological history of fundamental constants. *Physic Letters B*, 561:10–16, 2003. Cited on pages 3 and 24.

[178] Clifford M. Will. The confrontation between general relativity and experiment. `http://arxiv.org/abs/gr-qc/0103036`, 2001. Cited on pages 3, 5, 16, 17, 18, 19, 20, 21, 22, and 187.

[179] Clifford M. Will. The confrontation between general relativity and experiment. `http://www.livingreviews.org/lrr-2006-3`, 2006. Cited on page 22.

[180] James G. Williams, Slava G. Turyshev, and Dale H. Boggs. Progress in lunar laser ranging tests of relativistic gravity. *Physical Review Letters*, 93:261101, 2004. Cited on pages 6 and 19.

[181] Jason Williams, Sheng wey Chiow, Nan Yu, and Holger Müller. Quantum test of the equivalence principle and space-time aboard the international space station. *New Journal of Physics*, 18, 2016. Cited on page 67.

[182] Nils Winter. nn. Master's thesis, nn, 2010. Cited on pages 104 and 122.

[183] D. Wuensch. The fifth dimension: Theodor kaluza's ground-breaking idea. *Annalen der Physik (Leipzig)*, 12:519–542, 2003. Cited on page 23.

[184] Randall Munroe (xkcd.com). Einstein. `http://www.xkcd.com/1206/`. This work is licensed under a Creative Commons Attribution-NonCommercial 2.5 License. Cited on page 245.

[185] Maic Zaiser. *Eine Quelle quantenentarteter Gase für die Atominterferometrie*. PhD thesis, Leibniz Universität Hannover, 2010. Cited on page 123.

[186] L. Zhou, Z. Y. Xiong, W. Yang, B. Tang, W. C. Peng, K. Hao, R. B. Li, M. Liu, J. Wang, and M. S. Zhan. Development of an atom gravimeter and status of the 10-meter atom interferometer for precision gravity measurement. *Gen. Relat. Gravit.*, 43:1931–1942, 2011. Cited on pages 33, 36, and 63.

[187] Lin Zhou, Shitong Long, Biao Tang, Xi Chen, Fen Gao, Wencui Peng, Weitao Duan, Jiaqi Zhong, Zongyuan Xiong, Jin Wang, Yuanzhong Zhang, and Mingsheng Zhan. Test of equivalence principle at 10^{-8} level by a dual-species double-diffraction raman atom interferometer. *Physical Review Letters*, 115:013004, 2015. Cited on pages 6 and 7.

[188] P. Zorabedian and Jr. W. R. Trutna. Interference-filter-tuned, alignment-stabilized, semiconductor external-cavity laser. *Optics Letters*, 13:826–828, 1988. Cited on pages 120 and 121.

Part VI.

Appendix

A. Technology Readiness Level (TRL)

Instruments and spacecraft sub-systems are classified according to a “Technology Readiness Level” (TRL) on a scale of 1 to 9. Levels 1 to 4 relate to creative, innovative technologies before or during mission assessment phase. Levels 5 to 9 relate to existing technologies and to missions in definition phase.

If the TRL is too low, then a mission risks being jeopardized by delays or cost over-runs. It is a responsibility of the Advanced Studies and Technology Preparation Division to promote the technology readiness at a very early stage in order to make new missions feasible.

ESA Technology Readiness Level Summary

TRL	**Level description**
1	Basic principles observed and reported
2	Technology concept and/or application formulated
3	Analytical & experimental critical function and/or characteristic proof-of-concept
4	Component and/or breadboard validation in laboratory environment
5	Component and/or breadboard validation in relevant environment
6	System/subsystem model or prototype demonstration in a relevant environment (ground or space)
7	System prototype demonstration in a space environment
8	Actual system completed and “Flight qualified” through test and demonstration (ground or space)
9	Actual system “Flight proven” through successful mission operations

B. STE-QUEST orbit simulation

The orbit simulation is organised in the C++ class `KeplerProgram`, which automatically initialises the orbit, contains the orbit propagation loop and some helper methods for saving the data. Thus, it is possible to write a complete orbit simulation for STE-QUEST within less than 30 lines of code, as demonstrated in listing B.1. The header file of the class `KeplerProgram` is displayed in listing B.2, the source code is in listing B.3

Listing B.1: Exemplary main program of the STE-QUEST orbit simulation.

```
//===============================================================================//
// Name        : main.cpp                                                        //
// Author      : Ulrich Velte                                                    //
// Date        : 2013-03-20                                                      //
// Version     : 2.1                                                             //
// Copyright   : GNU GPL                                                         //
// Description : This calculates the sensitivity of the STE-QUEST mission        //
//               on a per-orbit base. The integrated sensitivity starting from   //
//               beginning of the mission and some other parameters are          //
//               calculated and written to file. The orbit is varied over a      //
//               a five year period according to the baseline orbit defined in   //
//               Mission Analysis Guidelines, MAG, Issue 1, Revision 2,          //
//               as of 01/2012.                                                  //
//                                                                               //
//               The output is written to one files:                             //
//                1. out_outerloop, summary for every orbit                      //
//                2. Verbose output for single events, out_all, is deactivated   //
//=================================================================================

#include "KeplerProgram.h"

// Calculate drift of the orbit over the 5 year mission
// Inptut: mission time in orbits = days*3/2 = years*365*3/2
// returns: perigee altitude [m]
double DriftOrbit (double orbit) {
 return  2200e3*cos((orbit/(365*3/2)-2.95)/M_PI*1.34);
}


int main() {
  // Create Simulation object
  KeplerProgram *KP = new KeplerProgram();
  KP->verbose=0;

  // Set Kepler Elements
```

```
  KP->perigee=DriftOrbit(0);
  KP->SMA=32090e3;

  double IntSens = 0; // Integrated sensitivity
  double N_shots=0; // Number of measurements during mission

  // Turn on gravity gradient
  KP->g_grad=1;

  // Open files, write file header
  KP->InitOuterFiles("../OrbitData/DriftOrbit_grad.ASC");
  KP->out_outerloop << "# Sensitivity STE-QUEST AI, depending on orbit height\n";
  KP->out_outerloop << "# mission time [orbits]\tperigee[m]\talt_max[m]\tN_shots\t
                        t_int[s]\tS_eta per orbit\toverall S_eta\n";

  // START OF OUTER LOOP FOR PARAMETER VARIATION
  for (int orbit = 1; orbit<=6*365*3/2; orbit++) {
    KP->perigee=DriftOrbit(orbit);
    KP->OrbitSimulationLoop();
    // For identical orbits (identical orbits only)
    //IntSens+=pow(KP->S_eta_orbit,2);
    // Sum up individual measurements rather than orbits
    IntSens+=pow(KP->S_eta_orbit*KP->N_shots,2);
    // Overall number of measurements during mission
    N_shots+=KP->N_shots;
    // Write results to file
    KP->out_outerloop << orbit << "\t" << KP->perigee << "\t" << KP->h_AI
                      << "\t" << KP->N_shots << "\t" << KP->N_shots*KP->timestep
                      << "\t" << KP->S_eta_orbit << "\t" << "\t"
                      << sqrt(IntSens)/N_shots << endl;
    // Write results to screen
    cout << "****** day " << (int)(orbit/3*2) << ": perigee = "
         << KP->perigee/1000 << " km -> integrated sensitivity = "
         << sqrt(IntSens)/N_shots << " ******\n";
  }
  // END OF PARAMETER VARIATION LOOP

  // Close Files
  KP->CloseFiles();

  // Close output streams
  delete KP;
}

//EOF
```

Listing B.2: Header file of the STE-QUEST orbit simulation.

```
//===============================================================================//
// Name        : KeplerProgram.h                                                 //
// Author      : Ulrich Velte                                                    //
// Date:       : 2012/11/01                                                      //
// Version     : 2.0                                                             //
```

```
// Copyright   : GNU GPL                                                         //
// Description : Header file for the class KeplerProgram.                        //
//===============================================================================//

#include "lutils.h"
#include "kepler.h"
#include <cmath>
#include <iostream>
#include <fstream>
using namespace std;


class KeplerProgram {


public:
  KeplerProgram(); // Constructor
  ~KeplerProgram(); //Destructor

// Methods
  int InitOuterFiles(char outer_name[]);
  void InitOrbitFiles(char all_name[], char sens_name[], char part_name[]);
  void CloseFiles();
  void OrbitSimulationLoop();
  void OrbitSimulationLoop(double nu_end);

// Kepler propagator and Kepler elements
  tkepl kepl;
  tkepl_elem elements;

// Verbose settings
  // 0: run silently
  // 1: output EP results
  // 2: output Kepler parameters also
  // 3: output results for every step in numerical orbit simulation
  int verbose;

// Some constants
  static const double GM = 398600.44150E+09; // GM value for earth
  static const double R_E = 6371e3; // Earth radius
  static const double kB = 1.3806488e-23; // [J/K]
  static const double m_87Rb = 1.443e-25; // atomic mass [kg]
  // If your compiler doesn't like doubles to be declared in the header file,
  // move them to the source file

// Variables used in the simulation
  double pos[3];
  double vel[3];
  double t; // set start time to zero
  double N_orbits; // Number of orbits to reach target sensitivity
  double N_shots; // Number of shots below alt_max
  double D_eta;
  double S_eta;
```

```
  double S_eta_orbit;
  double r_old;
  double nu_old;
  double h_AI;
  int step;

// Parameters of the atomic source
  double sigma_r; // initial size of the atom cloud [m]
  double T_at; // temperature of atomic cloud at release time [K]

// Parameters of the AI
  double k_eff;//2*1.6e7; // effective k vektor for double diffraction
  double T; // time T between Raman pulses [s]
  double t0; // time between release of atoms and first Raman pulse [s]
  double sshot;//1.75e-12; // Single-shot sensitivity in m/s^2
  double timestep; // Repetition rate = timesteps for the simulation
  double C0; // Contrast (w/o gravity gradient reduction)
  double C_grad; // Contrast due to gravity gradients

// Specs for the EP test
  double target_eta; // target sensitivity

// Parameters for the simulation
  int rotation_scenario;  // Rotation scenario
    // 1: pointing-stabilised satellite
    // 2:  non-rotating satellite
    // 3: constant rotation rate synchronised with orbital period
  int g_grad; // switch on/off gravity gradient effect on contrast

// Kepler elements
  double perigee;
  double SMA;
  double eccentricity;

// Output files and parameters
  ofstream out_all, out_sens, out_part, out_outerloop;
  //string name_all, name_sens, name_part, name_outer;
  int save_orbitdata;
  int save_outerloop;

private:

};

//EOF
```

Listing B.3: Source code of the STE-QUEST orbit simulation.

```
//===============================================================================//
// Name        : KeplerProgram.cpp                                               //
// Author      : Ulrich Velte                                                    //
// Date:       : 2012/11/06                                                      //
// Version     : 2.0                                                             //
```

```
// Copyright   : GNU GPL                                                          //
// Description : Source code for the class KeplerProgram.                         //
//================================================================================//

#include "KeplerProgram.h"

/***********************************************************************************
* CONSTRUCTOR                                                                      *
***********************************************************************************/
KeplerProgram::KeplerProgram() {

  // Verbose settings
    // 0: run silently
    // 1: output EP results
    // 2: output Kepler parameters also
    // 3: output results for every step in numerical orbit simulation
    verbose = 0;

  // Parameters of the atomic source
    sigma_r = 60e-6; // initial size of the atom cloud [m]
    T_at = 0.07e-9; // temperature of atomic cloud at release time [K]

  // Parameters of the AI
    k_eff = 4*2*M_PI/780e-9;// effective k vektor for double diffraction
    T = 5; // time T between Raman pulses [s]
    t0 = 1.4; // time between release of atoms and first Raman pulse [s]
    sshot = sqrt(2)*0.001/(k_eff*T*T);// Single-shot sensitivity in m/s^2
    timestep = 10+2*T; // Repetition rate = timesteps for the simulation
    C0 = 1; // Contrast (w/o gravity gradient reduction)
    C_grad = 1; // Contrast due to gravity gradients

  // Specs for the EP test
    target_eta = 1e-15; // target sensitivity

  // Simulation Parameters
    rotation_scenario = 2; // Rotation scenario
      // 1: pointing-stabilised satellite
      // 2:  non-rotating satellite
      // 3: constant rotation rate synchronised with orbital period
    g_grad = 1; // switch on/off gravity gradient effect on contrast

  // Kepler Elements, use baseline orbit by default
    perigee = 700e3;
    SMA = 32027.356e3;
    // eccentricity is calculated from perigee and SMA

  // Open output files
    save_orbitdata = 0;
    save_outerloop = 0;

  // Initialize Kepler orbit: The Kepler engine needs (arbitrary) initial values,
  // The Kepler parameters used in the simulation are being set later
  kepl.kepler_init(t, pos, vel, elements, GM);
```

```

}


//*****************************************************
// Open files for outer loop
//*****************************************************
int KeplerProgram::InitOuterFiles(char outer_name[]="dummy_outer.ASC")
{
  save_outerloop = 1;
  // Open outer loop file
  if (save_outerloop) {
    cout << endl << "Open files out_outerloop " << outer_name;
    out_outerloop.open(outer_name);
    if (!out_outerloop.good()) {
      printf(" Bad input stream. Abort!\n");
      return 1;
    }
    else cout << " Ok." << endl;
  }
return 0;
}


//*****************************************************
// Open files for inner loop
//*****************************************************
void KeplerProgram::InitOrbitFiles(char all_name[]="dummy_all.ASC",
         char sens_name[]="dummy_sens.ASC", char part_name[]="dummy_part.ASC")
{
   save_orbitdata = 1;
  // Output file for complete orbit
  if (save_orbitdata) {
    cout << endl << "Open files out_all... " << all_name;
    out_all.open(all_name);
    if (!out_all.good()) {
      printf(" Bad input stream. Abort!\n");
      //break;
    }
    else cout << " Ok." << endl;
    out_all << " Orbit parameters for STE-QUEST orbit\n";
    out_all << " t[s]\tnu[rad]\tdnu/dt[mrad/s]\tr[m]\tv[m/s]\tg(r)[m/s^2]\teta\n";

    // Output file for part of the orbit up to alt_max
    cout << endl << "Open files out_sens... " << sens_name;
    out_sens.open(part_name);
    if (!out_sens.good()) {
      printf(" Bad input stream. Abort!\n");
      //break;
    }
    else cout << " Ok." << endl;
    out_sens << "# Orbit parameters for STE-QUEST orbit\n";
    out_sens << "# h_AI[m]\tsigma_eta/orbit\tn_shots\n";
```

```

    // Output file for part of the orbit up to alt_max
    cout << endl << "Open files out_part... " << part_name;
    out_part.open(sens_name);
    if (!out_part.good()) {
      printf(" Bad input stream in out_all. Abort!\n\n");
      //break;
    }
    else cout << " Ok." << endl << endl;
    out_part << " Orbit parameters for STE-QUEST orbit\n";
    out_part << " t[s]\tnu[rad]\tdnu/dt[mrad/s]\tr[m]\tv[m/s]\tg(r)[m/s^2]\teta\n";
  }

}


//******************************************************
// Close Files
//******************************************************
void KeplerProgram::CloseFiles() {
  // Close output streams for orbit data
  if (save_orbitdata) {
    if (verbose>0) cout << "Close orbit data files.\n";
    out_all.close();
    out_sens.close();
    out_part.close();
    save_orbitdata = 0;
  }
  // Close output streams for parameter variation data
  if (save_outerloop) {
    out_outerloop.close();
    out_outerloop.clear();
    if (verbose>0)  cout << "Close outer loop file.\n";
    save_outerloop = 0;
  }
  if (verbose>0) cout << endl;
}


//******************************************************
// DESTRUCTOR
//******************************************************
KeplerProgram::~KeplerProgram() {
  // Close output streams for orbit data
  if (save_orbitdata) {
    out_all.close();
    out_sens.close();
    out_part.close();
  }
  // Close output streams for parameter variation data
  if (save_outerloop) out_outerloop.close();
  if (verbose>1) cout << "Close outer loop file.\n";
}
```

```


//*****************************************************
// ORBIT SIMULATION LOOP
//*****************************************************
void KeplerProgram::OrbitSimulationLoop() {
  OrbitSimulationLoop(M_PI);
}

void KeplerProgram::OrbitSimulationLoop(double nu_end=M_PI) {

  //*****************************************************
  // PREPARE ORBIT SIMULATION
  //*****************************************************
  // Initialise variables
  t=0;
  h_AI = 750e3;
  r_old = 0;
  nu_old = 0;
  D_eta = 0; // Error for one shot (used temporarily only during simulation)
  S_eta = 0; // Sensitivity
  S_eta_orbit = 0; // Temporarily used during simulation
  step = 0;

  // Initialise AI parameters
  sshot = sqrt(2)*0.001/(k_eff*T*T);//1.75e-12; // Single-shot sensitivity in m/s^2
  timestep = 10+2*T; // Repetition rate = timesteps for the simulation

  // Calculate eccentricity as a function of perigee altitude
  eccentricity = 1 - (perigee+R_E)/SMA;

  // Set Kepler parameter:
  elements.typeorbit = EllEqu;
  elements.a = SMA; // SMA in Meter, nicht km!!!
  elements.ecc = eccentricity;
  elements.incl = 0; // Inclination = 0 -> coordinate system in orbital plane
  elements.argp = 0; // Arg. of periapsis = 0 -> coordinate system in orbital plane
  elements.nu = 0; // Start value of true anomaly set to zero
  elements.omega = 0; // RAAN
  elements.lonper = 0; // Longitude of periapsis

  // set start position to perigee, although reduntant with true anomaly nu
  // it does not work without setting mean anomaly
  elements.meananom = 0;
  elements.meananom_start = 0;

  // convert from kepler elements to cartesian coordinates and back,
  // to initalize missing kepler elements
  kepl.coe2rv(elements, elements.GM, pos, vel);
  kepl.rv2coe(pos,vel,GM,elements);

  if (verbose>1) {
      cout << "*** Initial Parameters ***\n";
```

```
      cout << "a=" << elements.a << ", ecc=" << elements.ecc << ", incl="
           << elements.incl << endl;
      cout << "argp=" << elements.argp << ", omega=" << elements.omega
           << ", nu=" << elements.nu << endl;
      cout << "m=" << elements.m << ", p=" << elements.p << ", b=" << elements.b
           << endl;
      cout << "meanmot=" << elements.meanmot << ", periodtime="
           << elements.periodtime << endl;
      cout << "coe2rv\n";
      cout << "\nnu=" << elements.nu  << ", r=" << absvecl(pos) << endl;
  }


//******************************************************
// START ORBIT SIMULATION LOOP
//******************************************************

  // Run loop starting at pergiee and ending at apogee
  for(t=0; elements.nu<=nu_end; t+=timestep){
    if (verbose>1) cout << "  t = " << t << "\r";

    // propagate orbit, convert propagated kepler elements to cartesian coordinates
    kepl.set_new_anomalies(t, elements);
    kepl.coe2rv(elements, elements.GM, pos, vel);

    if (verbose>1) {
        cout << "set_net_anomalies\ncoe2rv\n";
        cout << "\nnu=" << elements.nu  << ", r=" << absvecl(pos) << endl;
        cout << "r_per=" << elements.r_per << ", r_apo=" << elements.r_apo << endl;
        cout << "h_per=" << elements.r_per-R_E << ", h_apo=" << elements.r_apo-R_E
             << endl;
        cout << "meananom_start=" << elements.meananom_start << endl;
    }

    // Calculate single shot error on Eoetvoes ratio
    D_eta = (1/C0)*sshot/(GM/absvecl(pos)/absvecl(pos));

    // Choose rotation scenario
    // rotation_scenario == 1 -> pointing stabilised towards Earth
    if (rotation_scenario == 2) D_eta = D_eta/cos(elements.nu); // non-rotating
    else if (rotation_scenario == 3) { // constant rotation rate
      D_eta = D_eta/(cos(elements.nu-2*M_PI*t/elements.periodtime));
    }

    // Influence of gravity gradient on contrast
    double G_rr = -2*GM/pow(absvecl(pos),3); // gravity gradient in z direction
    if (g_grad) {
    double sigma_v = sqrt(kB*T_at/m_87Rb); // velocity distribution of atomic cloud
      double G_zz = cos(elements.nu)*G_rr + sin(elements.nu)*G_rr/2;
      C_grad = exp(-0.5*pow(k_eff*sigma_r*G_zz*T*T,2))
        * exp(-0.5*pow(k_eff*sigma_v*(t0+T)*G_zz*T*T,2));
      D_eta = D_eta/C_grad;
    }
```

```

    // integrate errors
    if (t==0) { // at perigee
      S_eta += D_eta*D_eta;
      step++;
      S_eta_orbit = sqrt(S_eta)/step;
      if (save_orbitdata) {
        out_part << t << "\t"
        << elements.nu << "\t"
        << (elements.nu-nu_old)*1000/timestep << "\t"
        << absvecl(pos) << "\t"
        << absvecl(vel) << "\t"
        << GM/absvecl(pos)/absvecl(pos) << "\t"
        << D_eta << endl;
      }
    }
    else { // since orbit is symmetrical only one half of the orbit is calculated
      S_eta += 2*D_eta*D_eta;
      step+=2;
      // Check if integrated sensitivity gets better or worse.
      if (sqrt(S_eta)/step<S_eta_orbit) {
        // If better, save data
        S_eta_orbit = sqrt(S_eta)/step;
        h_AI = absvecl(pos)-R_E;
        N_shots = step;
        if (verbose>1) cout << "D_eta = " << D_eta << ", S_eta = " << S_eta
                            << ", S_eta_orbit = " << S_eta_orbit << ", h_AI = "
                            << h_AI << ", N_shots = " << N_shots << endl;
        // Write results to file out_part (orbit up to h_AI)
        if (save_orbitdata) {
            out_part << t << "\t"
            << elements.nu << "\t"
            << (elements.nu-nu_old)*1000/timestep << "\t"
            << absvecl(pos) << "\t"
            << absvecl(vel) << "\t"
            << GM/absvecl(pos)/absvecl(pos) << "\t"
            << D_eta << endl;
        }
      }
      // If worse, S_eta_orbit is not altered and stores the best achievable
      // sensitivity for this orbit.
      // N_shots stores the number of shots for this sensitivity.
      // Nevertheless the orbit is simulated completely.
    }

    // Print results to screen
    if (verbose>2) {
         cout << "t=" << t << "s"
         << ", nu=" << elements.nu/2/M_PI*360 << "deg"
         << ", nu_t=" << (elements.nu-nu_old)*1000/timestep << "mrad/s"
         << ", r=" << absvecl(pos)/1000 << "km"
         << ", v=" << absvecl(vel) << "m/s"
         << ", g(r)=" << GM/absvecl(pos)/absvecl(pos) << "m/s^2"
```

```
       << ", eta=" <<  D_eta
       << ", G_rr=" << G_rr
       << ", C=" << C_grad*C0
       << ", S_eta_orbit=" << S_eta_orbit << endl;
  }

  // Write results to file out_all (complete orbit)
  if (save_orbitdata) {
      out_all << t << "\t"
      << elements.nu << "\t"
      << (elements.nu-nu_old)*1000/timestep << "\t"
      << absvecl(pos)/*-6371e3*/ << "\t"
      << absvecl(vel) << "\t"
      << GM/absvecl(pos)/absvecl(pos) << "\t"
      << D_eta << endl;
  }

        // Write results to file out_sense
  if (save_orbitdata) {
      out_sens << absvecl(pos)-R_E << "\t" << sqrt(S_eta)/step << "\t" << step
               << "\n";
  }


  r_old = absvecl(pos);
  nu_old = elements.nu;

}


// Print final Kepler parameters to screen
if (verbose>1) {
  cout << "\n*** Final Kepler Parameters ***\n";
  cout << "a=" << elements.a << ", ecc=" << elements.ecc << ", incl="
       << elements.incl << endl;
  cout << "argp=" << elements.argp << ", omega=" << elements.omega << ", nu="
       << elements.nu << endl;
  cout << "m=" << elements.m << ", p=" << elements.p << ", b=" << elements.b
       << endl;
  cout << "meanmot=" << elements.meanmot << ", periodtime="
       << elements.periodtime << endl;
  cout << "r_per=" << elements.r_per << ", r_apo=" << elements.r_apo << endl;
  cout << "h_per=" << elements.r_per-R_E << ", h_apo=" << elements.r_apo-R_E
       << endl;
  cout << "GM=" << GM << endl;
  cout << "END" << endl;
}

// Print orbit results to screen
if (verbose) {
  cout << "\n*** Overall Eoetvoes error ***\n";
  cout << "AI runs up to " << h_AI/1000 << "km over ground, corresponds to "
       << N_shots*timestep << "s or " << N_shots << " shots.\n";
```

```
    cout << N_shots << " shots per orbit -> S_eta_orbit=" << S_eta_orbit
         << " for one orbit.\n";
    cout << "\nTarget sensitivity is target_eta=" << target_eta << "." << endl;
    N_orbits = (S_eta_orbit/target_eta)*(S_eta_orbit/target_eta);
    cout << "(b) -> N_orbits=" << N_orbits << ", corresponds to "
         << N_orbits*2/3 << " days or " << N_orbits*2/3/365
         << " years of mission time." << endl;
  }

}

//EOF
```

C. Schematic of the phase detector

The complete schematic is distributed to three documents:

1. Main diagram
2. Status LED
3. Power supply
4. Assembly print

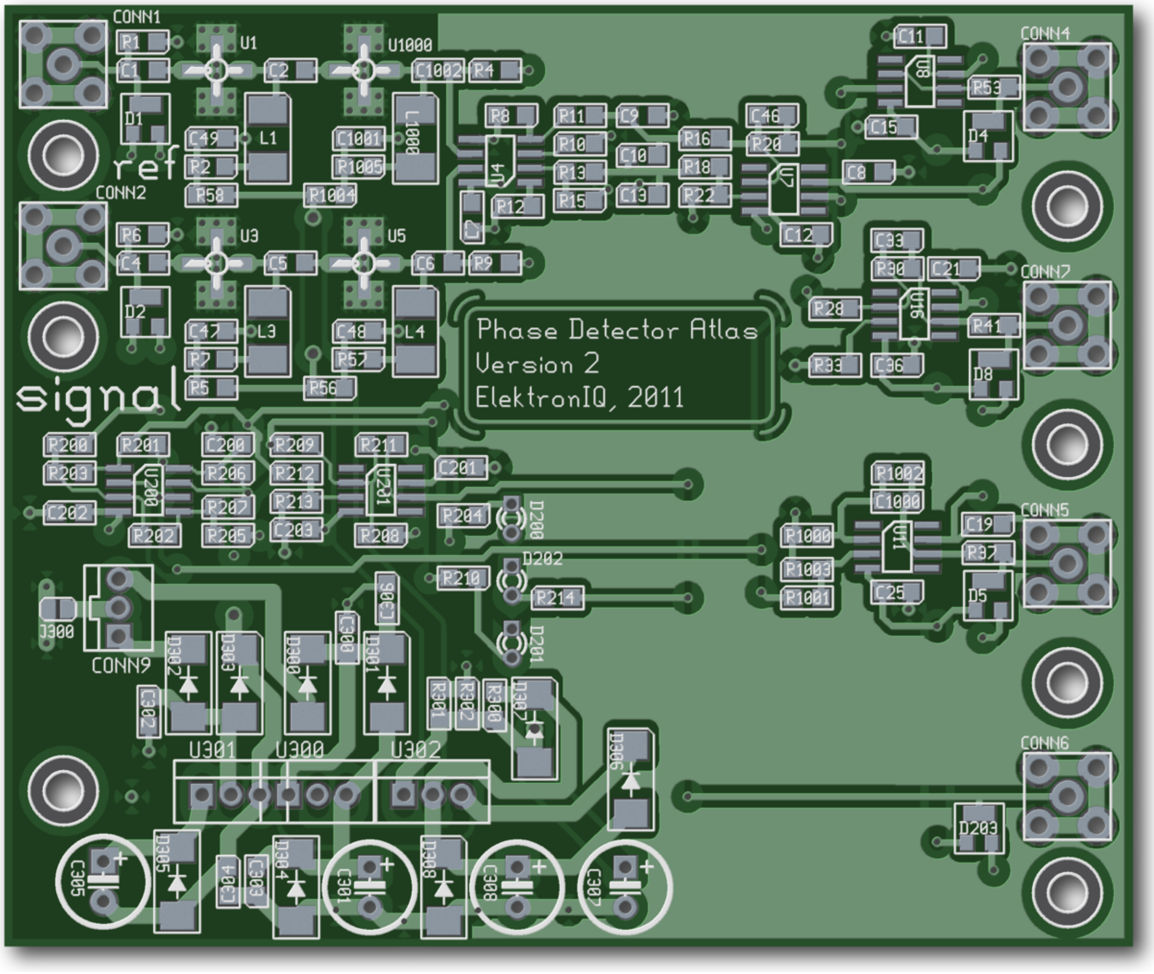

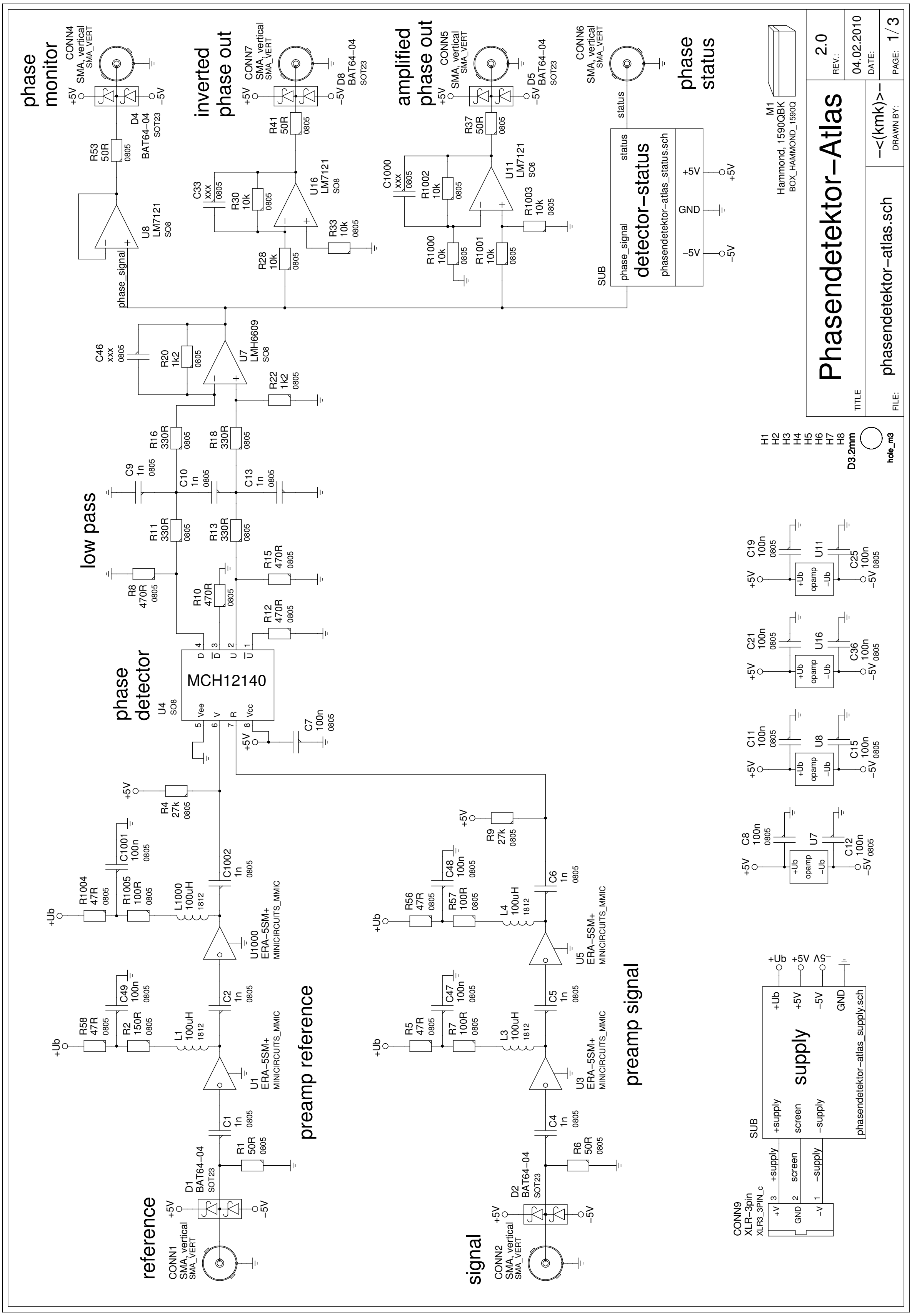
reference
CONN1
SMA_vertical
SMA_VERT
D1
BAT64–04
SOT23
R1
50R
C1
1n
U1
ERA–5SM+
MINICIRCUITS_MMIC
L1
100uH
1812
R2
150R
R58
47R
C49
100n
C2
1n
U1000
ERA–5SM+
L1000
100uH
R1005
100R
R1004
47R
C1001
100n
C1002
1n
R4
27k
preamp reference
signal
CONN2
D2
BAT64–04
R6
50R
C4
1n
U3
ERA–5SM+
L3
100uH
R7
100R
R5
47R
C47
100n
C5
1n
U5
ERA–5SM+
L4
100uH
R57
100R
R56
47R
C48
100n
C6
1n
R9
27k
preamp signal
phase detector
U4
SO8
MCH12140
Vee
V
R
Vcc
D
D̄
U
Ū
C7
100n
R8
470R
R10
470R
R12
470R
R15
470R
low pass
R11
330R
R13
330R
C9
1n
C10
1n
C13
1n
R16
330R
R18
330R
R22
1k2
U7
LMH6609
R20
1k2
C46
xxx
phase_signal
U8
LM7121
R53
50R
D4
BAT64–04
phase monitor
CONN4
SMA_vertical
U16
LM7121
R28
10k
R30
10k
C33
xxx
R33
10k
R41
50R
D8
BAT64–04
inverted phase out
CONN7
U11
LM7121
R1000
10k
R1001
10k
R1002
10k
R1003
10k
C1000
xxx
R37
50R
D5
BAT64–04
amplified phase out
CONN5
SUB
phase_signal
status
detector–status
phasendetektor–atlas_status.sch
+5V
GND
–5V
status
phase status
CONN6
SMA_vertical
M1
Hammond_1590QBK
BOX_HAMMOND_1590Q
Phasendetektor–Atlas
TITLE
phasendetektor–atlas.sch
FILE:
2.0
REV.:
04.02.2010
DATE:
–(kmk)>–
DRAWN BY:
1/3
PAGE:
H1 H2 H3 H4 H5 H6 H7 H8
D3.2mm
hole_m3
C19
100n
U11
C25
100n
C21
100n
U16
C36
100n
C11
100n
U8
C15
100n
C8
100n
U7
C12
100n
opamp
+Ub
–Ub
SUB
supply
phasendetektor–atlas_supply.sch
+supply
screen
–supply
+Ub
+5V
–5V
GND
CONN9
XLR–3pin
XLR3_3PIN_c
+V
GND
–V

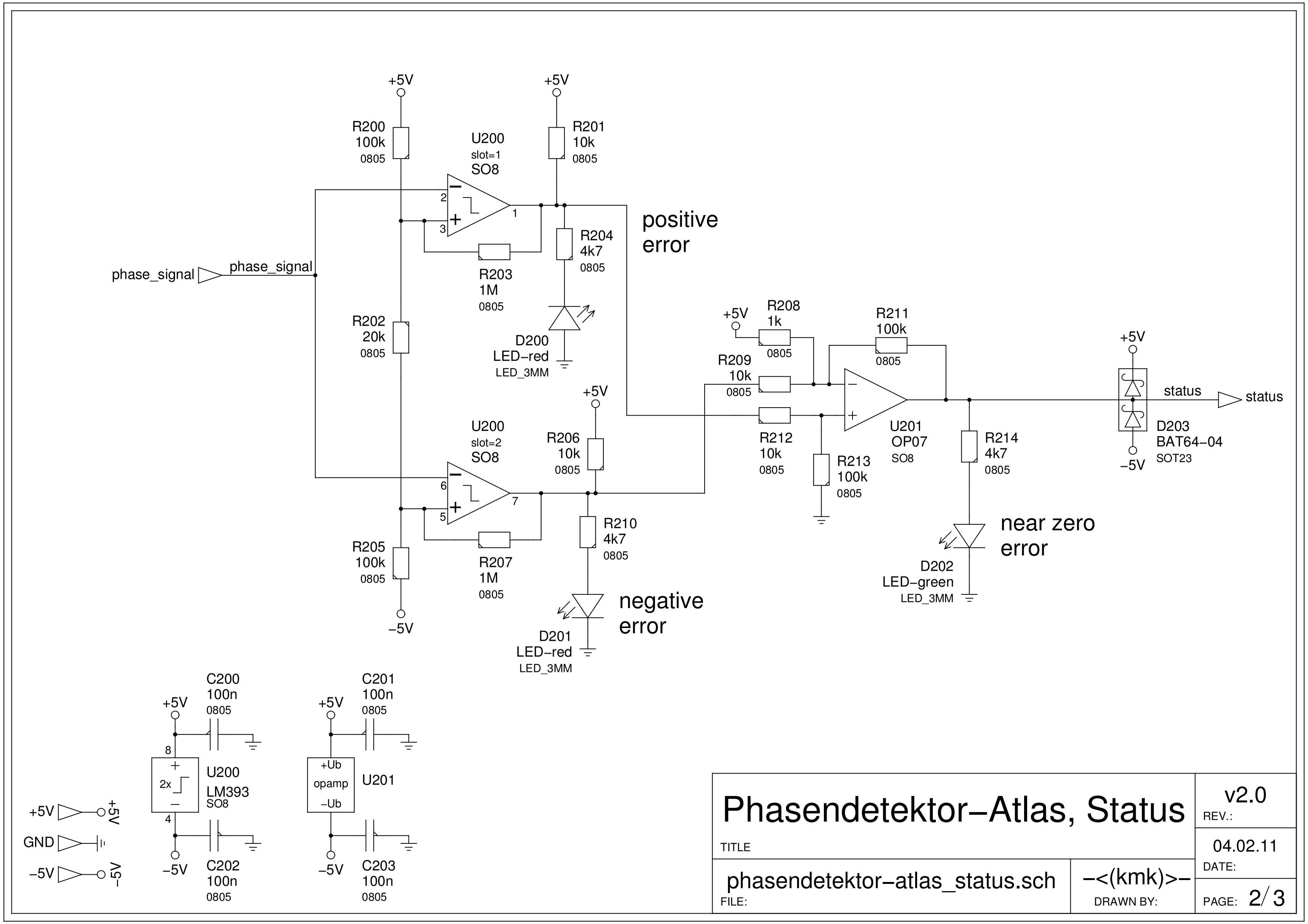

Phasendetektor–Atlas, Status

TITLE

v2.0

REV.:

04.02.11

DATE:

phasendetektor–atlas_status.sch

FILE:

–<(kmk)>–

DRAWN BY:

PAGE: 2/3

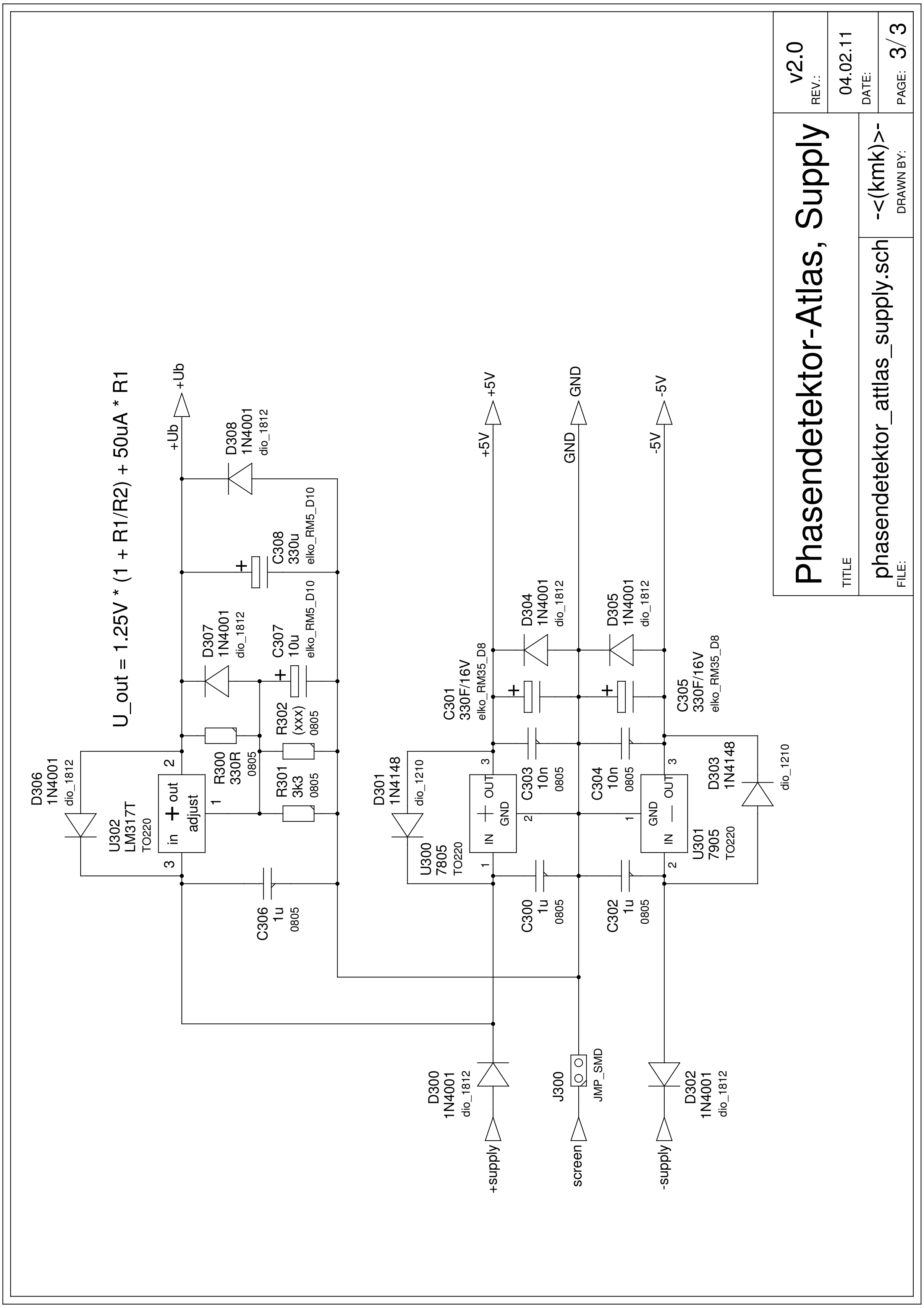
U_out = 1.25V * (1 + R1/R2) + 50uA * R1
+Ub
D308
1N4001
dio_1812
C308
330u
elko_RM5_D10
D307
1N4001
dio_1812
C307
10u
elko_RM5_D10
R302
(xxx)
0805
R300
330R
0805
R301
3k3
0805
D306
1N4001
dio_1812
U302
LM317T
TO220
in
out
adjust
C306
1u
0805
+5V
GND
-5V
C301
330F/16V
elko_RM35_D8
D304
1N4001
dio_1812
D305
1N4001
dio_1812
C305
330F/16V
elko_RM35_D8
D301
1N4148
dio_1210
C303
10n
0805
C304
10n
0805
D303
1N4148
dio_1210
U300
7805
TO220
IN
OUT
GND
U301
7905
TO220
C300
1u
0805
C302
1u
0805
D300
1N4001
dio_1812
J300
JMP_SMD
D302
1N4001
dio_1812
+supply
screen
-supply
Phasendetektor-Atlas, Supply
TITLE
phasendetektor_attlas_supply.sch
FILE:
-<(kmk)>-
DRAWN BY:
v2.0
REV.:
04.02.11
DATE:
3/3
PAGE:

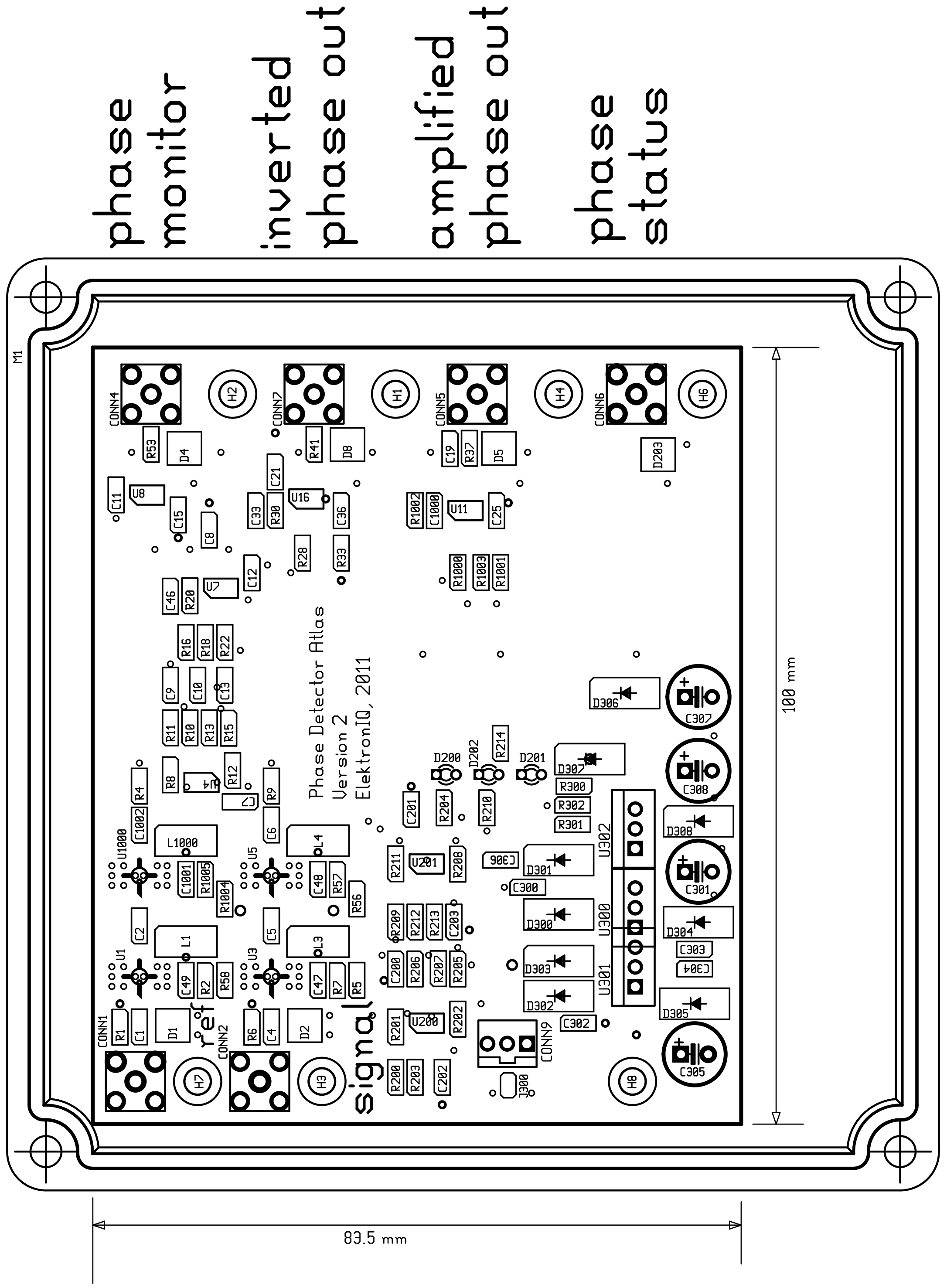
phase monitor
inverted phase out
amplified phase out
phase status
ref
signal
Phase Detector Atlas
Version 2
ElektronIQ, 2011
CONN1
CONN2
CONN4
CONN5
CONN6
CONN7
CONN9
H1
H2
H3
H4
H6
H7
H8
M1
U300
U301
U302
100 mm
83.5 mm

Grid (1 , 1)

D. Theoretical model of the open loop transfer function.

Listing D.1: Mathematica 7 script used for the simulation of the OPLL transfer function.

```
(* HOCHPASS *)
HP[s_,f_]:=(s)/(f+s);

(* TIEFPASS} *)
TP[s_,f_]:=f/(f+s);

(* LEAD-LAG FILTER *)
LeadLag[s_,fl_,fh]:=(1+s/fh)/(1+s/fl);

(* 2-ZERO 2-POLE NOTCH FILTER*)
Notch[s_,fc_,c_,d_]:=(s^2+2*d/c*fc*s+fc^2)/(s^2+1/c*fc*s+fc^2);

(* TIME-DELAY *)
DELAY[s_,delay_]:=Exp[-2*Pi*s*delay];

(* PID CONTROLLER *)
PID[s_,P_,I_,D_,K_]:=K*(P+I/(2*Pi*s)+D*2*Pi*s);

(* ECDL CURRENT PATH OF CONTROL LOOP *)
SPath[s_]:=spathK*HP[s,5000]*TP[s,322000]*DELAY[s,50*10^-9];
SPath2[s_]:=spathK*HP[s,5000]*LeadLag[s,322000,2000000]*DELAY[s,75*10^-9];
SPathC[s_]:=SPath[s]*HP[s,800]*Notch[s,160000,2,0.09];
SPathC2[s_]:=SPath2[s]*HP[s,800]*Notch[s,160000,2,0.09];
SPathCDC[s_]:=SPathDC[s]*HP[s, 800];
SPathPI[s_]:=SPathC[s]*PID[s,1,10000,0,1];

(* LOOP TRANSFER FUNCTIONS *)
GPZT[s_]:=(PID[s,0.2,100,0,4000]*TP[s,800])/s;
GPZT2[s_]:=(PID[s,0.2,100,0,4000]*TP[s,1])/s;
G[s_]:=(SPath[s]+PID[s,0.2,100,0,4000]*TP[s,800])/s;
GC[s_]:=(SPathC[s]+PID[s,0.2,100,0,4000]*TP[s,800])/s;
GC2[s_]:=(SPathC2[s]+PID[s,0.2,100,0,4000]*TP[s,800])/s;
GPI[s_]:=(SPathPI[s]+PID[s,0.2,100,0,4000]*TP[s,800])/s;
GPI2[s_]:=(SPathPI[s]+PID[s,0,400,0,4000]*TP[s,1])/s;
HC2[s_]:=GC2[s]/(1+GC2[s]);
HPI2[s_]:=GPI2[s]/(1+GPI2[s]);
ErC2[s_]:=1-HGC2[s];
ErPI2[s_]:=1-HPI2[s];
Improves[s_]:=ErPI2[s]/ErC2[s];

(* BODE PLOT *)
(* This is for Mathematica 7. In Mathematica >8.0 use BodePlot[] instead! *)
LogLinearPlot[20*Log10[Abs[GC[I*f]]],{f,1,10000000}]
LogLinearPlot[Arg[GC[I*f]]/(2*Pi)*360,{f,1,10000000}]
```

E. Schematic for the measurement of the open loop transfer function

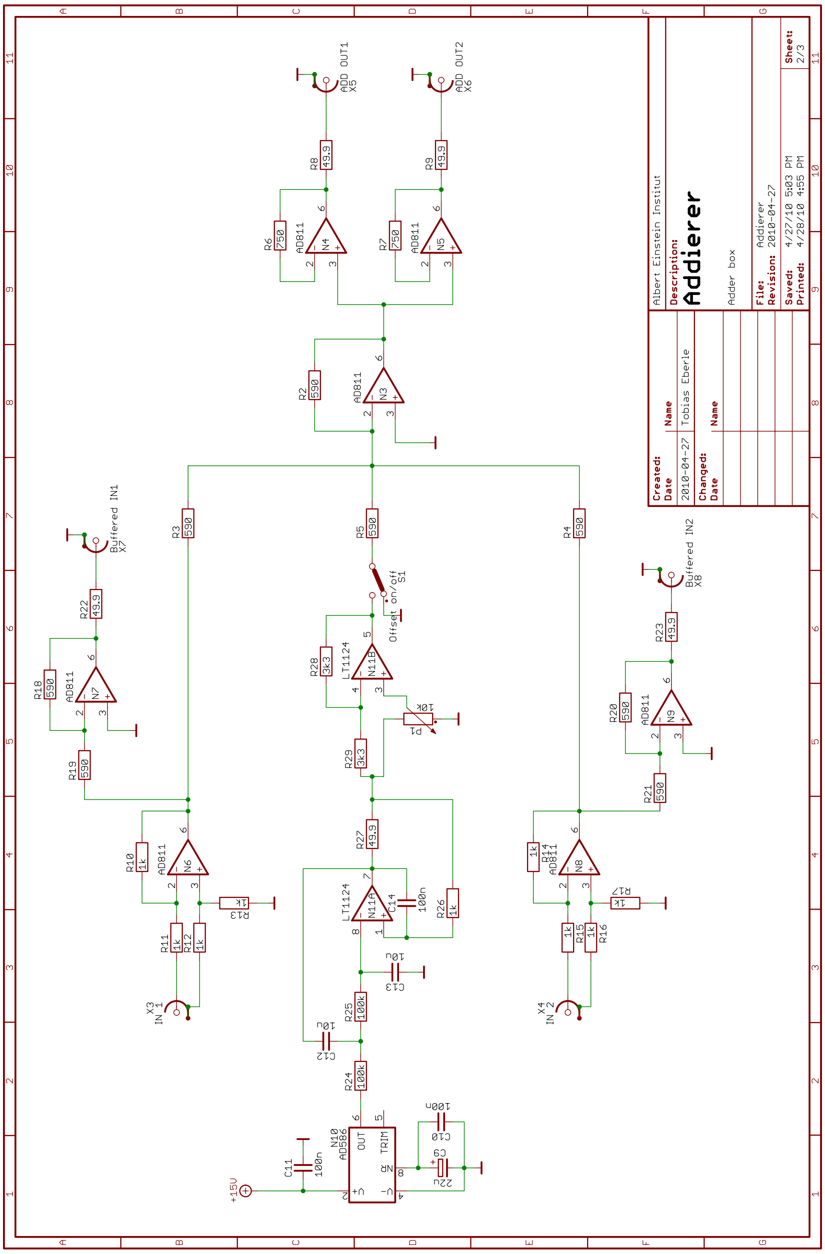

F. Schematic of the 6.9 GHz microwave generation

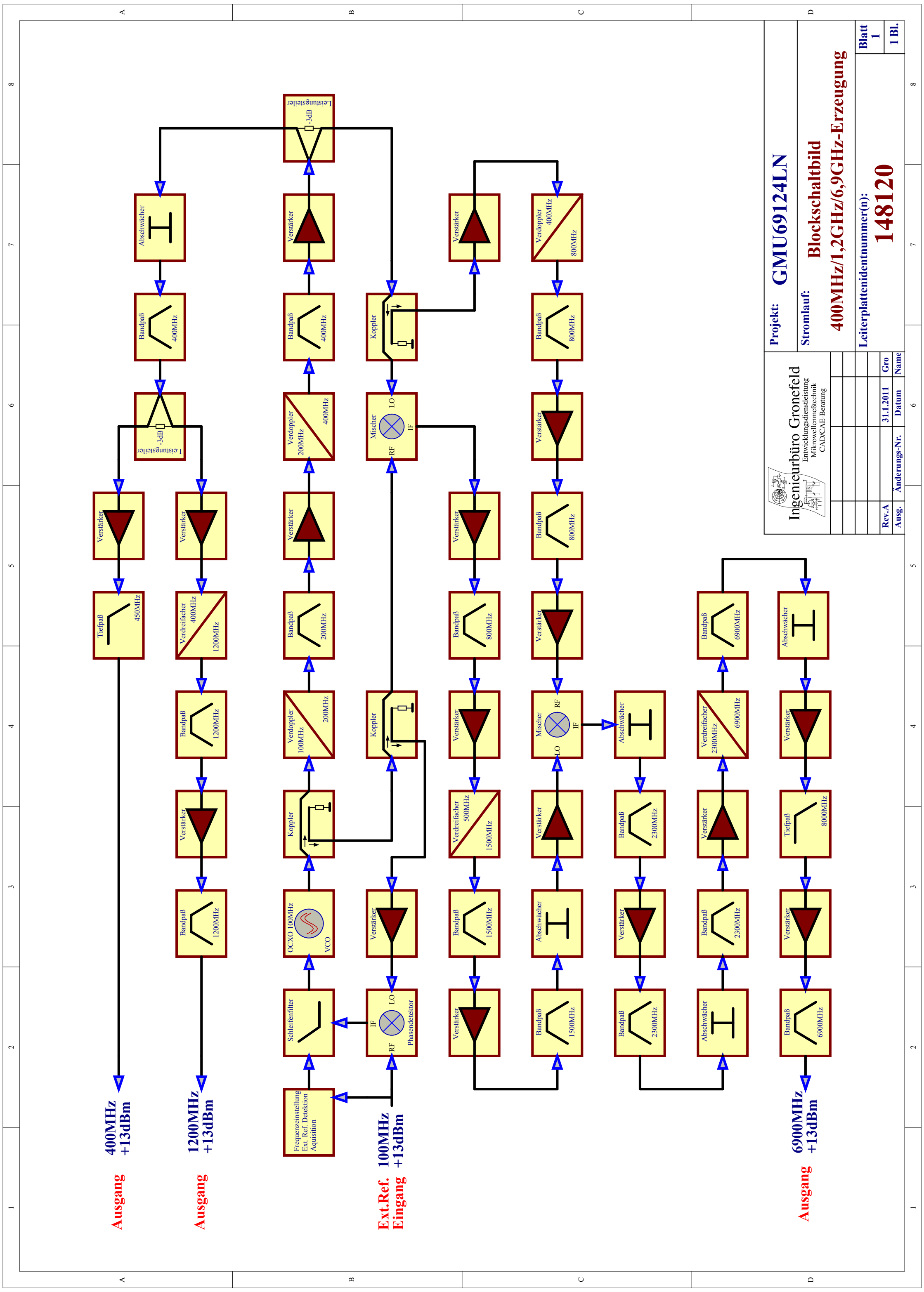
Projekt: GMU69124LN
Stromlauf: Blockschaltbild 400MHz/1,2GHz/6,9GHz-Erzeugung
Leiterplattenidentnummer(n): 148120
Blatt 1
1 Bl.
Ingenieurbüro Gronefeld
Entwicklungsdienstleistung
Mikrowellenmeßtechnik
CAD/CAE-Beratung
Rev.A
31.1.2011
Gro
Ausg.
Änderungs-Nr.
Datum
Name
Ausgang
400MHz
+13dBm
Ausgang
1200MHz
+13dBm
Ext.Ref. Eingang
100MHz
+13dBm
Ausgang
6900MHz
+13dBm
Frequenzeinstellung Ext. Ref. Detektion Aquisition
Schleifenfilter
Phasendetektor
OCXO 100MHz
VCO
Koppler
Verdoppler 100MHz 200MHz
Bandpaß 200MHz
Verstärker
Verdoppler 200MHz 400MHz
Bandpaß 400MHz
Leistungsteiler -3dB
Abschwächer
Tiefpaß 450MHz
Verdreifacher 400MHz 1200MHz
Bandpaß 1200MHz
Mischer
RF
LO
IF
Bandpaß 800MHz
Verdreifacher 500MHz 1500MHz
Bandpaß 1500MHz
Verdoppler 400MHz 800MHz
Bandpaß 2300MHz
Verdreifacher 2300MHz 6900MHz
Bandpaß 6900MHz
Tiefpaß 8000MHz
A
B
C
D
1
2
3
4
5
6
7
8

Acknowledgement

Thank you to all human beings
who are thinking good things about the small
and the big things in our world! Be happy!

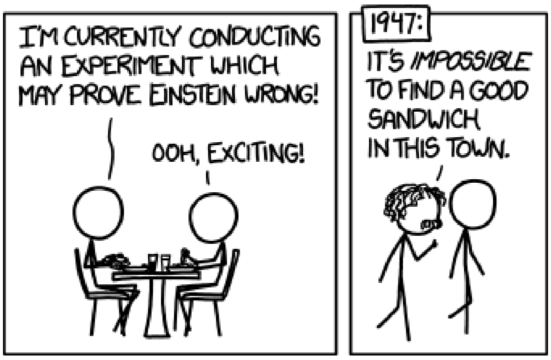

[184]